RICE UNIVERSITY

The Study of $W\gamma$ Production at DØ: Anomalous Coupling Limits and the Radiation Amplitude Zero

by

Gregory J. Pawloski

A Thesis Submitted
in Partial Fulfillment of the
Requirements for the Degree

DOCTOR OF PHILOSOPHY

Approved, Thesis Committee:

B. Paul Padley, Chair
Associate Professor of Physics and Astronomy

Marjorie Corcoran
Professor of Physics and Astronomy

David Damanik
Associate Professor of Mathematics

Houston, Texas

June, 2007

ABSTRACT

The Study of $W\gamma$ Production at DØ: Anomalous Coupling Limits and the Radiation Amplitude Zero

by

Gregory J. Pawloski

$W\gamma$ production is analyzed in the electron and muon decay channels with approximately 1 fb^{-1} of data from $p\bar{p}$ collisions that were produced at a center-of-mass energy of $\sqrt{s} = 1.96\ TeV$ and that were collected by the DØ detector at the Fermilab Tevatron collider. The inclusive $p\bar{p} \rightarrow \ell\nu\gamma$ cross section is measured in both channels and is found to be consistent with the Standard Model expectation of $2.08 \pm 0.05_{PDF}\ pb$ for events with a photon $E_T > 11\ GeV$, $\Delta R_{\ell\gamma} > 0.7$, and $\ell\nu\gamma$ transverse mass greater than 90 GeV. The observed cross section is measured to be $2.05 \pm 0.18_{stat} \pm 0.10_{sys} \pm 0.13_{lumi}\ pb$ and $1.72 \pm 0.19_{stat} \pm 0.15_{sys} \pm 0.10_{lumi}\ pb$ for the electron and muon channels respectively.

The photon E_T spectrum is examined for indications of anomalous $WW\gamma$ couplings. No evidence is found, and the following one-dimensional limits are set at a 95% confidence level: $-0.18 < \lambda < 0.18$ and $0.16 < \kappa < 1.84$.

The observed charge-signed photon-lepton rapidity difference is consistent with the Standard Model prediction and is indicative of the theoretically expected radiation amplitude zero. The distribution exhibits a bimodal structure which is expected from the destructive interference, with the unimodal hypothesis being ruled out at the 94% confidence level.

Contents

List of Figures

List of Tables

Preface

In this analysis, hadronic collisions are analyzed to sample events that are consistent with the signatures of $W\gamma$ production. Through this examination, the gauge structure of the Standard Model of particle physics is probed by analyzing the energy spectrum and angular distribution of the observed events to test for theoretically predicted features of the Standard Model and to search for evidence of nongauge interaction couplings between the W boson and the photon. In the case of a null discovery of new physics, limits on the coupling values are presented.

An introduction to the physical theory behind $W\gamma$ production and how the study of this state permits the validation of the Standard Model gauge theory is presented in the first chapter of this thesis (*The Physics*). In the second chapter an overview of the experimental apparatus needed to perform this analysis is provided (*The Instrumentation*). The third chapter explains how the data from detector measurement is reconstructed into physical quantities (*The Reconstruction*). The fourth chapter covers the selection of the reconstructed collision events that are consistent with $W\gamma$ production as well as the associated efficiencies and backgrounds (*The Event Selection, Efficiencies, and Backgrounds*). The fourth chapter covers the examination of the $W\gamma$ candidate sample (*The Analysis*). A summary of the results from this analysis is provided in the concluding chapter (*The Conclusion*).

Throughout this thesis, references will be made to terms and concepts that are commonly understood by individuals in the particle physics community, but may not be known by those who are not in the field. These terms, if not described in the text, are highlighted in boldface, and a brief description that is relevant to the thesis content is provided in a glossary that is found in the Appendix. Several acronyms will also be used throughout the text; an alphabetical listing of these acronyms can be found in the Appendix. Unless otherwise noted, the "natural" system of units where the speed-of-light (c) and Planck's constant ($\hbar$) are equal to one will be used throughout this document.

Chapter 1
The Physics

The Standard Model of particle physics represents the current physical understanding of the **electroweak** and **strong color-charged forces**. It is derived from the minimal mathematical representation of a quantum **field theory** that contains fields that are invariant under local $SU(2) \otimes U(1)$ **gauge transformations** for the electroweak interactions and fields that are invariant under local $SU(3)$ gauge transformations for the strong color-charged interactions. The requirement of local gauge invariance ensures that the apparent divergences, which appear in the theory, can be renormalized away. However, the particular set of gauge symmetries considered is not theoretically predetermined but is set according to experimental observation. A more detailed introduction into the theory behind the Standard Model can be found in [1] and [2].

1.1 The Standard Model Menagerie

Quantum excitations of the observed Standard Model fields are represented by particles which belong to one of two categories: **spin-$\frac{1}{2}$ fermions** or spin-1 **vector gauge bosons**. Within the theory, the fermions interact through the exchange of **bosons**, which mediate the forces. Among the bosons, there are the gluons (g) which mediate the strong color-charged interaction, the W and Z bosons which mediate the

weak force, and the photon (γ) which mediates the electromagnetic force.

The fermions are organized in two categories: quarks which carry a color-charge and leptons that are color-neutral. The fermions are further subdivided into three generations. Among each generation, the quarks and leptons are each classified by a **left-handed** doublet and **right-handed** singlets. Loosely defined, each generation can be considered a "copy" of the other generations in which the corresponding particles have different masses. For each force, the generations represent orthogonal eigenstates; however, these eigenstates are not necessarily the same for each interaction. Since in each generation the "related" particles have the same **quantum numbers**, it is possible for there to be a mixing (a linear combination) between the eigenstates of the various interactions. Through experiment, a mixing has been observed in both the quark and lepton sectors. This has interesting implications which are reviewed in [3]. A summary of the particle characteristics can be found in Table 1.1.

For each of the particles listed in Table 1.1, there is an antiparticle*, which has the set of opposite-valued charges. Note that some particles can be their own antiparticles, such as the photon and Z, which have zero-valued quantum numbers for charge. It remains an experimental question whether the neutrino, the only known neutral-charged fundamental fermion, is its own antiparticle.

*By convention, the antiparticle is represented by the particle symbol with a horizontal bar over it. For instance the positron, the antielectron, would be represented by $\bar{e}$.

Boson	**Mass** $[GeV]$	**Electric Charge** $[e^+]$	**Color Charge**
$W^{\pm}$	80.403 ± 0.029	± 1	–
Z	91.1876 ± 0.0021	–	–
γ (photon)	$m_{exp.} < 6 \times 10^{-26}$ $m_{theory} = 0$	–	–
g (gluon)	$m_{theory} = 0$	–	$r\bar{g}$, $r\bar{b}$, $g\bar{b}$, $g\bar{r}$, $b\bar{r}$, $b\bar{g}$, $\sqrt{1/2}(r\bar{r} - g\bar{g})$, $\sqrt{1/6}(r\bar{r} + g\bar{g} - 2b\bar{b})$

Quark	**Mass** $[GeV]$	**Electric Charge** $[e^+]$	**Color Charge**
u (up)	$0.0015 - 0.0030$	$+2/3$	r,b,g
d (down)	$0.003 - 0.007$	$-1/3$	r,b,g
c (charm)	1.25 ± 0.09	$+2/3$	r,b,g
s (strange)	95 ± 25	$-1/3$	r,b,g
t (top)	174.2 ± 3.3	$+2/3$	r,b,g
b (bottom)	4.20 ± 0.07	$-1/3$	r,b,g

Lepton	**Mass** $[MeV]$	**Electric Charge** $[e^+]$	**Color Charge**
e (electron)	$0.51099892 \pm 4 \times 10^{-8}$	-1	–
ν_e (e neutrino)	*not a mass eigentstate*	–	–
μ (muon)	$105.658369 \pm 9 \times 10^{-6}$	-1	–
ν_μ (μ neutrino)	*not a mass eigentstate*	–	–
τ	$1776.99^{+0.29}_{-0.26}$	-1	–
ν_τ (τ neutrino)	*not a mass eigentstate*	–	–

Table 1.1 The observed fundamental particles. [3]

1.2 Gauge Theory of the Interactions

The electromagnetic current has a $U(1)$ structure with the electric-charge operator generating the symmetry group. It is this single generator and the requirement of invariance under local gauge transformations which implies the existence of a single boson that mediates the electromagnetic force. Similarly, for the strong color-charged force, the quarks are organized into an $SU(3)$ color group triplet with eight color-currents that contain the generators for the $SU(3)$ group. It is these eight generators and local gauge invariance which imply the existence of eight bosons that mediate the strong color-charged force.

Likewise, the charged-current of the weak interactions, which is mediated by the W, can be described by an $SU(2)$ theory in which only left-handed fermions or right-handed antifermions participate in the interaction. For the $SU(2)$ group there are three generators which imply the existence of three bosons. Two of them can be identified with the charged W. However, the third boson has the same quantum numbers as the boson from the $U(1)$ theory. Hence, it is theoretically possible that the physically observed neutral-charged mediators of the electromagnetic and weak interactions are linear combinations of these two bosons. Experimentally, this is determined to be the case, and the mixing leads to a neutral-current of the weak interaction that is mediated by the Z boson which couples to both left-handed and right-handed fermions. Because of the mixing between these mediators, the term,

electroweak interaction, is used to described the forces that are derived from the $SU(2) \otimes U(1)$ structure. Equations 1.1 and 1.2 show how the resulting photon field (A_μ) and Z field (Z_μ) are related to the initial neutral-charged mediators of $SU(2)$ theory (W^3_μ) and the $U(1)$ theory (B_μ):

$$A_\mu = \cos(\theta_{\mathrm{W}})\mathrm{B}_\mu + \sin(\theta_{\mathrm{W}})\mathrm{W}^3_\mu, \tag{1.1}$$

$$Z_\mu = -\sin(\theta_{\mathrm{W}})\mathrm{B}_\mu + \cos(\theta_{\mathrm{W}})\mathrm{W}^3_\mu. \tag{1.2}$$

By requiring that the mixture produces the observed photon of the electromagnetic interaction, the value of the mixing angle (θ_W) is completely constrained by the values of the electromagnetic **coupling** (α_e) and the weak coupling (α_w). This leaves four remaining free parameters in the electroweak theory*. They are α_e, G_F†, and the masses of the Z (m_Z) and W (m_W). These parameters have been measured through experiment (see Table 1.2), and hence the electroweak theory is fully constrained.

α_e:	$7.297352568 \times 10^{-3} \pm 2.4 \times 10^{-11}$
G_F:	$1.16637 \times 10^{-5} \pm 1 \times 10^{-10}\ GeV^{-2}$
m_W:	$80.403 \quad \pm 0.029 \quad GeV$
m_Z:	$91.1876 \pm 0.0021\ GeV$

Table 1.2 The free parameters of the electroweak theory. [3]

As presented here, the electroweak theory is not completely self-consistent. For the theory to be truly invariant under local gauge transformations and hence be

*Higgs mechanisms will further constrain the theory by relating m_Z and m_w.

†G_F is the Fermi constant and is related to the weak coupling by $G_F = \frac{\alpha_w \pi}{\sqrt{2} m_W^2}$.

renormalizable, the bosons cannot be massive. Furthermore, in order for the theory to maintain a left-handed $SU(2)$ gauge invariance, the fermions must also be massless. However, nature is observed to violate both of these conditions. To preserve the gauge symmetry, additional structure must be included in the theory to provide a mechanism for spontaneous symmetry breaking that reveals the particle masses. The nature of this process has not been experimentally observed; however, there are various Higgs mechanisms that can potentially satisfy this condition. A complete discussion of this process would be a digression from the current topic, but more information can be found in [1] and [2].

1.3 Probing the $SU(2) \otimes U(1)$ Gauge Structure

Electroweak theory permits the self-interaction of the gauge fields with the structure of the interactions being completely fixed by the gauge symmetry of the theory and the experimental measurement of the free parameters. Hence, the study of the boson-only interaction vertices is a powerful probe of the electroweak sector. Experimentally, it is possible to examine the triple gauge boson coupling though the analysis of the coproduction of two bosons in **hadronic** collisions as shown in Figure 1.1. In particular the $W\gamma$ process, allows for the study of some very distinct features of the gauge symmetry.

It can be shown that for a certain region of phase space, the leading order perturbative calculation of the interaction amplitude can vanish for a process that involves the

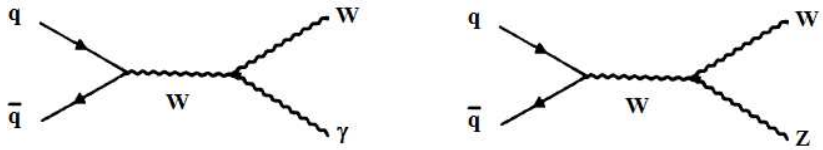

Figure 1.1 The triple gauge coupling vertex for some select diboson processes.

emission of a massless gauge boson and an arbitrary number of external charged particles, if all the couplings are described by a local gauge theory [4]. For a photon with **four-momentum**, q, and n particles with electric-charge, Q_i, and four-momentum, p_i, these zero amplitudes occur if:

$$\frac{Q_i}{p_i \cdot q} = \frac{Q_j}{p_j \cdot q}, \text{ for all } i \text{ and } j. \tag{1.3}$$

For a $2 \to 2$ particle process, like $q\bar{q} \to W\gamma$, this simplifies to an angular dependence:

$$\cos(\theta^*) = \frac{Q_1 - Q_2}{Q_1 + Q_2}, \tag{1.4}$$

where Q_1 and Q_2 are the electric-charges of the incoming particles, and θ^* is the **center-of-mass** angle of the photon with respect to the direction of particle 2. For $W\gamma$ production, if θ^* is defined with respect to the antiquark, then this reduces to $\cos(\theta^*) = \frac{1}{3}$ $(-\frac{1}{3})$ for the positively (negatively) charged final state. This point is known as the radiation amplitude zero (RAZ) and is caused by the complete destructive interference of the leading order $W\gamma$ production diagrams shown in Figure 1.2. At higher orders, loop diagrams contribute to the production amplitude; since the loop momentum is not fixed, these loop corrections do not exhibit a zero [4].

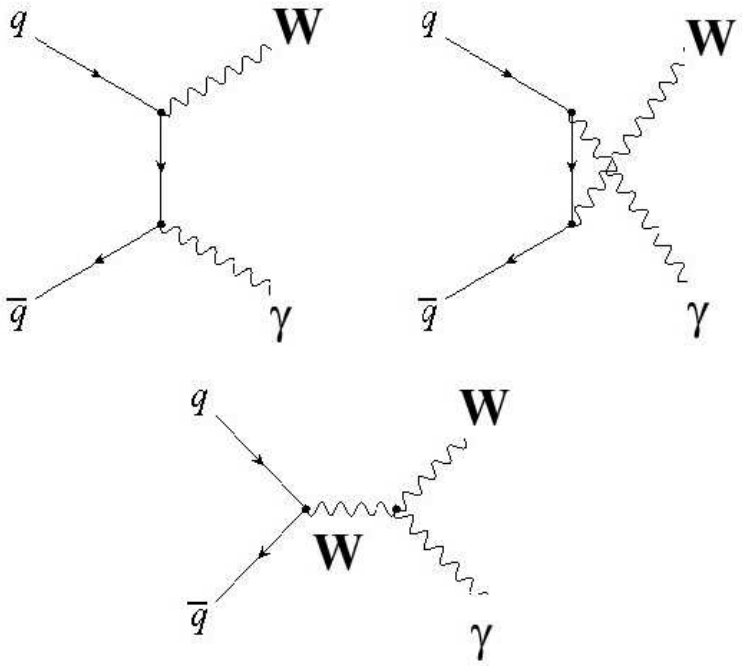

Figure 1.2 The leading order prompt $W\gamma$ production diagrams from quark annihilation.

There are many experimentally observable implications that arise from this destructive interference. Typically, the single Z production rate from hadronic collisions is about half that of the W production rate. This is because the Z-quark vertex coupling is almost half that of the W-quark. However for moderate energies, this is the opposite for prompt $W\gamma$ and prompt $Z\gamma$ production which can be seen in Figure 1.3 [5]. The leading order destructive interface leads to a dramatic decrease in the $W\gamma$ production **cross section**. Furthermore, the interference produces distinct features in the differential cross sections. Naturally, it creates a pronounced dip in the angular

distribution of the photon production as shown in Figure 1.4. However, because this interference is at large scattering angles, there is also a reduction in the number of photons produced with large **transverse energy** (E_T). This means that the $W\gamma$ photon E_T spectrum will fall off more rapidity than for the $Z\gamma$ spectrum that has no such interference [4]. See Figure 1.5.

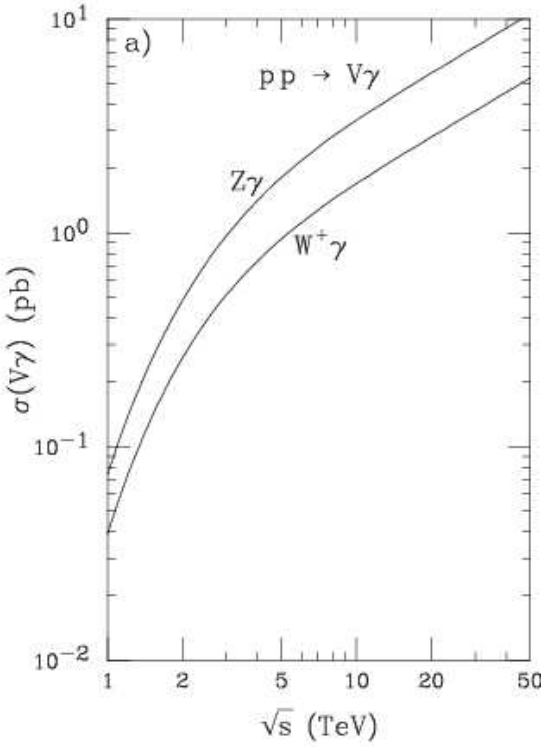

Figure 1.3 The leading order Born cross section for prompt $W\gamma$ and prompt $Z\gamma$ production. [5]

The inclusion of physics beyond the Standard Model may effectively alter the $WW\gamma$ coupling and hence reduce the destructive interference, spoiling the exact can-

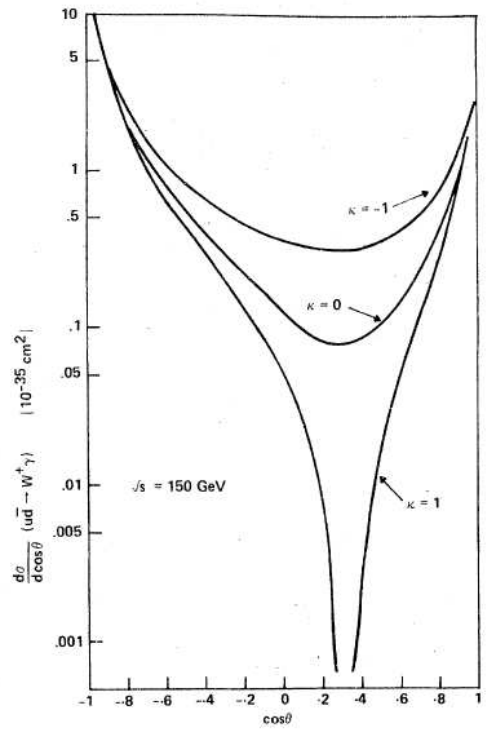

Figure 1.4 The center-of-mass angular distribution for $W\gamma$ production from quark annihilation. [6]

cellation at $\cos(\theta^*) = \pm\frac{1}{3}$. This would then cause an increase in the total production cross section, a slower falling photon E_T spectrum, and a less prominent dip, if any, in the angular distribution. Unaccounted for loop contributions from potential Technicolor [7] [8], Super-Symmetric [9], and two Higgs-doublet [10] theories can produce this effective behavior.

It is possible to represent the potential divergences, in a model-independent way, by constructing an effective **Lagrangian density**. The most general Lorentz invariant form that maintains the minimal electromagnetic gauge invariance and is also

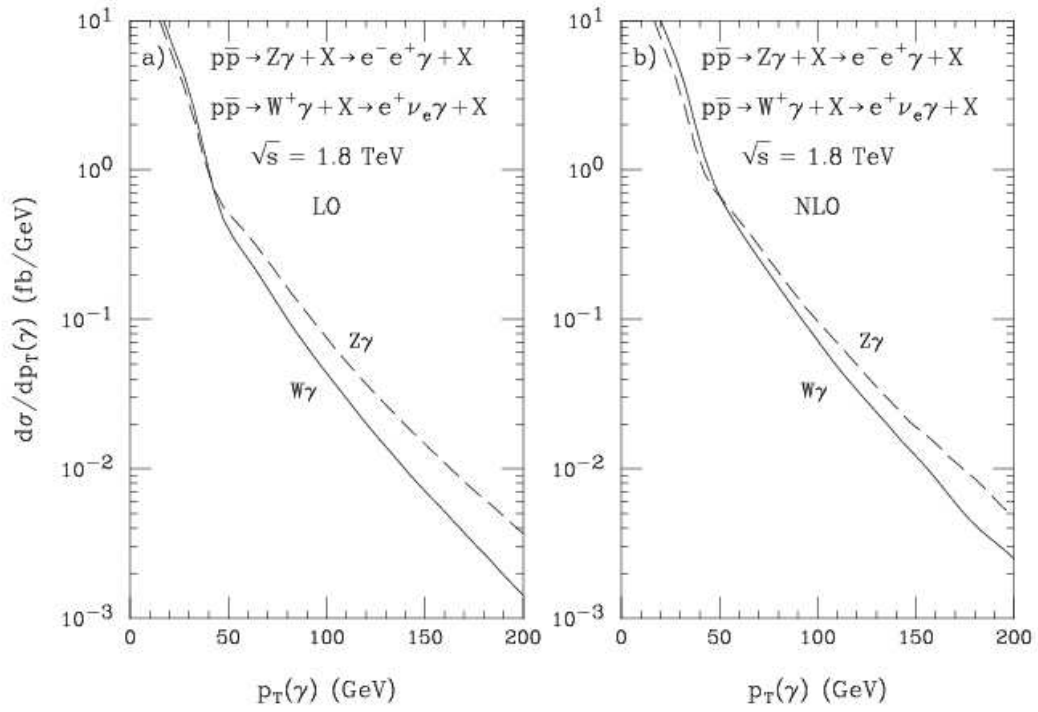

Figure 1.5 The photon E_T spectrum for prompt $W\gamma$ and prompt $Z\gamma$ production. [5]

invariant under both particle-antiparticle conjugation (C) and spatial inversion (P) can be expressed in following form:

$$L_{WW\gamma} = -ie\left[\left(W^\dagger_{\mu\nu}W^\mu A^\nu - W^\dagger_\mu A_\nu W^{\mu\nu}\right) + \kappa W^\dagger_\mu W_\nu F^{\mu\nu} + \frac{\lambda}{m^2_W} W^\dagger_{\alpha\mu} W^\mu_\nu F^{\nu\alpha}\right], \quad (1.5)$$

where A^μ is the photon field, W^μ is the W^- field, $W_{\mu\nu} = \partial_\mu W_\nu - \partial_\nu W_\mu$, and $F_{\mu\nu} = \partial_\mu A_\nu - \partial_\nu A_\mu$. In this formalism, the first term is fixed by the charge of the W boson and represents the minimal coupling of the W and photon fields, while the additional couplings, κ and λ, are related to the magnetic dipole moment (μ_W) and the electric

quadrupole moment (Q_W) of the W^+ by the following relations:

$$\mu_W = \frac{e}{2m_W}(1 + \kappa + \lambda), \tag{1.6}$$

$$Q_W = -\frac{e}{2m_W^2}(\kappa - \lambda), \tag{1.7}$$

Within the Standard Model, $\kappa = 1$ and $\lambda = 0$. For any other values, the $SU(2)\otimes U(1)$ gauge symmetry will be violated, and the $W\gamma$ production amplitude will grow as $\lambda\hat{s}$ and $\Delta\kappa\sqrt{\hat{s}}$, where $\sqrt{\hat{s}}$ is the parton-level center-of-mass energy and $\Delta\kappa = \kappa - 1$. In order to maintain a finite $W\gamma$ production cross section, it is conventional to replace the couplings in Equation 1.5 with the following dipole form factors:

$$\lambda \rightarrow \frac{\lambda}{(1 + \frac{\hat{s}}{\Lambda^2})^2}, \tag{1.8}$$

$$\Delta\kappa \rightarrow \frac{\Delta\kappa}{(1 + \frac{\hat{s}}{\Lambda^2})^2}. \tag{1.9}$$

Λ is the form factor scale which loosely represents the energy frontier at which new phenomena outside of the Standard Model becomes evident. A more detailed description of the potential anomalous structure of the $WW\gamma$ vertex can be found in [11].

1.4 Experimentally Observing the Effects of the Radiation Amplitude Zero

A quantitative statement about the radiation amplitude zero in an experimentally observed $W\gamma$ angular distribution has never been made; previous experiments have

been statistically limited due to the small size of the prompt $q\bar{q} \rightarrow W\gamma$ cross section. The primary purpose of this analysis is to make the first quantitative statement about this destructive interference. In this analysis, hadronic collisions are analyzed to sample events that are consistent with the signatures of $W\gamma$ production. Since the W boson almost immediately decays it is necessary to look for event signatures that contain the daughter particles and a photon. This analysis is restricted to events where the W decays leptonically to an electron (or positron) and a neutrino ($W\gamma \rightarrow e\nu_e$) or to a muon (or antimuon) and a neutrino ($W\gamma \rightarrow \mu\nu_e$)*. Decays to the quark sector are not considered, since these event signatures will be overwhelmed by **QCD** backgrounds.

Unfortunately, direct observation of the $\cos(\theta^*)$ distribution is problematic at hadron colliders. Since the neutrino can only interact through the weak force, its energy is not measured at a collider detector. Instead its presence is determined by an imbalanced of transverse momentum in the detector. The neutrino momentum parallel to the direction of the hadronic collision cannot be extracted from the momentum imbalance since the initial longitudinal momentum of the **partons** involved in the collision is unknown. The unknown neutrino momentum introduces an ambiguity in the reconstruction of the center-of-mass angle. However, it has been shown that the destructive interference in the angular distribution is manifest in the charge-signed

*The horizontal bar over the antiparticle is being ignored, but it is implied by the charge of the W boson being considered

rapidity difference of the final state lepton and the photon at $\eta(\gamma) - \eta(\lambda) \approx \mp 0.3$ for $W^{\pm}\gamma$ production [12]. See Figure 1.6

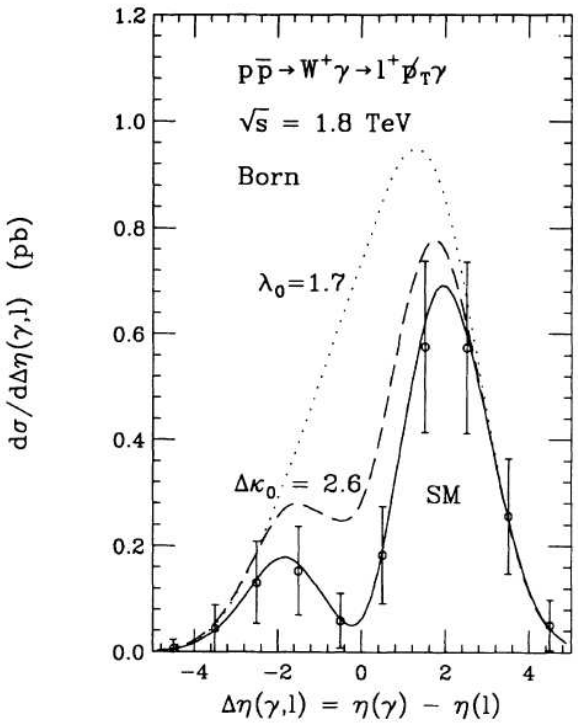

Figure 1.6 The charge-signed rapidity difference from $W\gamma$ Monte Carlo for the Standard Model and for two choices of anomalous couplings. The events are chosen so that the photon $E_T > 5\ GeV$, the lepton $ET > 20\ GeV$, the missing transverse energy is greater than $20\ GeV$, the lepton $|\eta| < 3.5$, the photon $|\eta| < 3$, the three-body transverse mass is greater than $90\ GeV$, and the photon and lepton are spatially separated with a $\Delta R > 0.7$. The form factor scale (Λ) is set to $1\ TeV$ and the errors bar shows the statistical error for $22\ pb^{-1}$ of integrated luminosity. [12]

Chapter 2
The Instrumentation

This analysis uses the sample of hadronic collisions that were measured by the DØ detector at the Fermi National Accelerator Laboratory Tevatron collider during the "Run IIa"* data taking period of the experiment. The collection of the data sample is a technically complex task that requires the controlled production of the hadronic collisions, an assortment of detectors to measure the collision products, and the readout and storage of the detector data. A description of this process is presented in the following sections.

2.1 The Accelerator

To produce hadronic collisions, Fermilab utilizes a series of increasingly energetic accelerators to collide a beam of protons and a beam of antiprotons at a center-of-mass energy of 1.96 TeV with an instantaneous **luminosity** that varies from an order of $10^7 b^{-1}s^{-1}$ to $10^8 b^{-1}s^{-1}$.† The chain of accelerators is diagramed in Figure 2.1 and begins with a bottle of hydrogen gas (H_2).

The hydrogen is ionized into H^- inside a Cockcroft-Walton and accelerated by a positive voltage to an energy of 750 keV. The ions enter a linear accelerator (linac) which uses an oscillating electric field to accelerate the hydrogen to 400 MeV. Upon

*This corresponds to data taken between April 2002 and February 2006. The accelerator and detector descriptions presented here only reflect the instrumentation during this period.

†A barn (b) is a unit of area. 1 b = 10^{-28} m^2

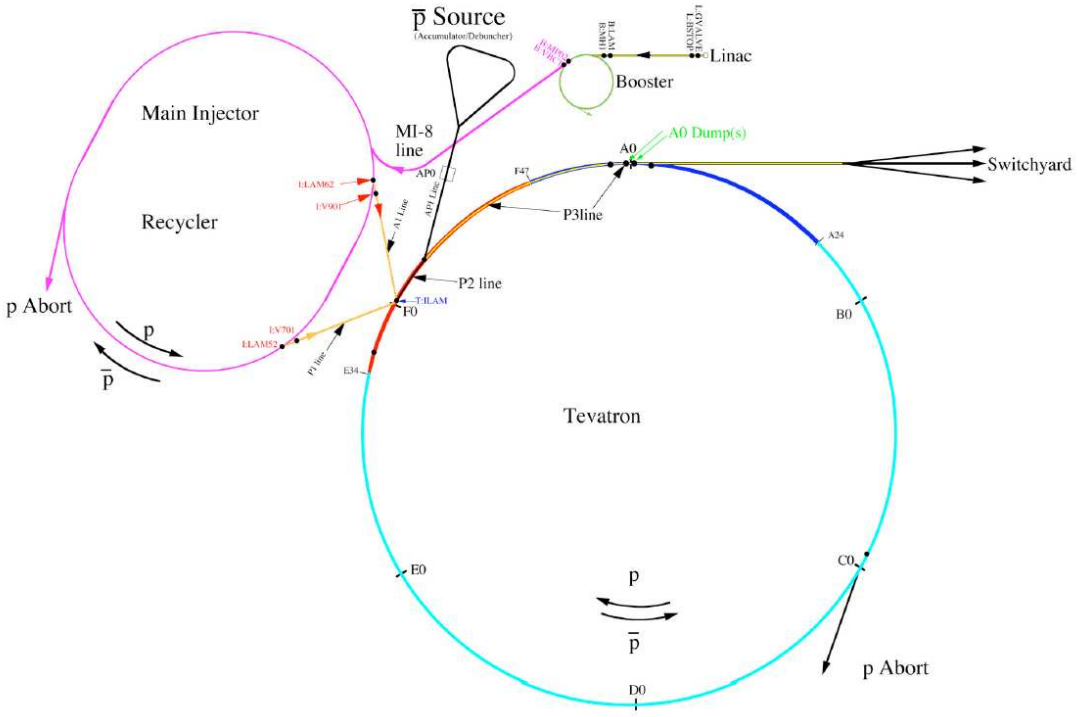

Figure 2.1 The chain of Fermilab accelerators. [13]

exiting the linac, the hydrogen passes through a carbon foil that strips the electrons from the proton. The protons then enter a circular accelerator (Booster) which further accelerates the particles to an energy of 8 GeV and injects them into the Main Injector which performs the following tasks:

- The Main Injector accelerates some of the protons to 120 GeV and sends them to the Antiproton Source, where antiprotons are created and collected. The Antiproton Source is composed of a target, the Debuncher, and the Accumulator:

  - The 120 GeV protons are brought into collision with a nickel target which results in the random production of secondary particles. A small fraction (10^7 for 10^{12} protons [14]) of the secondary particles will be 8 GeV antiprotons, which are selectively directed towards the Debuncher through the application of a magnetic field.
  - The Debuncher collects the 8 GeV antiprotons and reduces the momentum spread of the particles.
  - The antiprotons are stored in the Accumulator which further reduces the momentum spread and injects the accumulated antiprotons into the Main injector.

- The Main Injector receives the accumulated antiprotons and accelerates them and the remaining protons in counter-rotating orbits to an energy of 150 GeV.
- The Main Injector injects 36 bunches of 150 GeV protons and 36 bunches of 150 GeV antiprotons into the Tevatron synchrotron. The bunches are divided into 3 super bunches that are spaced 2.64 μs apart. Within each super bunch, there a twelve bunches that are spaced 396 ns apart.

The Tevatron performs the final acceleration of the 36 bunches of protons and antiprotons by accelerating them in opposite directions along two nonintersecting helical orbits. The protons and antiprotons are then brought to collision at the centers of

the CDF [15] and DØ detectors [16]. A more technical description of the accelerator system can found in [13] and [14].

2.2 The DØ Detector

The DØ detector measures the properties of long-lived decay products that interact through the electromagnetic or strong color-charged forces. The detector, shown in Figures 2.2 and 2.3, consists of the following series of subdetectors:

- The Silicon Microstrip Tracker.
- The Central Fiber Tracker.
- The Luminosity Monitor.
- The Preshower Detectors.
- The Calorimeter.
- The Muon Detector.

The tracking systems detect the presence of electric-charge and are contained within a 2 Tesla solenoid magnet. By applying a magnetic field, the detectors can measure particle charge and transverse momentum, p_T, from the curvature of the particle trajectories. The trackers are designed to perform a nondestructive measurement and hence only remove minimal energy from the incident particles.

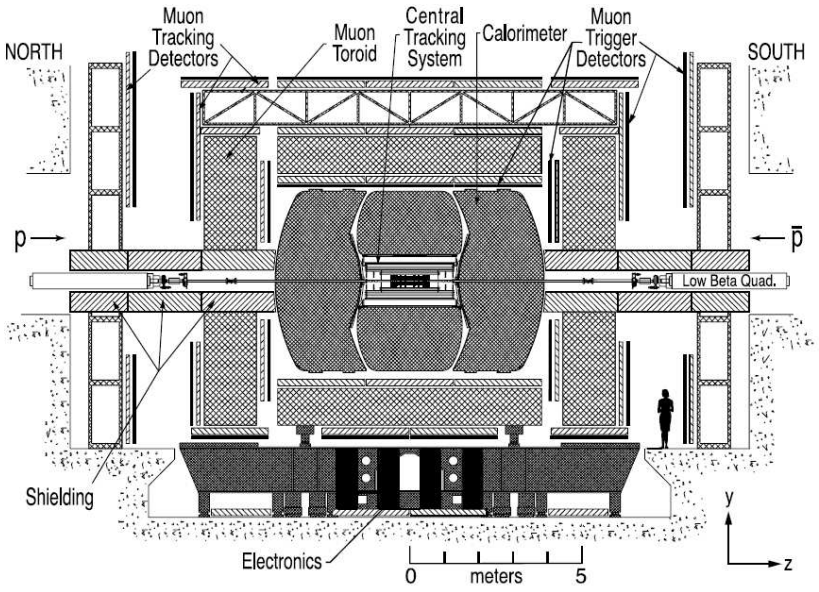

Figure 2.2 The DØ detector. [16]

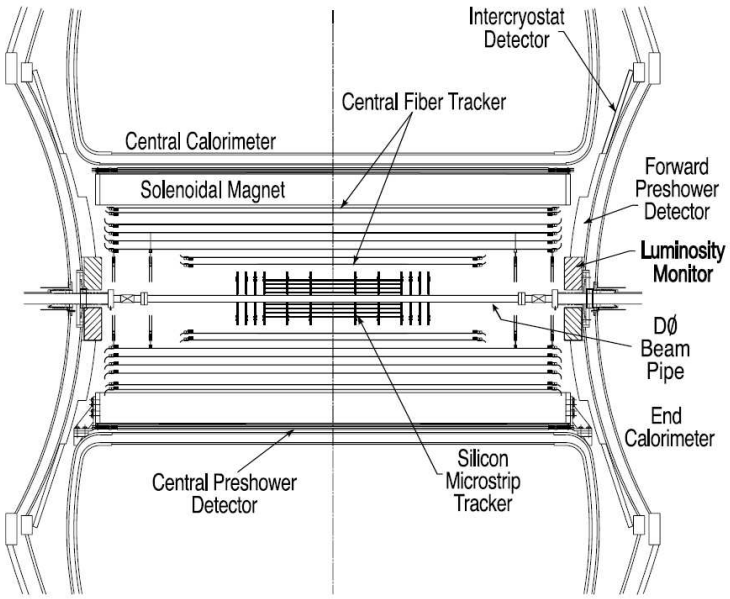

Figure 2.3 The innermost components of the DØ detector. [16]

Surrounding the solenoid is the preshower and calorimeter detectors. The calorimeter performs a destructive measurement of the energy and position of electrons, photons, and hadronic particles. The calorimeter has sufficient thickness for the incident particles to interact with the medium and to produce a shower (a cascade of lower energy particles) that deposits all of the energy in the detector. The preshower detector is a scintillator based system that is mounted on the inner walls of the calorimeter. It detects particle showers that may have developed in the solenoid and tracking detectors.

Muons are minimum ionizing and will escape the calorimeter. Hence a muon detector is placed outside of the calorimeter. The muon system uses drift tubes, scintillators, and a 1.8 toroid magnetic field to measure the trajectory and p_T of the electric-charged particle.

Located at small scattering angles between the tracker and endcap calorimeters is the luminosity monitor which determines the instantaneous luminosity of the $p\bar{p}$ collisions by measuring the rate of inelastic collisions. A brief description of the subdetectors is presented in the following subsections. The information is taken from a more detailed description of the DØ detector which can be found in [16]. In describing the subdetectors, references will be made to a customary DØ coordinate system. A brief introduction to this coordinate system is described below.

2.2.1 Coordinate System

The DØ detector is described by a right-handed Cartesian coordinate system with an origin at the center of the detector. The z axis is defined to be along the direction of the incoming protons, and the y axis is aligned vertically upward. It is common to use the variables ϕ, θ, and r, where ϕ is the angle with respect to the x axis in the x-y plane, θ is the scattering angle which is measured with respect to the z axis, and $r^2 = x^2 + y^2$. When referring to particle trajectories, ϕ and θ are measured with the origin located at the interaction vertex. When detector components are under consideration it is common to refer to a detector θ that is measured with the origin at the detector center*. Typically, the **pseudorapidity**, $\eta = -\ln[\tan(\theta/2)]$, is used in place of θ. An advantage of this parameterization is that differences in particle pseudorapidity are Lorentz invariant in the limit that the ratio of the particle mass to energy goes to zero ($m/E \to 0$).

2.2.2 Silicon Microstrip Tracker (SMT)

The SMT is the first subdetector that surrounds the the 38.1 mm diameter beryllium beam pipe. The tracking system is composed of 6 barrel shaped detectors and 16 disk shaped detectors (see Figure 2.4). The barrel shaped detectors permit the measurement of the $r - \phi$ coordinate and the disks permit the measurement of the

*The z position of the interaction point will vary about the detector center with a standard deviation of approximately 25 cm.

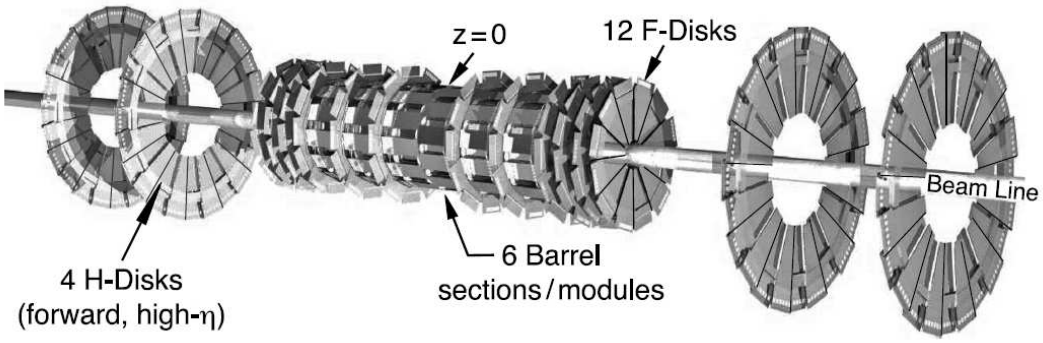

Figure 2.4 The SMT detector. [16]

$r \times z$ and $r \times \phi$ coordinates. In each barrel region there are 4 layers, with layers 1 and 2 containing 12 silicon modules and layers 3 and 4 containing 24 silicon modules. The disk regions are separated into F-disk and H-disk detectors, with the F-disks consisting of 12 wedge-shaped silicon modules, and the H-disks consisting of 24 wedge-shaped modules. The silicon modules are divided into strips with a 50 μm pitch. When a charge particle passes through the strips, it will create electron-hole pairs which will produce a charge pulse that is integrated and readout via custom-made SVXIIe chips [17]. The collection of spatial information from these hits allows for the reconstruction of the particle path or track.

2.2.3 Central Fiber Tracker (CFT)

Surrounding the SMT is the CFT, which extends from a cylindrical radius of 20 cm to 52 cm. The CFT consists of strands of scintillating optical fiber that are mounted along eight concentric cylinders. The fibers are organized into a doublet

layer as shown in Figure 2.5. For each cylinder there are two doublet layers with the first layer having fibers that are aligned along the axis of the cylinder and the second layer having fibers that are oriented at a stereo angle of $+3^o$ or -3^o. The cylinders alternate between axial plus $+3^o$ doublet layers and axial plus -3^o doublet layers.

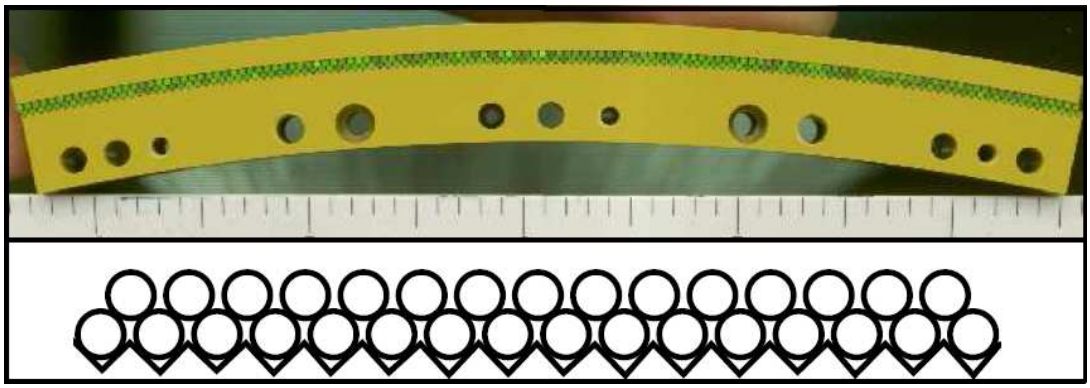

Figure 2.5 The top (bottom) image is a photograph (diagram) of a ribbon of CFT fibers. [16]

The optical fibers have a diameter of 835 μm with a core of polystyrene that is surrounded by two claddings. The inner cladding is 25 μm thick and made with polymethylmethacrylate. The outer cladding is also 25 μm thick and made of fluoro-acrylic. The fibers have a length of 1.66 m for the two innermost cylinders and a length of 2.52 m for the outermost cylinders. The polystyrene is doped with a fluorescent dye, paraterphenyl, and a wave-shifting dye, 3-hydroxyflavone. When a charged particle passes through a fiber it excites the polystyrene which in turn leads to an excitation of the paraterphenyl. The paraterphenyl then decays through the

emission of 340 nm light. The 340 nm light only has a mean free path of a few hundred microns in the polystyrene, but 3-hydroxyflavone absorbs the 340 nm light and reemits it at 530 nm which has an **attenuation length** of about 5 m in the scintillating fiber.

The light is collected through clear fiber waveguides from one end of the scintillating fiber, while the other end of the scintillating fiber has an aluminum coating which has a 90% reflectivity. The clear fiber waveguides have the same diameter as the scintillating fibers and are chemically identical to the scintillating fibers, except they have not be doped with dyes. The waveguides have an attenuation length of about 8 m and guide the light to visible light photon counters (VLPCs). The VLPCs convert the light to an electric signal. SIFT chips receive the signal, integrate the charge, and transmit the signals to two types of receivers. The first type consists of SVXIIe chips which are used for precision readout. The second type consists of discriminators which fire if the charge exceeds a threshold. The discriminator hits are used for the determination of event triggers.

The CFT and SMT have a combined vertex resolution of 35 μm along the beamline and an expected p_T resolution that is shown in Figure 2.6.

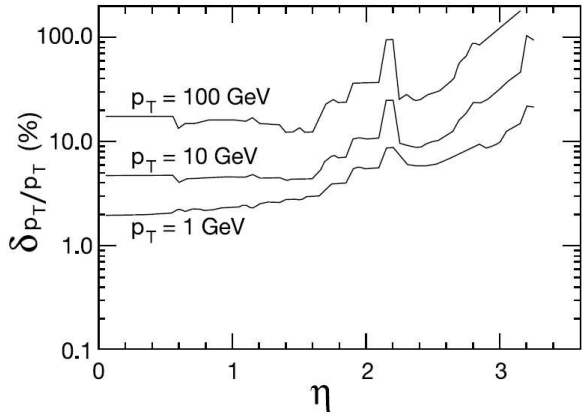

Figure 2.6 The expected p_T resolution of the combined SMT and CFT tracking system as a function of pseudorapidity for 3 different p_T scales. [16]

2.2.4 Preshower Detectors

With the solenoid magnet, the tracking system presents a substantial mass* to particles passing through it, hence it is likely that a particle shower will developed before an incident particle even enters the calorimeter. To compensate for this effect, scintillating preshower detectors are mounted between the solenoid and the calorimeter. The preshower detectors consist of 3 layers of plastic scintillator strips for central pseudorapidities ($|\eta| < 1.3$) and 4 layers of plastic scintillator strips for forward pseudorapidities ($1.5 < |\eta| < 2.5$). The strips have the shape of a triangular prism and are made from polystyrene that has been doped with p-terphenyl and diphenyl stilbene. A cross sectional view of a the strip layout can be seen in Figure 2.7. Running through the length of each strip is a wavelength-shifting fiber that collects the lights

*The solenoid is 0.9 **radiation lengths** thick at normal incidence.

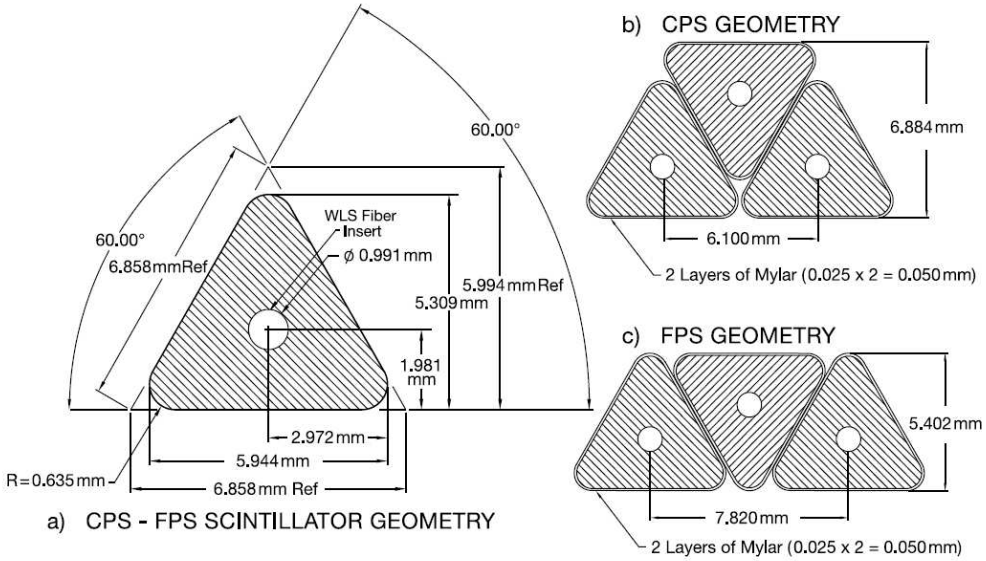

Figure 2.7 Cross sectional view of a the CPS and FPS strips. [16]

and transmits it to clear fiber waveguides that are connected at then end of the detector. The readout system for the preshower is similar to the CFT and uses the same waveguides, VLPCs, and readout electronics.

Central Preshower (CPS)

The CPS covers the region with $|\eta| < 1.3$ and is composed of three cylindrical layers of strips. For the innermost layer, the strips are aligned in the axial direction. For the center layer, the strips are aligned at a 23.774^o stereo angle. For the outermost layer, the strips are aligned at a -24.016^o stereo angle. Mounted between the solenoid and the CPS is an lead layer which adds an additional radiation length of material.

Forward Preshower (FPS)

The FPS covers a pseudorapidity range of $1.5 < |\eta| < 2.5$. The FPS is a four layer system that is sectioned off into 22.5^o wedges as shown in Figures 2.8 and 2.9. The inner two layers are known as the MIP layer and are oriented so that the strips are at a 22.5^o stereo angle with respect to each other. The outer two layers are known as the shower layers and have an orientation that is identical to the MIP layer. The design of the MIP layers takes advantage of the fact that the solenoid only extends to $|\eta| < 1.65$ by essential including additional layers of tracking in the region with $1.65 < |\eta| < 2.5$. This permits the additional discrimination between neutral and charged particles. Located between the MIP and shower layers at $1.65 < |\eta| < 2.5$ is a two radiation length thick lead absorber which induce particles showers in region that is not within the "shadow" for the solenoid.

2.2.5 Calorimeter (CAL)

The DØ calorimeter is a **compensating sampling calorimeter** with a liquid argon active medium. The detector, shown in Figure 2.10, is divided into three regions: a central calorimeter (CC) that covers a region of $|\eta| \lesssim 1$ and two endcaps (EC) that extend the coverage to $|\eta| \lesssim 4$. All three regions are divided into an electromagnetic (EM) section, a fine hadronic section, and a coarse hadronic section. Interlaid between the active medium are layers of absorber that induce a cascade of lower energy

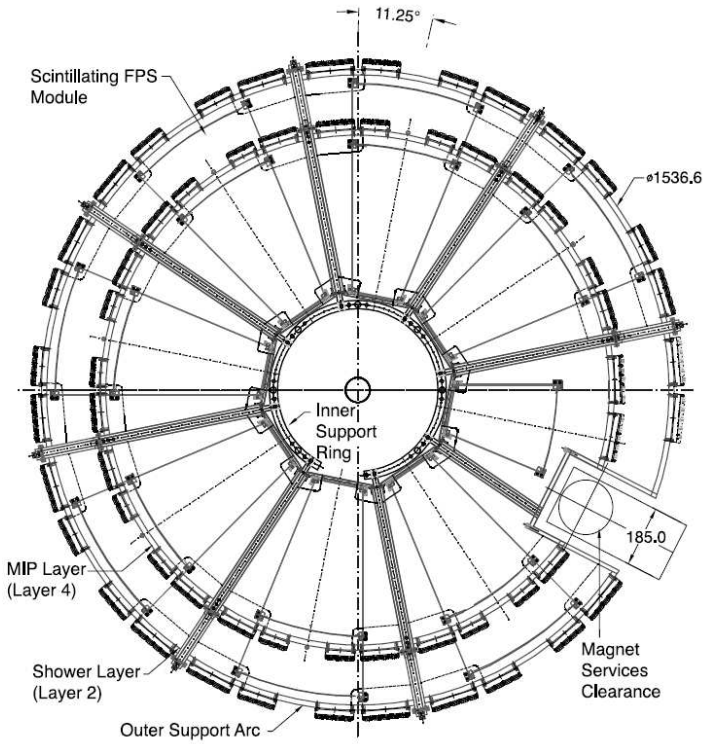

Figure 2.8 $r \times \phi$ view of the FPS. [16]

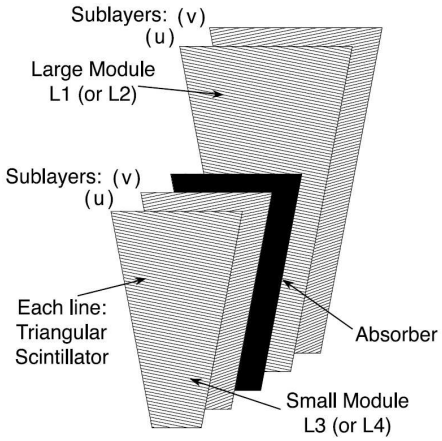

Figure 2.9 Four layer wedge segment of the FPS. [16]

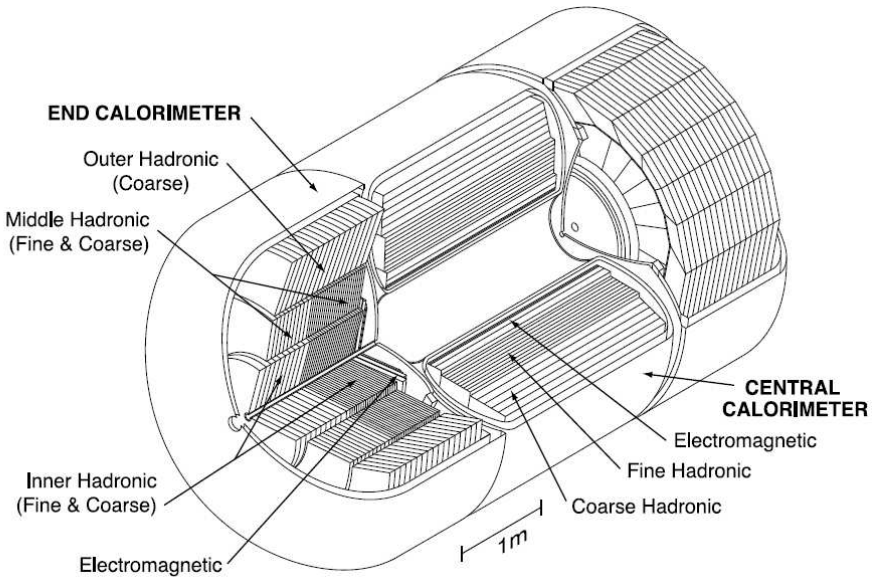

Figure 2.10 The DØ calorimeter. [16]

particles. In the EM sections the absorbers are made of depleted uranium. In the fine hadronic section the absorbers are made from a uranium-niobiun alloy. In the coarse hadronic the absorbers are plates are copper for the CC and stainless steel for the EC.

The calorimeter is further segmented into cells that have a transverse size that is comparable to the expected shower width of 1-2 cm for the EM showers and 10 cm for typical hadronic jets. A diagram of a calorimeter cell is shown in Figure 2.11. In a cell, the absorber plates are grounded while the resistive surface is held at a potential of 2.0 kV. When a charge particle passes through the cell it ionizes the argon creating a current across the potential difference with a mean electron drift time

of approximately 450 ns. The cells are ganged into towers that are approximately projective in η and have a width of 0.1 in η-space and 0.1 in ϕ-space. A schematic view of the tower configuration can be found in Figure 2.12. The EM section is divided into four layers of readout cells in the CC and EC. Starting with the innermost layer, the CC layers have a respective thickness of 1.4, 2.0, 6.8, and 9.8 radiation lengths, and the EC layers have a respective thickness of 1.6, 2.6, 7.9, and 9.3 radiation lengths. The EM shower maximum typically occurs at the third layer. In the CC, the fine hadronic section is separated into three layers and the coarse hadronic layer consists of a single module. The EC has a more complicated geometry as seen in Figure 2.10. The inner and middle fine hadronic region consists of four layers, and the inner, middle, and outer coarse hadronic region consist of one layer. The **nuclear absorption lengths** of the hadronic layers are provided in Table 2.1.

The liquid argon calorimeter lacks sufficient sampling at the boundary of the CC and EC which is located at a pseudorapidity of $0.8 < |\eta| < 1.4$. To compensate for this, a scintillating intercryostat detector (ICD) is mounted on the edge of the EC calorimeters at a pseudorapidity of $1.1 < |\eta| < 1.4$. The ICD consists of a circular arrangement of scintillating tile wedges (see Figures 2.13 and 2.13). The wedges have a dimension of 0.3×0.4 in $\eta \times \phi$ space and are separated into 12 subtiles that are optically isolated from each other. The emitted light is collected and transmitted through wavelength shifting fibers to clear optical fibers that terminate at photomul-

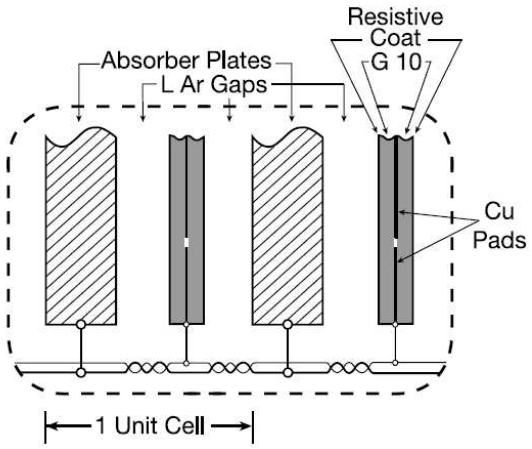

Figure 2.11 Schematic of a calorimeter cell. [16]

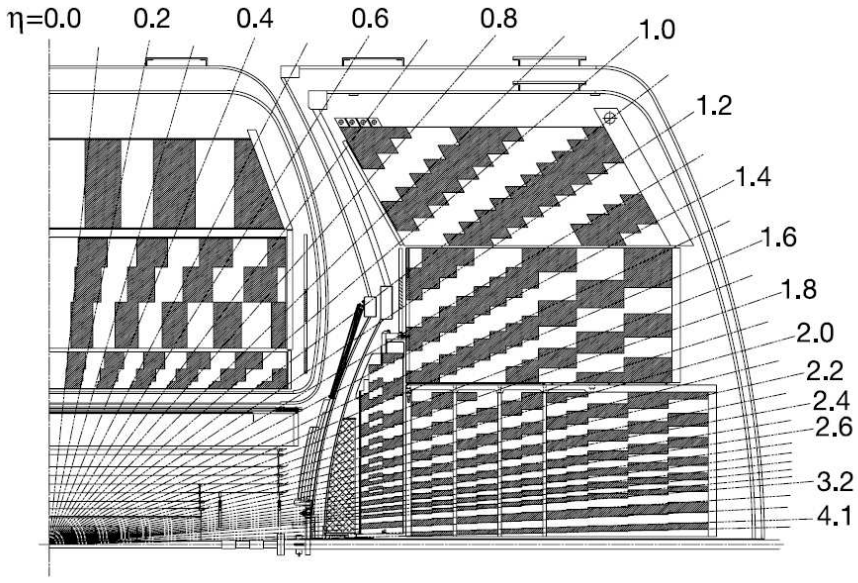

Figure 2.12 Schematic of a calorimeter cell. [16]

Hadronic Layer	Absorption Length
Fine CC Layers	
1 (innermost)	1.3
2	1.0
3	0.76
Coarse CC Layer	
1	3.2
Fine Inner Layers	
1 (innermost)	1.1
2	1.1
3	1.1
4	1.1
Fine Middle Layers	
1 (innermost)	0.9
2	0.9
3	0.9
4	0.9
Coarse Inner Layer	
1	4.1
Coarse Middle Layer	
1	4.4
Coarse Outer Layer	
1	6.0

Table 2.1 Absorption lengths of the hadronic layers.

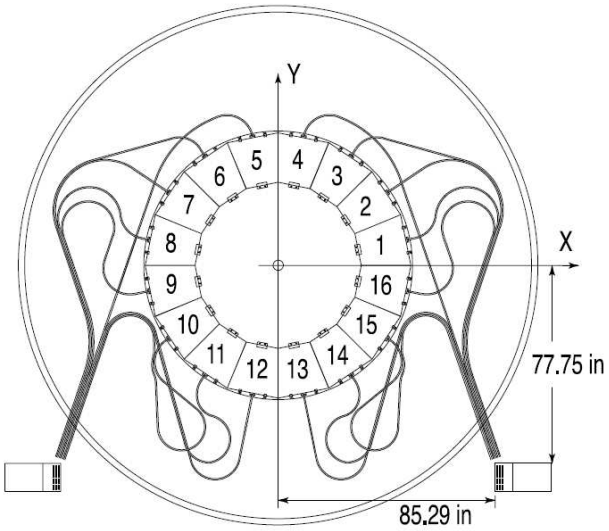

Figure 2.13 The ICD arrangement on the endcap calorimeters. [16]

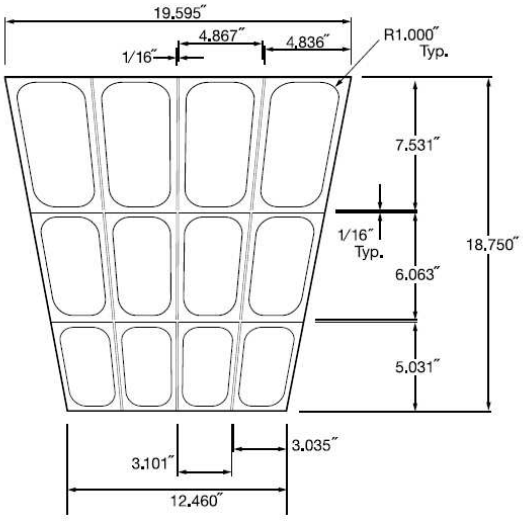

Figure 2.14 An ICD scintillating tile. [16]

tiplier tubes (PMT).

The calorimeter E_T resolution for central jets that are reconstructed within a cone of $\Delta R = \Delta\phi^2 + \Delta\eta^2 < 0.7$ is shown in Figure 2.15.

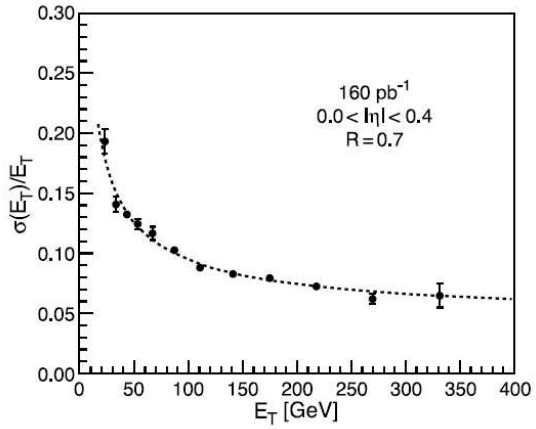

Figure 2.15 Calorimeter E_T resolution for jets at central psuedorapidities. [16]

2.2.6 Muon Detector

The muon detector measures the position and momentum of muon tracks with a system of scintillators, drift tubes, and toroidal magnets. The detector is a three layered system with each layer typically consisting of a wire chamber of drift tubes that is surrounded by a layer of scintillator. The innermost layer (the A layer) is located between the toroidal magnet and the calorimeter. Outside the toroid is the B layer which is followed by the C layer. The muon system is divided further into a central section that covers the region with $|\eta| \lesssim 1.0$ and two forward sections that cover

the region with $1.0 \lesssim \eta \lesssim 2.0$. Exploded views of the wire chambers and scintillators are shown in Figures 2.16 and 2.17.

Two types of drift tube designs are utilized in the muon system. The central region contains chambers of proportional drift tubes (PDTs) that are filled with a gas mixture of argon, methane, and CF_4. The chambers are composed of cells that are 10.1 cm across. Each chamber consists of 3 to 4 decks of cells with a typically deck being 24 cells wide. Running through the center of each cell is an anode wire that is set to a potential of 4.7 kV. Along the top and bottom of a cell there are cathode pads that are set to a voltage of 2.3 kV.

The forward region contains mini drift tubes (MDTs) that are filled with a CF_4-CH_4 gas mixture. Each layer contains three or four planes of tubes, with each tube containing 8 cells. A cell has width and height of 9.4 mm. Stretched across the center of each cell is an anode wire that is held at ground while a -3.2 kV is applied to the cathode.

The muon system has reduced coverage at $4.25 < \phi < 5.15$ for $|\eta| < 1.1$. This corresponds to the bottom center of the detector and can be seen in Figures 2.16 and 2.17. This area is referred to as the hole region of the muon system and is due to the fact the inner detectors require mechanical supports.

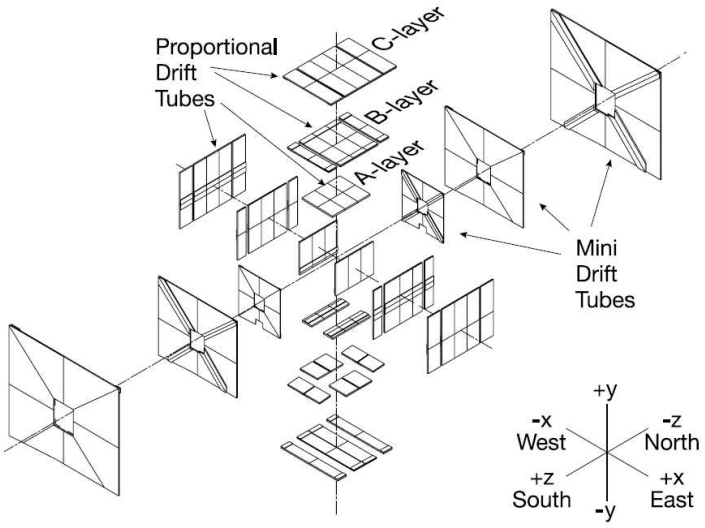

Figure 2.16 Exploded view of the muon wire chambers. [16]

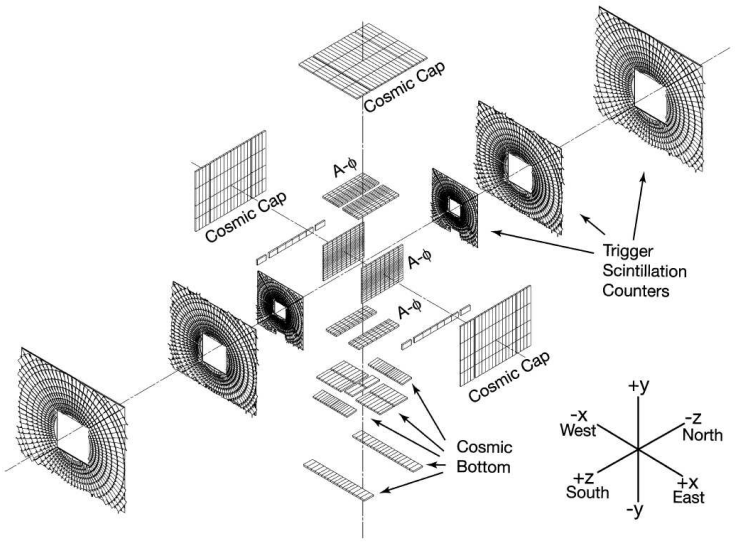

Figure 2.17 Exploded view of the muon scintillators. [16]

2.2.7 Luminosity Monitor

The luminosity monitor uses an array of plastic scintillation counters to measure the number of inelastic collisions that occur at small scattering angles. The counters are wedge shaped and are mounted in circular pattern (see Figure 2.18) on the front of the endcap calorimeters. The luminosity monitor covers the range of $2.7 < |\eta| < 4.4$ as shown in Figure 2.19.

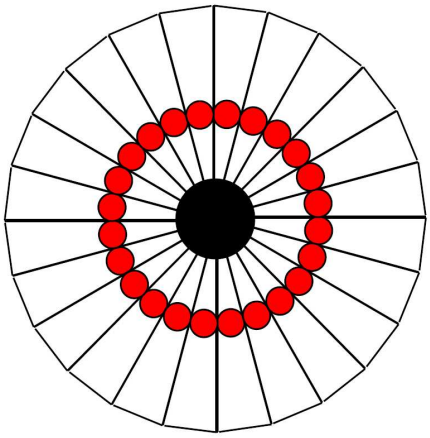

Figure 2.18 Geometry of the luminosity monitors. The red dots are PMTs. [16]

The instantaneous luminosity is determined from the average number of inelastic collisions that occur per beam crossing over a 60 second interval. This time interval is referred to as a luminosity block and is chosen because the instantaneous luminosities are effectively constant over this period of time.

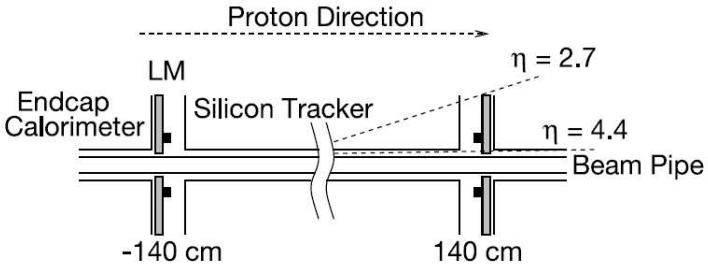

Figure 2.19 Location of the luminosity monitors. [16]

2.3 Data Collection

The collection of digital information from the detector channels corresponds on average to approximately 200 kB of data per beam crossing. With 36 beam crossings in 21 μs, the potential output rate of the detector would be about 350 GB/s. The DØ front-end detector electronics cannot be readout at this rate; furthermore the bulk of the collision data would be "uninteresting" QCD interactions*. To select interesting physics events for recording, the readout of detector data is triggered by a sophisticated event trigger system.

The DØ trigger system is a three level system with each successive level processing fewer events with increasingly sophisticated algorithms. The level-1 trigger uses specialized electronics to examine the event data for signatures in the subdetectors that are consistent with high p_T objects. The rate at which the system can accept events does not exceed a 2 kHz event rate and is restricted by the maximum readout rate

*For reference, at the highest instantaneous luminosities, W boson production occurs on average once per 3×10^5 crossings.

of the detector subsystems and the dead time that is associated with the readout. During the determination of the level-1 trigger result, detector data is stored in a pipeline of first-in/first-out (FIFO) buffers which gives the trigger system 3.5 μs to form a decision.

Event data that satisfy the level-1 criteria are filtered by the level-2 system. The level-2 trigger is a collection of specialized hardware and embedded microprocessors that identify physical objects across subdetectors. The level-2 system has a maximum accept rate of 1 kHz. Events that satisfy the level-2 criteria are fully readout and sent to the level-3 system.

The level-3 trigger is comprised of a farm of microprocessors with individual event data being assigned a dedicated processor. The level-3 software performs a fast reconstruction of electrons, muon, taus, missing transverse energy ($\not\!\!E_T$), tracks, and the associated track vertices. The level-3 trigger selects events at a rate of 50 Hz. The selected data is stored to tape for offline reconstruction. A flow diagram of the trigger and data acquisition system is shown in Figure 2.20.

2.3.1 Level-1 Trigger

The level-1 system examines the collision event for localized, large-E_T deposits in calorimeter and for hits patterns consistent with high p_T tracks in the central tracking and muon detectors.

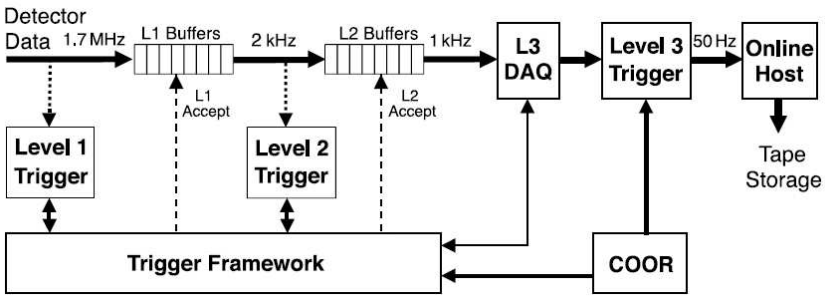

Figure 2.20 Flow of data in the DØ trigger and data acquisition system. [16]

L1CAL

The level-1 calorimeter (L1CAL) selection cuts are based on the EM energy or total energy (EM plus hadronic) in a trigger tower. A trigger tower is composed of a 2×2 array of the calorimeter towers described in section 2.2.5 and covers an 0.2×0.2 area in $\eta \times \phi$ space. An event can satisfy the calorimeter trigger requirement if a set number of triggers towers has an EM E_T or total E_T that is greater than a reference threshold. Since jets are typically wider than a trigger tower, the trigger can also be satisfied if the sum of the total E_T in 4×8 trigger tower region in $\eta \times \phi$ space exceeds a threshold*. The calorimeter trigger may also fire if the global sum of the tower E_Ts or the magnitude of calculated $\not\!\!E_T$ exceeds a threshold.

*The unusual geometry is a result of hardware limitations. This tower sum comes from the calculation of the $\not\!\!E_T$.

L1CTT

The level-1 central track trigger is performed by the L1CTT system which uses discriminator information from the CFT and preshower detectors. Tracks are found using the axial fiber hits from 4.5^o sectors in ϕ with hit information being shared among the neighboring sectors to find tracks that may have crossed the boundaries. The hit patterns are compared to predefined track equations to find tracks in four p_T ranges: 1.5-3 GeV, 3-5 GeV, 5-10 GeV, and > 10 GeV. The trigger selection is made based on the number of tracks, the number of isolated tracks, matching preshower clusters, the total tracking p_T, and the number of FPS clusters.

L1MUON

The muon trigger uses track information from the L1CTT as well as hits from the muon layers to identify signatures that are consistent with a muon. It is capable of triggering on two types of patterns. In one case, it looks for correlations between L1CTT tracks and hits in the A layer scintillator (loose scintillator trigger) or the A and B layers (tight scintillator trigger). In the other case, hits from each wire chamber layer are used to find track stubs which must match a correlated scintillator hit in the A layer (loose scintillator trigger) or both A and B layers (tight scintillator trigger).

2.3.2 Level-2 Trigger

The level-2 trigger is a two tiered systems. The first tier relies on detector-specific preprocessing algorithms to identify objects at the subsystem-level and sends the object information to the second tier of processors, L2GLOBAL, which examines the data for object correlations among the subdetectors and selects events for full readout and examination by the level-3 trigger system. The preprocessors identify coarse physics objects in the calorimeter, preshowers, CFT, SMT, and muon detectors.

L2CAL

For the L2CAL, the preprocessors form coarse EM showers and hadronic jets by identifying clusters of trigger towers with large-E_T deposits. The jet algorithm sums the total E_T in a 5×5 grouping of trigger towers and the EM algorithm identifies clusters of two neighboring trigger towers. In addition to clustering, the EM algorithms can also require an isolation criterion, by requiring that there be a minimal fraction of energy in the surrounding trigger towers.

L2PS

At level-2 preshower clusters centriods at each layer are matched to form 3-dimensional clusters. The η and ϕ position of the clusters are calculated, and the clusters are matched to calorimeter trigger towers. CPS clusters are identified as electrons or photons by the presence of an associated L1CTT track.

L2STT

A primary function of the L2STT is to calculate the track **impact parameter**. The value of this quantity can be used to identify and trigger on long-lived particles. The L2STT receives a list of tracks from the L1CTT and refines the track calculation with the inclusion of SMT axial hits. The L2STT constructs a 2 mm road about the L1CTT track and associates the SMT hits that are within the road to the track. The particle is then reconstructed using the SMT hits and the hits from the innermost and outermost CFT layer. For a reconstructed track to be accepted, at least 3 of the 4 SMT layers must have a hit. A diagram of this procedure is shown in Figure 2.21. The resulting track information is sent to the L2GLOBAL and L2CTT processors.

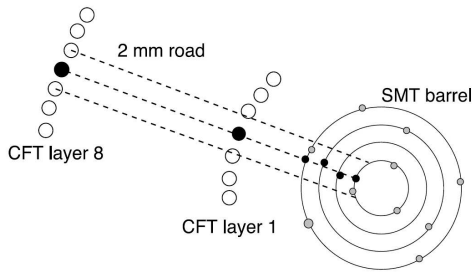

Figure 2.21 The road method used by the L2STT. [16]

L2CTT

The L2CTT runs in two modes. In one mode it receives tracking information from the L1CTT and in the other mode it receives data from the L2STT. In the first mode,

the L2CTT takes the list of level-1 tracks and improves the p_T measurement by using additional hit information. The L2CTT determines the projected ϕ coordinates of the track position at the beamline and at the third layer of the EM calorimeter. The L2CTT calculates isolation variables for the tracks and sends a p_T-sorted list of the reconstructed tracks to the L2GLOBAL processors. In the second mode, the L2CTT receives a list of tracks from the L2STT and calculates the two ϕ coordinates and isolation values for the tracks. It then reports two lists of tracks to the L2GLOBAL processors: one that is p_T-sorted and another that is sorted by impact parameter.

L2MUON

For the L2MUON, collections of parallel digital signal processors (DSPs) examine the wire chamber and scintillator hits to find track segments (stubs) in localized regions (A or B+C layers) of the muon detector. These stubs are assigned a quality and are grouped to form muon track candidates that are sent to the L2GLOBAL processors.

The muon candidates are assigned a quality that is based on the associated stub qualities [18]. A stub can have loose, medium, or tight quality. The criteria for determining this value depends on the location of the stub. The quality of an A layer stub in the central muon detector is determined by the following criteria:

- The stub is assigned a loose quality if it has at least 3 PDT hits.

- The stub is assigned a medium quality if it satisfies the loose quality requirement and has either a scintillator hit or drift times that satisfy a specified tolerance.
- The stub is assigned a tight quality if it satisfies the loose quality requirement and has both a scintillator hit and drift times that satisfy a specified tolerance.

The quality of a B+C layer stub in the central muon detector is determined by the following criteria:

- The stub is assigned a loose quality if it has at least 3 PDT hits.
- The stub is assigned a medium quality if it satisfies the loose quality requirement and has either a scintillator hit in the cosmic caps or hits that are in both B and C layers.
- The stub is assigned a tight quality if it satisfies the loose quality requirement and has both a scintillator hit in the cosmic caps and hits that are in both B and C layers.

The quality of an A layer stub in the forward muon detectors is determined by the following criteria:

- The stub is assigned a loose quality if the total number of scintillator hits and MDT planes with hits exceeds 2.

- The stub is assigned a medium quality if the total number of MDT planes with hits exceeds 2.

- The stub is assigned a tight quality if it satisfies the medium quality requirement and has a scintillator hit.

The quality of a B+C layer stub in the forward muon detectors is determined by the following criteria:

- The stub is assigned a loose quality if either the total number of B layer MDT planes with hits exceeds 1 or the total number of C layer MDT planes with hits exceeds 1.

- The stub is assigned a medium quality if both the total number of B layer MDT planes with hits exceeds 1 and the total number of C layer MDT planes with hits exceeds 1.

- The stub is assigned a tight quality if it satisfies the medium quality requirement and has a scintillator hit.

The quality of the muon candidates in the central muon detector is determined by the following criteria:

- The muon candidate has loose quality if it consists of a stub of loose or higher quality.

- The muon candidate has medium quality if it consists of both an A layer stub of loose or higher quality and a B+C layer stub of loose or higher quality.
- The muon candidate has tight quality if it consists of both an A layer stub of medium or higher quality and a B+C layer stub of medium or higher quality.

The quality of the muon candidates in the forward muon detectors is determined by the following criteria:

- The muon candidate has loose quality if it satisfies one of two conditions:
  - It consists of both an A layer stub of loose or higher quality and a B+C layer stub of loose or higher quality.
  - It consists of a stub of medium or higher quality.
- The muon candidate has medium quality if it consists of both an A layer stub of loose or higher quality and a B+C layer stub of loose or higher quality.
- The muon candidate has tight quality if it satisfies one of three conditions:
  - It consists of a loose A layer stub and a tight B+C layer stub.
  - It consists of a tight A layer stub and a loose B+C layer stub.
  - It consists of a medium or higher quality A layer stub and a medium or higher quality B+C layer stub.

L2GLOBAL

L2GLOBAL receives the preprocessor objects and executes scripts. The scripts identify global physics objects from the preprocessor objects and apply selection criteria. If a script condition is satisfied then the event will pass the level-2 requirement. The set of scripts that are executed are determined by the set of level-1 triggers that were satified. Each script is associated with a level-1 trigger, and the association is specified by a trigger list that can be modified with every data-taking run.

The scripts run a series of "filters" and requires a minimum number of objects to pass each filter. The filter uses "tools" to reconstruct a global object from the preprocessor data and imposes cuts on the object properties.

2.3.3 Level-3 Trigger

The level-3 decision is based on the result of scripts. The scripts are a collection of filters that call tools and impose selection criteria on the tool objects. The object identification properties are specified by programmable reference sets through the trigger list. The specific set of trigger criteria used for this analysis is presented in Chapter 5 and in the Appendix; however a general description of the level-3 object identification is provided below:

Level-3 Tracks

Level-3 tracking utilizes information from the CFT and SMT to form three classes of tracks: CFT-only, SMT-only, and global SMT+CFT tracks. The CFT-only tracking algorithm forms clusters from neighboring hits and attempts to fit circular arcs that intersect with the detector origin through the axial layer clusters. The algorithm starts with the outer layer and works inward joining cluster hits that are consistent with the curvature. The longest path from the initial cluster link is chosen to be a track candidate. The CFT-only tracks are used to find the primary vertex z-coordinate with a resolution of 0.5 mm.

For the SMT-only tracking, particle tracks are either formed from seeds that were found by an earlier tool or by linking associated track segments (starting with the outermost layers and working in). Higher quality SMT+CFT tracks candidates are found by taking CFT tracks and searching for potential extensions in the SMT.

Level-3 Muons

Muons tracks are reconstructed in the regions that were identified by the level-2 trigger. The muon tool identifies potential track segments in the scintillators and wire chambers. Muons are reconstructed from the segements if there are a specified minimuim number of hits in each layer. The muon candidates are further examined to determine if they have matching central tracks and if they are isolated in the

calorimeter.

Level-3 Calorimeter Objects

Calorimeter objects are formed by using the calorimeter precision readout and the primary vertex position. Jet and electrons are identified by calculating the amount of E_T that is deposited in a cone-shaped region of $\eta \times \phi$ space. The basic electron identification requires that there be at least a specified amount of E_T in a cone of radius, $\Delta R = \sqrt{(\Delta\eta)^2 + (\Delta\phi)^2} = 0.25$. In addition, the electron candidate is required to have a transverse shower shape that is consistent with an electron and to have a fraction of E_T in the electromagnetic layers that is greater than 0.9. The $\not\!\!E_T$ is calculated by using the vector sum of calorimeter cell energies in rings of pseudorapidity and by correcting the ring sums with the position of the primary vertex.

Chapter 3
The Reconstruction

In order to perform a physics analysis on the collider data, the detector signals must be processed to identify physical objects and to measure corresponding properties (energy, charge, position, *etc.*) of the identified objects. Object reconstruction is performed at offline computing farms with a software package (DØRECO) that scans over the raw event data that is stored to tape. A description of the object reconstruction that is relevant to this analysis is presented in the following sections.

3.1 Reconstruction of Particle Tracks in the Central Tracker

Reconstruction of charge particle tracks from fiber and strip hits in the CFT and SMT is performed by two tracking algorithms, the Histogram Track Finder (HTF) and the Alternate Algorithm (AA). Detailed information about the HTF and AA algorithms can be found at [19] and [20] respectively. A brief overview is supplied below:

3.1.1 HTF Tracking Algorithm

A charge particle will follow a helical path as it travels through the longitudinally oriented magnetic field of solenoid. The projection of this path on the $x \times y$ plane will form a circle of radius $\rho = \frac{qB}{p_T}$ and position ϕ, where q is the charge of the particle, B is the magnitude of the magnetic field, p_T is the transverse momentum

of the track, and ϕ is the angular direction of the particle at the distance of closest approach (DCA) to the beam spot. Since all points along the true path will have identical values for ρ and ϕ, it is possible to identify hits that belong to the same particle track by forming a histogram of the hits in the $\rho \times \phi$ coordinate space. A single hit in $x \times y$ coordinate space will correspond to a line of potential values in $\rho \times \phi$ coordinate space. The collection of lines from hits* belonging to the same track will intersect at the true path coordinate in $\rho \times \phi$ coordinate space and produce a peak in the resulting histogram.

For the CFT-only tracks, a two-dimensional Kalman filter [21] is applied to remove background candidates. The filter uses an algorithm that takes into account material effects to start with a partially reconstructed track and propagate along the entire length of the potential track to reject candidates with large errors and produce a smoothed refit track that will have smaller track parameter errors. The filtered CFT-only track candidates and the SMT-only track candidates are then passed through an additional filter that utilizes the longitudinal information from the hits. In this process, a histogram is formed in $z_0 \times C$ coordinate space, where z_0 is the z coordinate position where the track intersects with the beam line and $C = \frac{\Delta r}{\Delta z}$ is the inclination of the track. A single hit will correspond to a line of potential values in $z_0 \times C$ coordinate space with the collection of lines from hits that belong to the same track

*The CFT and SMT collection of hits are considered separately to form an initial list of CFT and SMT only track candidates.

intersecting at the true track coordinate.

For the remaining SMT-only candidates, background hits are further reduced by requiring that the hits associated with a particular track be consistent with a particle track that is moving away from the beam spot. This is done by considering the value of the z-coordinate of the hits belonging to a track candidate and by sorting the set of hits by increasing value of the radial coordinate. The resulting sequence of z-coordinates is then required to be either monotone increasing or monotone decreasing. A three-dimensional Kalman filter is applied to build the final SMT-only tracks and to attempt to extrapolate outward into the CFT to build complete track candidates.

For the remaining CFT-only candidates, a two-dimensional Kalman filter is applied using the hit information in the $r \times z$ plane. The reduced set of candidates is then processed through a three-dimensional Kalman filter which builds the final CFT-only tracks and attempts to extrapolate inward into the SMT to build complete track candidates. The list of tracks that were seeded by the SMT and CFT are combined and duplicates are removed.

3.1.2 AA Tracking Algorithm

In the alternative algorithm, a pool of track candidates are created by using an extrapolation based on a cluster of 3 hits in the SMT. The clusters are identified by beginning with an initial seed hit in the SMT barrels or F-disks and by identifying an associated hit in another layer that is within a $|\Delta\phi| < 0.08$ of the original hit. If

a third hit lies along a circular arc that fits the previous two hits and the fit satisfies three criteria, then the candidate cluster is identified. In order for the candidate to be considered, the arc must have a radius greater than 30 cm (corresponding to a $p_T > 0.18\ GeV$), the DCA must be less than 2.5 cm, and the χ^2 of the fit must be less than 16. Based on the extrapolated arc fit, hits in neighboring layers are added to the track hypothesis, if the χ^2 value remains less than 16. If multiple hits satisfy the criteria then multiple track candidates are formed for each hit. The algorithm permits layers to have missing hits and will continue until it reaches the end of the tracker or until it has three consecutive missing hits. Candidates are rejected based on the number of layers with hits and the number missing layers. The pool of potential tracks are then sorted with precedence being given to the candidates with the greatest number of hits. For candidates with the same number of hits, precedence is given to those with the least number of missing layer. In the case of a double degeneracy, precedence is given to a candidate with the smallest χ^2. In this method, it is possible for multiple track candidates to be formed from the same hits. To reduce false candidates a veto, based on the number of shared hits, is applied to candidates with a lower precedence.

Using the list of SMT seeded tracks, the position of the primary interaction vertices can be determined. With this additional information, a track finding method based

on CFT seeds is implemented*. A cluster of 3 CFT hits is formed using the method described in the SMT section; however in this case the track candidate is required to pass near one of the primary vertices. In a method that is similar to what was done for the SMT seed method, track candidates are formed by adding hits from additional layer starting with the innermost CFT layers and working outward. The CFT-only candidate are then extrapolated into the SMT to collect additional silicon hits. The collection of track candidates from the AA and HTF methods are combined and duplicates are removed.

3.2 Reconstruction of Preshower Clusters

Three dimensional clusters are formed from neighboring strips in and across the layers of the preshower. The reconstruction process is similar for the central and forward preshowers; however due to differences in the configurations there a some differences.

For the CPS [22], the cluster formation begins at the individual layers. Single layer clusters are formed by grouping a continuous sequence of neighboring strips with a hit. If the single layer cluster contains more than 5 strips, a subcluster algorithm is performed. The subcluster algorithm begins with the highest energy strip and adds neighboring strips until either 60% of the original cluster energy is contained within

*This allows for the creation of track candidates with less than 3 SMT hits. The constraint from the primary vertex creates a significant reduction in processing time that would otherwise be introduced by the larger number of hit-combinations that can result from the CFT axial and stereo layers and the lack of longitudinal segmentation.

the new subcluster or the subcluster reaches a maximum width of 5 strips. The subcluster algorithm is then performed on remaining strips from the original cluster. A three dimensional cluster is formed by matching single layer cluster from the three layers. The matching is initially performed in the stereo layers by finding the point of intersection between the single layer clusters. From this information the ϕ position can be calculated and stereo layers can be matched to an axial layer cluster.

For the FPS [23], single layer clusters or channel clusters are formed by combining a continuous sequence of strips with a hit. Using an energy weighted average, the radial positions at the opposite edges of the detector wedge are calculated. The position of the channel cluster is given by the arc along the wedge surface that connects the two radial positions. Three dimensional clusters are formed separately in the MIP and shower layers by find the point of intersection between the arcs that define the channel cluster postion in the u and v layer. For each detector wedge, a list of candidate clusters in generated and sorted by the energy correlation parameter:

$$C_{uv} = 1 - \frac{|E_u - E_v|}{E_u + E_v}, \tag{3.1}$$

where E_u and E_v are the corresponding channel cluster energies. For each wedge, only a preset number of clusters with the best energy correlation are kept as candidates.

3.3 Reconstruction of Electromagnetic Clusters

Electromagnetic clusters [24] [25] are found with a simple cone algorithm that is seeded by an EM tower with transverse energy greater than 0.5 GeV. The algorithm forms a cluster by adding energy from neighboring towers within a radius of $\Delta R = \sqrt{\Delta\eta^2 + \Delta\phi^2} < 0.2$. The cluster is accepted if the transverse energy is greater 1.5 GeV and the energy deposition is consistent with an EM shower with at least 90% of the energy being deposited in the EM layers and the isolation (defined in Equation 3.2) being less than 0.2.

$$iso = \frac{E_{TOT}(0.4) - E_{EM}(0.2)}{E_{EM}(0.2)}. \tag{3.2}$$

Here $E_{TOT}(0.4)$ is the total energy within a cone of $\Delta R < 0.4$ and $E_{EM}(0.2)$ is the EM energy within a cone of $\Delta R < 0.2$. A cluster satisfying these basic criteria will be assigned an ID of 10. If the cluster also has an associated track within $|\Delta R| < 0.05$ and $|\Delta\phi| < 0.05$, then it will be assigned an ID of ± 11 where $+11$ designates an electron and -11 designates a positron.

Requirements can be placed on the quality of the spatial track match by cutting on the χ^2 probability. The χ^2 value is determined by the following equation:

$$\chi^2 = (\frac{\Delta\phi}{\sigma_\phi})^2 + (\frac{\Delta z}{\sigma_z})^2, \tag{3.3}$$

where $\Delta\phi$ is the difference between the ϕ position of the EM cluster at the third EM layer of the calorimeter and the extrapolated track position, Δz is the difference

between the z position of the EM cluster at the third EM layer of the calorimeter and the extrapolated track position, and σ_ϕ and σ_z are the corresponding resolutions.

To reduce hadronic backgrounds, additional cuts can be applied to multivariate quantities such as the H-matrix and the electron likelihood. The H-matrix is a χ^2 test based on seven variables:

- The fraction of energy in the first layer of the EM calorimeter.
- The fraction of energy in the second layer of the EM calorimeter.
- The fraction of energy in the third layer of the EM calorimeter.
- The fraction of energy in the fourth layer of the EM calorimeter.
- The cluster size at the third EM layer of the calorimeter.
- The z position of the primary vertex.
- The base-10 logarithm of the cluster energy.

The covariance matrix is created with events from test beam data and Monte Carlo simulations. The inverse of the covariance matrix is calculated, and the χ^2 is determined from the following equation:

$$\chi^2 = \sum_i \sum_j (x_i - \bar{x_i})(x_j - \bar{x_j}) H_{ij}, \tag{3.4}$$

where x_i is the value of the i^{th} variable for the EM cluster, $\bar{x_i}$ is the expected value of the i^{th} variable, and H_{ij} is the corresponding element from the inverse of the covariance matrix.

The electron likelihood [26] is related to the probability that an EM cluster is an electron given the value of seven variables:

- The EM fraction.
- The H-matrix value.
- The spatial track match χ^2 probability.
- The ratio of the calorimeter E_T to the track p_T.
- The DCA of the associated track.
- The numbers of tracks (including the associated track) in a cone of radius, $\Delta R < 0.05$.
- The total p_T of the tracks (excluding the associated track) in a cone of radius, $\Delta R < 0.4$.

The value of the likelihood (L) is determined by a weighted probability given below:

$$L(x_1, ..., x_7) = \frac{P_{sig}(x_1, ..., x_7)}{P_{sig}(x_1, ..., x_7) + P_{bkg}(x_1, ..., x_7)}, \tag{3.5}$$

$$P_{sig}(x_1, ..., x_7) = \prod_i P'_{sig}(x_i), \tag{3.6}$$

$$P_{bkg}(x_1, ..., x_7) \;=\; \prod_i P'_{bkg}(x_i). \tag{3.7}$$

Here x_i represents each of the seven variables, $P'_{sig}(x_i)$ is the probability for the EM object to be an electron given the value of x_i, and $P'_{bkg}(x_i)$ is the probability for the EM object to be a jet given the value of x_i. The probabilities are obtained from the distribution of each variable in a signal and background sample.

3.4 Reconstruction of Hadronic Jets

Hadronic jets are reconstructed with the use of a cone algorithm [27] [28] [29]. The formation of the cones occurs in three stages: preclustering, proto-jet formation, and correction for overlapping proto-jets.

In the preclustering stage, a cluster of towers that are potentially associated with a jet are identified. The clusters are formed by using the list of seed towers with total transverse momentum greater than 0.5 GeV. Starting with the seed with the highest transverse momentum, a precluster is formed by adding towers* within a radius of $\Delta R < 0.3$. The rapidity of the precluster is then calculated from the four-vector sum of tower momenta. Additional preclusters are then formed, in order of decreasing seed p_T, from the seed towers that have not already been included in a precluster. Only preclusters that consist of more than one tower or have a transverse momentum greater than 1 GeV are used in the proto-jet stage.

The formation of a proto-jet is an iterative process. In the first iteration a proto-

*To be considered, the towers must have a transverse momentum greater than 1 MeV.

jet is formed from a precluster by adding neighboring towers within a radius of $\Delta R < R_{cone}$†. The value of R_{cone} varies between algorithms and is set to 0.5 for JCCB jets and 0.7 for JCCA jets. In the second iteration, the rapidity of the proto-jet is calculated, and the proto-jet is reformed based on the new value of rapidity and by selecting towers within a radius of $\Delta R < R_{cone}$. The iterations continue until one of three conditions are met:

- The proto-jet has a $p_T < 3\ GeV$.
- The recalculated rapidity is within 0.001 of the previous iteration.
- The number of iterations exceed 50.

The proto-jets are formed in order of precluster transverse momentum, starting with the highest p_T precluster. If a precluster is within a $\Delta R < \frac{R_{cone}}{2}$ of a preexisting proto-jet it is not used to seed the formation of a new proto-jet. Furthermore duplicate proto-jets are removed by requiring that a new proto-jet cannot have the same p_T and position as a pre-existing jet (*i.e.* the ratio of transverse momenta cannot be within 1% of each other and the ΔR cannot be less than 0.005).

The precluster-based method can miss jets from soft radiation. Hence the proto-jet formation is also repeated using the midpoint* location between all combinations

†When considering proto-jets the actual rapidity is used in the calculation of ΔR instead of the pseudorapidity.

*The midpoints are calculated from the p_T weighted average values of rapidity and ϕ.

of proto-jets that have $\Delta R > R_{cone}$ and $\Delta R < 2R_{cone}$. The process used to form proto-jet is identical to the precluster method expect no restrictions are place on the separation between the midpoints and the preexisting proto-jets, and duplicates are not removed.

The combined list of precluster-based and midpoint-based proto-jets are then corrected for overlapping proto-jets. If more than 50% of the transverse momentum is shared between two proto-jets, then the proto-jets are merged together. If less than 50% of the transverse momentum is shared between two proto-jets, then the two proto-jets are split by removing the common tower from the proto-jet that is further away in ΔR.

3.5 Reconstruction of Muon Tracks in the Muon Detector

Muons are identified through the reconstruction of local muon track candidates in the muon spectrometer [30] [31] [32]. These candidates are formed by combining track segments from the A layer and B and C layers. Segments are formed at each layer by identify wire chamber hits that fit a straight line. If possible, these segments are then matched to scintillator hits in the corresponding layers. Complete track candidates are formed by matching segments across the layers and by taking into account potential deflections that will occur as the muon travels through the magnetic field of the toroid which is located between the A and B layers. This deflection, shown in Figure 3.1,

then provides a coarse measurement* of the muon momentum and charge.

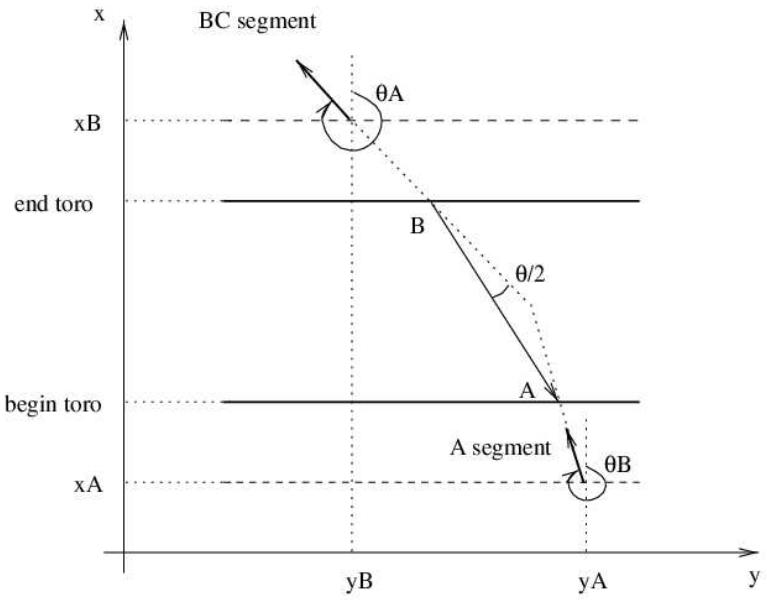

Figure 3.1 Deflection of a muon track in the toroid magnetic field.[32]

The muon candidates are assigned a quality based on the number of hits. This quality can take on three values which are referred to as tight, medium, and loose. A muon is assigned a tight quality if the following requirements are met:

- The local muon candidate has both A and B+C layer segments.
- The local muon candidate has at least two wire hits in the A layer.
- The local muon candidate has at least one scintillator hit in the A layer.
- The local muon candidate has at least three wire hits in the B+C layer.

*Compared to the central tracking detectors.

- The local muon candidate has at least one scintillator hit in the B+C layer.
- The fit between the A and B+C layers converged.

A muon is assigned a medium quality if it passes either of the following four sets of criteria:

- The local muon candidate has both A and B+C layer segments and:
  - The local muon candidate has at least two wire hits in the A layer.
  - The local muon candidate has at least one scintillator hit in the A layer.
  - The local muon candidate has at least two wire hits in the B+C layer.
  - The local muon candidate has at least one scintillator hit in the B+C layer, or it is a central muon with less than four B+C wire hits.
- The local muon candidate has only B+C layer segments and:
  - The local muon candidate has a central track match.
  - The local muon candidate is located in the bottom two octants of the detector with $|\eta_{Muon}| < 1.6$*.
  - The local muon candidate has at least one scintillator hit in the B+C layer.
  - The local muon candidate has at least two wire chamber hits in the B+C layer.

*η_{Muon} is the pseudorapidity measured in the local muon system with respect to the center of the detector.

- The local muon candidate has only A layer segments and:
  - The local muon candidate has a central track match.
  - The local muon candidate is located in the bottom two octants of the detector with $|\eta_{Muon}| < 1.6$.
  - The local muon candidate has at least one scintillator hit in the A layer.
  - The local muon candidate has at least two wire chamber hits in the A layer.
- The local muon candidate has only A layer segments and:
  - The local muon candidate has a central track match.
  - The local muon candidate is of low momentum and has less than 0.7 probablity of reaching the B+C layer

A muon is assigned a loose quality if it passes either of the following three sets of criteria:

- The local muon candidate has both A and B+C layer segments and:
  - The local muon candidate has at least one scintillator hit.
  - The local muon candidate passes at least two of the following conditions:
    - The local muon candidate has at least two wire hits in the A layer and at least one scintillator hit in the A layer.

    - The local muon candidate has at least two wire hits in the B+C layer.
    - The local muon candidate has at least one scintillator hit in the B+C layer, or it is a central muon with less than four B+C wire hits.

- The local muon candidate has only B+C layer segments and:
    - The local muon candidate has a central track match.
    - The local muon candidate has at least one scintillator hit in the B+C layer.
    - The local muon candidate has at least two wire chamber hits in the B+C layer.

- The local muon candidate has only A layer segments and:
    - The local muon candidate has a central track match.
    - The local muon candidate has at least one scintillator hit in the A layer.
    - The local muon candidate has at least two wire chamber hits in the A layer.

The muon candidates are matched to tracks from the central tracking detectors [33]. To be considered for the matching, the central track must be within $|\Delta\eta| < 1$ and $|\Delta\phi| < 1$ and have at least a momentum of 2 GeV and a $p_T > 1$ GeV. In order to match, the track must have a $\chi^2 \times (d.o.f.)$ that is less than 1000. If the muon candidate has both an A layer segment and a B or C layer segment, then the local

muon momentum is measured, and the χ^2 will be calculated using 4 variables: three that are related to position and one that is related to the momentum. If a momentum measurement is not made, then the χ^2 is calculated with the three position variables. For the case with the local momentum measurement, the matching is done either at the distance of closest approach to the beam line or at the A layer. When the matching is done at the DCA, the variables are θ, ϕ, z, and the ratio of charge to transverse momentum (q/p_T). When the matching is done at the A layer, the variables are θ, ϕ, q/p_T, and y-local, where y-local is a local spatial coordinate at the A layer. When there is no local momentum measurement, the matching is done at either the A or B layer, and the three variables that are used are θ, ϕ, and y-local.

Chapter 4
The Event Selection, Efficiencies, and Backgrounds

To examine the $W\gamma$ process, events that are consistent with the $W\gamma \rightarrow \ell\nu\gamma$ ($\ell = \mu, e$) signatures are selected from the DØ Run IIa data sample. In order for the measured event properties to be useable, the detector subsystems must have been functioning properly during the event measurement. Hence, only the subsample of Run IIa events for which the calorimeter, SMT, CFT, and preshowers were not in a bad or unknown state are analyzed. For the muon channel events, the muon detector could not have been in a bad or unknown state. Furthermore, the events are required to pass a suite of single lepton triggers (see the section on event selection), and only luminosity blocks that can be normalized for the luminosity calculation are considered. By constraining the trigger and luminosity blocks, it is possible to normalize model predictions for comparison against the observed data events. The selected data samples correspond to an integrated luminosity of $1031 \pm 63\ pb^{-1}$ and $963 \pm 59\ pb^{-1}$ for the electron and muon channels respectively. Much of the content presented in this chapter can also be found in [34].

4.1 Selection

4.1.1 Muon Channel Selection

Event Trigger

Selected events are required to satisfy one of four muon triggers:

- MUW_A_L2M3_TRK10
- MUW_W_L2M3_TRK10
- MUH1_TK12
- MUH1_TK12_TLM12

The triggers correspond to the different versions of the trigger list that were loaded for the particular run*. Hence, each data recording run is associated with only one trigger, and events are selected, only if the associated trigger fired. The different trigger criteria reflect the instantaneous luminosities at which the Tevatron was running; at higher instantaneous luminosities more restrictive triggers are required to maintain a desired accept rate. The amount of integrated luminosity for the collisions sampled by each trigger is found in Table 4.1. A detailed description of each trigger term can be found in Appendix A.

Muon Trigger	**Integrated Luminosity (pb^{-1})**
MUW_A_L2M3_TRK10	50 ± 3
MUW_W_L2M3_TRK10	251 ± 15
MUH1_TK12_TLM12	645 ± 39
MUH1_TK12	17 ± 1

Table 4.1 Integrated luminosity sampled by the muon triggers.

*The MUW_A_L2M3_TRK10 and MUW_W_L2M3_TRK10 triggers actually appear in the same versions of the trigger list.

Muon Identification

Selected muon channel events must contain a reconstructed muon of medium quality that passes the following set of criteria:

- The muon must be matched to a track with $p_T > 20\ GeV$.
- The momentum measured in the muon detector must be greater than 8 GeV. This reduces background from in flight decays of long lived particles that produce a muon.
- The DCA of the track matched to the muon must be less than 0.2 cm. This assures that the track comes from the beam and not from alternative sources such as cosmic rays.
- The muon track must be within the trigger acceptance of the CFT, and thus must have an $|\eta_{CFT^D}| < 1.6$*.
- The muon must not be in the "hole" region of the muon detector ($|\eta_{MUON^D}| < 1.1$ and $4.25 < \phi < 5.15$). This region is outside of the acceptance of the tight scintillator trigger.
- The muon must be isolated in the calorimeter and tracker:

*The notation η_{yyy^D} refers to the pseudorapidity in the relevant detector frame.

- In the calorimeter, the total transverse energy in a hollow cone of ΔR(0.4-0.1)† must be less than 2.5 GeV.
- The total transverse momentum of central tracks in a cone of ΔR < 0.5 must be less than 3.5 GeV. The track that is matched to the muon is excluded from this sum.

Photon Identification

Selected events must contain a reconstructed EM simple cone object with ID = 10 or ±11* that passes the following set of criteria:

- Photon candidate must have an $E_T > 11\ GeV$. The choice of this value will be explained later.
- The photon candidate must be isolated in the calorimeter and tracker:
  - The photon candidate must have a value of calorimeter isolation less than 0.07 where calorimeter isolation is defined as:

$$\text{isolation} = \frac{\mathrm{E_{TOT}}(0.4) - \mathrm{E_{EM}}(0.2)}{\mathrm{E_{EM}}(0.2)}. \tag{4.1}$$

  Here $E_{TOT}(0.4)$ is the total energy in a cone of ΔR < 0.4 and $E_{EM}(0.2)$ is the EM energy in a cone of ΔR < 0.2.

†Note, as defined previously, ΔR is the radius in $\eta \times \phi$ space.
*The simple cone ID was defined in Section 3.3.

  - The total track p_T in a hollow cone of ΔR(0.4-0.05) must be less than 2.0 GeV. To be included in the sum, the z-position of the track vertices must be within 2.0 cm of the lepton's associated track vertex.

- 97% of the photon energy must be deposited in the electromagnetic layers.

- The photon candidate must be identified as a neutral particle with the spatial track match χ^2 probability being less than 0.001.

- The photon candidate must be within the full fiducial acceptance of the CC and EC calorimeters and have $|\eta_{CAL^D}| < 1.1$ or $1.5 < |\eta_{CAL^D}| < 2.5$.

- The photon candidate must have an associated preshower cluster. This confirmation provides rejection against EM objects that are reconstructed from spurious calorimeter-only signals (for example noise or unidentified random electronic failures).

- The photon candidate must have a transverse shower shape that is consistent with an EM shower:

  - For photons in the central calorimeter, the energy weighted mean square width in the ϕ direction at the third layer of the EM calorimeter must be less than 14 cm^2.

  - For photons in the forward calorimeters, the energy weighted mean square

width at the third layer of the EM calorimeter in the ϕ direction must be less than $(5.96|\eta_D^2|$- 30.6 $|\eta_D|$+ 40.7) cm^2.

– An additional cut is applied on the z-width of the forward photons. The energy weighted mean square width in the z direction at the third layer of the EM calorimeter must be less than $(2.74|\eta_D^2|$ -16.3$|\eta_D| + 25.0)$ cm^2. This cut is not applied to central photons, because the z-width in the central calorimeter is not modeled accurately in Monte Carlo simulations.

- The z-vertex position of the central photons is extrapolated using the position of the energy deposits in the CPS and EM layers and must be within 10 cm of the primary vertex*.

Additional Event Cuts

- For neutrino identification, the missing transverse energy ($\not\!\!E_T$) is required to be greater than 20 GeV. Since the reconstructed $\not\!\!E_T$ only uses calorimeter information, it is corrected for the central track momentum of the muon.

- The $\not\!\!E_T$ calculation in the muon channel is heavily dependent on the identification of muons. Due to this dependency, the prompt $Z\gamma$ ($Z\gamma \rightarrow \mu\mu\gamma$) and radiative $Z\gamma$ ($Z \rightarrow \mu\mu \rightarrow \mu\mu\gamma$) processes are a significant background. To limit this background, a veto is applied to events that contain an additional medium

*The resolution of this extrapolation is measured to have an RMS of ~ 3 cm.

quality muon or another isolated track that originates from the same vertex with $p_T > 15\ GeV$ and $|\eta_{CFT^D}| < 1.8$. The isolated track must pass the track isolation defined in the muon selection and be within 3 cm of the selected lepton track vertex. $Z\gamma$ events in which neither a track or muon are reconstructed will then fake the $W\gamma$ signature as shown in Figure 4.1.

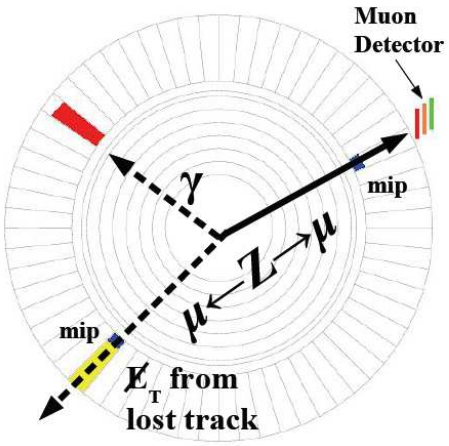

Figure 4.1 Cartoon of a $Z\gamma$ event faking a $W\gamma$ signature.

- The event is removed if the difference between the z position of the primary vertex used by the $\not\!\!E_T$ calculation and the vertex of the track that is associated with the muon is greater than 3 cm. This cut is required to reduce mismeasured $\not\!\!E_T$ which would result from the misplaced vertex.

- The ΔR between the lepton and photon must be greater than 0.7. This is both a theoretical and an experimental necessity. Without an explicit minimal

separation, collinear divergences would appear in the perturbative calculations. Furthermore, the objects must have a minimal separation that is consistent with the reconstruction cone requirements.

The selected candidate events will contain contributions from prompt $W\gamma$ production as shown in Figure 4.2 and radiative $W\gamma$ events that result from the final-state radiation (FSR) from the charged lepton as shown in Figure 4.3.

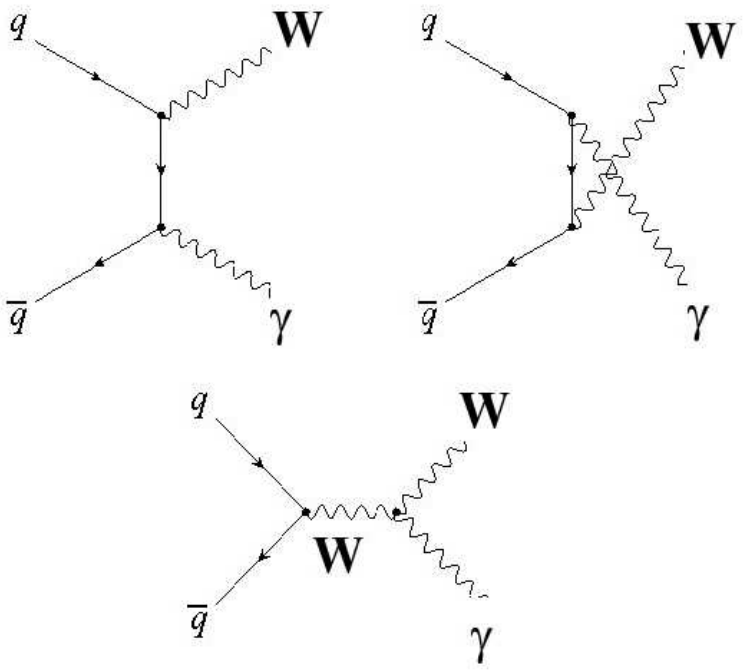

Figure 4.2 The leading order prompt $W\gamma$ production diagrams from quark annihilation.

The destructive interference of the prompt $W\gamma$ production is obscured by the more dominant FSR contribution. In order to suppress the FSR a minimum threshold,

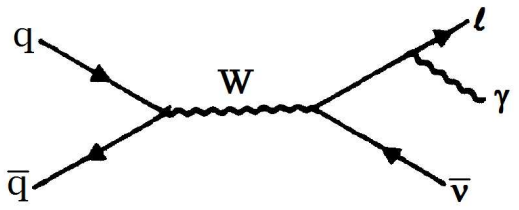

Figure 4.3 Diagram of final-state radiation in W production.

which is much greater than the W mass, is applied to the three-body transverse mass of the $\ell\nu\gamma$ system. The definition of the three-body transverse mass can found in Equation 4.2.

$$M_{T^3}^2(\ell\gamma; \not\!\!E_T) = \left((M_{\ell\gamma}^2 + |\mathbf{p_T}(\gamma) + \mathbf{p_T}(\ell)|^{\mathbf{2}})^{\frac{\mathbf{1}}{\mathbf{2}}} + \not\!\!E_T\right)^2 - |\mathbf{p_T}(\gamma) + \mathbf{p_T}(\ell) + \not\!\!E_T|^{\mathbf{2}}. \quad (4.2)$$

A demonstration of how the FSR overwhelms the expected prompt $W\gamma$ production and how the three-body mass is expected to remedy this effect is shown in Figure 4.4. For the muon channel, the following three-body transverse mass cut is applied:

- $M_{T^3}(\ell\gamma; \not\!\!E_T)$ must be greater than 105 GeV. The value of this cut was chosen to reduce the FSR contribution to less than 5%.

Figures of the selected muon channel candidate distributions can be found in Appendix A

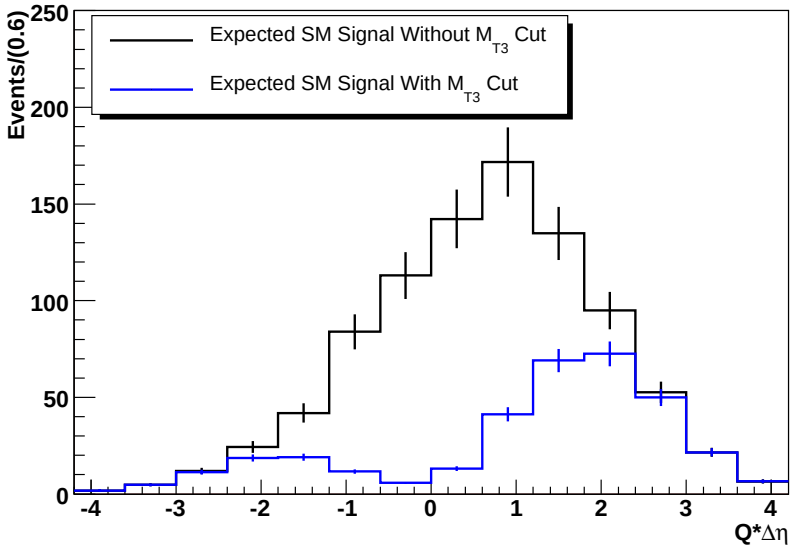

Figure 4.4 The expected signal distribution of the charge-signed rapidity difference for the combined electron and muon channels.

4.1.2 Electron Channel Selection

Event Trigger

Selected events must satisfy one of five suites of single electron triggers, which will be referred to as:

- The pre-v11 suite
- The v11 suite
- The v12 suite
- The v13 suite

- The v14 suite

The suites are arranged by trigger list version and consist of a collection of electron triggers that were available for the corresponding trigger list. Each suite is subdivided into groups of triggers, which represent a logical OR of the corresponding trigger conditions. For the event to be selected, at least one of the triggers in the trigger group must have fired. Only one trigger group is considered per data taking run.

The reason for multiple trigger groups within a particular suite is due to variations in the trigger **prescale** settings. If a trigger group were to contain triggers with an assortment of prescales, it would complicate the luminosity calculation. The standard method of dealing with individually prescaled triggers is to simply remove them from the trigger group for the relevant data taking runs.

The pre-v11 suite of triggers is composed of the following trigger groups:

- Group 1 (considered if none of the triggers are prescaled)
  - EM_HI
  - EM_HI_SH
  - EM_HI_2EM5_SH
- Group 2 (considered if otherwise)
  - EM_MX

  - EM_MX_SH

The v11 suite of triggers is composed of the following trigger groups:

- Group 1 (considered if none of the triggers are prescaled)
  - EM_HI
  - EM_HI_SH
  - EM_HI_2EM5_SH
- Group 2 (considered if otherwise)
  - EM_MX
  - EM_MX_SH

The v12 suite of triggers is composed of the following trigger groups:

- Group 1 (considered if none of the triggers are prescaled)
  - E1_SH30
  - E1_SHT20
  - E2_SHT20
  - E3_SHT20
- Group 2 (considered if otherwise)

  - E1_SH30
  - E1_SHT20

The v13 suite of triggers is composed of the following trigger groups:

- Group 1 (considered if none of the triggers are prescaled)
  - E1_SH30
  - E1_SHT22
  - E2_SHT22
  - E3_SHT22
- Group 2 (considered if the E3_SHT22 trigger is prescaled)
  - E1_SH30
  - E1_SHT22
  - E2_SHT22
- Group 3 (considered if otherwise)
  - E1_SH30
  - E1_SHT22

The v14 suite of triggers is composed of one trigger group:

- Group 1
  - E1_SH35
  - E1_SHT25
  - E3_SH35
  - E3_SHT25
  - E1_T13SHT15
  - E1_T15SH20
  - E3_T13SHT15
  - E3_T15SH20

The triggers for the pre-v11 suite and the v11 suite are identical except for the η coverage at level-1. The pre-v11 suite of triggers only utilize calorimeter trigger towers out to an $|\eta|$ of 2.4 while all later triggers use trigger towers out to an $|\eta|$ of 3.2. The amount of integrated luminosity for the collisions sampled by each trigger group is found in Table 4.2. A detailed explanation of the trigger terms can be found in Appendix B.

Electron Identification

Selected events must contain a reconstructed EM simple cone object with ID = 10 or $\pm$11 that passes the following set of criteria:

Electron Trigger Group	Integrated Luminosity (pb^{-1})
pre-v11 suite	
Group 1	8.8 ± 0.5
Group 2	0.65 ± 0.05
v11 suite	
Group 1	60.06 ± 4
Group 2	5.26 ± 0.3
v12 suite	
Group 1	223 ± 14
Group 2	17 ± 1
v13 suite	
Group 1	322 ± 20
Group 2	33 ± 2
Group 3	24 ± 1
v14 suite	
Group 1	338 ± 21

Table 4.2 Integrated luminosity sampled by the electron triggers.

- The electron candidate must be within the full fiducial acceptance of the CC and EC calorimeters and have $|\eta_{CAL^D}| < 1.1$ or $1.5 < |\eta_{CAL^D}| < 2.5$.

- The electron candidate is required to have an $E_T > 25\ GeV$.

- The fraction of energy in the EM layers of the calorimeter is required to be greater than 0.90.

- The isolation as defined in Equation 4.1 must be less than 0.20.

- The electron likelihood as defined in Section 3.3 is required to be greater than 0.20

- For the electron identification to be disjoint from the photon identification, the electron must have a spatial track match χ^2 probability that is greater than 0.001.

Photon Identification

Selected events must contain an additional reconstructed EM simple cone object that passes the same set of photon identification criteria as in the muon channel.

Additional Event Cuts

- For neutrino identification, the $\not\!\!E_T$ is required to be greater than 25 GeV.

- The W transverse mass, as defined in Equation 4.3, is required to be greater than 50 GeV.

$$M_T^2(\ell \not\!\!E_T) = 2 \times p_T(\ell) \times \not\!\!E_T \times \left(1 - \frac{p_x(\ell) \times \not\!\!E_x + p_y(\ell) \times \not\!\!E_y}{\not\!\!E_T \times p_T(\ell)}\right) \tag{4.3}$$

- Since the EM shower from a photon and electron are nearly indistinguishable, it is possible for an electron to fake a photon signature if the associated track is not reconstructed as shown in Figure 4.5. To reduce the background from the $Z \rightarrow ee$ process, the two-body mass of the electron and photon cannot be in a mass window of 87-97 GeV. A more detailed discussion of this cut is found in Section 4.4.1.

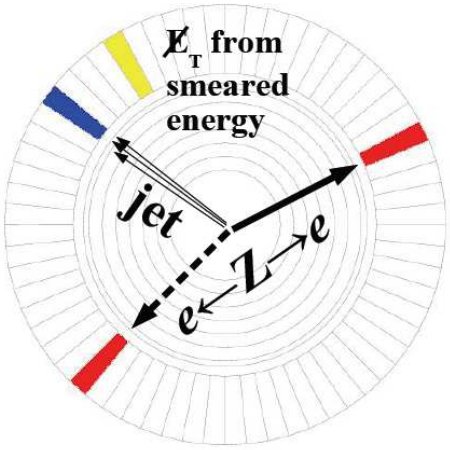

Figure 4.5 Cartoon of a $Z \rightarrow ee$ event faking a $W\gamma$ signature.

- The three-body transverse mass as defined in Equation 4.2 is required to be greater than 110 GeV. The value of this cut, along with the W transverse mass cut is chosen to reduce the FSR contribution to less than 5%.

- The event is removed if the difference between the z position of the primary vertex used by the $\not\!\!E_T$ calculation and the vertex of the track that is associated with the electron is greater than 3 cm. This cut is required to reduce mismeasured $\not\!\!E_T$ which would result from the misplaced vertex.

- The ΔR between the lepton and photon must be greater than 0.7.

- Since a sufficiently energetic photon could fire the single electron trigger and because no veto is required on the presence of any other EM objects, an explicit match is required between the trigger object that fired the single electron trigger

and the reconstructed electron.

Figures of the selected electron channel candidate distributions can be found in Appendix B

4.2 Efficiencies and Acceptances

Associated with the above the selection criteria are the corresponding efficiencies. To estimate the selection efficiencies, a Monte Carlo generator is used to create an event list of four-momentum vectors for the final-state particles from the $p\bar{p} \rightarrow W\gamma \rightarrow \ell\nu\gamma$ and $p\bar{p} \rightarrow W \rightarrow \ell\nu \rightarrow \ell\nu\gamma$ processes. To simulate detector measurements, the event four-vectors are processed by a parameterized software that randomly smears the event quantities within the detector resolutions. The geometric and kinematic cuts are applied to the smeared events, and the remaining events are randomly selected based on identification efficiencies that are stored in look-up-tables. The efficiencies that are stored in the look-up-tables are referenced by particle position and/or energy and are estimated from data samples that were collected from Monte Carlo simulations and real collider data*

4.2.1 Monte Carlo Generation

A list of final-state four-vectors from prompt and radiative $W\gamma$ production events with photon $E_T > 3\ GeV$ and $\Delta R_{\ell\gamma} > 0.4$ is created with the Baur Monte Carlo

*It is conventional to simply use the term, data, when referring real collider data and to use the acronym, MC, when referring to simulated data. Unless otherwise noted, this convention will be used throughout the document.

generator [35]. This generator produces event kinematics based on leading-order perturbative calculations. Since the kinematics are only calculated at leading-order, they do not adequately represent inclusive $W\gamma$ production which requires the inclusion of next-to-leading-order corrections from initial-state QCD radiation. The initial-state radiation effectively gives the $W\gamma$ system a boost; to compensate for this effect, a boost is applied to the Baur MC four-vectors. The value of the boost is determined by using the Pythia MC generator [36] to produce $W\gamma$ events with initial-state QCD radiation. Pythia does not accurately model the $W\gamma$ coupling, but the initial-state QCD radiation and the resultant boost to the $W\gamma$ is well-modeled. The value of the boost is extracted from the Pythia events and randomly added to the Baur MC four-vectors.

4.2.2 Smearing the Monte Carlo

Particle position and energy is extracted from the boosted four-vectors and smeared with a parameterized MC simulation. In this analysis, the parameterization found in the DØ PMCS [37] software package is used. The values of the smear parameters used in this analysis can be found in [38] and are described in Appendix C. Since the writing of [38], there have been updates to the energy smearing for EM objects [39] and the $\not\!\!E_T$ calculation [40]. The updated parameterizations are include in Appendix C, in place of the obsolete values.

4.2.3 Geometric and Kinematics Acceptance

The $W\gamma$ event acceptance is estimated by finding the number of smeared Monte Carlo events that pass the geometric and kinematic cuts and by dividing the number of selected events by the number of Monte Carlo events (prior to smearing) that pass the generator-level cuts ($\Delta R_{\ell\gamma} > 0.7$, $E_T(\gamma) > 11\ GeV$, and $M_{T^3} > 90\ GeV$) that the cross section is measured with respect to. The smeared parameters are randomly varied within their error values to obtain an ensemble of Monte Carlo experiments. The average acceptance from the ensemble is taken as the acceptance and the standard deviation is assessed as a systematic error. For the muon channel, the overall kinematic acceptance and overall geometric acceptance are estimated to be 0.660 $\pm$ 0.018 and 0.348 $\pm$ 0.002, respectively. For the electron channel, the overall kinematic acceptance and overall geometric acceptance are estimated to be 0.480 $\pm$ 0.003 and 0.350 $\pm$ 0.0015, respectively. Note the value of the acceptance is dependent on the choice of generator-level cuts that the MC cross section is measured with respect to.

On top of the uncertainties introduced by the smear parameter, there are additional uncertainties that come from the theoretical calculation. These uncertainties arise from the limited accuracy of the perturbative calculation and the assumptions that were made about the parton distributions (PDFs) within the colliding hadrons. To compensate for higher-order corrections (*i.e.* the next-to-next-to-leading-order or

NNLO corrections) which are not included in the perturbative calculation or Pythia boost, a 6% systematic error * is assessed on the overall normalization. To determine the systematic error from the choice of PDF the procedure recommended in [42] is used†. A 2.6% systematic error from PDF uncertainties is estimated for the expected $p\bar{p} \to \ell\nu\gamma$ production cross section. Futhermore, varying the PDFs also has a small effect on the shape of the charge-signed rapidity distribution, which is shown in Figure 4.6.

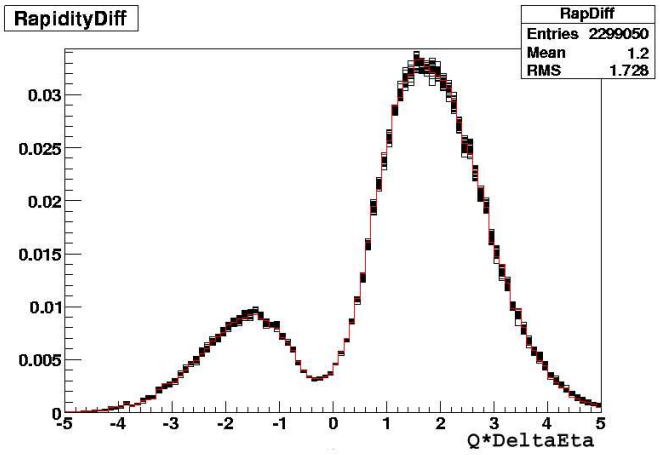

Figure 4.6 Variation in the charge-signed rapidity difference of NLO Baur MC with the CTEQ6 PDF sets. The red line is the central CTEQ6M value. The black lines represent the variation from 40 separate sets.

*The value of this error is taken from the previous DØ $W\gamma$ publication [41]. The Monte Carlo is identical to this analysis; hence the theoretical error is the same.

†In this method an ensemble of results are found by varying the theoretical parameters.

4.2.4 Efficiencies

Lepton identification and trigger efficiencies are estimated with two standard DØ software packages: muo_cert[43] and em_cert[44]. Both packages calculate efficiencies by implementing a "Tag-and-Probe" method on a collection of $Z \rightarrow \ell\ell$ data events. The premise behind the Tag-and-Probe method is to utilize a production resonance that produces pairs of identically flavored objects. One of the objects, the tag is required to pass a set of tight quality cuts. The tag cuts satisfy all of the criteria that were necessary for the event to have be readout and analyzed (*i.e.* trigger requirement) which leaves the second object (the probe) unbiased for efficiency studies. In addition, the tight quality requirement on the tag limits the amount background which increases the purity of the probe object.

To identify the probe object, a loose selection criterion must be applied. This minimal requirement is known as the preselection cut. Efficiencies are measured with respect to the preselection cut by collecting the sample of probes that pass the preselection cut and by finding the fraction of probes that pass the cut under study. In the case, where background is non-negligible, the amount of real lepton pairs can be extracted from the samples by fitting the invariant mass of the tag-probe system to a function (see Figure 4.7). The function is actually a sum of two functions: the first represents the contribution from the resonance and the second represents the background contribution. The amount of leptons in the probe sample can be

extracted from the signal contribution to the functional fit.

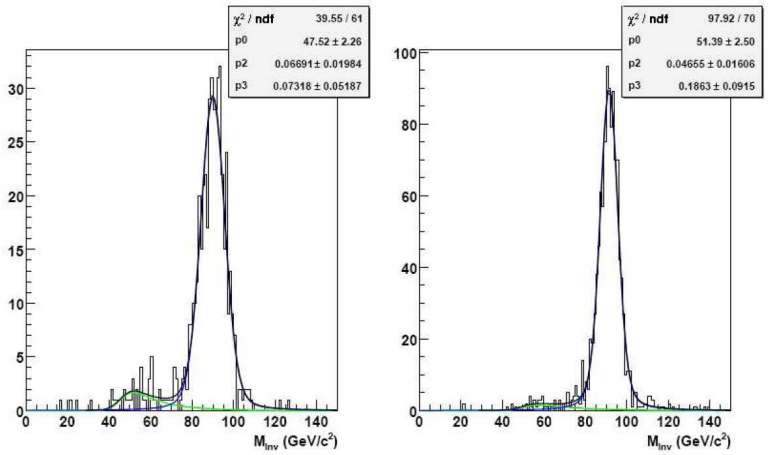

Figure 4.7 An example of the tag-probe invariant mass. The plot on the left represents the set of preselected probes. The plot of the right represents the set of probes that pass the cut under study. The black curve represents the total fit. The blue curve represents the contribution to the fit from the resonance. The green curve represents the contribution to the fit from the background [45].

Electron ID and Trigger Efficiencies

For the electron identification the following efficiencies are measured:

- The efficiency for an electron to be reconstructed as a simple cone object with $|ID| < 12$ with isolation less than 0.20 and EM fraction greater than 0.90 (Electron Preselection Efficiency).

- The efficiency for an electron that has passed the above cut to have a likelihood greater than 0.20 and a spatial track match probability greater than 0.001 (Electron ID Efficiency).

- The efficiency for an electron that passes the above cuts to have fired the trigger (Electron Trigger Efficiency).

To measure the electron preselection efficiency, the probe is selected by requiring that there be a high p_T track. The probe is tested by searching within a ΔR of 0.1 for an EM cluster that passes the electron preselection critera. Since the tracking and calorimeter cuts are uncorrelated the measured electron preselection efficiency is equivalent to an absolute efficiency with respect to all electrons.

The electron preselection efficiency is found as a function of $|\eta_{CAL^D}|$. A plot of the preselection efficiency is found in Figure 4.8. The efficiency is applied to the smear of the Wγ MC via a look up table that is referenced by $|\eta_{CAL^D}|$. The average electron preselection efficiency for Wγ events is found to be 0.991 $\pm$ 0.002.

The electron ID efficiency is found as a function of $|\eta_{CAL^D}|$ and E_T. Plots of the electron ID efficiency are found in Figure 4.9 and in Figures B.22- B.41 in Appendix B. These efficiencies are applied to the smear of the Wγ MC via a look up table that is referenced by $|\eta_{CAL^D}|$ and E_T. The average electron ID efficiency for Wγ events is found to be 0.84 $\pm$ 0.02.

The trigger efficiency is found as a function of E_T and is fit with a functional form, f, that permits two plateaux:

$$f = 0.5 \times [p_2(1 + Erf(\frac{E_T - p_0}{\sqrt{2}p_1})) + p_5(1 + Erf(\frac{E_T - p_3}{\sqrt{2}p_4}))]. \tag{4.4}$$

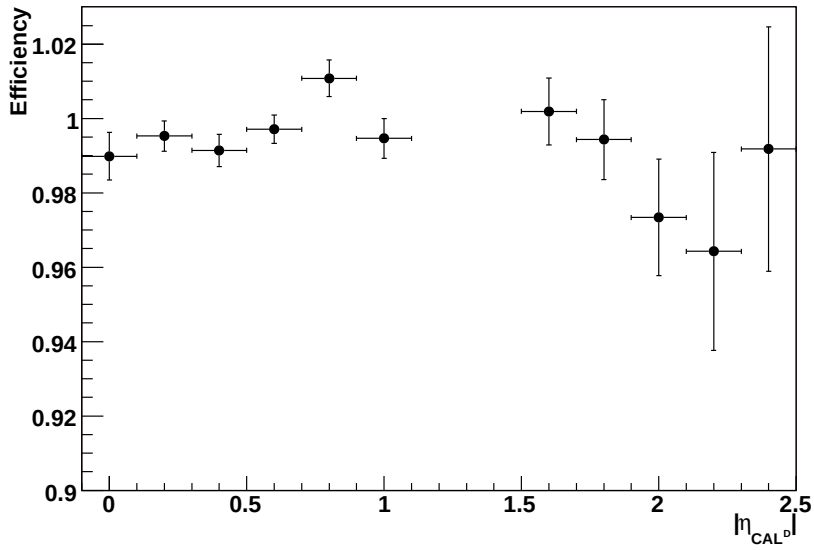

Figure 4.8 Electron preselection efficiency.

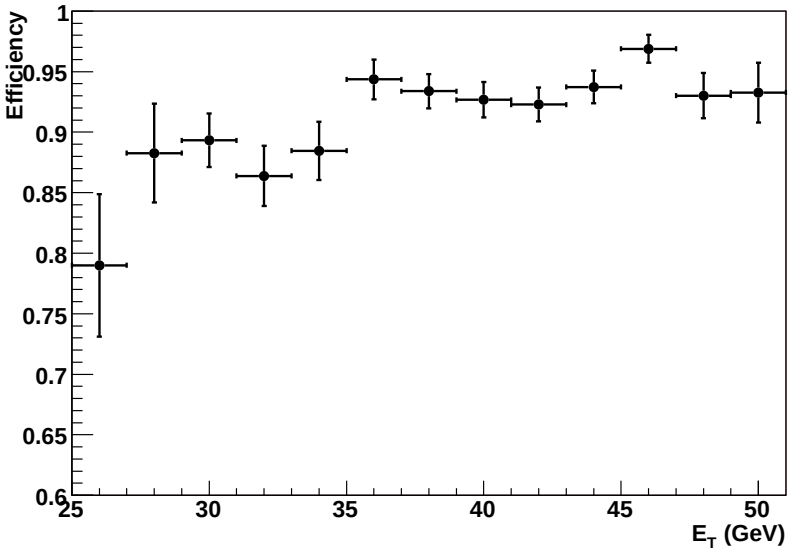

Figure 4.9 Electron ID efficiency for $1.0 \leq |\eta_{CAL^D}| < 1.1$.

Here $Erf()$ represents the error function:

$$Erf(x) = \frac{2}{\sqrt{\pi}} \int_0^x e^{-t^2} dt. \tag{4.5}$$

Plots of the turn on curves can be found in Figures 4.10- 4.11 and in Figures B.6-B.21 in Appendix B. The turn on curves are combined by calculating the luminosity weighted average with numbers found in Table 4.2. The weighted average efficiency is then applied to the smear of the Wγ MC via a look up table that is referenced by E_T. The average trigger efficiency for Wγ events is found to be 0.976 ± 0.002.

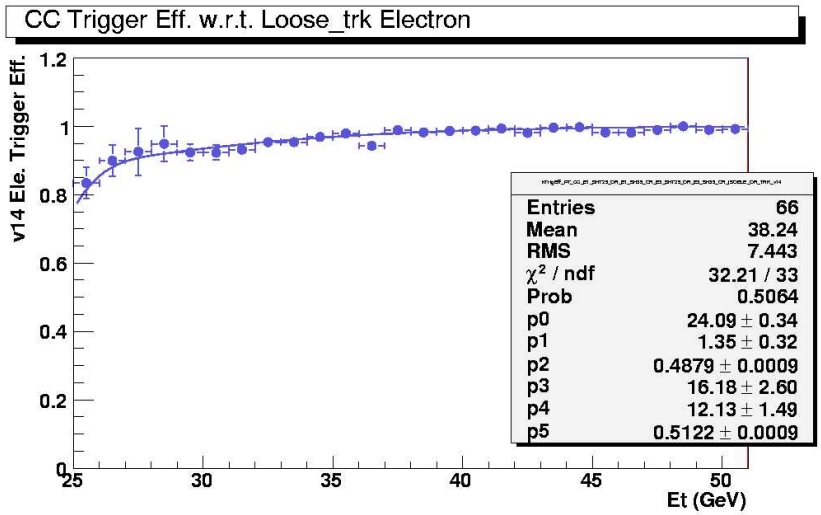

Figure 4.10 Central electron trigger efficiency for the v14 trigger suite.

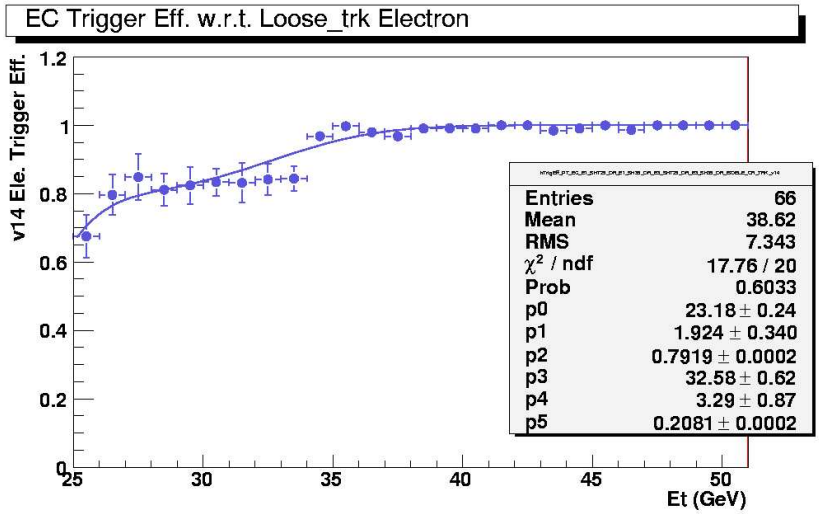

Figure 4.11 Forward electron trigger efficiency for the v14 trigger suite.

Muon ID and Trigger Efficiencies

For the muon identification the following efficiencies are measured:

- The efficiency for a muon to produce a track with a DCA $< 0.2\ cm$.
- The efficiency for a muon that passes the above cut to also produce a medium quality muon.
- The efficiency for a muon that passes the above cuts to pass the isolation requirements.
- The efficiency for a muon that passes the above cuts to pass the trigger require-

ments.

To measure the tracking efficiency, the probe is selected by requiring only muon detector information. The probe is tested by searching for a matching track*. Since the tracking and calorimeter cuts are uncorrelated the measured tracking efficiency is equivalent to an absolute efficiency with respect to all muons.

The muon track reconstruction efficiency is found as a function of η_{CFT^D} and the z vertex position. Plots of the tracking efficiency are found in Figure 4.12. These efficiencies are applied to the smear of the Wγ MC via a look up table that is referenced by η_{CFT^D} and the z vertex position. The average tracking efficiency for Wγ events is found to be 0.96 ± 0.01.

The medium muon reconstruction efficiency is found as a function of η_{Muon^D} and ϕ. Plots of the medium muon efficiency are found in Figure 4.13. These efficiencies are applied to the smear of the Wγ MC via a look up table that is referenced by η_{Muon^D} and ϕ. The average medium muon efficiency for Wγ events is found to be 0.80 ± 0.05.

The muon isolation efficiency is found as a function of η, ϕ, and track p_T separately. Plots of the muon isolation efficiency are found in Figure 4.14. Since the efficiencies are approximately flat in η and ϕ for $|\eta| < 1.6$, these efficiencies are applied to the smear of the Wγ MC via a look up table that is referenced by p_T. The average

*The matching condition is the loose χ^2 test described in the muon reconstruction section. Since this cut is so loose, the inefficiency associated with the matching criteria is negligible.

isolation efficiency for Wγ events is found to be 0.938 $\pm$ 0.004.

For each individual muon trigger, efficiencies are measured separately at Level 1, 2, and 3 as a function of η_{Muon^D}. Plots of the trigger efficiency can be found in Figures A.6- A.13 in Appendix A. The measured efficiencies at the three levels are multiplied together to obtain the overall efficiency of the corresponding single muon trigger. The single muon trigger efficiencies are then combined by calculating the luminosity weighted average using the luminosities found in Table 4.1. The weighted

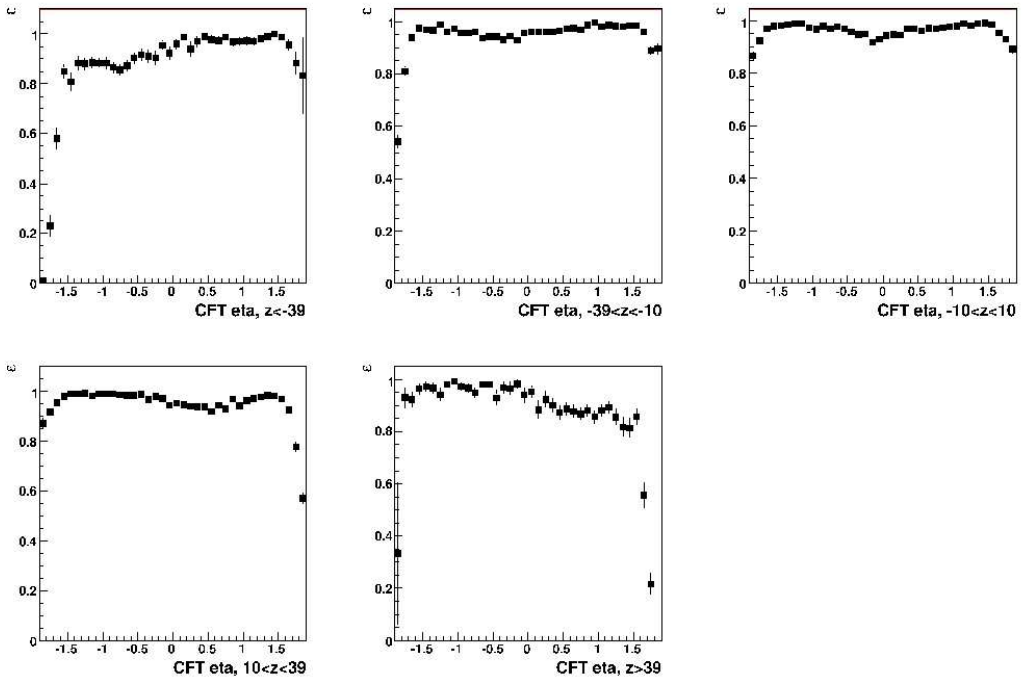

Figure 4.12 Muon tracking efficiency as a function of CFT detector η and the z-vertex.

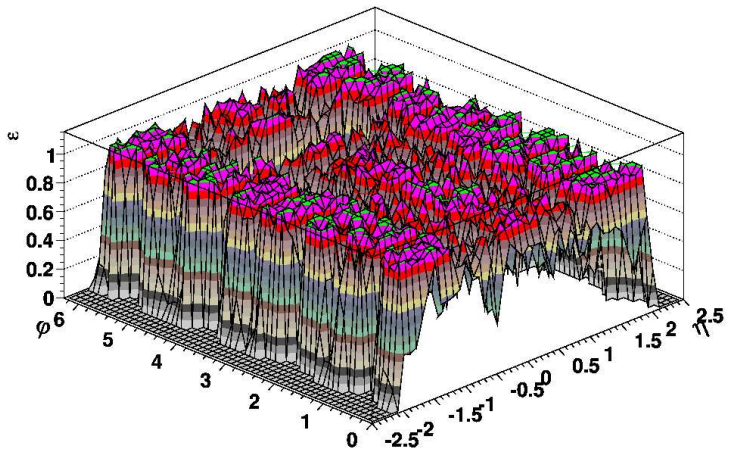

Figure 4.13 Medium muon efficiency.

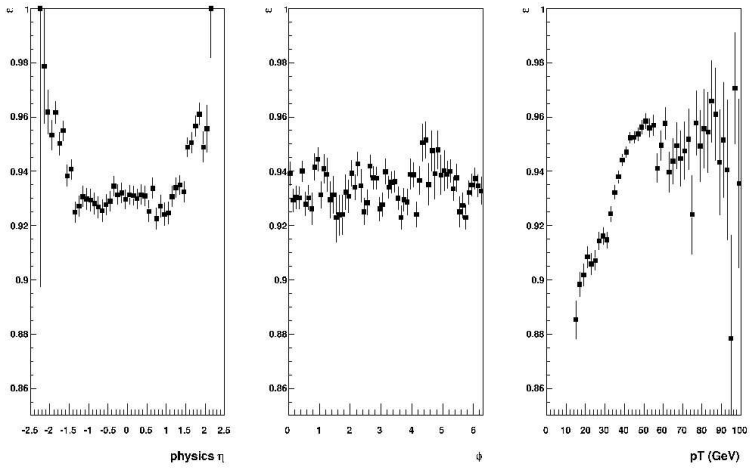

Figure 4.14 Muon isolation efficiency.

average efficiency is applied to the smear of the Wγ MC via a look up table that is referenced by η_{Muon^D}. The average trigger efficiency for Wγ events is found to be 0.655 ± 0.002.

$Z\gamma$ Veto Efficiency

The backgrounds that give rise to the additional muon signatures (noise, cosmics, QCD, etc.) should be the same for Z and $W\gamma$ events. Therefore, the efficiency of the $Z\gamma$ veto in the muon channel (the veto on additional isolated tracks or medium quality muons) is measured with a sample of $Z \rightarrow ee$ data events. The $Z \rightarrow ee$ events are selected by requiring that there be two electrons that pass the $W\gamma$ electron ID requirement. The events are then divided into two samples: those that pass the veto and those that fail the veto. The efficiency is then determined through three methods.

In the first method, the efficiency is calculated from the total number of events in both samples and is found to be 0.9647 ± 0.0007. In the second method, only events with an invariant mass between 80 and 100 GeV are used. The point of this method is to enrich the purity of the Z sample by selecting a mass range where the Z production dominates. An efficiency of 0.9652 ± 0.0007 is found with the second method. In the third method, an attempt is made to remove the background contamination from the samples by fitting a function to the invariant mass distributions of the two samples. The function consists of the sum of a background term ($f_{bkg}(M_{inv})$) and a signal term

($f_{sig}(M_{inv})$), which are defined in Equations 4.6 and 4.8.

$$f_{bkg}(M_{inv}) = p_3 Erfc(p_1(p_0 - M_{inv}))e^{-p_2(M_{inv}-M_Z)}, \tag{4.6}$$

where M_Z is the mass of the Z boson and $Erfc()$ is the complementary error function:

$$Erfc(x) = \frac{2}{\sqrt{\pi}} \int_x^\infty e^{-t^2} dt. \tag{4.7}$$

$$f_{sig}(M_{inv}) = p_6 Voigt(M_{inv} - p_4, p_5, p_4\Gamma_Z/M_Z), \tag{4.8}$$

where $Voigt()$ is the normamlized Voigt funcion found in the ROOT [46] software package, and Γ_Z/M_Z is the ratio of the Z boson width and mass. The plots of the fits to the invariant mass distributions of the two samples are found in Figure 4.15.

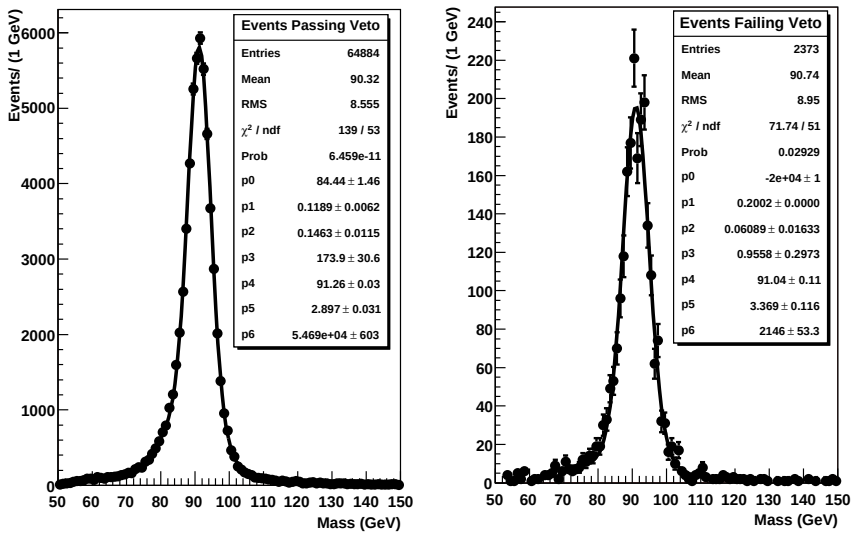

Figure 4.15 Invariant mass of Z→ee events. The plot on the left is the sample of events that pass the $Z\gamma$ veto. The plot on the right is the sample of events that fail the veto.

The number of Z events with an invariant mass between 80 and 100 GeV is extracted from the signal contribution to the two fits, and the veto efficiency is calculated to be 0.9625 ± 0.0015. The veto efficiency is assigned as the average of the three results, and the maximum difference between the three methods is assessed as a systematic error. This corresponds to an efficiency of 0.964 ± 0.003.

$\Delta z \leq 3.0$ *cm* Efficiency

Monte Carlo simulations are observed to always reconstruct the primary vertex at the position of the lepton track vertex; however this is not observed to be the case in data. To determine the fraction of Wγ events that have a reconstructed primary vertex with a z position that is within 3.0 cm of the lepton vertex, a sample of $W \rightarrow \mu\nu$ and $Z \rightarrow \mu\mu$ events are collected, and the fraction of events that pass the Δz cut are found for both samples. The two samples are considered due to the potential biases that are inherent to both samples. For the $W \rightarrow \mu\nu$ sample, a potential source of bias is mismeasured $\not\!\!E_T$ that comes from the misplaced primary vertex. For the $Z \rightarrow \mu\mu$ events, the additional track may bias the results.

Since the primary vertex reconstruction is correlated to the number of reconstructed tracks, only "one-legged" $Z \rightarrow \mu\mu$ events are used. In this situation two muons are reconstructed in the muon detector but only one has a central track match. To select the "one-legged" $Z \rightarrow \mu\mu$ events the following requirements are made:

- The event must pass the same trigger and run quality as the Wγ muon channel

- The event must have two and only two loose quality muons with local $p_T > 8$ GeV.
- Both muons must have A layer scintillator timing < 5 ns.
- The two muons must have a $\Delta R > 2.0$
- One muon must satisfy all of the Wγ muon ID cuts
- The other muon must have:
  - No central track match
  - The sum of the transverse energy in the calorimeter in a hollow cone of ΔR(0.4-0.1) is required to be smaller than 2.5 GeV.
  - The sum of the transverse momentum of tracks in a cone of ΔR < 0.5 is required to be smaller than 3.5 GeV.

The mass peaks for the "one-legged" $Z \rightarrow \mu\mu$ events are shown in Figures 4.16 and 4.17. The two-body mass is calculated with the track p_T of the track-matched muon and the local p_T of the muon without the track-match. The fraction of $Z \rightarrow \mu\mu$ events with $\Delta z > 3.0$ cm is summarized in Table 4.3 for various muon quality cuts and track separation requirements. The average value of the efficiency is used and the maximum difference between the measured efficiencies is set as an error. The efficiency of the Δz cut is measured to be 0.94 ± 0.01.

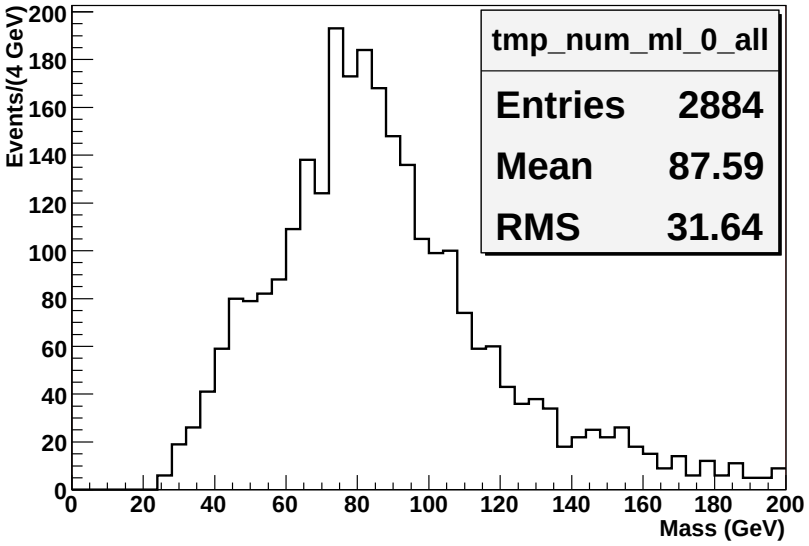

Figure 4.16 Mass of "one-legged" $Z \rightarrow \mu\mu$ events.

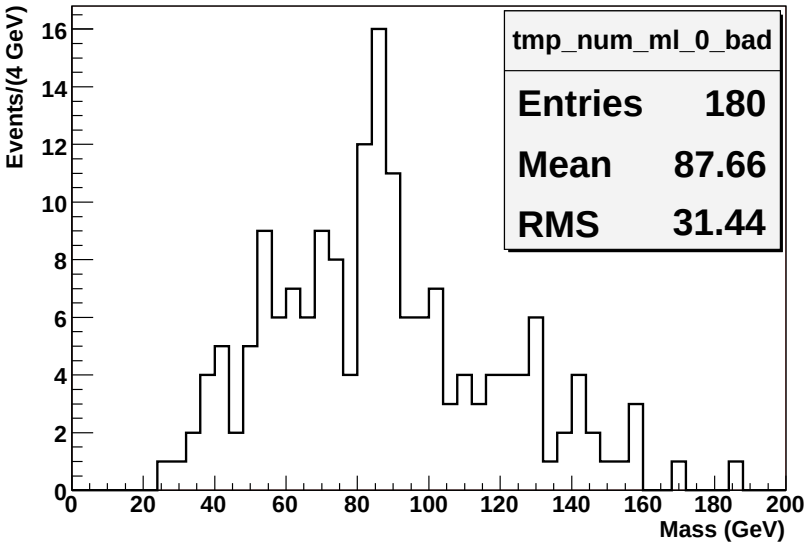

Figure 4.17 Mass of "one-legged" $Z \rightarrow \mu\mu$ events with $\Delta z > 3.0\ cm$.

Quality of muon with track match	**Quality of muon with no track**	**ΔR between trackless muon and nearest track from same vertex**	**Percent of events with $\Delta z > 3.0$ cm**
medium	loose	0.0	$(6.2 \pm 0.5)\%$
tight	tight	0.0	$(6.2 \pm 0.5)\%$
medium	loose	0.4	$(6.1 \pm 0.5)\%$
tight	tight	0.4	$(6.2 \pm 0.5)\%$
medium	loose	1.0	$(7.1 \pm 0.7)\%$
tight	tight	1.0	$(6.9 \pm 0.8)\%$

Table 4.3 Percentage of $Z \to \mu\mu$ events with $\Delta z > 3.0$ cm.

The $W \to \mu\nu$ sample is collected by requiring the events to pass the same selection criteria as $W\gamma$ muon channel, with the exclusion of the cuts that are related to the presence of a photon. The transverse mass of the selected $W \to \mu\nu$ sample is shown in Figure 4.18. The transverse mass of the events that fail the Δz cut are shown in Figure 4.19. The fraction of events that pass the Δz cut is found to be 0.9401 ± 0.0003, which is consistent with the number obtained from the $Z \to \mu\mu$ sample.

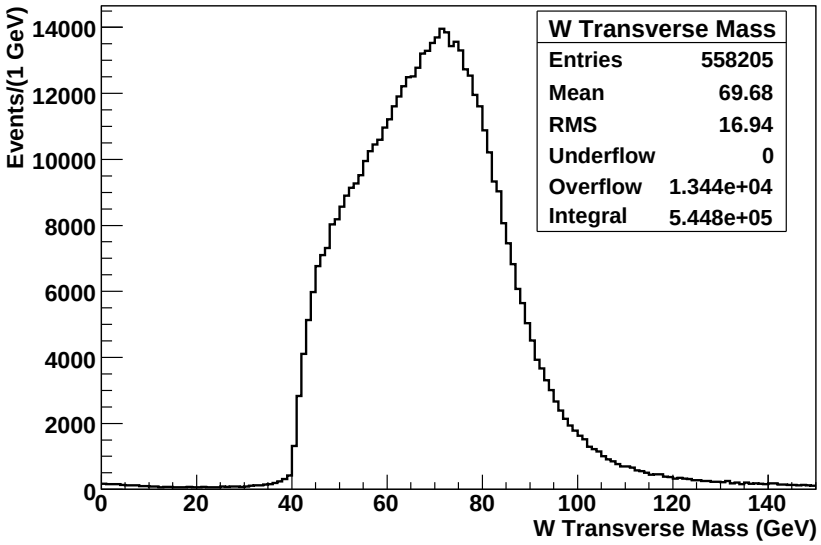

Figure 4.18 Transverse mass of the $W \rightarrow \mu\nu$ events.

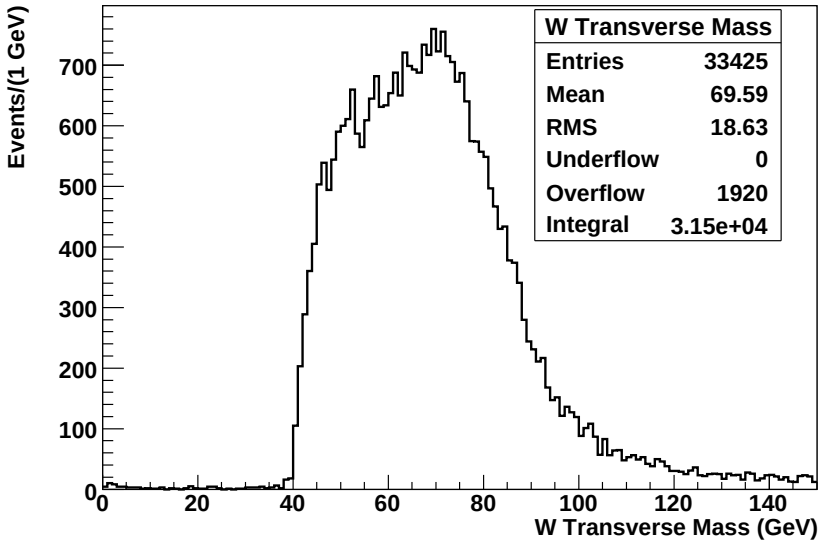

Figure 4.19 Transverse mass of the $W \rightarrow \mu\nu$ events with $\Delta z > 3.0\ cm$.

Photon Efficiency

Unlike the leptons, there is no statistically significant production resonance that will produce a pure sample of photons over the complete kinematic range that will be studied in this analysis. Hence the determination of the photon identification efficiency must rely on a combination of Monte Carlo simulations and corrections from data measurements. At the lowest transverse energies, it is possible to extract photon identification efficiencies from resonant $Z \rightarrow \ell\ell \rightarrow \ell\ell\gamma$ production, however a minimal set of cuts must be applied to identify the photon probe (Photon Preselection Cuts).

Photon Preselection Efficiency

The value of the preselection efficiency is determined through the use of the GEANT* [47] Monte Carlo simulation of the DØ detector on Pythia generated $W\gamma$ events†. The photon preselection criteria consists of the reconstruction of an EM simple cone object with $|ID| < 12$ that passes the isolation and EM fraction requirement. In order for this to be an acceptable preselection cut, the variables must be well modeled in the Monte Carlo. The behavior of the isolation and EM fraction cut

*This is a total emulation of the DØ detector, which takes into account all of the known material and electronics behavior of the real detector. To incorporate noise, event pileup, etc., real minimum bias events from collider data are overlaid with the Monte Carlo events.

†For the lepton efficiencies, the issue of using Monte Carlo to determine the preselection efficiency was skirted by taking advantage of the uncorrelated identification methods in the tracker and calorimeter/muon detectors. This additional handle does not exist for the photons.

are dependent on the amount of ambient energy in the calorimeter that is not from the photon. To determine if the ambient energy is accurately represented in the simulation, a comparison of the energy in a "quiet" region of the calorimeter is performed on data and Monte Carlo. The quiet regions are identified by selecting $Z \rightarrow ee$ data and Monte Carlo events and by examining the area between the electrons where there should be no objects from the hard scatter (see Figure 4.20). The amount of ambient

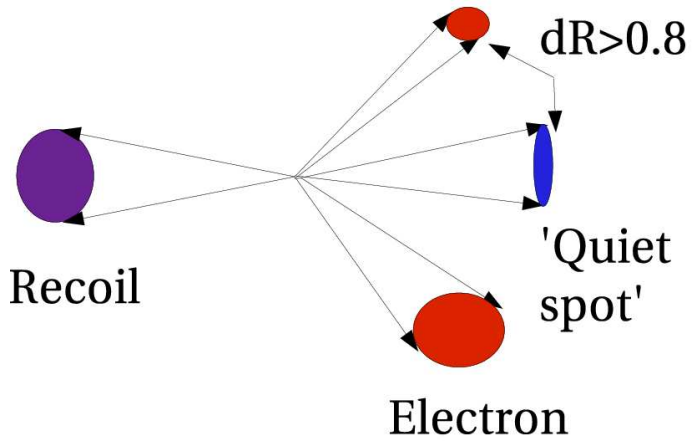

Figure 4.20 Cartoon of the quiet region in the calorimeter from $Z \rightarrow ee$ events.

energy within an isolation cone located in the quiet region is shown in Figures 4.21 and 4.22. The Monte Carlo is observed to accurately model the ambient energy; hence the photon preselection efficiency can be obtained from the Monte Carlo simulation.

Since the ambient energy will have a greater effect on lower energy photons, the photon preselection efficiency is measured with GEANT $W\gamma$ Monte Carlo as a function of energy. The efficiency for the central and forward calorimeters can be found

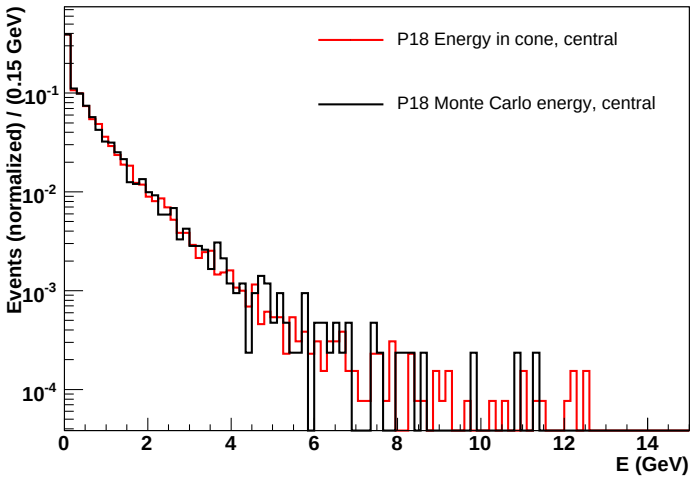

Figure 4.21 Comparison of the amount of ambient energy in an isolation hollow cone in the quiet region of $Z \rightarrow ee$ events. The quiet region is in the central calorimeter. P18 refers to the production release of the code that was used for the analysis.

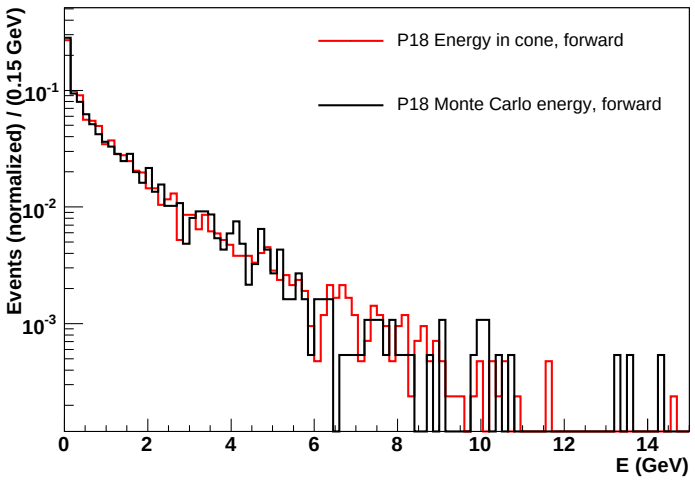

Figure 4.22 Comparison of the amount of ambient energy in an isolation hollow cone in the quiet region of $Z \rightarrow ee$ events. The quiet region is in the forward calorimeters. P18 refers to the production release of the code that was used for the analysis.

in Figures 4.23 and 4.24. A parameterized efficiency is extracted by fitting a function to the histograms. The equation used for the parameterization is as follows:

$$\epsilon = (1 - Ae^{B \times E}) \times C. \tag{4.9}$$

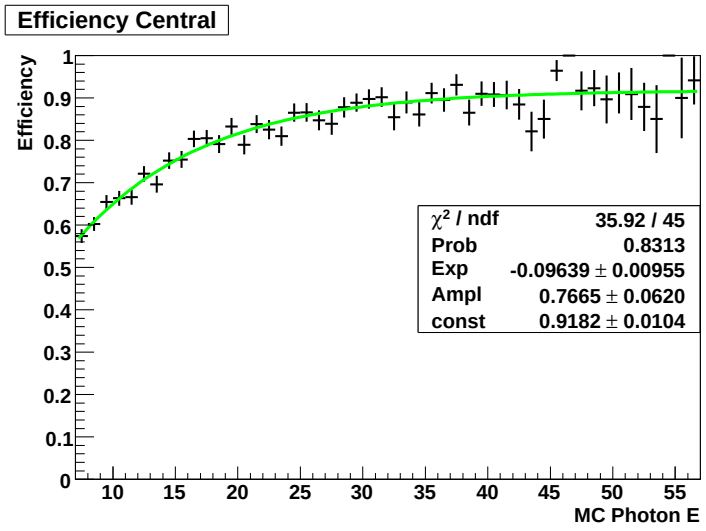

Figure 4.23 Photon preselection efficiency for central photons.

Low Energy Photon Efficiency

For transverse energies below 25 GeV, the photon identification efficiency is measured from a sample of radiative $Z\gamma$ events that are collected from collider data. In these events, the photon is radiated off of one of the final-state leptons and hence the three-body mass of the system will produce a resonance at the mass of the Z boson. To maximize the statistical power, both electron and muon decays are used.

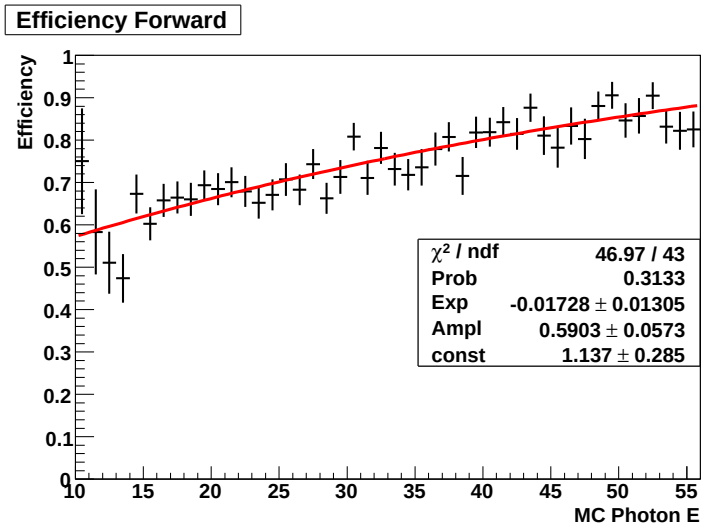

Figure 4.24 Photon preselection efficiency for forward photons.

The sample of $Z \rightarrow \mu\mu \rightarrow \mu\mu\gamma$ events are selected with the following cuts:

- There must be two muons of loose or higher quality that are both matched to a track with $p_T > 15\ GeV$.
- Both muons must be isolated from each other with ΔR>0.7.
- There must be one EM simple cone object with $|ID| < 12$ in the fiducial area of the calorimeter with $E_T > 7\ GeV$, isolation < 0.07, and EM fraction >0.97.
- Both muons must be isolated from the photon with ΔR>0.5.
- If each muon has a ΔR>0.7 from the photon, then the muon is also required to be isolated in the calorimeter and tracker with the following criteria:

  - The sum of E_T in the calorimeter in a hollow cone (ΔR(0.4-0.1) must be less than 2.5 GeV.
  - The p_T sum of tracks in a cone (ΔR=0.5) must be less than 3.5 GeV.

- Since some of the energy associated with the mass of the Z boson is carried off by a photon, the two-body mass of the muons must be less than 80 GeV.
- The event must satisfy the $W\gamma$ trigger criteria.
- The z-position of the muon track vertices must be within 3 cm of each other and the primary vertex.

The sample of $Z \rightarrow ee \rightarrow ee\gamma$ events are selected with the following cuts:

- There must be two EM simple cone objects with $|ID| < 12$ in the fiducial area of the calorimeter that each have $E_T > 15$ GeV, isolation < 0.15, EM fraction > 0.95, and a spatial track match χ^2 probability greater than 0.01.
- The two electrons must be isolated from each other with ΔR>0.8.
- At least one of the EM objects must have $E_T > 25$ GeV.
- Since some of the energy associated with the mass of the Z boson is carried off by a photon, the two-body mass of the electrons must be less than 80 GeV.

- In addition to the two electrons, there must be another EM simple cone object with $|ID| < 12$ in the fiducial area of the calorimeter with $E_T > 7\ GeV$, isolation < 0.07, and EM fraction >0.97.

- The photon must be isolated from the two electrons with ΔR>0.8.

- The z-position of the electron track vertices must be within 3 cm of each other and the primary vertex.

The selected events are divided into central and forward photon contributions. These samples are then separated into the sample of events that pass the photon identification and the sample of events that fail the photon identification. The three-body mass of the selected events is shown in Figures 4.25 and 4.26. The samples are further subdivided into bins of E_T with four bins in the central and three bins in the EC. The amount of signal is extracted from a fit of the three-body mass distribution for each of the seven bins. The efficiency is determined from the number of signal events that pass the photon identification cuts and the number of signal events that fail the photon identification cuts. The measured efficiencies are summarized in Table 4.4.

The efficiencies measured in data do not agree with the GEANT $W\gamma$ Monte Carlo expectation as shown in Figures 4.27 and 4.28. This discrepancy is largely due to the preshower confirmation and the veto on the track-match. Since neither the

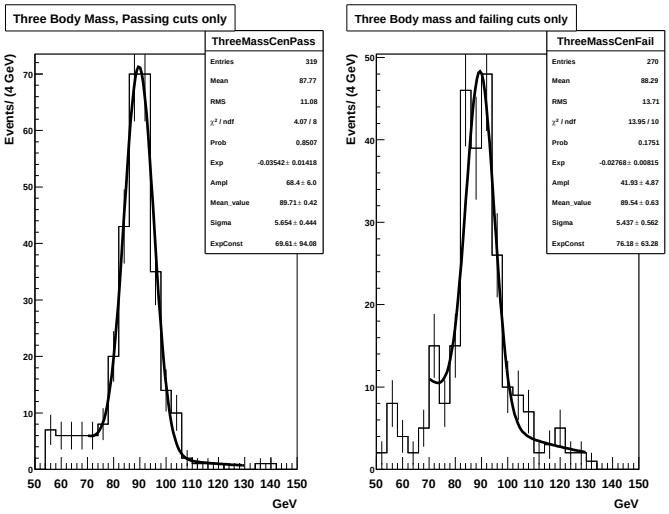

Figure 4.25 The three-body mass of the selected $Z \to \ell\ell \to \ell\ell\gamma$ events with central photons. The plot on the left is the sample of events that pass the photon identification cuts. The plot on the right is the sample of events that fail the photon identification cuts.

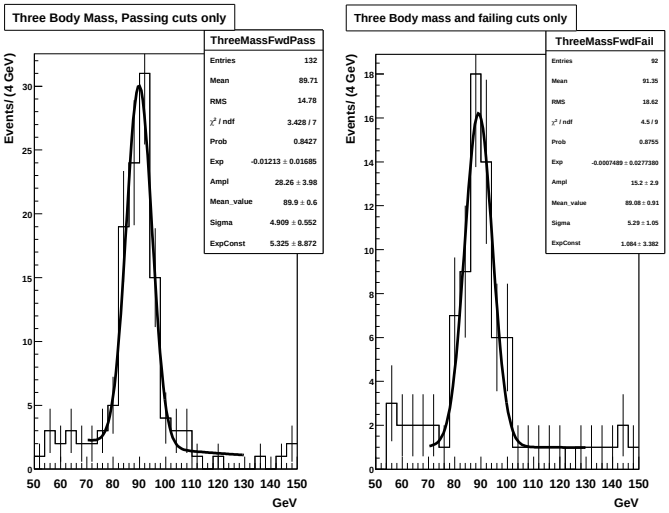

Figure 4.26 The three-body mass of the selected $Z \to \ell\ell \to \ell\ell\gamma$ events with forward photons. The plot on the left is the sample of events that pass the photon identification cuts. The plot on the right is the sample of events that fail the photon identification cuts.

E_T bin (GeV)	Efficiency	Statistical error
Central Photons		
7-9.6	0.52	0.06
9.6-12.3	0.54	0.06
12.3-15	0.56	0.06
15-30	0.66	0.03
Forward Photons		
7-11	0.61	0.07
11-15	0.85	0.07
15-30	0.81	0.06

Table 4.4 Measured photon identification efficiency for low E_T photons.

preshower confirmation nor the track-match veto is expected to be energy dependent, it should be possible to account for the discrepancy with an overall rescaling. To obtain a parameterized photon identification efficiency, a fit is made to the Monte Carlo expectation. This fit is then scaled down to match the data calculation as shown in Figures 4.29 and 4.30. Based on the χ^2 of the fit, the data is consistent with the rescaled Monte Carlo prediction of the shape*. The functional form of the parameterized fit is given below:

$$\epsilon = (1 - Ae^{B \times E_T}) \times C. \tag{4.10}$$

*As the photon E_T decreases, it appears that there might be an increasing discrepancy between the data and the rescaled Monte Carlo efficiencies. It should be noted that the efficiencies at the lowest E_T are not used in this analysis, due to the requirement that the selected photons have an $E_T > 11\ GeV$. Furthermore, the error on the scaling factor should compensate for plausible variations.

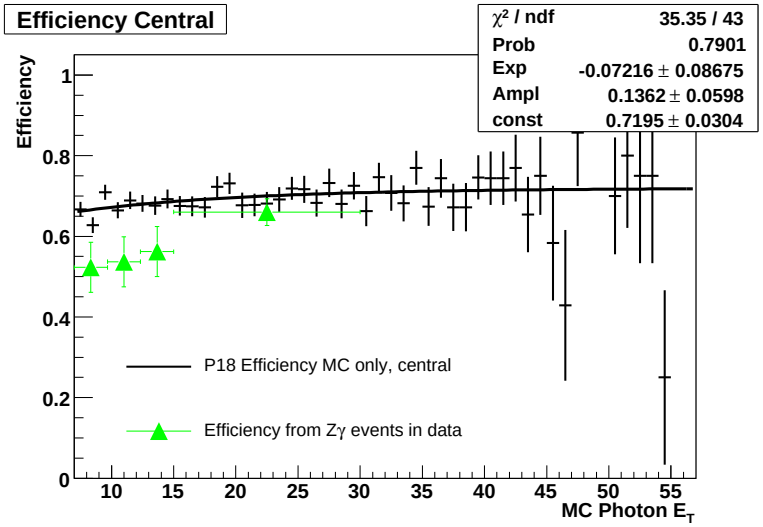

Figure 4.27 Central photon identification efficiency.

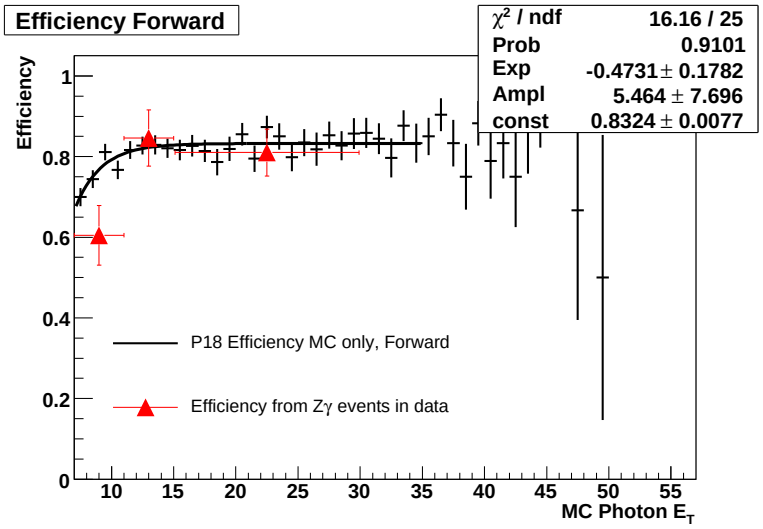

Figure 4.28 Forward photon identification efficiency.

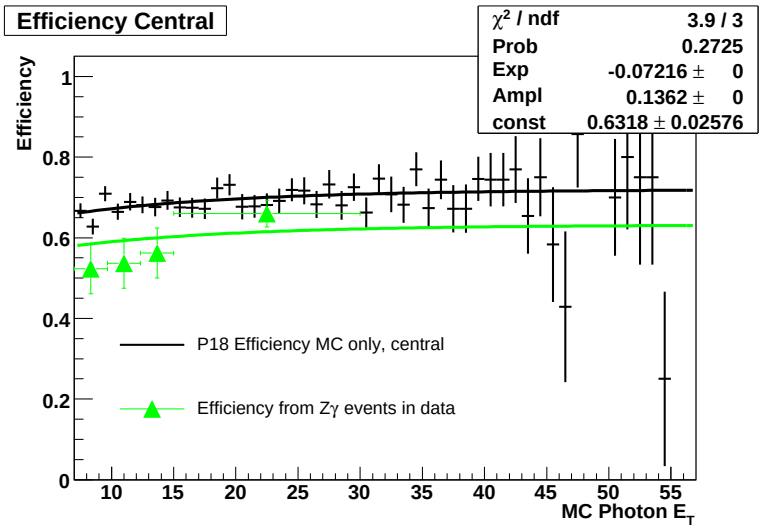

Figure 4.29 Central photon identification efficiency. The black line is the fit to the Monte Carlo points. The green line is the Monte Carlo fit scaled down to match the $Z\gamma$ data points.

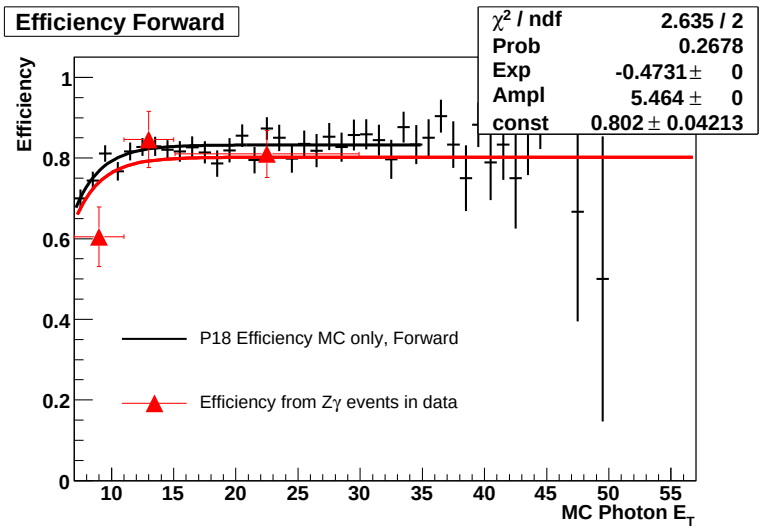

Figure 4.30 Forward photon identification efficiency. The black line is the fit to the Monte Carlo points. The red line is the Monte Carlo fit scaled down to match the $Z\gamma$ data points.

Medium Energy Photon Efficiency

Since the sample of radiative Zγ events lacks sufficient statistics above 25 GeV, photon efficiencies in this regime are determined within the photon_id_tools framework. The methodology is detailed in [48]. In this framework the GEANT Wγ Monte Carlo efficiency is corrected with a scaling factor that is calculated from the ratio of $Z \rightarrow ee$ data/MC efficiencies*. The efficiencies are calculated for the CC and EC separately. For $Z \rightarrow ee$ data events the following cuts are used:

- Require a tag electron satisfying the following requirements:
  - EM simple cone object with $|ID| < 12$
  - Electron is within the full fiducial area of the calorimeter and has $|\eta_{CAL^D}| <$ 1.1 or $1.5 < |\eta_{CAL^D}| < 2.5$
  - Isolation < 0.15
  - EM fraction > 0.90
  - Spatial track match probability > 0.01
  - Likelihood > 0.85
  - H-matrix < 12

*This method can be used since the EM cluster from an electron is very similar to the EM cluster produced by a photon. However, because of the inherit difference between a charged particle and a neutral particle, this method cannot be used to correct for the anti-track-match efficiency.

  - $E_T > 25.0\ GeV$
  - Fires one of the single electron triggers

- Require a probe electron satisfying the following requirements:
  - EM simple cone object with $|ID| < 12$
  - Electron is within the full fiducial area of the calorimeter and has $|\eta_{CAL^D}| <$ 1.1 or $1.5 < |\eta_{CAL^D}| < 2.5$
  - Isolation < 0.07
  - EM fraction > 0.97
- Event has same data quality and run range as the Wγ electron channel analysis

For Z→ee Monte Carlo events the following cuts are used:

- Require a probe electron satisfying the following requirements:
  - EM simple cone object with $|ID| < 12$
  - Electron is within the full fiducial area of the calorimeter and has $|\eta_{CAL^D}| <$ 1.1 or $1.5 < |\eta_{CAL^D}| < 2.5$
  - Isolation < 0.07
  - EM fraction > 0.97

For Wγ Monte Carlo events the following cuts are used:

- Require a probe photon satisfying the following requirements:
  - EM simple object with $|ID| < 12$
  - Photon is within the full fiducial area of the calorimeter and has $|\eta_{CAL^D}| < 1.1$ or $1.5 < |\eta_{CAL^D}| < 2.5$
  - Isolation < 0.07
  - EM fraction > 0.97

The efficiency for the probe object to pass the photon identification cuts (excluding the anti-track-match condition) is then calculated. The efficiencies can be found in figures 4.31-4.34. The difference between the data and Monte Carlo is assessed as a systematic error. The average efficiency for the CC (EC) is 0.72 ± 0.03 (0.86 ± 0.05). The efficiency associated with the anti-track-match condition is not included with this number but is obtained from the η parameterized fit found in [48]. It should be noted that the product of the anti-track-match efficiency and the efficiency found here is consistent with the plateau values found in the calculation of the low E_T photon efficiency. Not only is this convergence necessary for the two methods to be meaningful, but the convergence is also a cross-check of the accuracy of the efficiency calculations since both methods are independent.

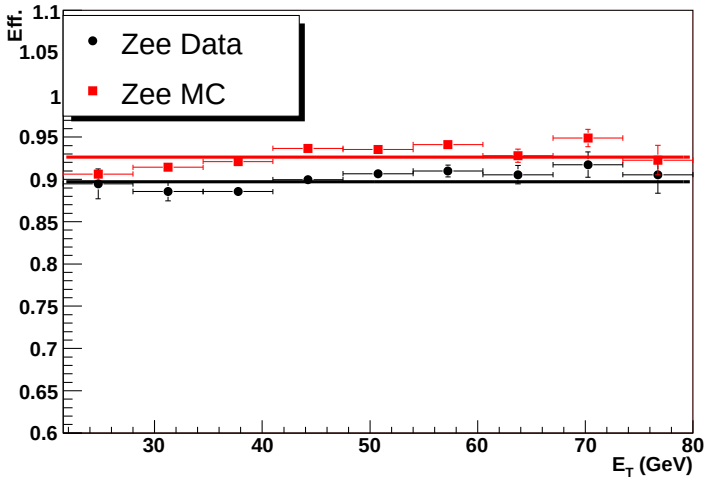

Figure 4.31 Efficiency for central electrons from Z decays to pass photon ID cuts (excluding anti-track-match).

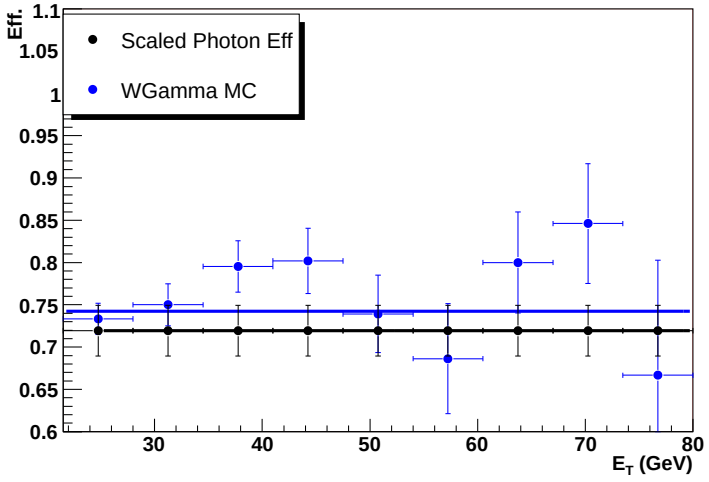

Figure 4.32 Efficiency for medium energy photons in the central calorimeter (excluding anti-track-match).

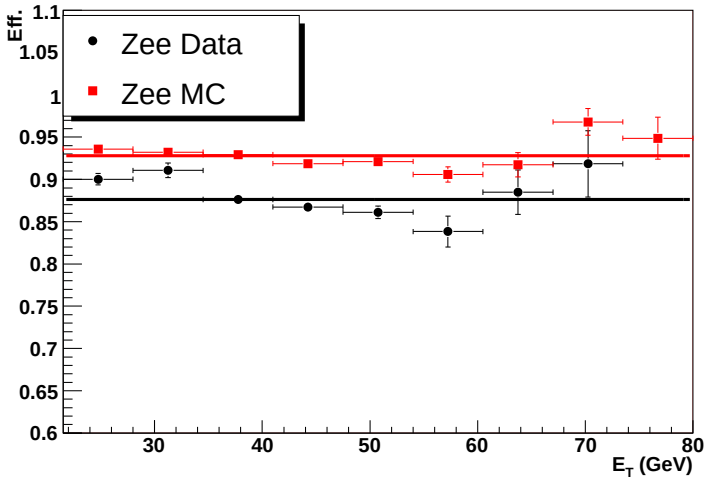

Figure 4.33 Efficiency for forward electrons from Z decays to pass photon ID cuts (excluding anti-track-match).

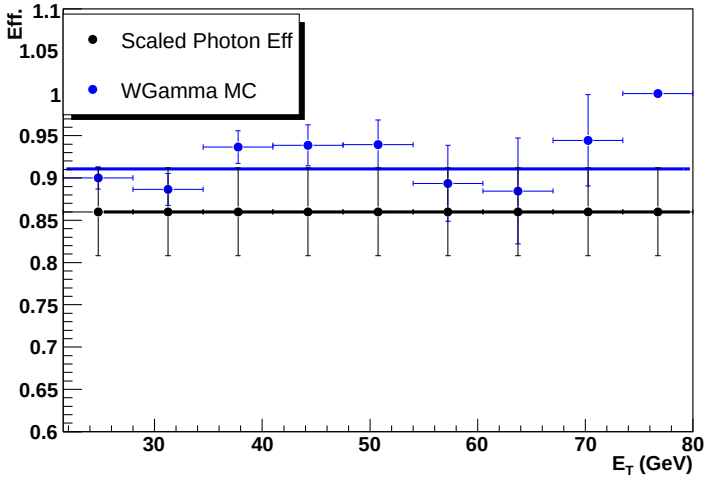

Figure 4.34 Efficiency for medium energy photons in the forward calorimeter (excluding anti-track-match).

Overall Event Efficiencies

A summary of the overall acceptance and efficiencies for the muon channel is supplied in Table 4.5. A summary of the overall acceptance and efficiencies for the electron channel is supplied in Table 4.6.

Cut		**Efficiency**
Acceptance		0.230 ± 0.007
	Kinematic	0.660 ± 0.018
	Geometric	0.348 ± 0.002
Muon ID		0.72 ± 0.05
Trigger		0.655 ± 0.002
Photon Preselection		0.93 ± 0.01
Photon ID		0.80 ± 0.02
Zγ Veto		0.964 ± 0.003
Δz		0.94 ± 0.01
Combined		0.073 ± 0.006

Table 4.5 Muon Channel Acceptance and Efficiencies

Cut		**Efficiency**
Acceptance		0.168 ± 0.001
	Kinematic	0.480 ± 0.003
	Geometric	0.350 ± 0.0015
Electron Preselection		0.991 ± 0.002
Electron ID		0.84 ± 0.02
Trigger		0.976 ± 0.002
Photon Preselection		0.92 ± 0.015
Photon ID		0.79 ± 0.02
Δz		0.94 ± 0.01
Combined		0.093 ± 0.004

Table 4.6 Electron Channel Acceptance and Efficiencies

4.3 Background Estimates

The significant backgrounds to the $W\gamma$ muon and electron channels are $W + j$, $Z\gamma$, 'ℓeX', and the $W\gamma$ events from the τ-decay channel. For both channels the dominant background is $W + j$, where the jet (j) is misidentified as a photon. For $Z\gamma$ events, a W signature is mimicked by mismeasured $\not\!\!E_T$, caused by either the loss of one of the leptons or a mismeasured jet in the event. 'ℓeX' events designate any process that produces a lepton, electron, and missing E_T. 'ℓeX' events provide a source of background due to electron tracking inefficiency. Finally, $W\gamma$ events from the τ-decay channel contribute to a small fraction of the observed muon and electron channel events.

4.3.1 $W + j$

A data-based method is implemented to estimate the number of $W + j$ events in the $W\gamma$ candidate sample. This method uses the assumption that the ratio of EM-like jets* that pass the photon identification to EM-like jets that fail the photon identification is the same for both the $W\gamma$ candidate sample and a QCD jet sample. This ratio will be referred to as the jet ratio or fake rate throughout this document.

In the method, a normalization sample of so called W+"*bad EM*" events are collected from the collider data. These events are selected with same selection re-

*An EM-like jet is a jet that fragments to a significant electromagnetic portion as shown in Figure 4.35. This can be due to the decays of the π^0, η, etc.

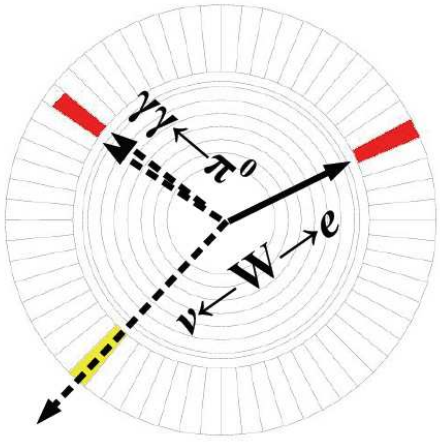

Figure 4.35 Cartoon of a $W + j$ event faking a $W\gamma$ signature.

quirements as the $W\gamma$ candidate samples, but the photon identification requirement is altered to select bad EM objects. The bad EM objects are objects that fail cuts that are efficient for real photons and electrons but inefficient for EM-jets. The number of observed $W + bad\ EM$ events is then scaled by the jet ratio to estimate the amount of $W + j$ contamination in the $W\gamma$ candidate sample.

Determination of the Jet Ratio

The ratio of the fraction of jets that pass the photon identification cuts to those that pass the bad EM cuts is calculated from a QCD sample as a function of E_T for 10 bins in calorimeter detector η_{CALD}. The ratios are measured from a subskim of events that created with the photon_id_tools package [48] with the following criteria:

- The event must have fired one of the following jet triggers*:

*A description of all the DØ triggers can be found in [49]. The JT_XXTT trigger requires

  - JT_ 15TT
  - JT_ 25TT_ NG
  - JT_ 45TT
  - JT_ 65TT
  - JT_ 95TT

- The event contains at least one JCCA jet with the following properties:
  - $p_T > 15\ GeV$
  - The jet is Good, which means it satisfies the following cuts:
    * A significant fraction of the jet transverse momentum cannot be from the coarse hadronic modules. The maximum acceptable coarse hadronic fraction (CHF) depends on the location of the jet and must satisfy at least one of the below criteria:
      · CHF < 0.4
      · CHF < 0.6 and $8.5 <| \eta_{CAL^D} | < 12.5$* and the minimal number of cells that contain 90% of the jet energy must be less than 20
      · CHF < 0.44 and $| \eta_{CAL^D} | < 0.8$
      · CHF < 0.46 and $1.5 <| \eta_{CAL^D} | < 2.5$

that there be jet with $E_T > XX$.
*In tower units for the EC middle hadronic modules.

* Jet must deposited some energy in the EM layers of the calorimeter. The EM fraction of the transverse momentum (EMF) must pass one of the following cuts:
  - EMF > 0.05
  - $1.3 > |\,|\eta_{CAL^D}| - 12.5\,| + max(0, 40 \times (\sigma_\eta - 0.1))$†
  - EMF > 0.03 and $11.0 < |\eta_{CAL^D}| < 14.0$†
  - EMF > 0.04 and $2.5 < |\eta_{CAL^D}|$
* The reconstructed jet must have confirmation from the level-1 readout. This is done by considering the ratio of measured p_T ($L1_{ratio} = \frac{p_T^{\text{L1 readout}}}{p_T^{\text{precision readout}}}$) where the precision measurement excludes the coarse hadronic energy. The jet must pass one of the $L1_{ratio}$ cuts:
  - $L1_{ratio} > 0.5$
  - $L1_{ratio} > 0.35$ and $p_T < 15$ and $1.4 < |\eta_{CAL^D}|$
  - $L1_{ratio} > 0.1$ and $p_T < 15$ and $3.0 < |\eta_{CAL^D}|$
  - $L1_{ratio} > 0.2$ and $p_T \geq 15$ and $3.0 < |\eta_{CAL^D}|$

– The jet is not an EM jet, which means there is no reconstructed EM cluster within $\Delta R < 0.4$ of the reconstructed jet.

- The event contains an EM simple cone object with:

†In tower units for the portion of the calorimeter with no EM modules (No EM Gap).

  - $E_T > 7\ GeV$
  - ID = 10 or ± 11
  - Isolation < 0.07
  - EM fraction > 0.97
  - $\mid \eta_{CAL^D} \mid < 1.1$ or $1.5 < \mid \eta_{CAL^D} \mid < 2.5$
  - In fiducial area of the calorimeter
  - At least one associated preshower cluster
  - ΔR > 0.9, where ΔR is defined as the separation between the EM object and any non-EM Good JCCA jet

- $\not\!\!E_T < 10\ GeV$
- The second highest p_T jet that is Good and not an EM jet must have $p_T < 10\ GeV$

Using the above subskim, the sample of EM objects that pass the photon identification cuts and the sample of EM objects that pass the bad EM object cuts are collected. A bad EM object must pass all of the photon identification requirements except for the track isolation in a hollow cone and transverse shape cuts. For these cuts, the bad EM object must pass an anti-cut:

- For central EM objects, the object must pass one of the below conditions:

  - The cluster energy weighted mean squared width in the ϕ direction is greater than 14 cm^2.
  - The sum of track p_T in a hollow cone is greater than 2 GeV.

- For forward EM objects, the object must pass one of the below conditions:
  - The cluster energy weighted mean squared width in the ϕ direction is greater than $(5.96 \mid \eta_{CAL^D} \mid^2 -30.6 \mid \eta_{CAL^D} \mid +40.7)cm^2$
  - The cluster energy weighted mean squared width in the z direction is greater than $(2.74 \mid \eta_{CAL^D} \mid^2 -16.3 \mid \eta_{CAL^D} \mid +25.0)cm^2$

The ratio, $N_{photon-like\ jets}/N_{badEM\ jets}$, is then determined as a function of E_T for 10 η bins ($\mid \eta_{CAL^D} \mid < 0.22$, $0.22 < \mid \eta_{CAL^D} \mid < 0.44$, $0.44 < \mid \eta_{CAL^D} \mid < 0.66$, $0.66 < \mid \eta_{CAL^D} \mid < 0.88$, $0.88 < \mid \eta_{CAL^D} \mid < 1.1$, $1.5 < \mid \eta_{CAL^D} \mid < 1.7$, $1.7 < \mid \eta_{CAL^D} \mid < 1.9$, $1.9 < \mid \eta_{CAL^D} \mid < 2.1$, $2.1 < \mid \eta_{CAL^D} \mid < 2.3$, and $2.3 < \mid \eta_{CAL^D} \mid < 2.5$).

Since these ratios are calculated using QCD events, one must address contamination in the sample of photon-like objects by real photons from QCD direct photon production. This effect becomes noticeable at high transverse energies. To compensate for the real photon background, a photon purity estimation, P, is made with Monte Carlo samples for the CC and EC as a function of E_T*. The measured value of the ratio is then corrected by multiplying it by the factor (1-P). The corrected

*For more information on this method see the p17 photon identification note [48].

points are then fit with the function,

$$f(E_T) = p_0 e^{-p_1 E_T} + p_2. \tag{4.11}$$

Plots of the calculated ratios can be found in Figures 4.36-4.37 and in Figures C.4-C.11 in the Appendix. In order to assess a systematic error on the direct photon subtraction, an alternate data-based method is used to determine the direct photon contribution.

In the second method, the initial data points are fit with a test function that contains a term for the actual ratio and a term for the direct photon contribution:

$$f(E_T) = f_{ratio}(E_T) + f_{directphoton}(E_T), \tag{4.12}$$

where

$$f_{ratio}(E_T) = p_0 e^{-p_1 E_T} + p_2, \tag{4.13}$$

and

$$f_{directphoton}(E_T) = p_3 e^{p_4 E_T}. \tag{4.14}$$

In order to keep the fit from pushing the terms to unphysical values, the fit is done iteratively. In the first iteration, only f_{ratio} is fit to data in the region where the direct photon contribution is expected to be small, 7 GeV to 46(37) GeV for the CC(EC). In the second step the parameters in f_{ratio} are fixed and the whole test function is fit over the full E_T range. In the third step, the parameters in $f_{directphoton}$ are fixed,

the parameters in f_{ratio} are freed, and the test function is again fit over the full E_T range. The final value of f_{ratio} is then used as the estimate of the ratio with direct photon subtraction. The results of this method are found in Figures 4.38-4.39 and in Figures C.12-C.19 in the Appendix. The difference between this method and the first is assigned as the systematic error on the photon subtraction, and the average value of the two methods as a function of E_T is assigned as the fake ratio.

W+j Calculation

To estimate the amount of $W + j$ background in the final $W\gamma$ candidate sample, $W + bad\ EM$ events are selected from the data sample. Events are required to pass all of the selection cuts, except the standard photon identification is replaced by the bad EM identification given above. The number of observed $W + bad\ EM$ events is binned by E_T and $|\eta_{CAL^D}|$. The number of bad EM objects in each bin is then multiplied by the corresponding ratio derived in the last section. For the final charge-signed rapidity distribution, the normalization sample is additionally binned in $Q * \Delta\eta$, and the background estimate is measured for each bin. The total number of calculated $W + j$ background events is shown in Table 4.7.

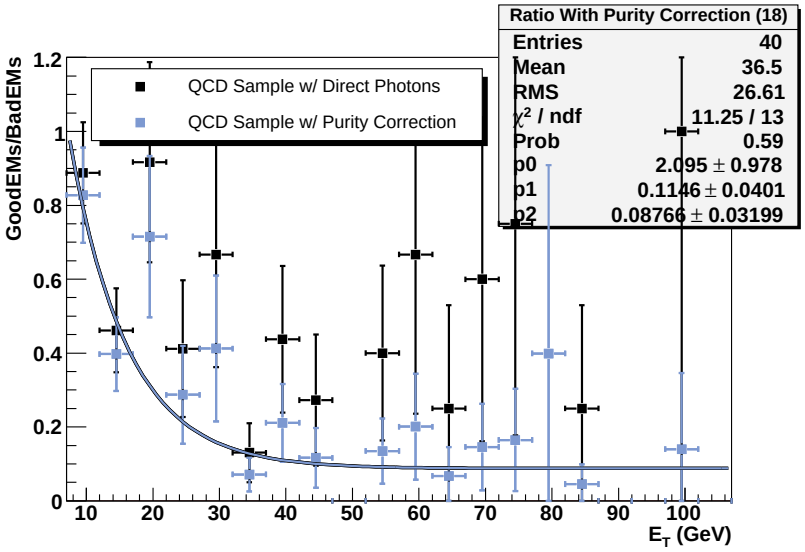

Figure 4.36 Jet ratio with MC purity correction for $\mid \eta_{CAL^D} \mid < 0.22$

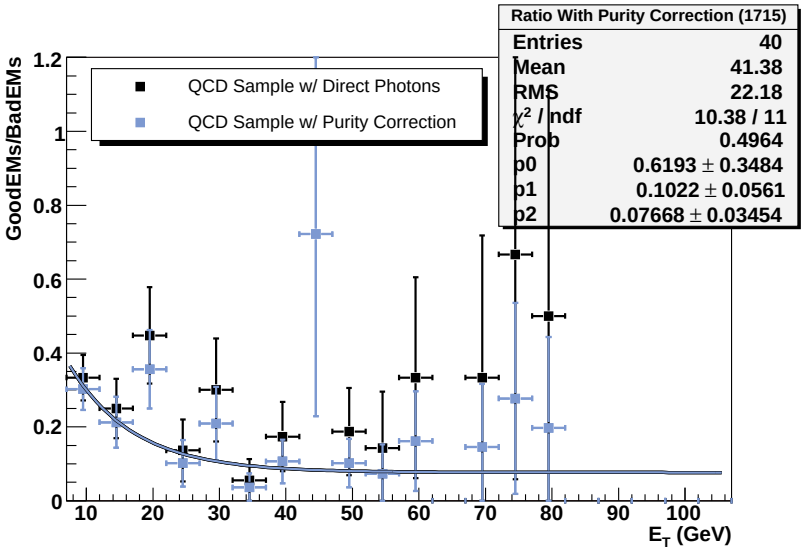

Figure 4.37 Jet ratio with MC purity correction for $1.5 < \mid \eta_{CAL^D} \mid < 1.7$

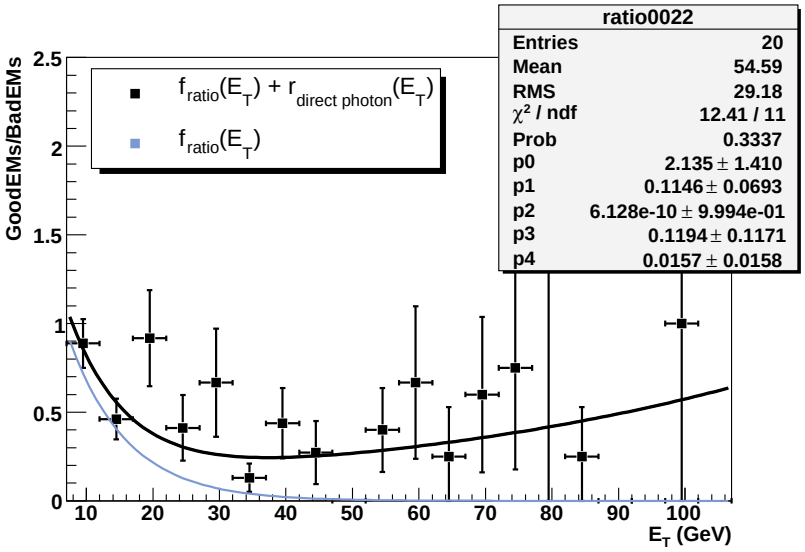

Figure 4.38 Jet ratio with fit method for $\mid \eta_{CAL^D} \mid < 0.22$

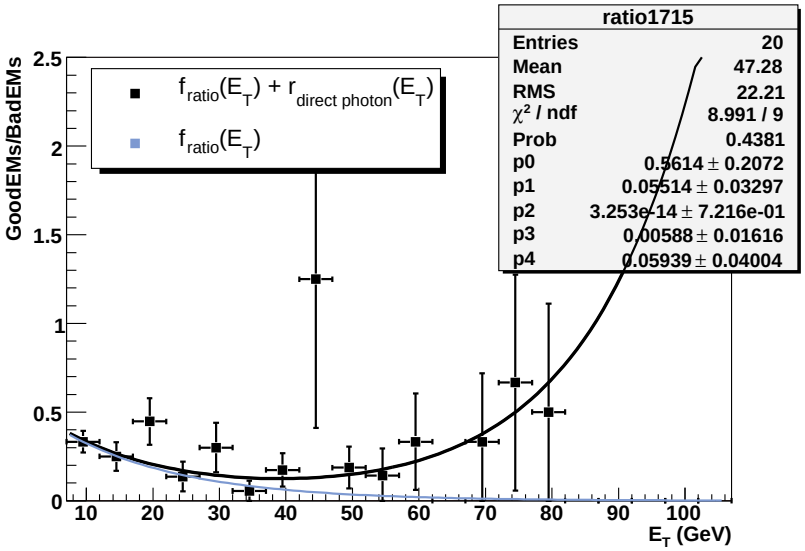

Figure 4.39 Jet ratio with fit method for $1.5 < \mid \eta_{CAL^D} \mid < 1.7$

Channel	Region	N_{W+j}	Stat. Error	Sys. Error
electron				
	CC γ	19	3	2
	EC γ	29	3	3
	Total	48	4	4
muon				
	CC γ	17	3	2
	EC γ	29	4	3
	Total	46	4	4

Table 4.7 Estimated Number of $W + j$ Background Events

4.3.2 ℓeX

The ℓeX background is composed of events where an electron is misidentified as a photon and is due to the inefficiency of the track isolation in discriminating against electrons. To estimate this background a data-based method is used. In this method a normalization sample of "W"+e events* are selected by requiring that all of the $W\gamma$ selection criteria are met except for the anti-track-match and track isolation in a hollow cone requirements. These track isolation cuts are replaced with a requirement that the χ^2 spatial track match probability be greater than 0.01. The normalization sample is then scaled by the appropriate tracking efficiencies to obtain an estimate of the amount of ℓeX contamination in the $W\gamma$ candidate sample.

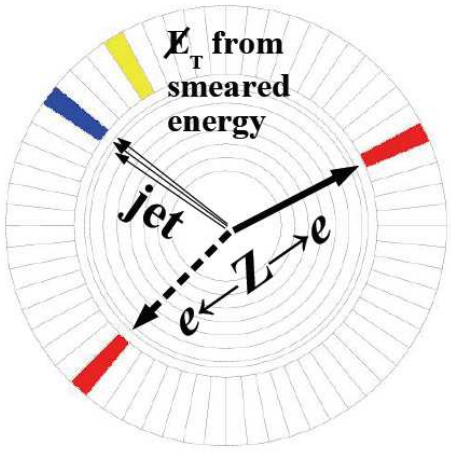

Figure 4.40 Cartoon of a $Z \to ee$ event faking a $W\gamma$ signature.

*Quotes are placed around the W, because these events do not necessarily contain a real W. The majority of the events are from $Z \to ee$ production as illustrated in Figure 4.40.

The normalization sample contains photon-like electrons that have a track match. Let the number of these events by denoted by $N_{tracked-matched}$. The total number of events ($N^{\dagger}_{\ell eX}$) with an electron that that passes or fails the track match condition is then given by:

$$N^{\dagger}_{\ell eX} = \frac{N_{tracked-matched}}{\epsilon_T}, \tag{4.15}$$

where ϵ_T is the efficiency for an electron to pass the track match requirement. The number of events ($N_{\ell eX}$) with an electron that that fails the track isolation requirements (anti-track-match and track isolation in a hallow cone) is then given by:

$$N_{\ell eX} = \epsilon_{TrkIso} N^{\dagger}_{\ell eX}, \tag{4.16}$$

where ϵ_{TrkIso} is the efficiency for an electron to pass the track isolation requirements. This can be rewritten as:

$$N_{\ell eX} = \frac{\epsilon_{TrkIso}}{\epsilon_T} N_{tracked-matched}. \tag{4.17}$$

The values of ϵ_{TrkIso} and ϵ_T are measured as a function of $\mid \eta_{CAL^D} \mid$ with a $Z \rightarrow ee$ Tag-and-Probe data sample. The sample was obtained with the photon_ id_ tools package [48] and the probe object was required to pass the photon ID calorimeter cuts. Plots of ϵ_{TrkIso} and ϵ_T are found in Figures 4.41 and 4.42. The ratio of the efficiencies (the rate by which the ℓeX normalization samples is scaled) is provided in Figure 4.43. The total number of calculated ℓeX background events is shown in Table 4.8.

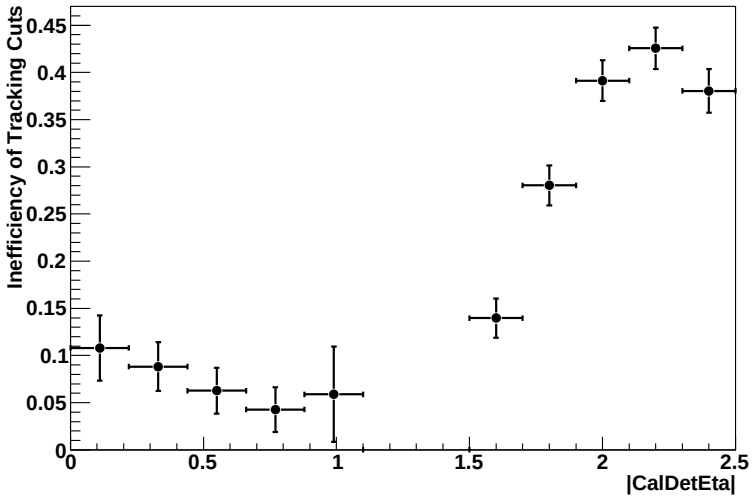

Figure 4.41 Inefficiency of the track isolation cuts (Efficiency for an electron to pass the photon tracking cuts).

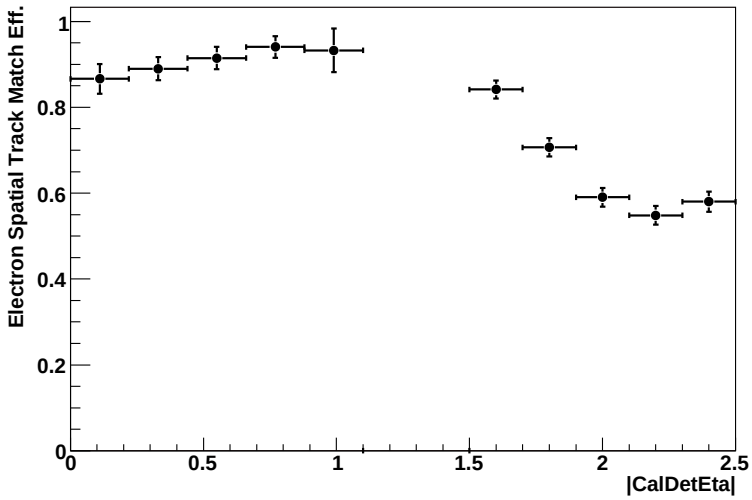

Figure 4.42 Electron track match efficiency.

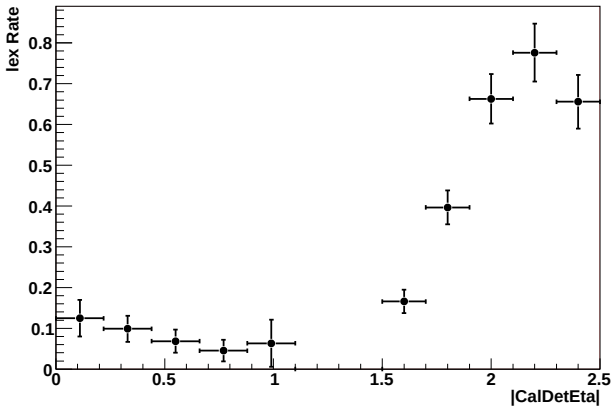

Figure 4.43 Rate used to scale ℓeX normalization samples (The ratio of the tracking efficiencies).

Channel	Region	$N_{\ell eX}$	Stat. Error	Sys. Error
electron				
	CC γ	11	1	2
	EC γ	21	4	1
	Total	32	4	2
muon				
	CC γ	0.6	0.2	0.1
	EC γ	6	2	0.3
	Total	7	2.1	0.3

Table 4.8 Estimated Number of ℓeX Background Events

4.3.3 $Z\gamma$

Due to the hermetic calorimeter, a negligible amount of $Z\gamma$ events in the electron channel will have sufficient mismeasured $\not\!\!E_T$ to pass the $W\gamma$ selection cuts. However, in the muon channel the measurement of the $\not\!\!E_T$ is highly dependent on corrections from the reconstructed tracks*. To reject $Z\gamma$ events in the muon channel, a veto is placed on additional medium quality muons and isolated tracks from the primary vertex. However, because of reconstruction efficiencies and incomplete subdetector acceptance a substantial fraction $Z\gamma$ events will pass the veto requirement. This background is estimated with Monte Carlo. The same method that was used to generate the $W\gamma$ Monte Carlo is used to generate the $Z\gamma$ Monte Carlo (from generation of Baur Monte Carlo four-vectors to a parameterized smearing and application of efficiencies). From this Monte Carlo sample, the total event efficiency is found for $Z\gamma$ events to pass all the $W\gamma$ selection requirements. The event-normalized photon E_T spectrum and charge-signed rapidity distributions are obtained from the events that pass. To reduce the systematic uncertainties from the Monte Carlo prediction and errors associated with the luminosity, the predicted number of $Z\gamma$ events is not used. Instead, the fraction of $Z\gamma$ events in the $W\gamma$ signal sample is used. This fraction is defined as:

$$f_{Z\gamma} = R_{\frac{Z\gamma}{W\gamma}} \times \frac{\epsilon_{Z\gamma}}{\epsilon_{W\gamma}}, \tag{4.18}$$

*The muons will only leave a MIP signature in calorimeter.

where $R_{\frac{Z\gamma}{W\gamma}}$ is the ratio of the $Z\gamma$ cross section times branching fraction to the $W\gamma$ cross section times branching fraction, and $\epsilon_{Z\gamma}$ and $\epsilon_{W\gamma}$ are the total event efficiencies for the $Z\gamma$ and $W\gamma$ events respectively. $(7 \pm 1)\%$ of the observed $W\gamma$ signal events in the muon channel are estimated to be from $Z\gamma$ events. The error on this fraction is determined from the standard deviation of an ensemble of results that were obtained by randomly varying the cross sections, smear, and efficiency parameters within their associated uncertainties.

4.3.4 τ-Channel Decays

A small percentage of the events obtained in the final sample of $W\gamma$ candidate events are from $W\gamma \rightarrow \tau\nu\gamma \rightarrow \ell\nu\gamma$ and $W \rightarrow \tau\nu \rightarrow \tau\nu\gamma \rightarrow \ell\nu\gamma$ events. This background is estimated with Monte Carlo. The same method that was used to generate the $W\gamma$ Monte Carlo in the other channels is used to generate the $W\gamma$ events in the τ channel; however the τ is further allowed to decay according to the appropriate branching fractions. From this Monte Carlo sample, the total event efficiency is found for the τ-channel events to pass all the $W\gamma$ selection requirements for each analysis channel. The event-normalized photon E_T spectrum and charge-signed rapidity distribution are obtained from the events that pass. The ratio between the total event efficiency for the τ-channel and the other lepton channels is calculated, with the appropriate branching fractions for the τ to decay to μ or e being taken into account in the acceptance contribution to the efficiency. To determine the error on

this fraction, the efficiencies, smear parameters, and MC cross section estimates are randomly varied within their errors to produce an ensemble of results. The error is obtained from the standard deviation of the ensemble of results. For the muon channel the fraction is estimated to be $f_{\tau,\mu} = 0.022 \pm 0.0015$. For the electron channel, this fraction is estimated to be $f_{\tau,e} = 0.0087 \pm 0.0007$.

4.4 Optimization of Kinematics Cuts

4.4.1 Electron-Photon Mass Cut

The electron channel is considerably more susceptible to backgrounds where the photon candidate is actually a misidentified electron. This is largely due to Z boson decays to two electrons where one of the electrons passes the lepton identification cuts and the track from the second electron is not reconstructed. This Z contamination leads to a pronounced peak in the background distribution of the electron-photon two-body mass. See Figure 4.44.

In order to reduce this background, a veto is applied to the electron-photon mass ($M_{e\gamma}$). The edges of the mass window are chosen to minimize the efficiency for selecting Z events without significantly reducing the $W\gamma$ selection efficiency. This trade-off is accomplished by maximizing the following quantity:

$$w_\epsilon = \epsilon_{W\gamma} \frac{\epsilon_{W\gamma}}{\epsilon_{W\gamma} + \epsilon_{\ell eX}}, \tag{4.19}$$

where w_ϵ is a weighted event efficiency, $\epsilon_{W\gamma}$ is the total $W\gamma$ event efficiency, and $\epsilon_{\ell eX}$ is the total ℓeX event efficiency. $\epsilon_{W\gamma}$ is measured with the $W\gamma$ Monte Carlo and $\epsilon_{\ell eX}$

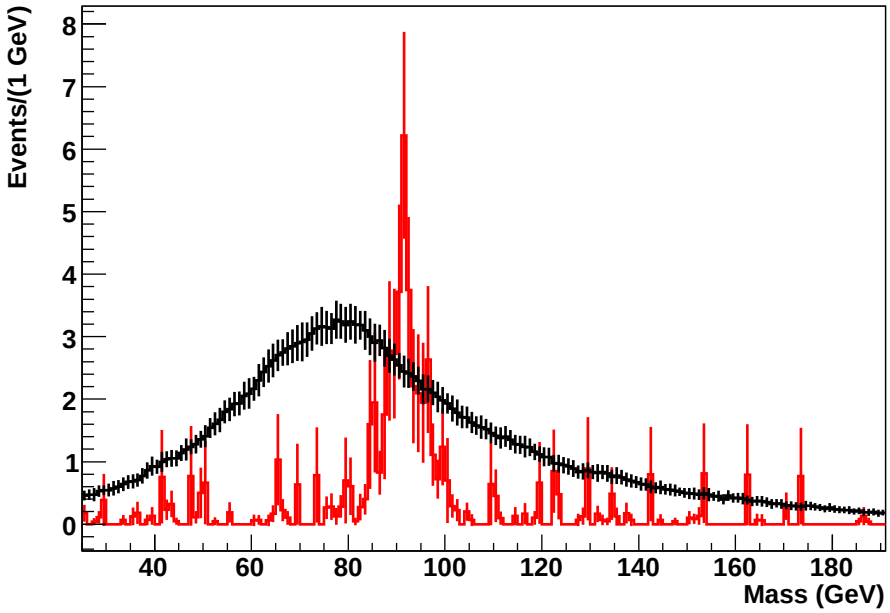

Figure 4.44 Electron-photon two-body mass. The black curve represents the SM Wγ Monte Carlo prediction. The red curve represents the estimated ℓeX background.

is measured by using the ℓeX background estimate. Since there are noticeably more Standard Model events below 91 GeV than above, the edges of the mass window are not expected to be symmetric about 91 GeV but rather shifted towards the higher mass values.

To determine the optimal value of the lower edge of the mass window, the value of the high edge of the window is set to 100 GeV, and the value of the lower edge is initially set to 99 GeV. The mass veto for this window is then applied to the Standard Model Monte Carlo and the background estimate, and the event efficiencies are computed. The value of the lower edge is then reduced by 1 GeV and the procedure

is repeated. Figure 4.45 shows how the weighted efficiency is expected to change for the chosen value of the lower edge. The weighted efficiency is maximized by choosing the lower edge to be at 87 GeV.

To determine the value of the higher edge, the same method is used but this time the value of the lower edge is set to 87 GeV and the value of the higher edge is incremented. Figure 4.46 shows how the weighted efficiency is expected to change for the chosen value of the higher edge. The weighted efficiency is maximized by choosing the higher edge to be 97 GeV.

4.4.2 Choice of Photon E_T and M_{T^3} Cut

The primary purpose of this analysis is to make a quantitative statement about the destructive interference that is responsible for the radiation amplitude zero. The sensitivity of this measurement will be impaired by background (specifically the $W+j$ background which is the dominate background in both channels) and final-state radiation which will obscure the expected dip in the charge-signed rapidity distribution. The choice of E_T cut influences the mixture of $W + j$ and FSR in the candidate sample, since both of these contributions fall off more rapidly in E_T than prompt $W\gamma$ production. However, in lowering these contributions, the amount of observed prompt $W\gamma$ will also be reduced, and the loss in statistics may have a greater effect on the sensitivity than the uncertainties associated with the backgrounds. In addition, although the FSR can be reduced to less than 5% of the signal with a M_{T^3} cut of 110

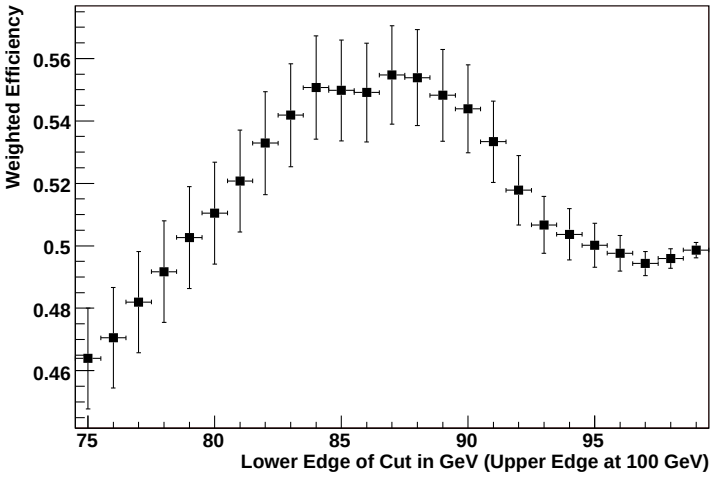

Figure 4.45 Change in the weighted efficiency verse the low edge of the electron-photon mass veto (high edge set at 100 GeV).

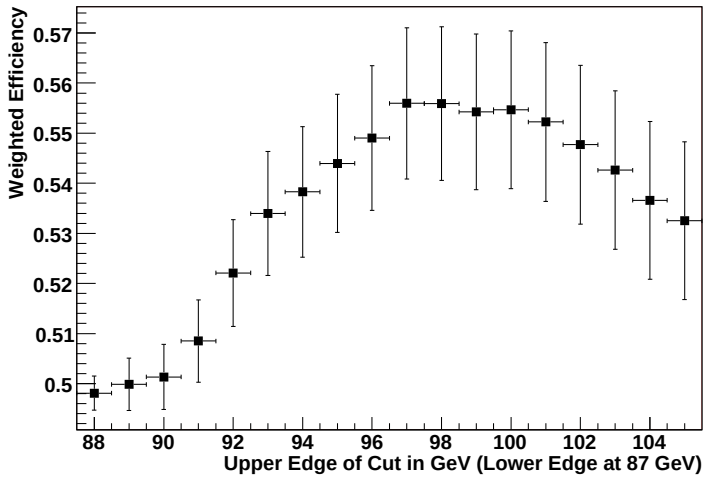

Figure 4.46 Change in the weighted efficiency verse the high edge of electron-photon mass veto (low edge set at 87 GeV)

GeV (105 GeV) for the electron (muon) channel. It may be more prudent to lower these cuts to increase the acceptance of prompt $W\gamma$ events. To determine the value of the kinematic cuts that will give the optimal expected sensitivity for observing the radiation amplitude zero, a scan is performed over potential E_T and M_{T^3} cuts*.

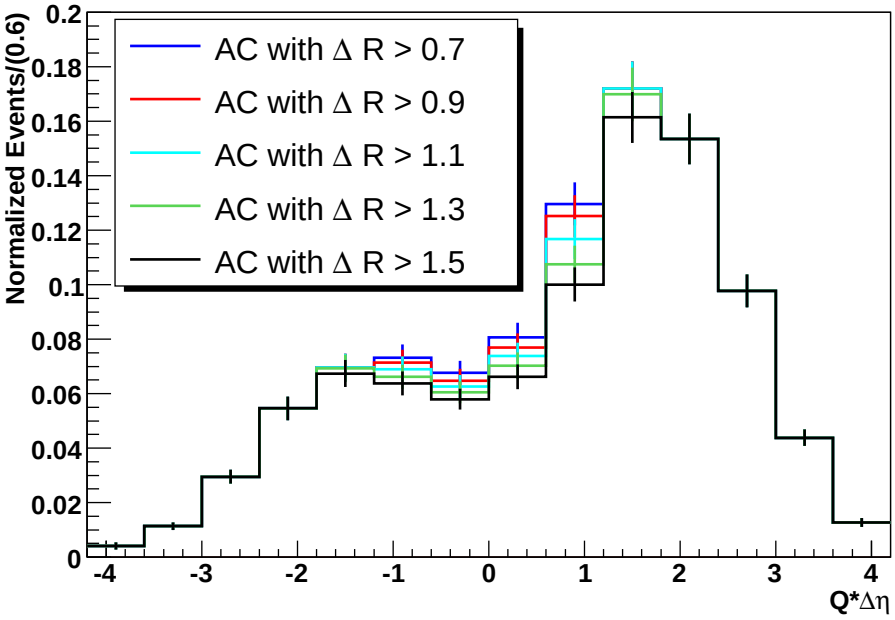

Figure 4.47 Artificial enhancement of a dip in the charge-signed rapidity difference for Monte Carlo with an anomalous $WW\gamma$ coupling.

In this scan, the photon E_T cut is varied from 7 GeV to 15 GeV in 1 GeV increments, while the M_{T^3} cut is varied in 5 GeV increments from 90 GeV to 110 GeV (105

*The choice of ΔR cut will also influence the amount of FSR, since the photons will preferentially be radiated closer to the lepton. However, increasing the ΔR cut can artificially enhance the dip as shown in Figure 4.47. So as not to artificially increase the sensitivity to the amplitude zero, the ΔR cut is not allowed to increase.

GeV) for the electron (muon) channel. The M_{T^3} cut is independently varied in both channels, since the muon and electron resolutions are different. For each set of cuts, the combined channel rapidity distribution is calculated from the background estimates and for two $W\gamma$ Monte Carlo samples. One sample is for the Standard Model coupling ($\kappa = 1, \lambda = 0$), while the other sample is for an anomalous $WW\gamma$ coupling ($\kappa = -1, \lambda = 0$). In addition an ensemble of expected experimental observations is constructed by combining the SM and background expectations and by varying the distributions according to Poisson counting fluctuations and the uncertainties on the background and signal estimates. For each of the Monte Carlo experiments in the ensemble, the significance of the dip in the "observed" candidate rapidity distribution is determined by performing a shape test between the bimodal SM hypothesis and a unimodal hypothesis which is given by the shape of the anomalous coupling (AC).

In the shape test, the SM distribution is combined with the background distribution; however the normalization of the SM distribution is allowed to float to produce the best fit with the "observed" candidate rapidity distribution. Using the best fit distribution the negative log likelihood (NLLH)* is calculated for the "observed" candidate rapidity distribution and the SM prediction. The same is done for the AC distribution. The average NLLH difference is then found for the ensemble. The set of cuts with the maximum difference is expected to have the most sensitivity to the

*More information on the likelihood calculation is provided in Section 5.2.1

dip from the radiation amplitude zero. This occurs for a photon $E_T > 11\ GeV$ and $M_{T^3} > 110\ GeV$ (105 GeV) for the electron (muon) channel.

The particular anomalous $WW\gamma$ coupling is chosen for two reasons. First, it is an anomalous coupling that belongs to the class of couplings that turns off the magnetic dipole moment of the W boson. Second, the shape of the rapidity distribution is approximately at the boundary of the set of couplings that have no observable dip from the destructive interference and the set of couplings that have an observable dip form the interference (*i.e.* It almost has a horizontal line going across the expected dip region). A plot of the expected rapidity distribution for some example couplings is shown in Figure 4.48.

It has been suggested that the set of couplings that turn off the magnetic dipole moment and that is closest to the SM in $\kappa \times \lambda$ space be used for the unimodal hypothesis. However, the shape from this set of couplings ($\kappa = 0$,$\lambda = -1$) has a significantly larger fraction of events in the expected dip region as can be seen in Figure 4.48. Since the set of couplings with $\kappa = -1$ and $\lambda = 0$ appears to be closer to the boundary between the class of couplings that have a unimodal shape and the class of couplings that have a bimodal shape, ($\kappa = -1$,$\lambda = 0$) is used for the optimization study.

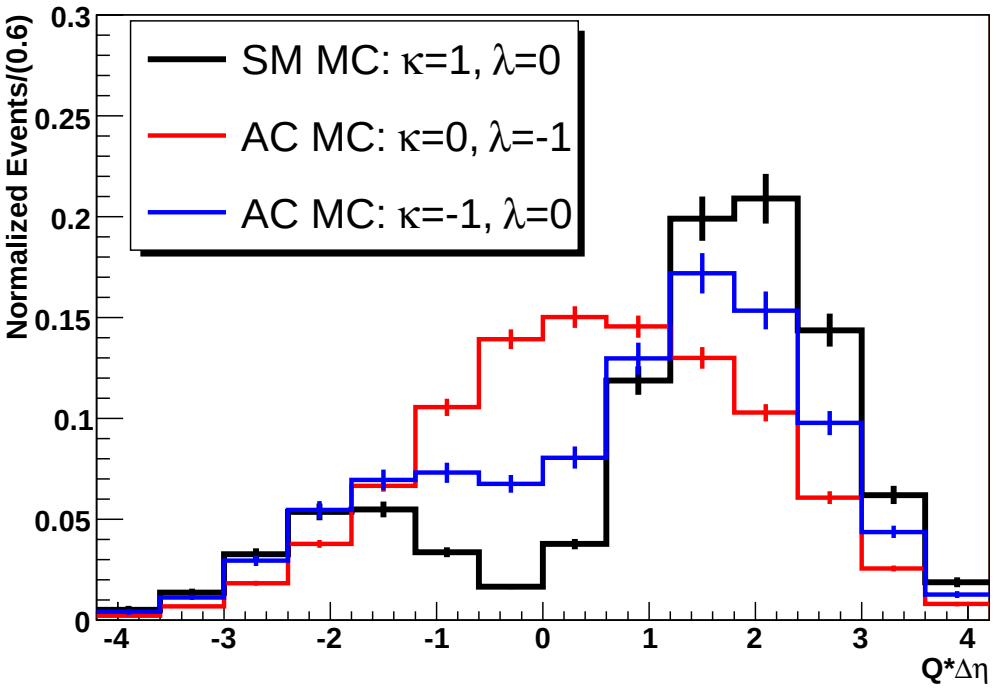

Figure 4.48 Monte Carlo comparison of the event normalized charge-signed rapidity difference for various $WW\gamma$ couplings.

Chapter 5
The Analysis

With the expected efficiencies and background estimates a quantitative examination of the $W\gamma$ candidate sample can be performed to test the predictions from Section 1.3. In this chapter the $W\gamma$ production rate is measured and compared to the SM expectation. In addition, a search for anomalous $WW\gamma$ couplings is performed through an examination of the photon E_T spectrum which is the distribution that is most sensitive to variations in the couplings. Finally, the charge-signed rapidity distribution will be analyzed for evidence of the destructive interference that gives rise to the radiation amplitude zero. Much of the content presented in this chapter can also be found in [34].

5.1 Cross Section Measurement

A summary of the number of $W\gamma$ candidates, estimated backgrounds, and expected signal can be found in Table 5.1. For each lepton (ℓ) channel, the inclusive $p\bar{p} \to \ell\nu\gamma$ cross section can be extracted from the measured number of signal events with the following formula:

$$\sigma_{p\bar{p}\to\ell\nu\gamma} = \frac{S_\ell}{\epsilon_{Total,\ell} \cdot L_\ell} \tag{5.1}$$

where $\epsilon_{Total,\ell}$ is the product of all the individual event efficiencies and acceptances for the ℓ-channel, L_ℓ is the luminosity for the ℓ-channel, and S_ℓ is the measured number

	Electron Channel	**Muon Channel**
Luminosity	$1031 \pm 63\ pb^{-1}$	$963 \pm 59\ pb^{-1}$
$W + j$ Background	$48 \pm 4_{stat} \pm 4_{sys}$	$46 \pm 4_{stat} \pm 4_{sys}$
ℓeX Background	$32 \pm 4_{stat} \pm 2_{sys}$	$7 \pm 2.1_{stat} \pm 0.3_{sys}$
τ-Channel Background	$1.7 \pm 0.15_{stat} \pm 0.14_{sys}$	$2.7 \pm 0.30_{stat} \pm 0.22_{sys}$
$Z\gamma$ Background	-	$8 \pm 1_{stat} \pm 1_{sys}$
Candidates	280	185
Measured Signal	$198 \pm 17_{stat} \pm 5_{sys}$	$121 \pm 13_{stat} \pm 4_{sys}$
Expected Signal	$200 \pm 9_{sys} \pm 12_{lumi}$ $\pm 5_{PDF} \pm 12_{LO}$	$147 \pm 13_{sys} \pm 9_{lumi}$ $\pm 4_{PDF} \pm 9_{LO}$

Table 5.1 Summary of candidate, background, and signal events. *stat* and *sys* stand for statistical errors and systematic errors, respectively. *lumi*, *PDF*, and *LO* are normalization errors that are the result of uncertainties from the luminosity, PDFs, and higher-order corrections, respectively.

of signal events in the ℓ-channel. The value of S_ℓ is obtained from the number of candidate events and the background estimates with the following equations:

$$S_e = \frac{(N_e - B_{Wj,e} - B_{\ell eX,e})}{1 + f_{\tau,e}} \tag{5.2}$$

$$S_\mu = \frac{(N_\mu - B_{Wj,\mu} - B_{\ell eX,\mu})}{1 + f_{\tau,\mu} + f_{Z\gamma}} \tag{5.3}$$

Here N_ℓ is the number of observed candidate events, $B_{Wj,\ell}$ is the the estimated number of $W+j$ background events, $B_{\ell eX,e}$ is the estimated number of ℓeX background events, $f_{\tau,\ell}$ is the fraction of signal events that are from the $\tau - channel$ decays, and $f_{Z\gamma}$ is the fraction of signal events that are from $Z\gamma$ production.

The $W\gamma$ cross section must be measured with respect to a minimal photon E_T and ΔR cut. Since this analysis required that the photons have an $E_T > 11\ GeV$ and a $\Delta R > 0.7$, the cross section will be measured with respect to these values.

Furthermore, the $\ell\nu\gamma$ final-state contains contributions from both prompt $W\gamma$ production and FSR. The FSR is the dominant contribution to the cross section for $M_{T^3} < 90\ GeV$, while the prompt $W\gamma$ production is the dominant contribution for $M_{T^3} > 90\ GeV$. Since the process of interest for this analysis is prompt $W\gamma$ production, the cross section will be measured with respect to $M_{T^3} > 90\ GeV$. The above set of cuts are taken into account in the acceptance measurement which is folded into $\epsilon_{Total,\ell}$ along with the other efficiencies such as the identification, trigger, and veto efficiencies. In the electron channel, the $W\gamma$ cross section times branching ratio is measured to be $2.05 \pm 0.18_{stat} \pm 0.10_{sys} \pm 0.13_{lumi}\ pb$. In the muon channel, the $W\gamma$ cross section times branching ratio is measured to be $1.72 \pm 0.19_{stat} \pm 0.15_{sys} \pm 0.10_{lumi}\ pb$. Both of these values are consistent with the SM expectation of $2.08 \pm 0.05_{PDF}\ pb$. These results are summarized in Table 5.2.

Observed Electron Channel	$2.05 \pm 0.18_{stat} \pm 0.10_{sys} \pm 0.13_{lumi}\ pb$
Observed Muon Channel	$1.72 \pm 0.19_{stat} \pm 0.15_{sys} \pm 0.10_{lumi}\ pb$
SM Expectation	$2.08 \pm 0.05_{PDF}\ pb$

Table 5.2 The $W\gamma$ cross section times branching ratio measured with respect to the following kinematics: $\Delta R_{\ell\gamma} > 0.7$, $E_T(\gamma) > 11\ GeV$, and $M_{T^3} > 90\ GeV$.

5.2 Anomalous $WW\gamma$ Coupling Limits

To produce limits on potential anomalous couplings, the combined channel candidate photon E_T spectrum is compared against the Monte Carlo predictions for

various $WW\gamma$ couplings including the SM value. For each Monte Carlo spectrum, the probability, or likelihood, for the experiment to produce the observed candidate distribution is calculated. Using the resulting distribution of likelihoods, 95% confidence level (CL) limits can be placed on the potential values of κ and λ. The complete method is detailed below.

5.2.1 Likelihood Calculation

The probability of observing N events when μ are expected is given by the Poisson probability:

$$P = \frac{e^{-\mu}\mu^{N}}{N!} \tag{5.4}$$

For multiple samples (*i.e.* bins in a histogram of the photon E_T), the total probability is the product of the individual probabilities from each sample:

$$P = \prod_{i} \frac{e^{-\mu_i}\mu_i^{N_i}}{N_i!}, \tag{5.5}$$

where N_i (μ_i) is the observed (expected) number of events for the i^{th} sample. For the combined channel photon E_T spectrum, the expected number of candidate events in each E_T bin depends on multiple parameters:

$$\mu_i = S_i + \sum_{j} B_{j,i}, \tag{5.6}$$

$$S_i = \epsilon_{\mu,i}\sigma L_{\mu} + \epsilon_{e,i}\sigma L_{e}. \tag{5.7}$$

Here S_i is the expected number of signal events and $B_{j,i}$ are the estimated number of events from the various backgrounds. σ is the cross section which is dependent on the

choice of coupling values. L_ℓ is the luminosity of the ℓ-channel. $\epsilon_{\ell,i}$ is the ℓ-channel efficiency* which is dependent of the choice of coupling value. These nuisance parameters have an associated uncertainty which must be folded into the calculation of the likelihood. Assuming the parameters are Gaussian distributed, it is straightforward to integrate out the uncertainties on the nuisance parameters and obtain the average likelihood, $\bar{P}$:

$$\bar{P} = \int dx_{\mathcal{L}} \int dx_{\epsilon} \int dx_{Wj} \int dx_{\ell eX} \int dx_{\tau,Z\gamma}\ f(x_{\mathcal{L}}, x_{\epsilon}, x_{Wj}, x_{\ell eX}, x_{\tau,Z\gamma}), \tag{5.8}$$

$$\begin{aligned} f(x_{\mathcal{L}}, x_{\epsilon}, x_{Wj}, x_{\ell eX}, x_{\tau,Z\gamma}) &= G(x_{\mathcal{L}})G(x_{\epsilon})G(x_{Wj})G(x_{\ell eX})G(x_{\tau,Z\gamma}) \\ &\times \prod_i \frac{\mu_i(x_{\mathcal{L}}, x_{\epsilon}, x_{Wj}, x_{\ell eX}, x_{\tau,Z\gamma})^{N_i}}{e^{-\mu_i(x_{\mathcal{L}}, x_{\epsilon}, x_{Wj}, x_{\ell eX}, x_{\tau,Z\gamma})} N_i!}, \end{aligned} \tag{5.9}$$

$$\begin{aligned} \mu_i(x_{\mathcal{L}}, x_{\epsilon}, x_{Wj}, x_{\ell eX}, x_{\tau,Z\gamma}) &= S_i + (x_{\mathcal{L}} \cdot \sigma_{\mathcal{L},i}) + (x_{\epsilon} \cdot \sigma_{\epsilon,i}) \\ &+ B_{Wj,i} + (x_{Wj} \cdot \sigma_{Wj,i}) \\ &+ B_{\ell eX,i} + (x_{\ell eX} \cdot \sigma_{\ell eX,i}) \\ &+ B_{\tau,Z\gamma,i} + (x_{\tau,Z\gamma} \cdot \sigma_{\tau,Z\gamma,i}). \end{aligned} \tag{5.10}$$

In the above relations, $G(x)$ is a normalized Gaussian function with mean of zero and standard deviation of one. S_i is the expected number of signal events for the i^{th} bin. $\sigma_{\mathcal{L},i}$ is the uncertainty on S_i from the luminosity, cross section, and higher-order corrections. $\sigma_{\epsilon,i}$ is the uncertainty on S_i from the efficiency. $B_{Wj,i}$ is the estimated number of $W + j$ background events for the i^{th} bin. $\sigma_{Wj,i}$ is the uncertainty on

*This efficiency also folds in the fraction of $W\gamma$ events that are found in the particular E_T bin.

$B_{Wj,i}$. $B_{\ell eX,i}$ is the estimated number of ℓeX background events for the i^{th} bin. $\sigma_{\ell eX,i}$ is the uncertainty on $B_{\ell eX,i}$. $B_{\tau,Z\gamma,i}$ is the estimated number of $Z\gamma$ and τ-channel background events for the i^{th} bin. $\sigma_{\tau,Z\gamma,i}$ is the uncertainty on $B_{\tau,Z\gamma,i}$.

The form of Equation 5.10 assumes that for each nuisance parameter, the uncertainties are 100% correlated between the photon E_T bins. This assumption is approximately true for the systematic errors; however errors from the statistical uncertainties associated with the number of events in the background normalization samples will not be correlated. For comparison the likelihood will also be calculated with the assumption that there are no bin-to-bin correlations. To perform this calculation, the integration in Equation 5.10 need to be performed inside the multiplication.

5.2.2 Generation of the Monte Carlo Photon E_T Spectra

Using a fast parameterized Monte Carlo process, the photon E_T spectra for 351,201 different values of the $WW\gamma$ coupling are produced at a form factor scale of $\Lambda = 2\ TeV$. The spectra are generated in a 501×701 grid in $\kappa \times \lambda$ space with the value of λ ranging from -1.992 to 1.992 and the value of κ ranging from -1.9925 to 3.9925. A non-uniform grid spacing is used with a finer spacing being utilized near the SM coupling values. Along the λ axis there are 100 evenly spaced grid points from -1.992 to -0.408, 301 evenly spaced grid points from -0.3987 to 0.3987, and 100 evenly spaced grid points from 0.408 to 1.992. Along the κ axis, there are 100 evenly spaced grid points from -1.9925 to -0.5075, 501 evenly spaced grid points from -0.497

to 2.497, and 100 evenly spaced grid points are generated from 2.5075 to 3.9925. To produce 351,201 spectra in a reasonable timeframe, a fast parameterized process that takes advantage of known theoretical extrapolations is implemented. This process consists of four steps, of which the first three are identical to the method that was used to produce the SM Monte Carlo, while the fourth step introduces a method of extrapolation.

In the first step, Baur Monte Carlo four-vectors are generated at $\Lambda = 2\ TeV$ for 91 different sets of $WW\gamma$ coupling values. These sets are generated in a 13×7 grid in $\kappa \times \lambda$ space, with κ varying in increments of 0.3 from -0.8 to 2.8, and λ varying in increments of 0.13 from -0.39 to 0.39. In the second step, the four-vectors are randomly given a boost using the Pythia Monte Carlo sample. In the third step, the appropriate PMCS smearings, efficiencies, and associated uncertainties are applied, and the photon E_T spectra for the 91 different coupling values are obtained.

Using this set of spectra, it is possible to take advantage of known theoretical constraints and produce the photon E_T spectra for intermediate couplings values via an extrapolation. The first of these constraints is the knowledge that the $W\gamma$ production amplitude is linear in κ and λ with the amplitude growing as $\lambda\hat{s}$ and $\Delta\kappa\sqrt{\hat{s}}$. Therefore, the expected number of events will be described by a bivariate second-degree polynomial:

$$S = c_0 + c_1\lambda^2 + c_2\lambda + c_3\lambda\kappa + c_4\kappa + c_5\kappa^2. \tag{5.11}$$

In addition, it is also known that the introduction of anomalous $WW\gamma$ couplings will increase the $W\gamma$ cross section. This further constrains Equation 5.11, by requiring that the minimum occurs at the SM values of $(\kappa = 1, \lambda = 0)$. This constraint can be folded into the equation by requiring that the partial derivatives be zero at the SM values:

$$0 = \frac{\partial S}{\partial \lambda} = 2c_1\lambda + c_2 + c_3\kappa, \text{ for } \kappa = 1, \lambda = 0, \tag{5.12}$$

$$\Rightarrow c_2 = -c_3, \tag{5.13}$$

$$0 = \frac{\partial S}{\partial \kappa} = 2c_5\kappa + c_4 + c_3\lambda, \text{ for } \kappa = 1, \lambda = 0, \tag{5.14}$$

$$\Rightarrow c_4 = -2c_5, \tag{5.15}$$

$$\Rightarrow S = c_0 + c_1\lambda^2 + c_2\lambda - c_2\lambda\kappa - 2c_5\kappa + c_5\kappa^2. \tag{5.16}$$

The number of expected events for intermediate coupling values can then be calculated by fitting Equation 5.16 to the number of expected events found in the 91 Monte Carlo samples. Since the enhancement in cross section will intrinsically be E_T dependent, with the quadratic growth being more apparent at the highest E_T, the function is independently fit to each E_T bin in the spectra. The photon E_T spectrum is then calculated for 351,201 grid points by evaluating these fits at the various coupling values. For each E_T bin, the fractional uncertainty on the expected number of events is taken to be the maximum fractional uncertainty from the original 91 Monte Carlo events. This provides a conservative estimate on the error without over inflating

the uncertainty; the maximum fractional uncertainty is always with 0.01 of the SM uncertainty of approximately 0.10-0.13. A diagram of the extrapolation process can be found in Figure 5.1. Plots of the fit to the highest E_T bin can be found in Figure 5.2-5.3. Plots of the other fits can be found in Figures C.20-C.33 in the Appendix. The χ^2 value of the fits is provided in Table 5.3.

Photon E_T Bin	**χ^2 for 87 d.o.f.**
$E_T > 241\ GeV$	4.1
$176\ GeV < E_T < 241\ GeV$	13.0
$128\ GeV < E_T < 176\ GeV$	47.2
$91\ GeV < E_T < 176\ GeV$	62.9
$62\ GeV < E_T < 91\ GeV$	72.2
$40\ GeV < E_T < 62\ GeV$	45.2
$23\ GeV < E_T < 40\ GeV$	25.3
$11\ GeV < E_T < 23\ GeV$	20.5

Table 5.3 χ^2 of fits to expected number of events from 91 Monte Carlo samples.

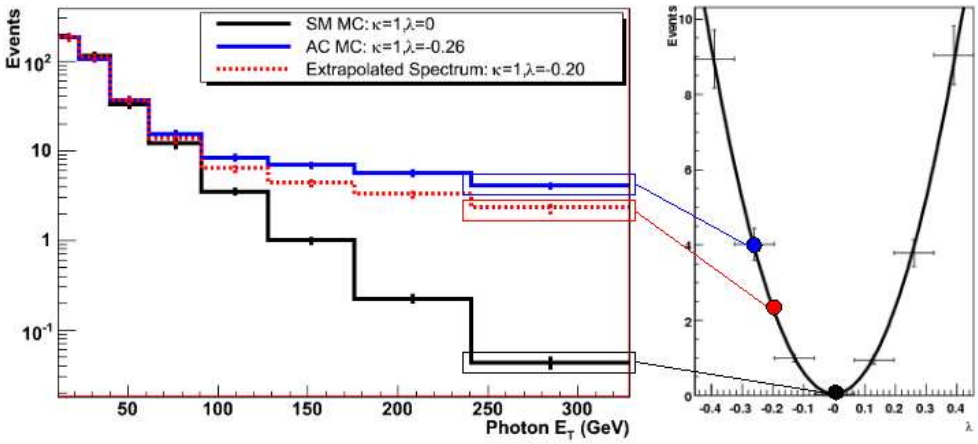

Figure 5.1 Diagram of how the extrapolation of the photon E_T spectrum is performed for an arbitrary $WW\gamma$ coupling.

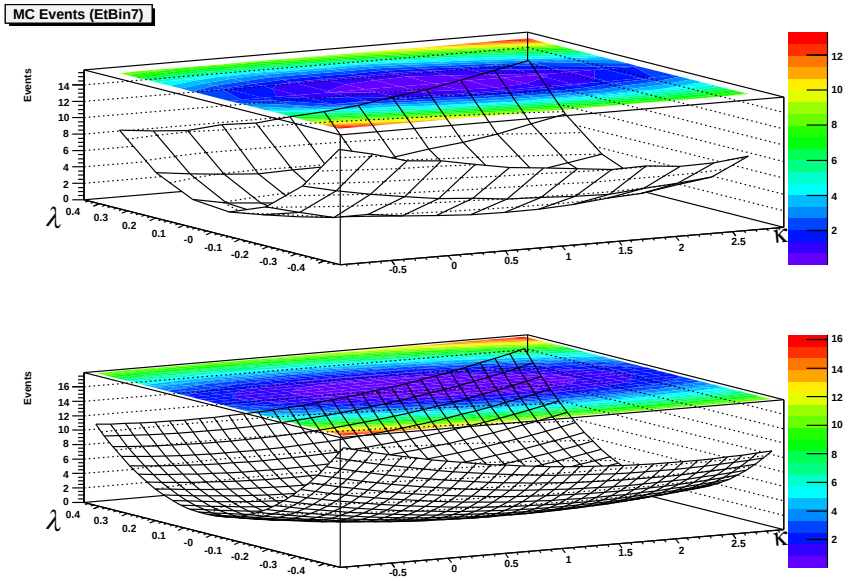

Figure 5.2 Expected number of $W\gamma$ Monte Carlo events for photon $E_T > 241\ GeV$. The top plot is the expectation from 91 Monte Carlo samples. The bottom plot is a fit to the top plot.

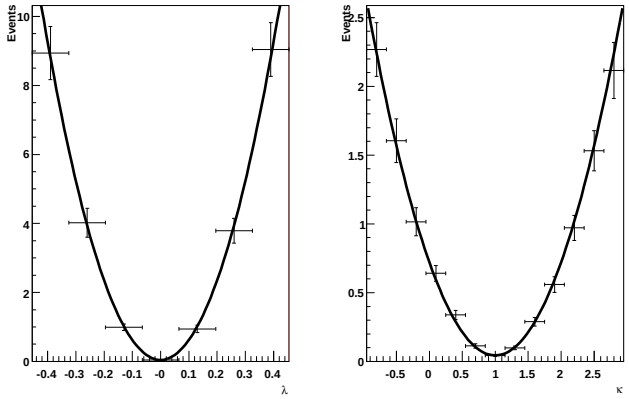

Figure 5.3 Expected number of $W\gamma$ Monte Carlo events for photon $E_T > 241\ GeV$. The plot on the left is for $\kappa = 1$. The plot on the right is for $\lambda = 0$. The points with errors are from the Monte Carlo samples. The black curve is the fit to the expected number of events.

5.2.3 Calculation of the Coupling Limits

The combined channel candidate photon E_T spectrum (shown in Figure 5.4) is compared against the 351,201 Monte Carlo predictions through the calculation of the likelihood. The resulting histogram of the likelihood surface is shown in Figures 5.5 and 5.6. It should be noted that the SM is not at the point of maximum likelihood

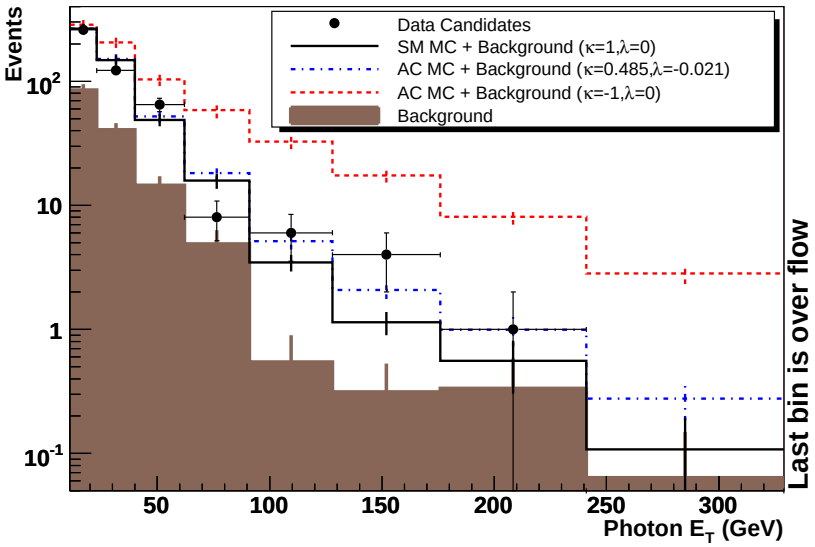

Figure 5.4 The combined channel photon E_T spectrum. The black points are the data with statistical errors. The black curve is the SM plus background expectation. The blue curve is the background plus AC that best fits the data. The red curve is the background plus AC that turns off the magnetic dipole moment of the W boson.

which is found to occur at $(\kappa = 0.485, \lambda = -0.021)$ and $(\kappa = 1.515, \lambda = 0.021)$. However, this does not suggest evidence for anomalous couplings. Since the likelihood calculation is most sensitive to the number of events in the highest E_T bins, if the

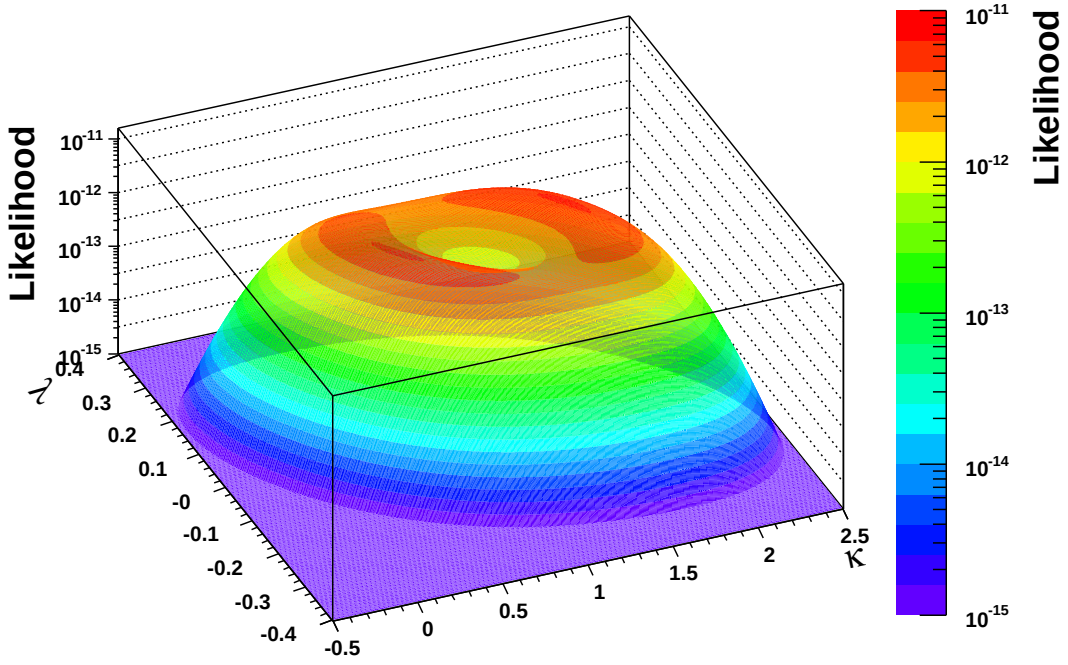

Figure 5.5 Likelihood of the $WW\gamma$ couplings to produce the observed combined channel candidate photon E_T spectrum from data.

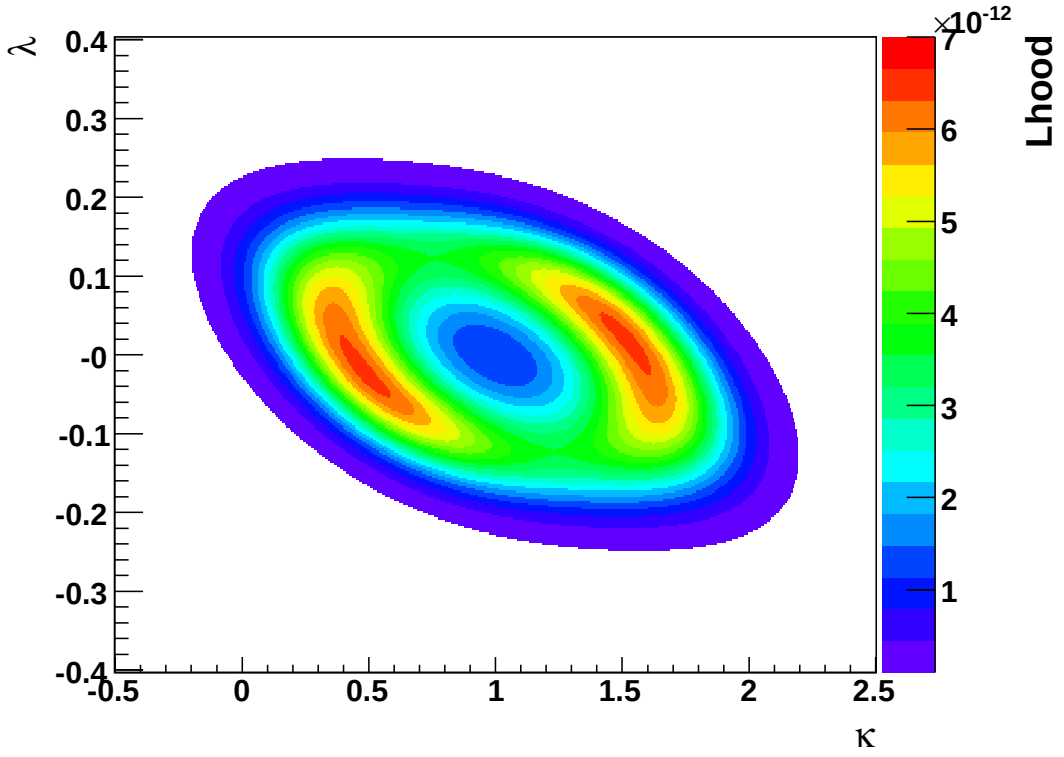

Figure 5.6 Likelihood of the $WW\gamma$ couplings to produce the observed combined channel candidate photon E_T spectrum from data.

observed events in those bins where to fluctuate high, the SM would most likely not be at the point of maximum likelihood. A more quantitative statement will be made about this later.

Two-dimensional limits are placed on the $WW\gamma$ coupling values at 95% CL, by finding the minimal-area in $\kappa \times \lambda$ space that contains 95% of the volume under the likelihood surface. Due to the fine granularity of the grid spacing and the wide range of values contained within the grid*, the numerical integration can sufficiently be calculated with a histogram of the likelihood. To find the minimal-area that contains 95% of the volume under the likelihood surface, an iterative method is used to identify the histogram bins with the highest value of likelihood. In the n^{th} iteration, the histogram bin with the n^{th} highest value of likelihood is selected. The process terminates when the selected histograms contain 95% of the total volume. The area defined by the selected histogram bins maps out the contour of the 95% CL limit. A plot of the two-dimensional limits can be found in Figure 5.7. Note the SM couplings are contained within this contour. Using a conventional terminology, the SM can loosely be interpreted as being within 2σ of the coupling values that have the maximum likelihood†.

One-dimensional limits can independently be set on the values of κ and λ by

*The values of likelihood at the edge of the grid are less than 10^{-23} times the maximum likelihood within the grid.

†This is analogous to what is typically done for a Gaussian probability distribution in which a 2σ deviation is at the boundary of the interval of minimal-size that contains 95% of the area under the curve.

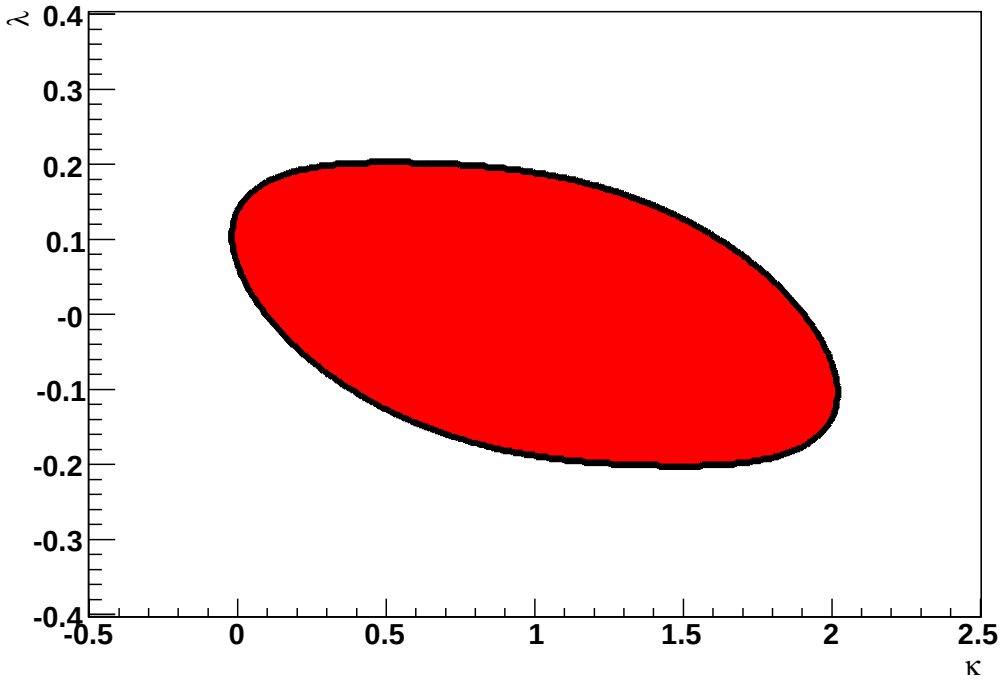

Figure 5.7 Two-dimensional $WW\gamma$ couplings limits at 95% CL. The bins from the likelihood histogram that contribute to the contour are shaded red.

assuming that only one of the coupling values varies from the SM value at a time. The histograms of the likelihoods that are obtained from these one-dimensional slices are given in Figures 5.8 and 5.9. Limits are set by the finding the interval that contains 95% of the area under the likelihood curve. This interval is found by adding the area in neighboring bins, starting with the SM value and working out. The one-dimensional 95% CL limits are $-0.18 < \lambda < 0.18$ and $0.16 < \kappa < 1.84$.‡

‡If no bin-to-bin correlations are assumed (except for those from the overall normalization, which must be correlated) the one-dimensional limits are found to be: $-0.17 < \lambda < 0.17$ and $0.26 < \kappa < 1.75$.

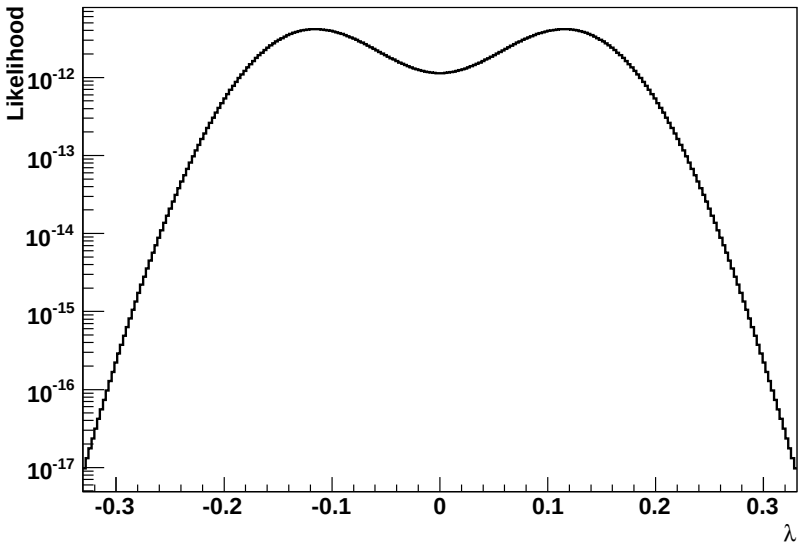

Figure 5.8 Histogram of the likelihood when $\kappa = 1$.

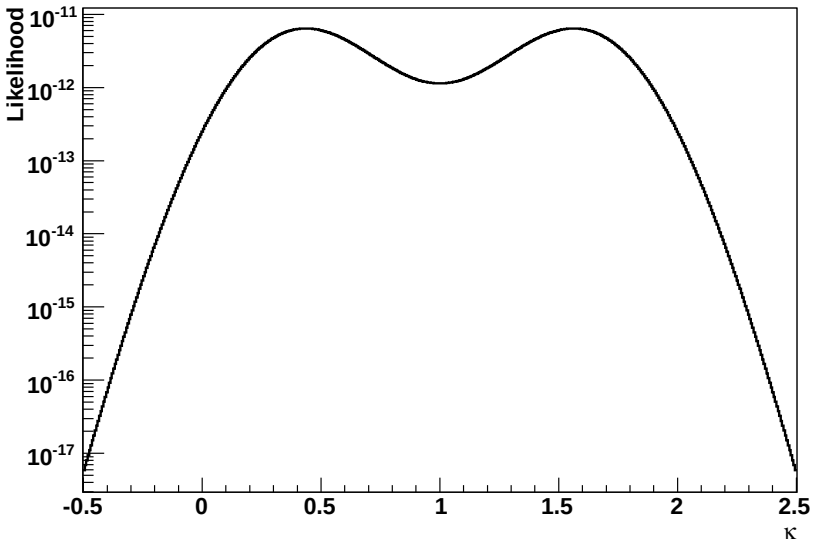

Figure 5.9 Histogram of the likelihood when $\lambda = 0$.

5.3 Charge-Signed Rapidity Difference

It is important to examine the distribution of the combined channel charge-signed rapidity difference to determine if it is suggestive of a physical process that would lead to a depletion of events or dip in the observed distribution (*i.e.* the radiation amplitude zero). However, before this can be done, it is necessary to demonstrate that the detector/selection requirements do not artificially produce a dip in the observed distribution.

5.3.1 Detector Asymmetry Check

From Monte Carlo, such as the plot in Figure 4.48, the detector/selection requirements are not expected to artificially induce a dip, but it is ideal to have a data measurement to confirm this. To perform this cross check in data, a sample of $Z\gamma$ production events is selected. These events have some similar characteristics to the $W\gamma$ sample, but should not have an asymmetry in the rapidity distribution.

Z events are selected by requiring that there be two leptons of the same flavor that pass the $W\gamma$ lepton identification requirements. These events are then made to resemble W decays by randomly assigning one of the leptons to behave like a neutrino. For the electron channel, the E_T of the neutrino-tagged lepton must be added to the measured $\not\!\!E_T$. For the muon channel, the p_T of the neutrino-tagged lepton must be left out of the $\not\!\!E_T$ correction. The other lepton is treated as normal, and the events are required to pass all of the remaining $W\gamma$ selection criteria. The

plot of the resulting rapidity difference is shown in Figure 5.10. The distribution does not exhibit an artificial dip or any other unexpected asymmetry as shown Figure 5.11. The positive and negative $Q * \Delta\eta$ contributions are consistent with being symmetric with a χ^2 of 4.9 for 7 degrees of freedom.

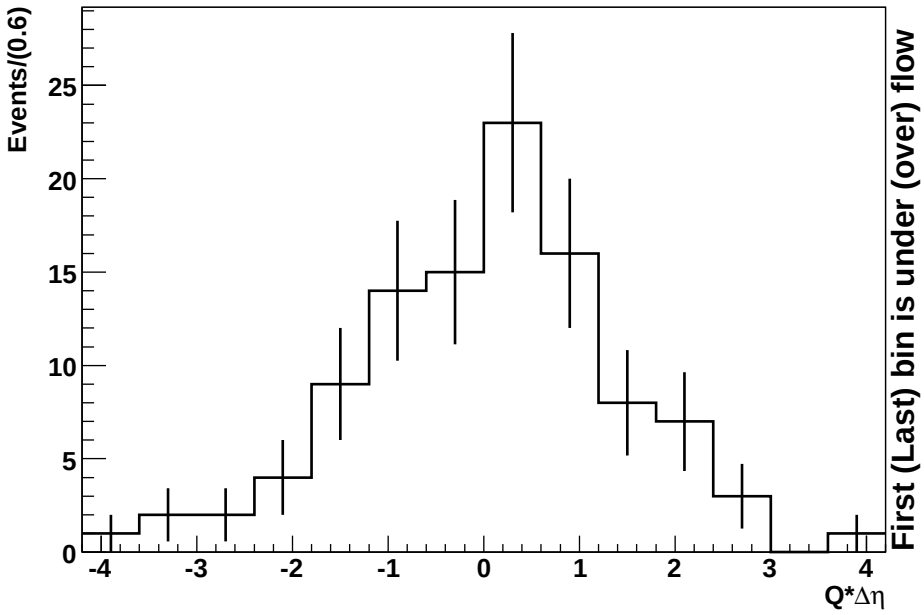

Figure 5.10 Combine channel charge-signed rapidity difference from $Z\gamma$ data events.

5.3.2 Rapidity Difference with Radiative *W* Decays

Before examining the rapidity distribution from the prompt $W\gamma$ events, the sample of combined $W\gamma \rightarrow \ell\nu\gamma$ and $W \rightarrow \ell\nu \rightarrow \ell\nu\gamma$ events is analyzed. These events are selected by excluding the three-body transverse mass requirement from the $W\gamma$

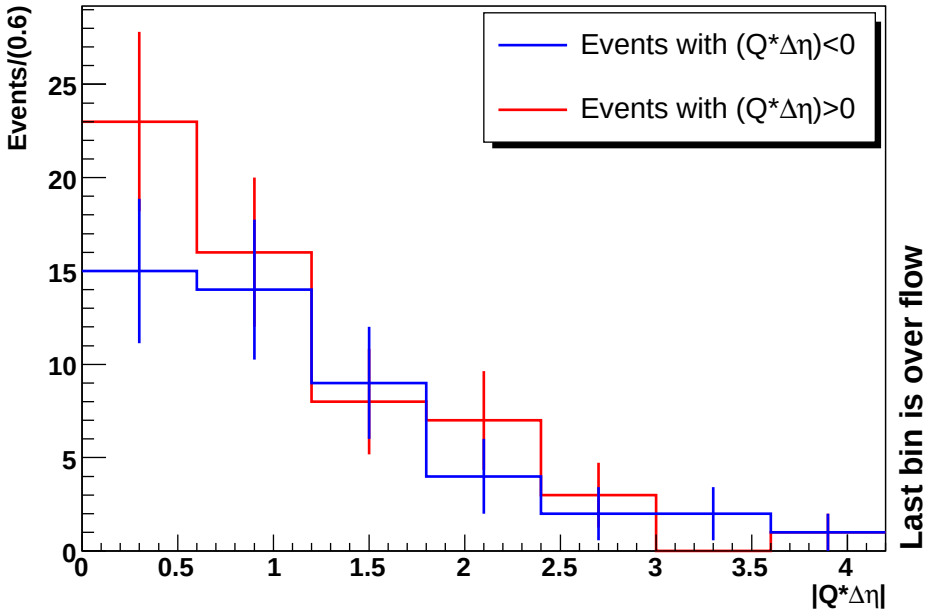

Figure 5.11 Combine channel charge-signed rapidity difference from $Z\gamma$ data events.

selection criteria. Without the M_{T^3} mass cut the events will be dominated by FSR (as was shown in Figure 4.4), and hence should have no apparent dip. The resulting combined channel candidate distribution is shown in Figure 5.12. The distribution does not exhibit an artificial dip. Furthermore, it is consistent with the background and signal expectations, with a χ^2 of 16 for 14 degrees of freedom*. This indicates that the rapidity distribution is well-modeled within the known uncertainties and correlations.

*The associated χ^2 probability is 0.31. The χ^2 value takes into account the covariance matrix. More information on this calculation will be provided in Section 5.3.3.

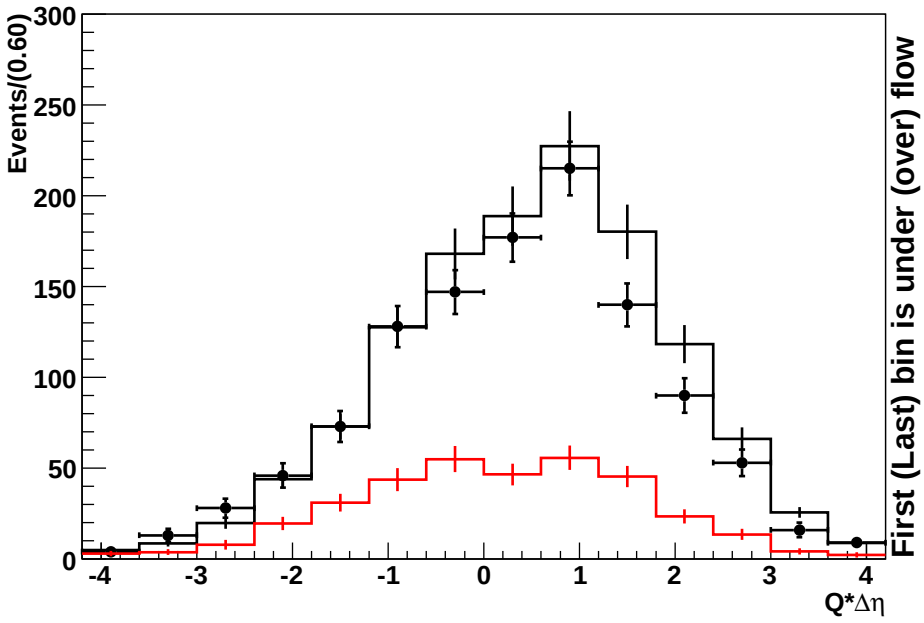

Figure 5.12 Charge-signed rapidity difference for the combine channel candidate events when no M_{T^3} cut is applied. The black points represent the data with statistical uncertainties. The red curve is the background estimate with the associated systematic errors. The black curve is the SM Monte Carlo expectation plus background estimate. The uncertainty shown with the black curve is the combined systematic error for the signal and background estimate. Note the systematic errors have significant bin-to-bin correlations.

5.3.3 Rapidity Difference for Prompt $W\gamma$ Production

Applying the full set of the $W\gamma$ selection criteria, a sample of predominately prompt $W\gamma$ events is obtained. The resulting charge-signed rapidity difference for the combined channel candidate distributions is provided in Figure 5.13. The background subtracted distribution can be found in Figure 5.14.

To test if the observed distribution is consistent with the Standard Model expec-

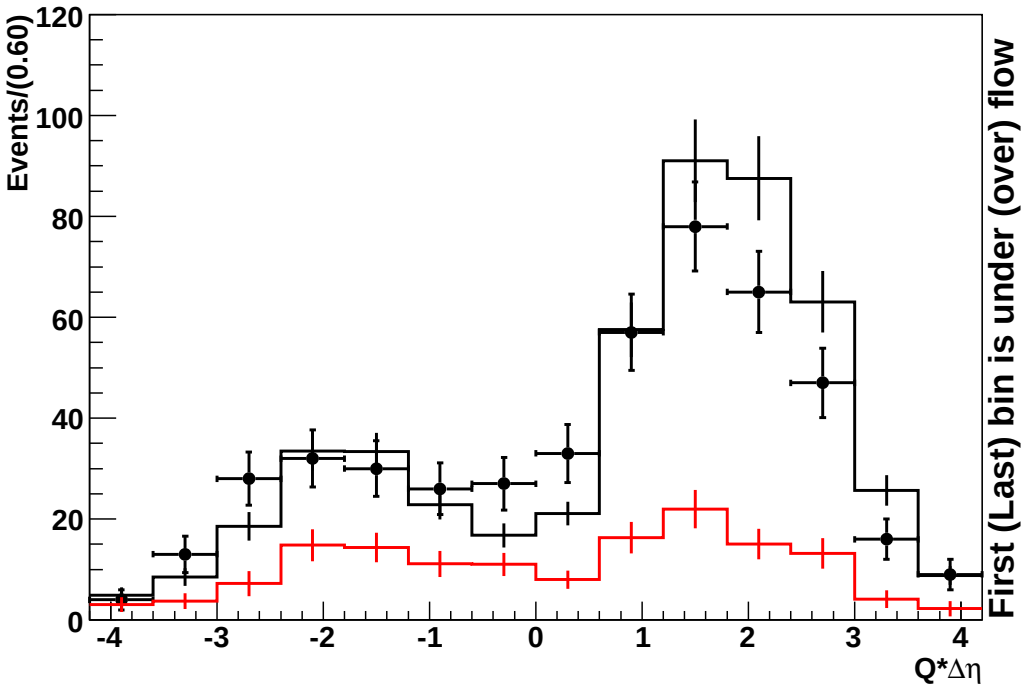

Figure 5.13 Charge-signed rapidity difference for the combine channel candidate events with all selection criteria applied. The black points represent the data with statistical uncertainties. The red curve is the background estimate with the associated systematic errors. The black curve is the SM Monte Carlo expectation plus background estimate. The uncertainty shown with the black curve is the combined systematic error for the signal and background estimate. Note the systematic errors have significant bin-to-bin correlations.

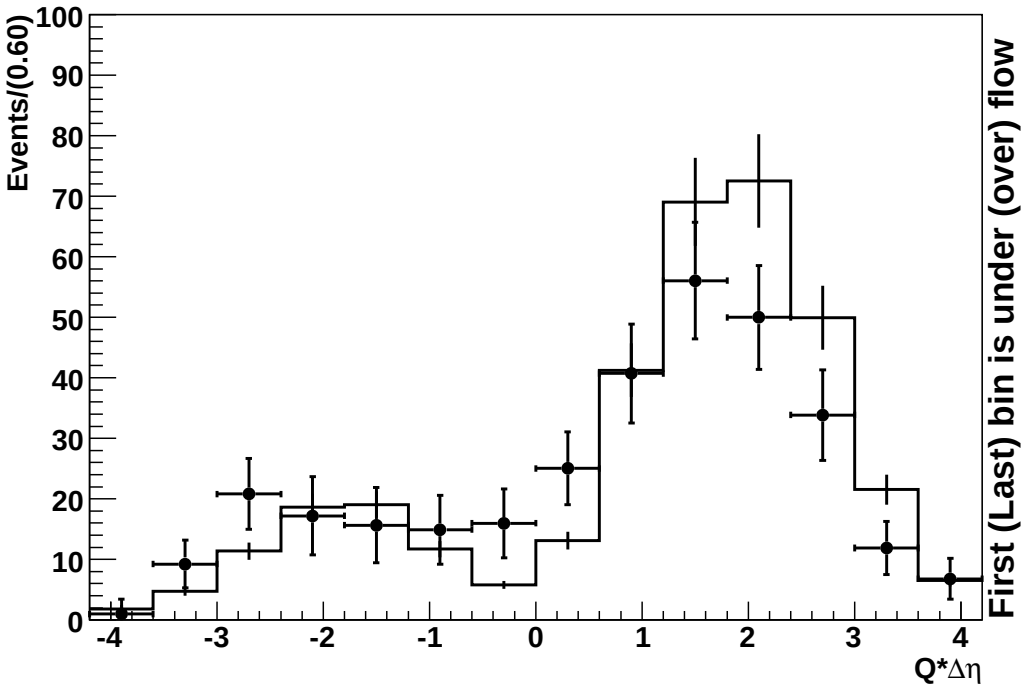

Figure 5.14 Charge-signed rapidity difference for the combine channel background subtracted events. The black points represent the background subtracted data. The errors on the points include the statistical uncertainties and the systematic uncertainties from the background estimate. The black curve is the SM Monte Carlo expectation. The uncertainty shown with the black curve is the systematic error from the signal. Note the systematic errors have significant bin-to-bin correlations.

tation, a χ^2 test is performed. Since there are significant bin-to-bin correlations, the χ^2 value is calculated with the full covariance matrix:

$$\chi^2 = \sum_i \sum_j (N_i - \mu_i) \times (N_j - \mu_j) \times w_{ij}, \tag{5.17}$$

where N_i is the number of observed candidate events in the i^{th} bin, μ_i is the number of expected candidate events in the i^{th} bin, and w_{ij} is the corresponding element from the inverse of the covariance matrix (V) given by:

$$w_{ij} = (V^{-1})_{ij}, \tag{5.18}$$

$$V_{ij} = cov(x_i, x_j), \tag{5.19}$$

$$cov(x_i, x_j) = < x_i x_j > - < x_i >< x_j > . \tag{5.20}$$

Here x_i represents the sum of the samples that contribute to the i^{th} bin. The final covariance matrix (V) is obtained from the sum of the diagonal covariance matrix containing the $\sqrt{N_i}$ Poisson statistical fluctuations and the covariance matrix containing the systematic errors from the signal and background estimates. The covariance matrix of the systematic errors is calculated from Equation 5.20 by producing an ensemble of background and signal estimates. The ensemble of estimates is made by randomly varying the parameters that went into the calculation of the estimates by their associated uncertainties.

Based on the χ^2 test, the observed distribution is found to be consistent with the

SM expectation with a χ^2 of 22 for 14 degrees of freedom*. Although the distribution is consistent with the SM, the question remains if there is sufficient statistical evidence to demonstrate the destructive interference from the radiation amplitude zero. Since the distinguishing feature of the interference is the resulting bimodal distribution, a test statistic can be produced by comparing the observed distribution against the unimodal hypothesis.

Shape Test

One method of comparing the shape of the rapidity difference against the set of unimodal hypotheses is to utilized the Monte Carlo predicted shapes from different values of the $WW\gamma$ couplings. A plot of the class of expected shapes of the rapidity distribution for various $WW\gamma$ couplings is shown Figure 5.15. Note, if there is no destructive interference, the distribution would resemble the shape that is produced by the set of couplings with $(\kappa = 0, \lambda = -1)$. As destructive interference is introduced to the system, the shape begins to flatten out and eventually forms a dip near $Q * \Delta\eta \approx -0.3$. At this boundary, the distribution would resemble the shape that is produced by the set of couplings with $(\kappa = 0, \lambda = -1)$. Pass this boundary, the bimodal distribution becomes more pronounced as the amount of destructive interference increases. The most prominent dip occurs for the complete destructive interference from the SM radiation amplitude zero.

*This corresponds to a χ^2 probability of 0.08.

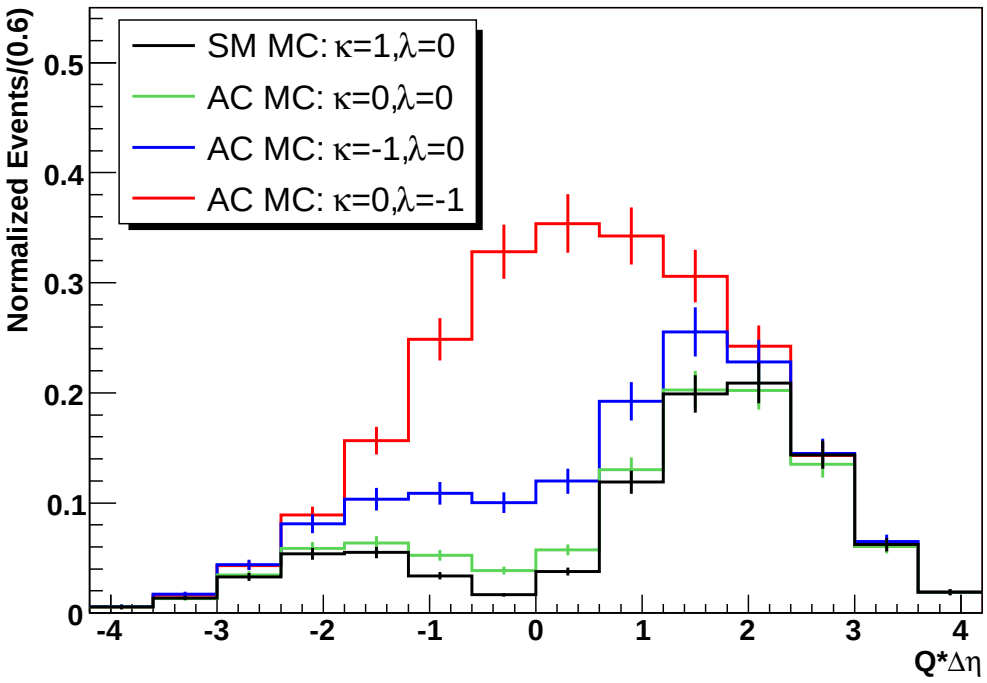

Figure 5.15 The class of shapes expected for the charge-signed rapidity difference. To better illustrate how the shape in the dip region changes with the amount of destructive interference, the distributions have been normalized to have the same number of events in the last bin.

For the shape test, the predicted shapes from the two sets of couplings with ($\kappa = 0, \lambda = -1$) and ($\kappa = -1, \lambda = 0$) are used. Since this is a shape test, the normalization for the two anomalous couplings is allowed to float to produce the best fit with the observed background subtracted data. A plot of the best fits to the observed distribution is shown in Figure 5.16. A χ^2 test that utilizes the covariance matrix is then performed to compare the best fitting distributions to the data. Since the normalization is allowed to float, the uncertainties that are associated with the overall

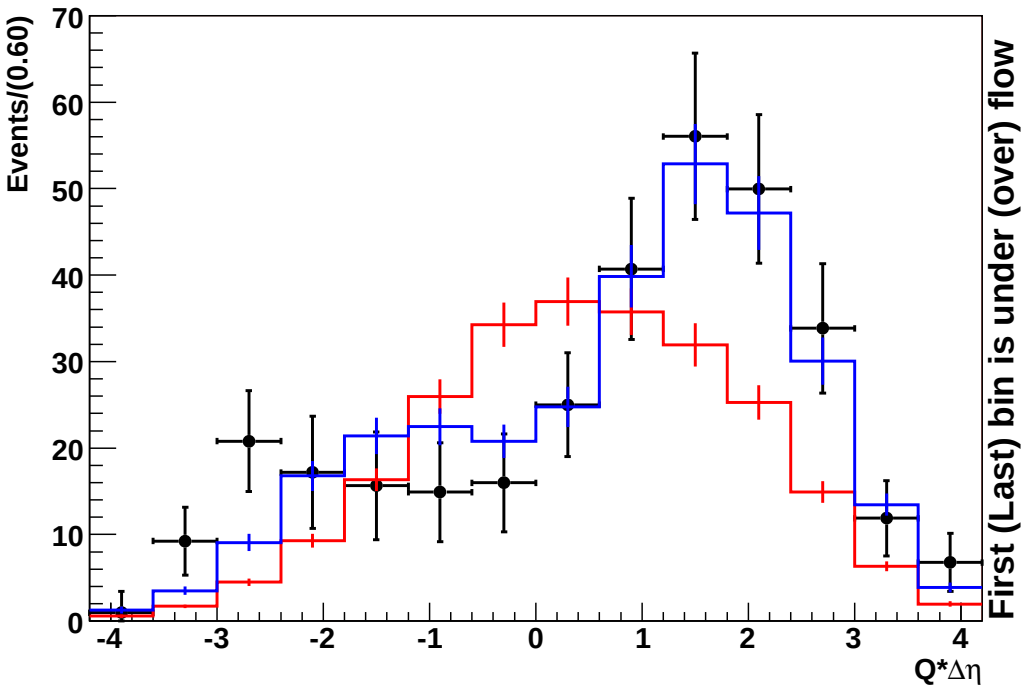

Figure 5.16 Charge-signed rapidity difference for the combine channel background subtracted events. The black points represent the background subtracted data. The errors on the points include the statistical uncertainties and the systematic uncertainties from the background estimate. The blue curve is the fit-normalized Monte Carlo expectation for $(\kappa = -1, \lambda = 0)$. The red curve is the fit-normalized Monte Carlo expectation for $(\kappa = 0, \lambda = -1)$. The uncertainties shown with the Monte Carlo curves are from the systematic error on the signal.

scale (luminosity and cross section) are excluded from the covariance matrix. The unimodal shape with ($\kappa = 0, \lambda = -1$) that would represent the class of shapes with little or no destructive interference is inconsistent with the observed data distribution with a χ^2 of 54 for 13 degrees of freedom. However, the unimodal shape with ($\kappa = -1, \lambda = 0$) that represents a class of shapes with partial destructive interference is consistent with the observed data distribution with a χ^2 of 11 for 13 degrees of freedom. It should be noted that the couplings with ($\kappa = -1, \lambda = 0$) have been ruled out by the photon E_T spectrum.

Dip Test

To obtain a probability that the observed distribution represents a statistical fluctuation from an underlying unimodal distribution, a dip test is used to determine the statistical significance of the depletion of events in the expect region. This test is performed by constructing a histogram of the combined channel candidate events with three equal width bins. The first bin is chosen to sample events from the smaller peak in the distribution. The second bin is chosen to sample events from the dip. The third bin is chosen to sample events from the larger peak of the distribution. The position of the bin edges is determined with SM Monte Carlo (see Figure 5.17). A double Gaussian mixture is fit to the MC events, and the bin width is determined by requiring that all values of the fit that are within the bins that sample the peaks are greater than all values of the fit that are within the bin that samples the dip. The

bin edges are found to be at -2.57, -1.11, 0.35, and 1.81.

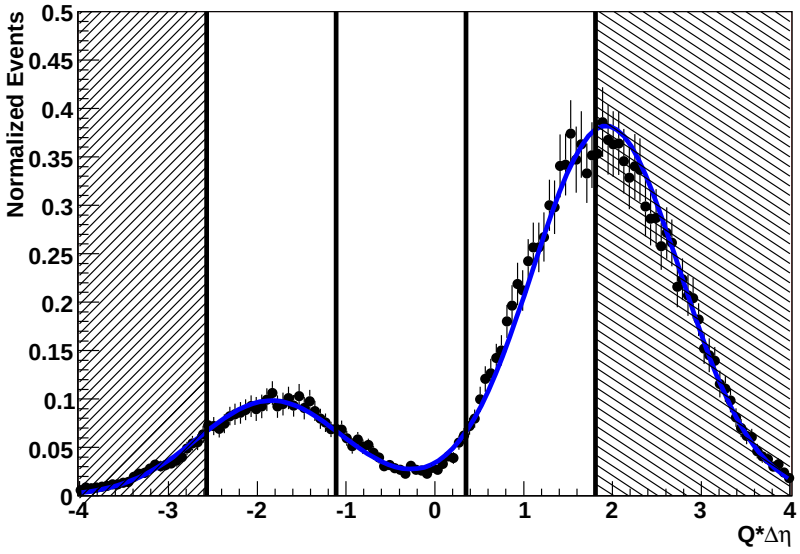

Figure 5.17 The bins used for the dip test. The points represent the charge-signed rapidity difference for the SM predicted combine channel signal events. The curve is a fit to this distribution. The vertical lines represent the selected bin edges.

Define R_1 and R_2 as:

$$R_1 = \frac{N_{dip}}{N_{peak1}} \tag{5.21}$$

$$R_2 = \frac{N_{dip}}{N_{peak2}} \tag{5.22}$$

where N_{peak1} is the number of candidate events in the leftmost bin, N_{dip} is the number of candidate events in the middle bin, and N_{peak2} is the number of candidate events in the rightmost bin. By definition, if $R_1 < 1$ and $R_2 < 1$, then there is a depletion of events in the expected region. R_1 and R_2 are the relevant test statistics for this

method. For the combined channel background subtracted distribution, $R_1 = 0.793 \pm 0.254$ and $R_2 = 0.315 \pm 0.084$ (see Figure 5.18).

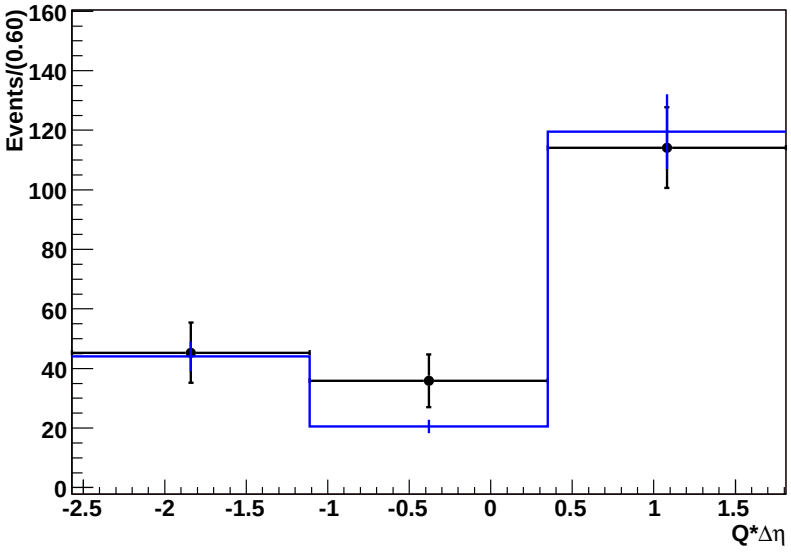

Figure 5.18 The combined channel background subtracted charge-signed rapidity difference for the dip test binning. The points are the background subtracted data events. The errors on the points includes the statistical uncertainty and the systematic uncertainty from background estimate. The blue line is the SM expectation with systematic uncertainties.

Since R_1 has substantially lower significance than R_2, the significance of the dip is determined by R_1 alone to good approximation. Assuming the uncertainty on R_1 is Gaussian, the probability, p, for R_1 to be greater than one (*i.e.* The dip is simply a statistical fluctuation from a unimodal distribution) is calculated by integrating the normal distribution from z to $+\infty$, where z is defined below:

$$z = \frac{1 - R_1}{\sigma_{R_1}} = \frac{1 - 0.793}{0.254} = 0.815 \tag{5.23}$$

p is calculated to be 0.21. Based on this method, the unimodal hypothesis is ruled out at 79% confidence level.

It should be noted that this method will produce a conservative result. The assumption that only the unimodal distributions will have a value of $R_1 > 1$ is not correct. Based on Monte Carlo expectations, in the limiting case ($\kappa = -1, \lambda = 0$), the rapidity distribution is still increasing in the interval between -2.57 and -1.11 and flattens across the region where the dip from the radiation amplitude zero is expected. For this hypothesis N_{peak1} would be less than N_{dip} as demonstrated in Figure 5.19. Furthermore, in order to produce a probability, the ratio-of-bins method depended on the assumption that the test statistic is Gaussian distributed.

To produce a more accurate calculation of the probability, the observed value of R_1 is compared against the expected distribution of values that are obtained from an ensemble of Monte Carlo experiments for both the SM hypothesis and the unimodal hypothesis with ($\kappa = -1, \lambda = 0$). The unimodal hypothesis has been scaled to have the same number of events as the SM expectation. Although the value of the scale will cancel out in the calculation of the ratio, the size of the fractional uncertainty on the ratio will depend on the choice scale. By scaling the unimodal hypothesis to the number of SM events, both sets of ensembles will have comparable fractional uncertainties from the statistical and systematic fluctuations. The resulting distribution of R_1 values for the ensemble of SM Monte Carlo experiments is shown

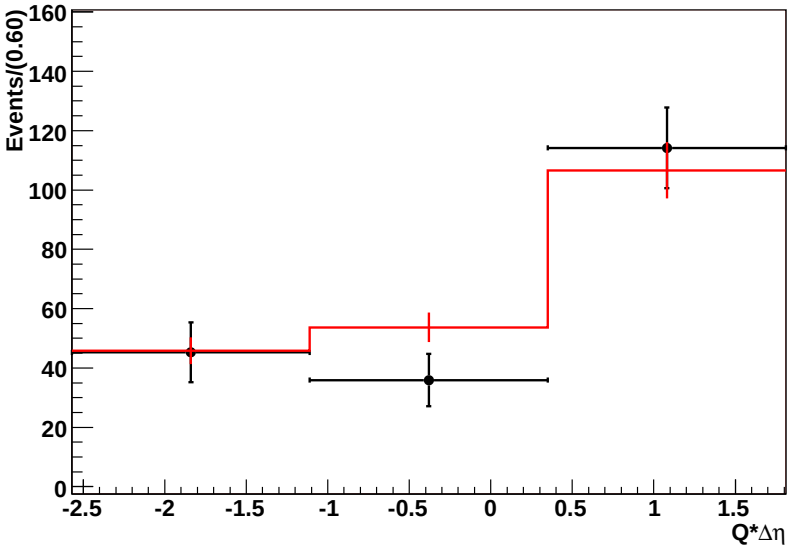

Figure 5.19 The combined channel background subtracted charge-signed rapidity difference for the dip test binning. The points are the background subtracted data events. The errors on the points includes the statistical uncertainty and the systematic uncertainty from background estimate. The red line is the MC expectation for $(\kappa = -1, \lambda = 0)$. The MC has been scaled to produce the best fit with to the full data distribution. The errors shown with the MC are the scaled systematic uncertainties.

in Figure 5.20. 13% of the SM Monte Carlo experiments are expected to produce a value of $R_1 > 0.793$. The resulting distribution of R_1 values for the ensemble of unimodal Monte Carlo experiments is shown in Figure 5.21. 6% of the unimodal Monte Carlo experiments are expected to produce a value of $R_1 < 0.793$. The data is indicative of the bimodal hypothesis, with the unimodal hypothesis being ruled out at the 94% confidence level.

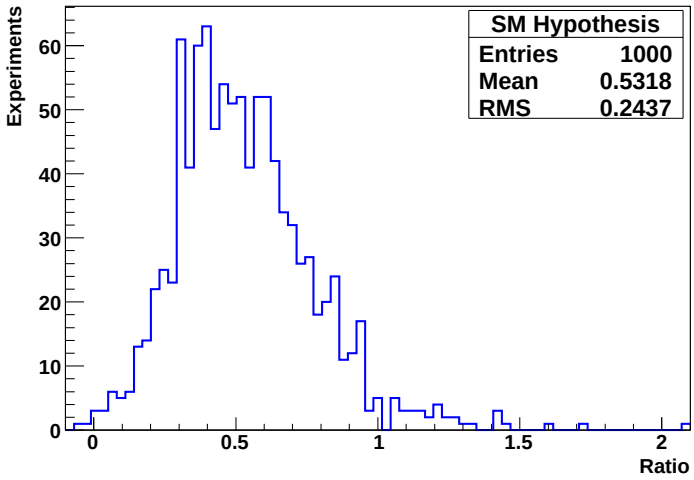

Figure 5.20 The distribution of values of R_1 from the ensemble of SM Monte Carlo experiments.

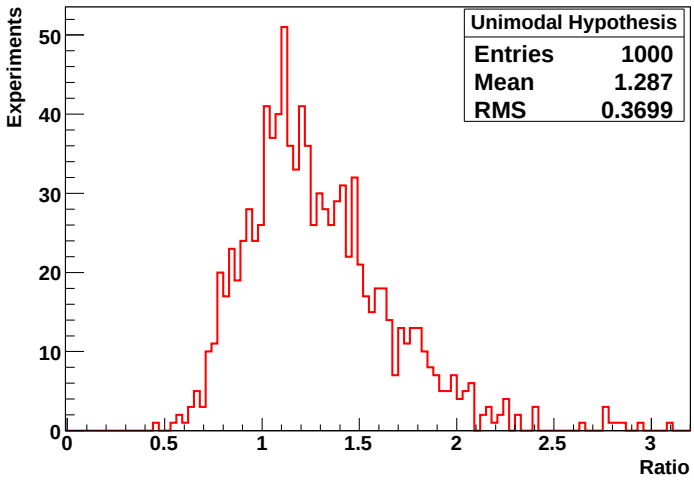

Figure 5.21 The distribution of values of R_1 from the ensemble of unimodal Monte Carlo experiments.

Chapter 6
The Conclusion

The $W\gamma$ production process has been analyzed in two decay modes. The observed production rates are consistent with the Standard Model expectation. The inclusive $p\bar{p} \rightarrow \ell\nu\gamma$ cross section for events with photon $E_T > 11\ GeV$, $\Delta R_{\ell\gamma} > 0.7$, and $M_{T^3} > 90\ GeV$ has been measured. In the electron channel, the observed cross section is measured to be $2.05 \pm 0.18_{stat} \pm 0.10_{sys} \pm 0.13_{lumi}\ pb$. In the muon channel, the observed cross section is measured to be $1.72 \pm 0.19_{stat} \pm 0.15_{sys} \pm 0.10_{lumi}\ pb$.

A search for anomalous $WW\gamma$ couplings has been performed by examining the combined channel photon E_T spectrum. The coupling values with the maximum value of likelihood are found to occur at $(\kappa = 0.485, \lambda = -0.021)$ and $(\kappa = 1.515, \lambda = 0.021)$, however the Standard Model couplings are within the 95% confidence level contour. The contour is shown in Figure 6.1. The one dimensional limits are $-0.18 < \lambda < 0.18$ and $0.16 < \kappa < 1.84$. These are the tightest constraints on the $WW\gamma$ couplings based on the direct observation of $W\gamma$ production. The previous limits were $-0.20 < \lambda < 0.20$ and $0.12 < \kappa < 1.96$ [41].

The observed charge-signed rapidity difference is consistent with the Standard Model prediction. The distribution exhibits a bimodal structure that is indicative of the theoretically expected radiation amplitude zero, with the unimodal hypothesis

being ruled out at the 94% confidence level.

A greater sensitivity to anomalous couplings may be achieved through the application of a photon p_T-dependent K-factor that is based on NLO MC. In this approach, one would forego the use of Pythia MC to apply a momentum boost to the LO Baur MC events, and would instead apply a photon p_T-dependent rescaling to the LO events. This is expected to increase the number of predicted events at the highest photon transverse momentums, and hence will increase the sensitivity to the $WW\gamma$ anomalous coupling values.

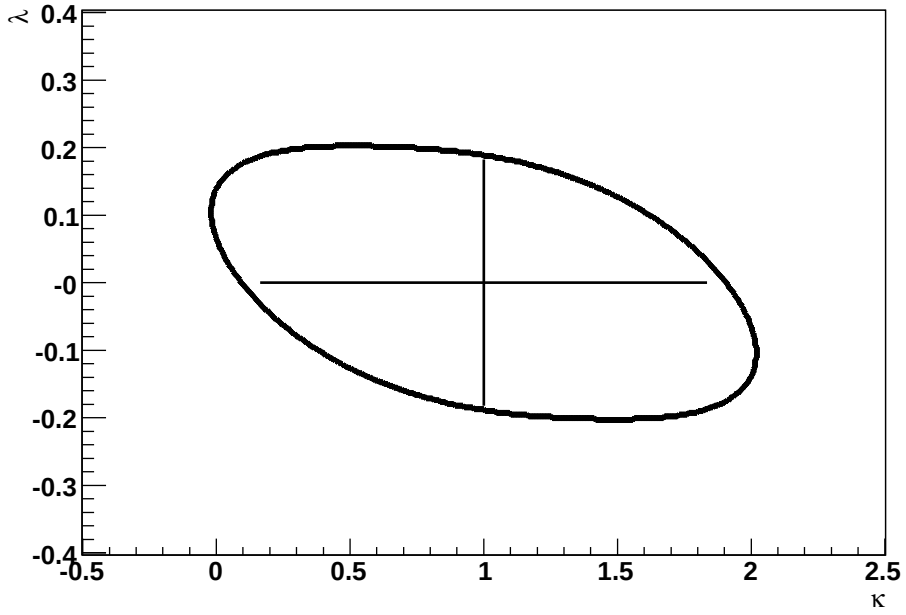

Figure 6.1 $WW\gamma$ couplings limits at 95% CL. The contour represents the two-dimensional limits. The cross hairs represent the one-dimensional limits.

Appendix A
Muon Channel Figures

A.1 Candidate Distributions

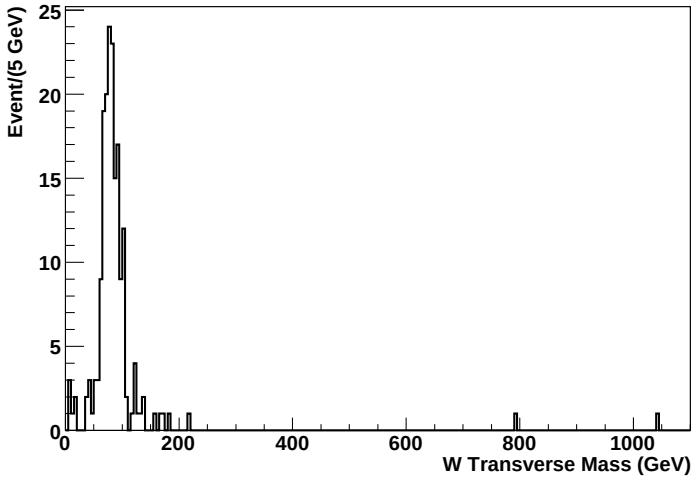

Figure A.1 W transverse mass of the W$\gamma \rightarrow \mu\nu\gamma$ candidates. Not shown is an additional candidate event at 4529 GeV. Additional information about this mismeasured event can be found in Section A.3.

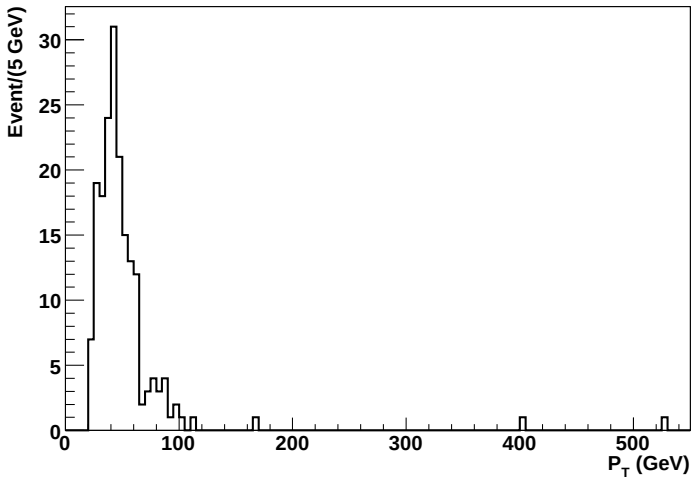

Figure A.2 Track p_T of the W$\gamma \rightarrow \mu\nu\gamma$ candidates. Not shown is an additional candidate event at 2269 GeV.

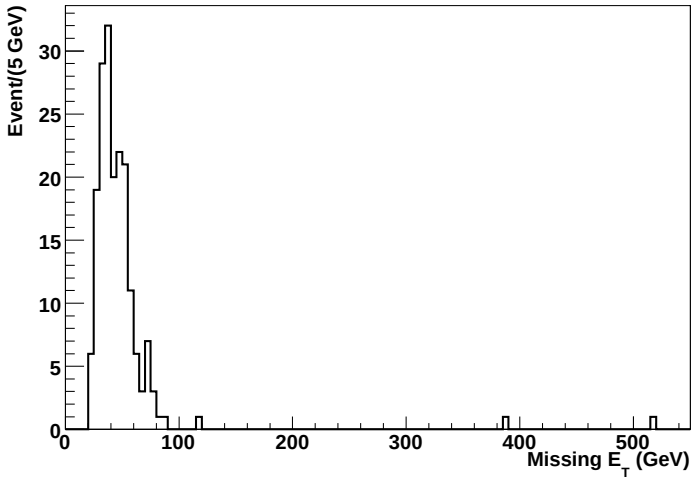

Figure A.3 Missing transverse energy of the W$\gamma \rightarrow \mu\nu\gamma$ candidates. Not shown is an additional candidate event at 2251 GeV.

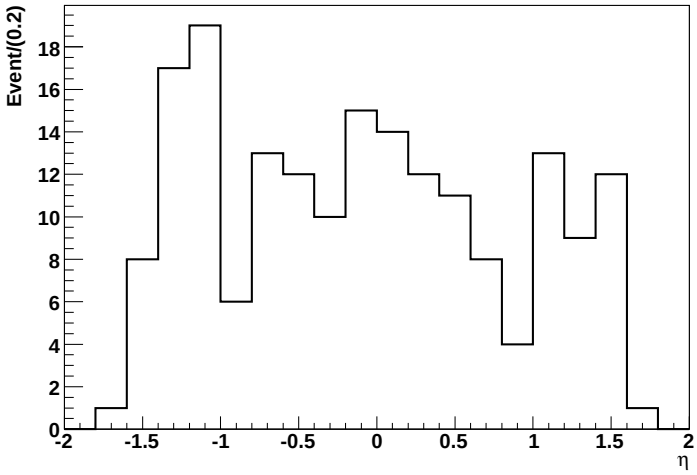

Figure A.4 Track η of the W$\gamma \rightarrow \mu\nu\gamma$ candidates.

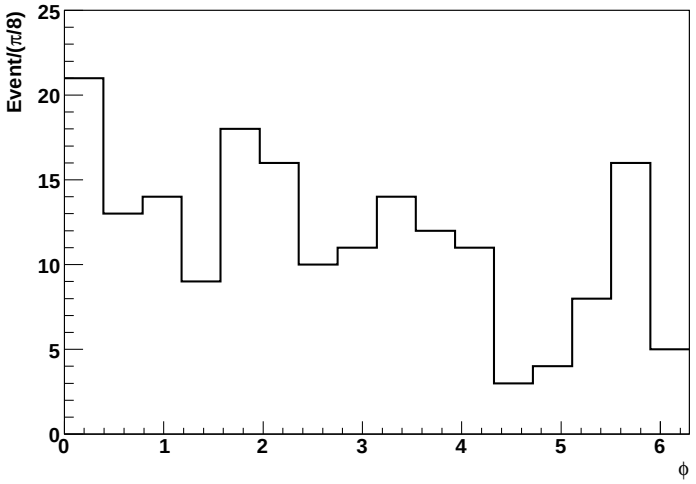

Figure A.5 Track ϕ of the W$\gamma \rightarrow \mu\nu\gamma$ candidates.

A.2 Trigger Efficiencies

The muon triggers are organized by the following run ranges:

- For Run Range: 173482 - 194566:
  - If unprescaled: MUW_A_L2M3_TRK10.
  - Else: MUW_W_L2M3_TRK10.
- For Run Range: 195229 - 195838: MUH1_TK12.
- For Run Range: 195839 - 215670: MUH1_TK12_TLM12.

For the MUW_A_L2M3_TRK10 trigger to be satisfied the following criteria must be met:

- At level-1 there must be at least one muon candidate that passes the tight scintillator and loose wire requirements.*
- At level-2 there must be at least one medium or higher quality muon candidate that has a p_T greater than 3 GeV.
- At level-3 there must be a track from the SMT and CFT subsystems that has a p_T greater than 10 GeV.

*Note trigger objects and associated terminology were introduced in Section 2.3.

The MUW_W_L2M3_TRK10 trigger is similar to the MUW_A_L2M3_TRK10 trigger, but with a more restricted geometric acceptance. At higher instantaneous luminosities, the MUW_A_L2M3_TRK10 trigger is prescaled so that the trigger is randomly inhibited from firing†. When the MUW_A_L2M3_TRK10 trigger is prescaled, the MUW_W_L2- M3_TRK10 trigger is required to fire. For the MUW_W_L2M3_TRK10 trigger to be satisfied, the following criteria must be met:

- At level-1 there must be at least one muon candidate with $|\eta_{MUON^D}| \lesssim 1.5$ that passes the tight scintillator and loose wire requirements.
- At level-2 there must be at least one medium or higher quality muon candidate that has a p_T greater than 3 GeV.
- At level-3 there must be a track from the SMT and CFT subsystems that has a p_T greater than 10 GeV.

The MUH1_TK12_TLM12 and MUH1_TK12 triggers are in fact the same trigger with a different name. For the trigger to be satisfied the following criteria must be met:

- At level-1 there must be at least one L1CTT track with $p_T > 10$ GeV and at least one muon candidate with $|\eta_{MUON^D}| \lesssim 1.5$ that passes the tight scintillator requirement.

†At the lowest prescale level, a trigger is randomly considered for only half of the events.

- At level-2 no restriction is placed on the event.
- At level-3 there must be a central track with p_T greater than 12 GeV that is matched to a muon candidate. The muon candidate is required to satisfy all of the following criteria:
  - It must have at least one A layer scintillator hit
  - It must have at least two A layer wire chamber hits
  - It must have at least one B or C layer scintillator hit
  - It must have at least two wire chamber hits from either the B or C layers or at least one wire chamber hit from both the B and C layers.

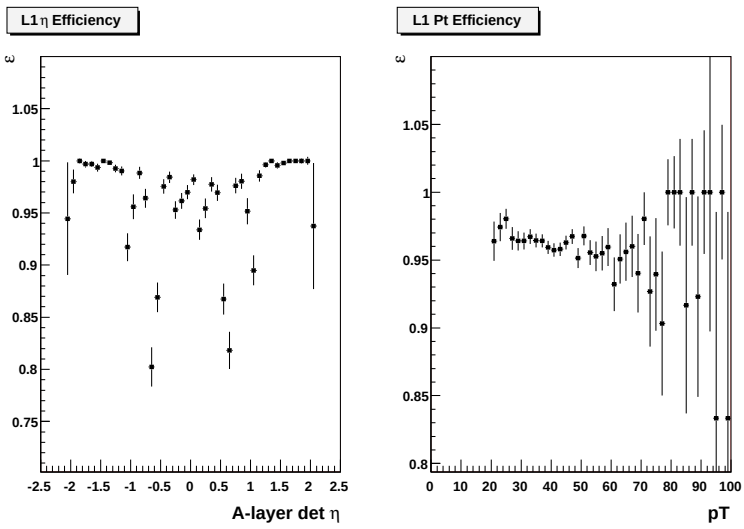

Figure A.6 L1 trigger efficiency for MUW_A_L2M3_TRK10.

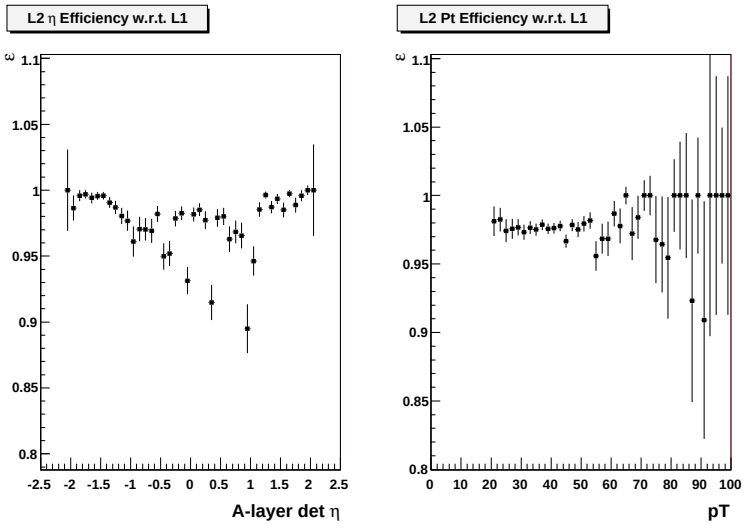

Figure A.7 L2 trigger efficiency for MUW_A_L2M3_TRK10.

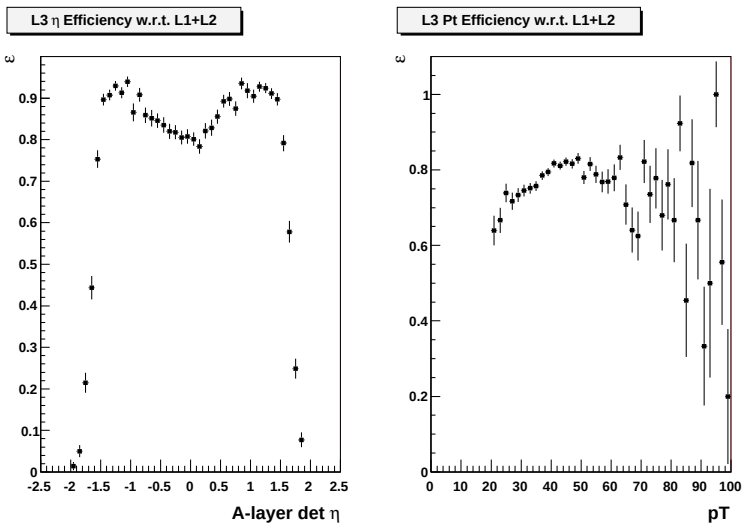

Figure A.8 L3 trigger efficiency for MUW_A_L2M3_TRK10.

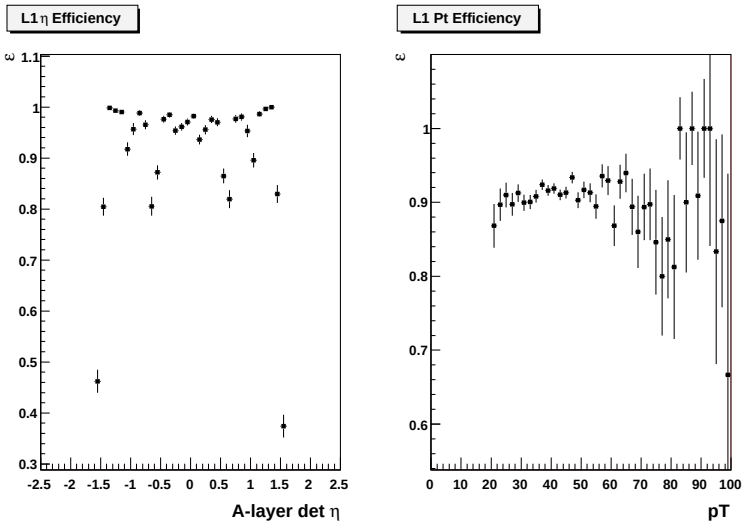

Figure A.9 L1 trigger efficiency for MUW_W_L2M3_TRK10.

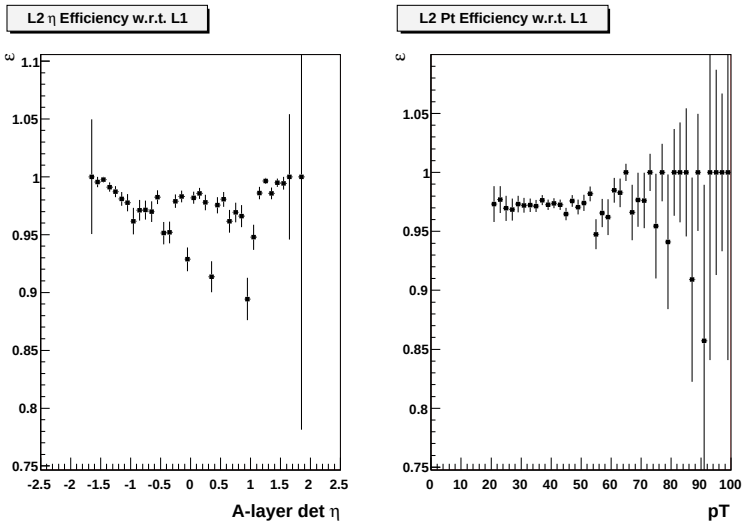

Figure A.10 L2 trigger efficiency for MUW_W_L2M3_TRK10.

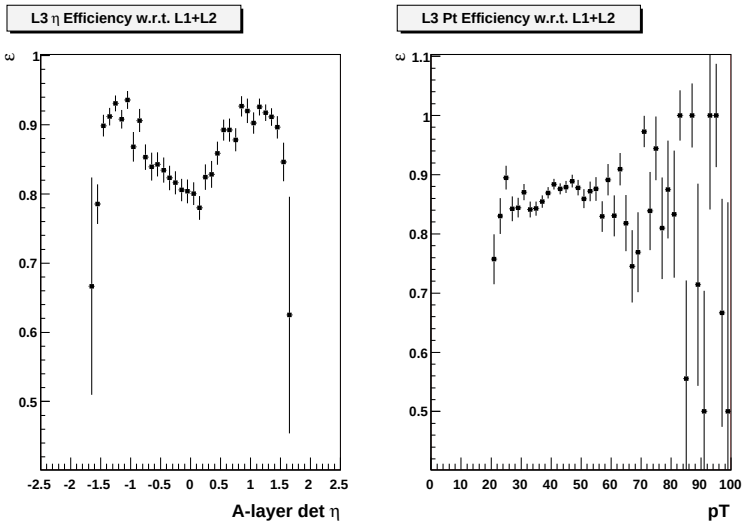

Figure A.11 L3 trigger efficiency for MUW_W_L2M3_TRK10.

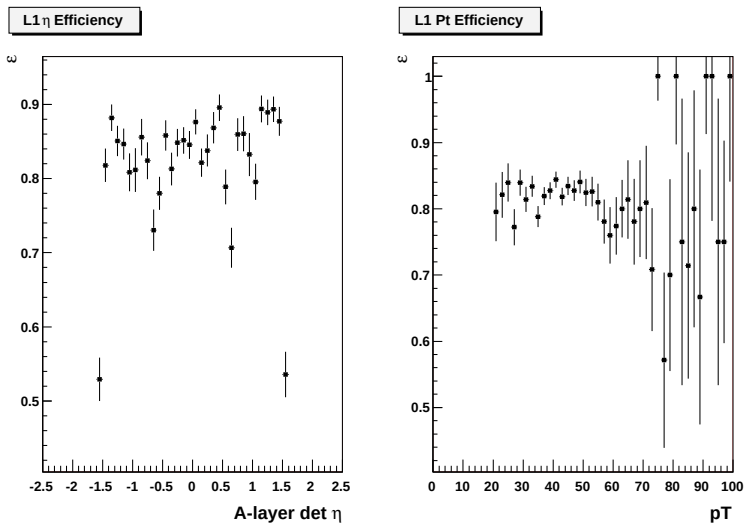

Figure A.12 L1 trigger efficiency for the v13-v14 single muon trigger.

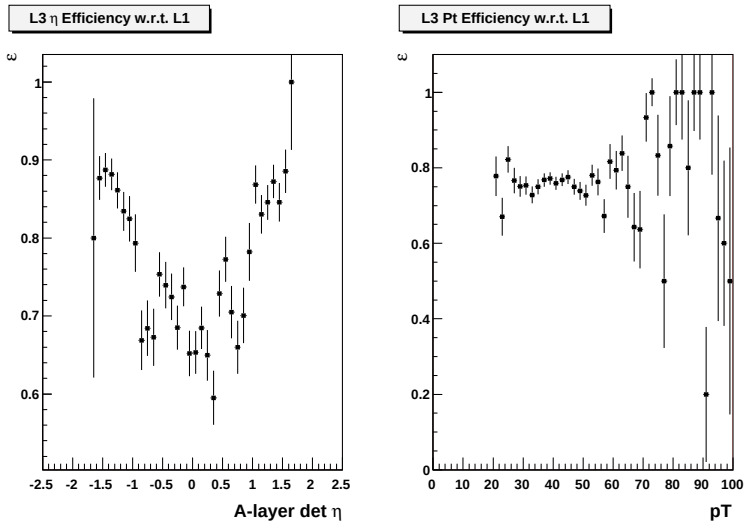

Figure A.13 L3 trigger efficiency for the v13-v14 single muon trigger.

A.3 Mismeasured High p_T Muon Event

Among the selected $W\gamma$ candidates, there is an event with a muon that has a reconstructed track p_T of 2251 GeV. This value of p_T is most likely mismeasured, since the local muon system only measured the transverse momentum to be 14 GeV. Mismeasurement of high p_T tracks is not unexpected and is accounted for in the parameterized Monte Carlo smearing that is described in Section C.1.3. The event corresponds to run number 189561 and event number 42229966. An event display of the event is shown in Figure A.14. This event has the following properties:

- Photon E_T = 15 GeV
- Local muon p_T = 14 GeV
- Number of SMT hits of track = 0
- Track p_T = 2269 GeV
- $\not\!\!E_T$ with only calorimeter corrections = 15 GeV
- $\not\!\!E_T$ with muon track correction = 2251 GeV
- W transverse mass = 4529 GeV

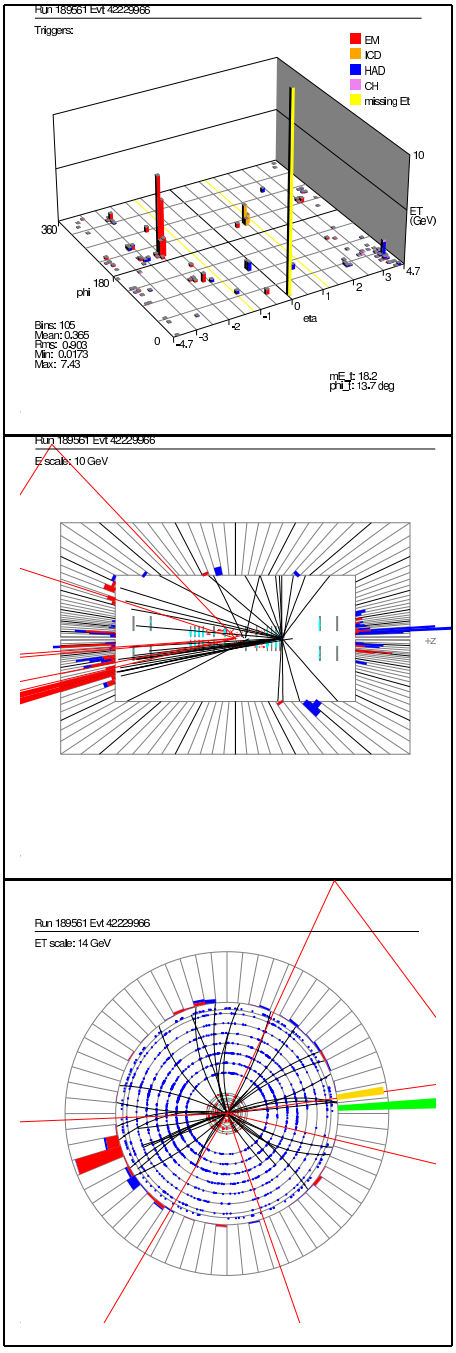

Figure A.14 Event display of event number 42229966 from run number 189561.

Appendix B
Electron Channel Figures

B.1 Candidate Distributions

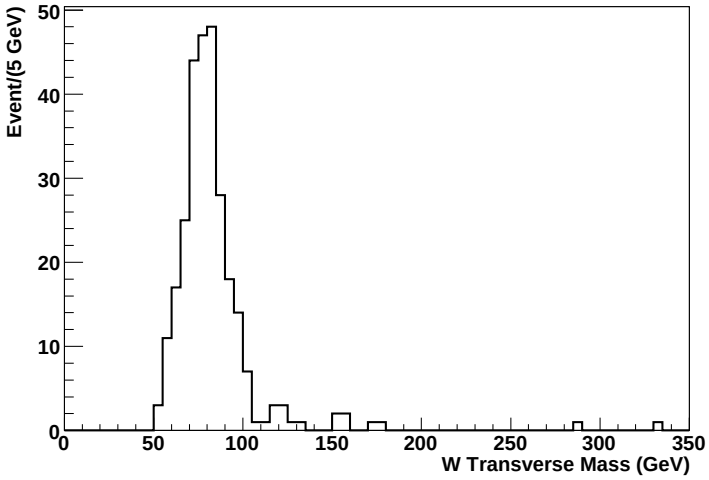

Figure B.1 W transverse mass of the W$\gamma \rightarrow e\nu\gamma$ candidates.

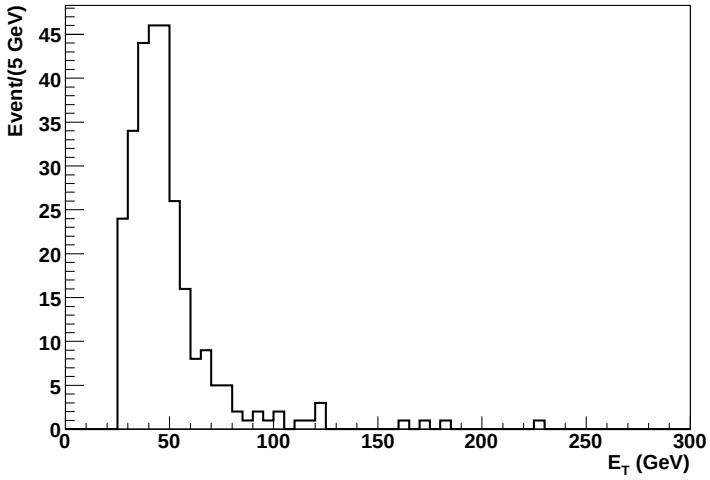

Figure B.2 Calorimeter E_T of the W$\gamma \rightarrow e\nu\gamma$ candidates.

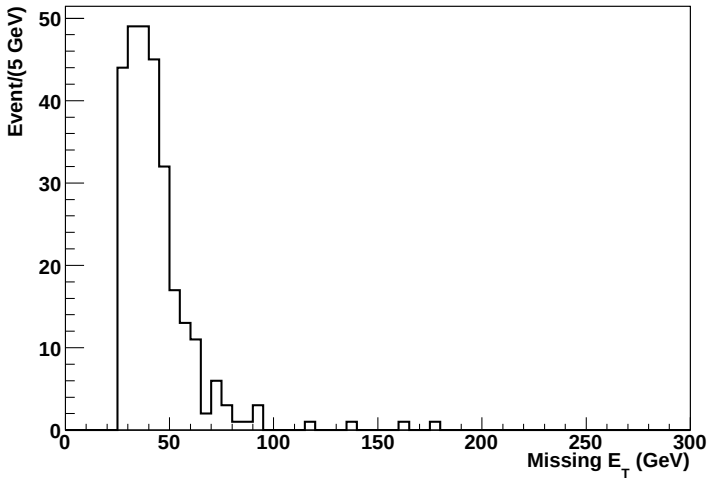

Figure B.3 Missing transverse energy of the W$\gamma \rightarrow e\nu\gamma$ candidates.

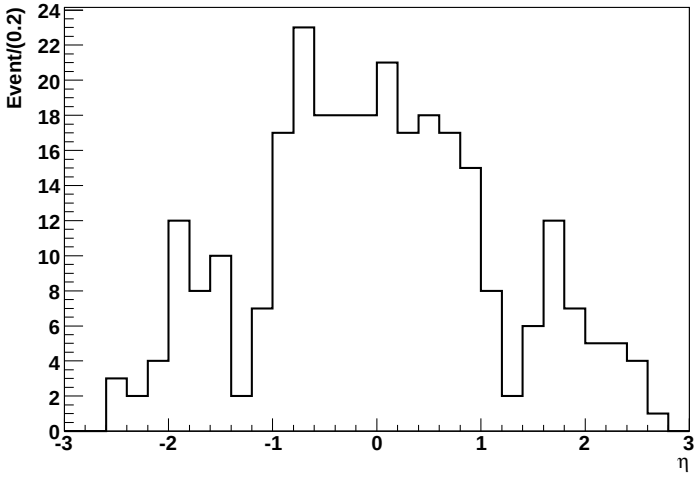

Figure B.4 Track η of the W$\gamma \rightarrow e\nu\gamma$ candidates.

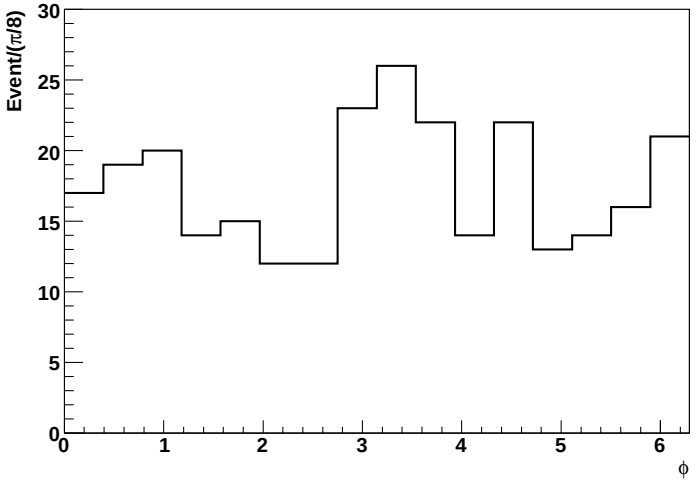

Figure B.5 Track ϕ of the W$\gamma \rightarrow e\nu\gamma$ candidates.

B.2 Trigger Efficiencies

The electron triggers are organized by the following run ranges:

- For Run Range: 174236 - 178720:
  - If unprescaled: EM_HI or EM_HI_SH or EM_HI_2EM5_SH.
  - Else: EM_MX or EM_MX_SH.
- For Run Range: 177313 - 194566:
  - If unprescaled: E1_SH30 or E1_SHT20 or E2_SHT20 or E3_SHT20.
  - Else: E1_SH30 or E1_SHT20.
- For Run Range: 194567 - 208500:
  - If unprescaled: E1_SH30 or E1_SHT22 or E2_SHT22 or E3_SHT22.
  - Else if unprescaled: E1_SH30 or E1_SHT22 or E2_SHT22.
  - Else: E1_SH30 or E1_SHT22.
- For Run Range: 207218 - 215670:
  - E1_SH35 or E1_SHT25 or E1_T13SHT15 or E1_T15SH20 or E3_SH35 or E3_SHT25 or E3_T13SHT15 or E3_T15SH20.

For the EM_HI trigger to be satisfied the following criteria must be met:

- At level-1 there must be at least one trigger tower with EM $E_T > 10\ GeV$.
- At level-2 there must be at least one EM candidate with $E_T > 12\ GeV$.
- At level-3 there must be at least one electron candidate with $E_T > 30\ GeV$. The electron candidate must be consistent with an EM shower, with at least 90% of the energy being deposited in the EM layers.

For the EM_HI_SH trigger to be satisfied the following criteria must be met:

- At level-1 there must be at least one trigger tower with EM $E_T > 10\ GeV$.
- At level-2 there must be at least one EM candidate with $E_T > 12\ GeV$.
- At level-3 there must be at least one electron candidate with $E_T > 20\ GeV$. The electron candidate must have deposited at least 90% of its energy in the EM layer and have a transverse shape that is consistent with an EM shower. Cuts are applied at the first, second, and third EM layers with the cluster shape* being required to be less than 0.09, 0.08, and 0.05 respectively.

For the EM_HI_2EM5_SH trigger to be satisfied the following criteria must be met:

- At level-1 there must be at least two trigger towers with EM $E_T > 5\ GeV$. This permits level-2 to form a two-tower cluster from individual towers that have a lower threshold than the previous triggers.

*The cluster shape or cluster width is an E_T weighted RMS in units of ΔR. In v12 and later versions of the trigger list, the widths are rescaled to account for η dependences and calorimeter cell boundary effects [50].

- At level-2 there must be at least one EM candidate with $E_T > 12\ GeV$.
- At level-3 there must be at least one electron candidate with $E_T > 20\ GeV$. The electron candidate must have deposited at least 90% of its energy in the EM layer and have a transverse shape that is consistent with an EM shower. Cuts are applied at the first, second, and third EM layers with the cluster shape being required to be less than 0.09, 0.08, and 0.05 respectively.

For the EM_MX trigger to be satisfied the following criteria must be met:

- At level-1 there must be at least one trigger tower with EM $E_T > 15\ GeV$.
- At level-2 no restriction is placed on the event.
- At level-3 there must be at least one electron candidate with $E_T > 30\ GeV$. The electron candidate must be consistent with an EM shower, with at least 90% of the energy being deposited in the EM layers.

For the EM_MX_SH trigger to be satisfied the following criteria must be met:

- At level-1 there must be at least one trigger tower with EM $E_T > 15\ GeV$.
- At level-2 no restriction is placed on the event.
- At level-3 there must be at least one electron candidate with $E_T > 20\ GeV$. The electron candidate must have deposited at least 90% of its energy in the

EM layer and have a transverse shape that is consistent with an EM shower. Cuts are applied at the first, second, and third EM layers with the cluster shape being required to be less than 0.09, 0.08, and 0.05 respectively.

The v12 suite of triggers and the v13 suite are very similar, except in two ways. The first is that the v12 suite of triggers does not require a level-2 condition while the v13 suite does. The second is that the E_T thresholds are higher for the v13 triggers. Because of the similarity the triggers are presented together below:

For the E1_SH30 trigger to be satisfied the following criteria must be met:

- At level-1 there must be at least one trigger tower with EM $E_T > 11\ GeV$.
- At level-2 no restriction is placed on the event for the v12 suite of triggers. For the v13 suite of triggers there must be a cluster with EM $E_T > 15\ GeV$
- At level-3 there must be at least one electron candidate with $E_T > 30\ GeV$. The electron candidate must be consistent with an EM shower, with at least 90% of the energy being deposited in the EM layers. In the CC, cuts are applied at the first, second, and third EM layers with the cluster shape being required to be less than 2.3, 1.7, and 1.5 respectively. In the EC, the cluster width of the first, second, and third EM layers are required to be less than 1.4, 1.35, and 1.4 respectively.

For the E1_SHT20 (E1_SHT22) trigger to be satisfied the following criteria must be met:

- At level-1 there must be at least one trigger tower with EM $E_T > 11\ GeV$.
- At level-2 no restriction is placed on the event for the v12 suite of triggers. For the v13 suite of triggers there must be a cluster with EM $E_T > 15\ GeV$
- At level-3 there must be at least one electron candidate with $E_T > 20\ GeV$ for the E1_SHT20 trigger or at least one electron candidate with $E_T > 22\ GeV$ for the E1_SHT22 trigger. The electron candidate must be consistent with an EM shower, with at least 90% of the energy being deposited in the EM layers. In the CC, cuts are applied at the first, second, and third EM layers with the cluster shape being required to be less than 1.8, 1.4, and 1.15 respectively. In the EC, the cluster width of the first, second, and third EM layers are required to be less than 1, 1, and 1.2 respectively.

For the E2_SHT20 (E2_SHT22) trigger to be satisfied the following criteria must be met:

- At level-1 there must be at least two trigger towers with EM $E_T > 6\ GeV$. This permits the higher-level triggers to form a two-tower cluster from individual towers that have a lower threshold than the previous trigger.

- At level-2 no restriction is placed on the event for the v12 suite of triggers. For the v13 suite of triggers there must be a cluster with EM $E_T > 15\ GeV$

- At level-3 there must be at least one electron candidate with $E_T > 20\ GeV$ for the E2_SHT20 trigger or at least one electron candidate with $E_T > 22\ GeV$ for the E2_SHT22 trigger. The electron candidate must be consistent with an EM shower, with at least 90% of the energy being deposited in the EM layers. In the CC, cuts are applied at the first, second, and third EM layers with the cluster shape being required to be less than 1.8, 1.4, and 1.15 respectively. In the EC, the cluster width of the first, second, and third EM layers are required to be less than 1, 1, and 1.2 respectively.

For the E3_SHT20 (E3_SHT22) trigger to be satisfied the following criteria must be met:

- At level-1 there must be at least one trigger tower with EM $E_T > 9\ GeV$ and at least one additional trigger tower with EM $E_T > 3\ GeV$. This permits higher-level triggers to form a two-tower cluster from towers that would not be available from the previous trigger.

- At level-2 no restriction is placed on the event for the v12 suite of triggers. For the v13 suite of triggers there must be a cluster with EM $E_T > 15\ GeV$

- At level-3 there must be at least one electron candidate with $E_T > 20\ GeV$ for

the E3_SHT20 trigger or at least one electron candidate with $E_T > 22\ GeV$ for the E3_SHT22 trigger. The electron candidate must be consistent with an EM shower, with at least 90% of the energy being deposited in the EM layers. In the CC, cuts are applied at the first, second, and third EM layers with the cluster shape being required to be less than 1.8, 1.4, and 1.15 respectively. In the EC, the cluster width of the first, second, and third EM layers are required to be less than 1, 1, and 1.2 respectively.

Among the v14 suite of triggers the terms beginning with "E1_" are identical (except for the level-2 condition) to the corresponding "E3_" trigger terms. Because of the similarity, the "E1_" and "E3_" terms are presented together below:

For the E1_SH35 (E3_SH35) trigger to be satisfied the following criteria must be met:

- At level-1 there must be at least one trigger tower with EM $E_T > 12\ GeV$.
- At level-2 the E1_SH35 trigger requires that there be a cluster with EM $E_T > 15\ GeV$. The E3_SH35 trigger requires that there be an isolated trigger tower with EM $E_T > 11\ GeV$. Isolation is measured with respect to a 3×3 area of trigger towers in $\eta \times \phi$ space that is centered on the seed tower. The EM tower is considered to be isolated if at least 80% of the total energy in the 3×3 area is within the seed EM tower.

- At level-3 there must be at least one electron candidate with $E_T > 35\ GeV$. The electron candidate must be consistent with an EM shower, with at least 90% of the energy being deposited in the EM layers. In the CC, cuts are applied at the first, second, and third EM layers with the cluster shape being required to be less than 2.3, 1.7, and 1.5 respectively. In the EC, the cluster width of the first, second, and third EM layers are required to be less than 1.4, 1.35, and 1.4 respectively.

For the E1_SHT25 (E3_SHT25) trigger to be satisfied the following criteria must be met:

- At level-1 there must be at least one trigger tower with EM $E_T > 12\ GeV$.
- At level-2 the E1_SHT25 trigger requires that there be a cluster with EM $E_T > 15\ GeV$. The E3_SHT25 trigger requires that there be an isolated trigger tower with EM $E_T > 11\ GeV$.
- At level-3 there must be at least one electron candidate with $E_T > 25\ GeV$. The electron candidate must be consistent with an EM shower, with at least 90% of the energy being deposited in the EM layers. In the CC, cuts are applied at the first, second, and third EM layers with the cluster shape being required to be less than 1.8, 1.4, and 1.15 respectively. In the EC, the cluster width of the first, second, and third EM layers are required to be less than 1, 1, and 1.2

respectively.

For the E1_T15SH20 (E3_T15SH20) trigger to be satisfied the following criteria must be met:

- At level-1 there must be at least one trigger tower with EM $E_T > 12\ GeV$.
- At level-2 the E1_ T15SH20 trigger requires that there be a cluster with EM $E_T > 15\ GeV$. The E3_ T15SH20 trigger requires that there be an isolated trigger tower with EM $E_T > 11\ GeV$.
- At level-3 there must be at least one electron candidate with $E_T > 20\ GeV$ that is matched to a track with p_T greater than 15 GeV. The electron candidate must be consistent with an EM shower, with at least 90% of the energy being deposited in the EM layers. In the CC, cuts are applied at the first, second, and third EM layers with the cluster shape being required to be less than 2.3, 1.7, and 1.5 respectively. In the EC, the cluster width of the first, second, and third EM layers are required to be less than 1.4, 1.35, and 1.4 respectively.

For the E1_T13SHT15 (E3_T13SHT15) trigger to be satisfied the following criteria must be met:

- At level-1 there must be at least one trigger tower with EM $E_T > 12\ GeV$.
- At level-2 the E1_T13SHT15 trigger requires that there be a cluster with EM

$E_T > 15\ GeV$. The E3_T13SHT15 trigger requires that there be an isolated trigger tower with EM $E_T > 11\ GeV$.

- At level-3 there must be at least one electron candidate with $E_T > 15\ GeV$ that is matched to a track with p_T greater than 13 GeV. The electron candidate must be consistent with an EM shower, with at least 90% of the energy being deposited in the EM layers. In the CC, cuts are applied at the first, second, and third EM layers with the cluster shape being required to be less than 1.8, 1.4, and 1.15 respectively. In the EC, the cluster width of the first, second, and third EM layers are required to be less than 1, 1, and 1.2 respectively.

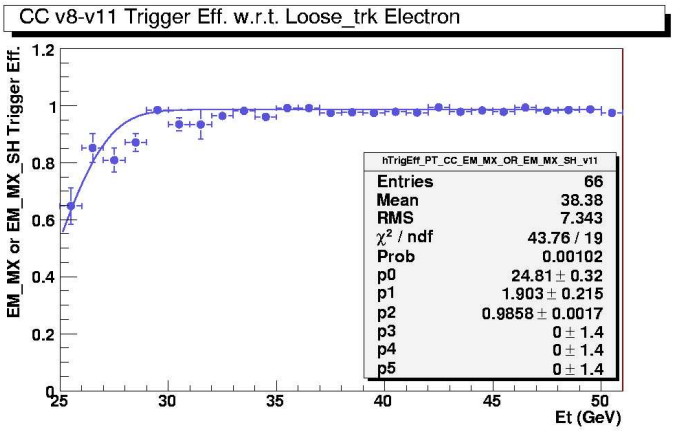

Figure B.6 Central electron trigger efficiency for Group 2 triggers from the pre-v11 and v11 trigger suite.

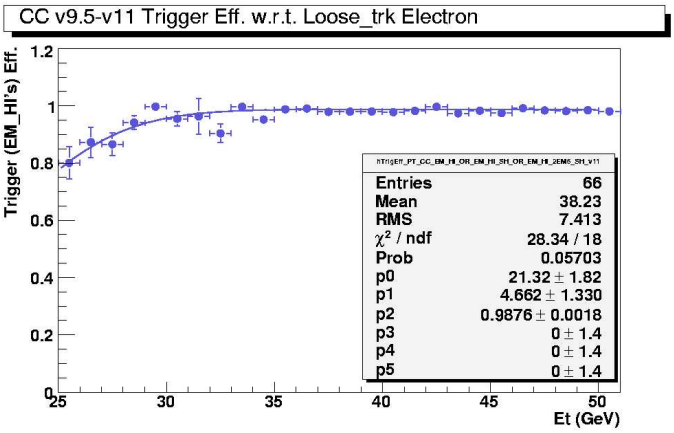

Figure B.7 Central electron trigger efficiency for Group 1 triggers from the pre-v11 and v11 trigger suite.

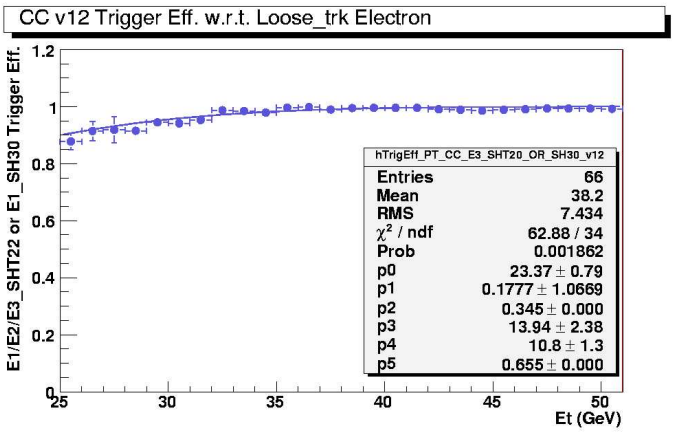

Figure B.8 Central electron trigger efficiency for Group 1 triggers from the v12 trigger suite.

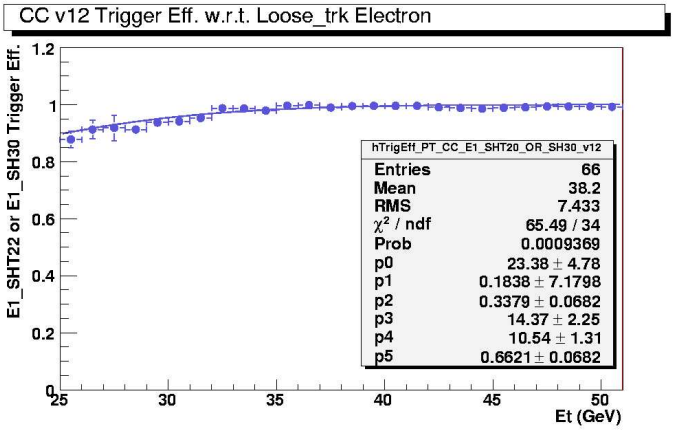

Figure B.9 Central electron trigger efficiency for Group 2 triggers from the v12 trigger suite.

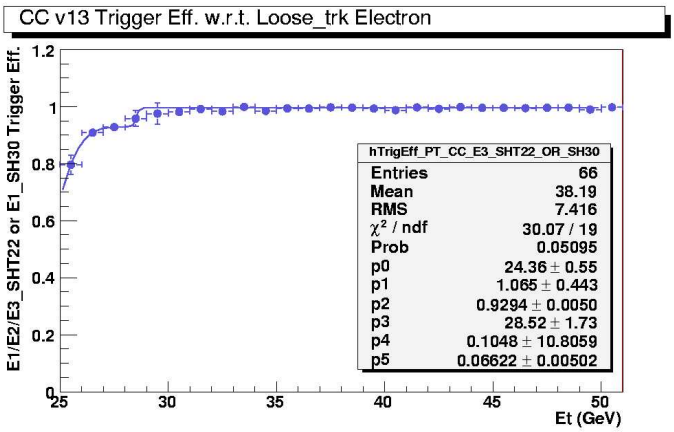

Figure B.10 Central electron trigger efficiency for Group 1 triggers from the v13 trigger suite.

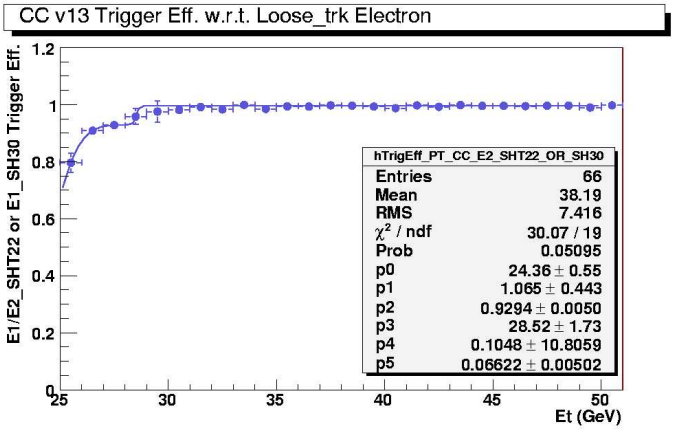

Figure B.11 Central electron trigger efficiency for Group 2 triggers from the v13 trigger suite.

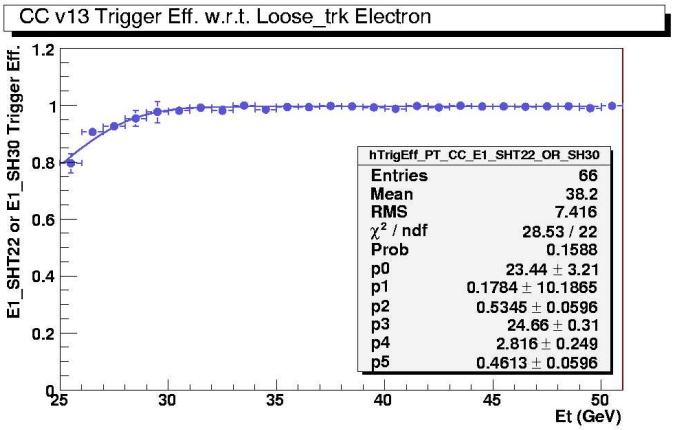

Figure B.12 Central electron trigger efficiency for Group 3 triggers from the v13 trigger suite.

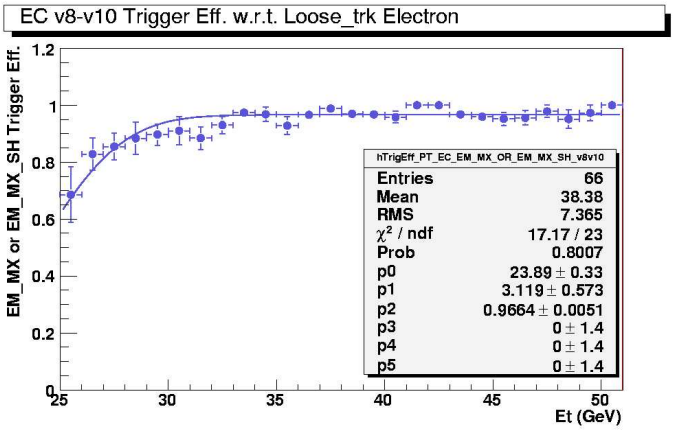

Figure B.13 Forward electron trigger efficiency for Group 2 triggers from the pre-v11 trigger suite.

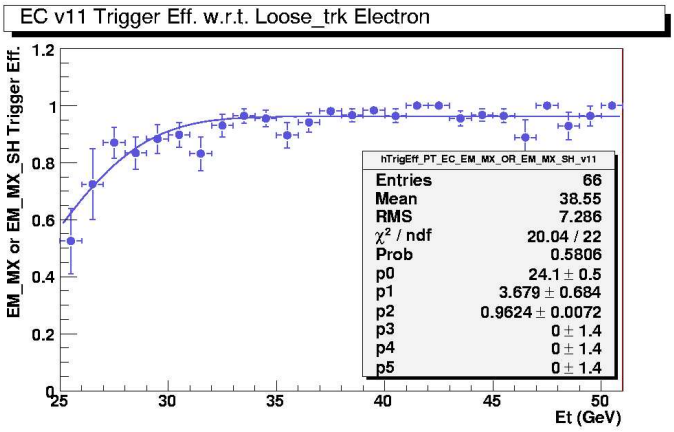

Figure B.14 Forward electron trigger efficiency for Group 2 triggers from the v11 trigger suite.

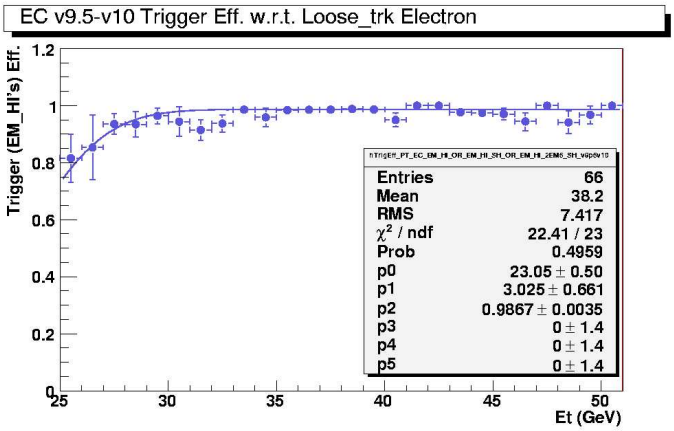

Figure B.15 Forward electron trigger efficiency for Group 1 triggers from the pre-v11 trigger suite.

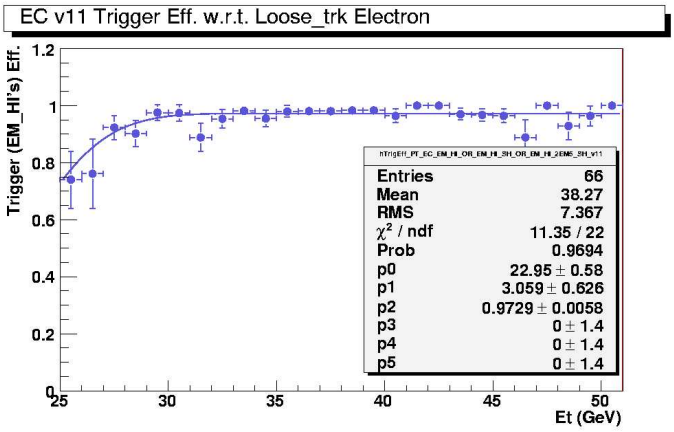

Figure B.16 Forward electron trigger efficiency for Group 1 triggers from the v11 trigger suite.

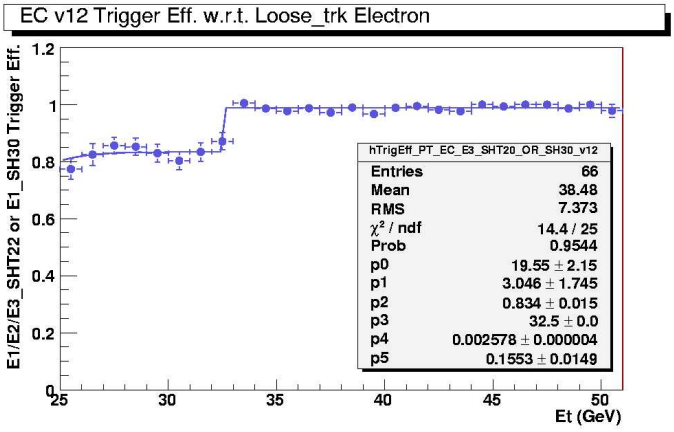

Figure B.17 Forward electron trigger efficiency for Group 1 triggers from the v12 trigger suite.

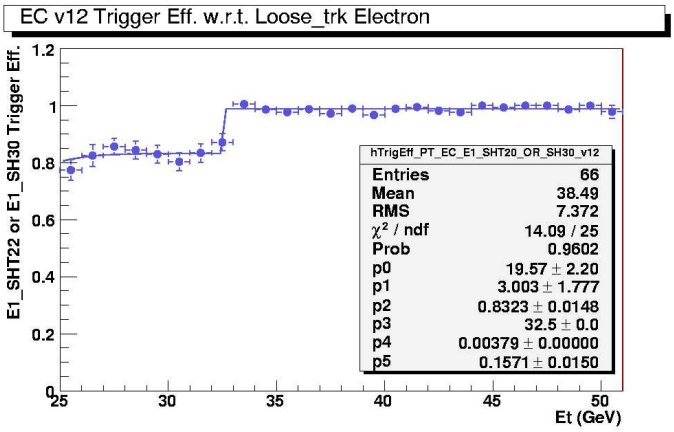

Figure B.18 Forward electron trigger efficiency for Group 2 triggers from the v12 trigger suite.

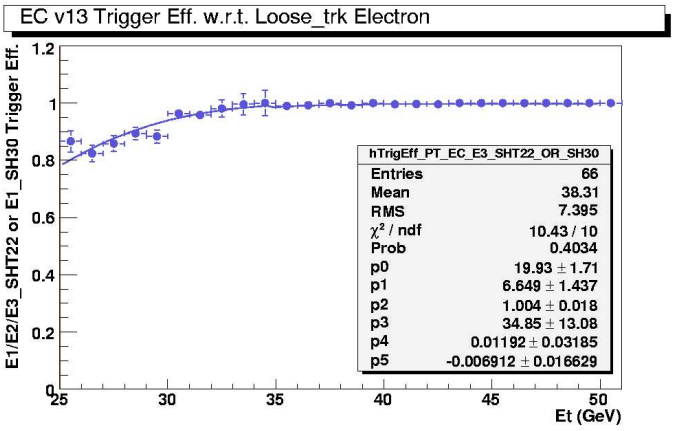

Figure B.19 Forward electron trigger efficiency for Group 1 triggers from the v13 trigger suite.

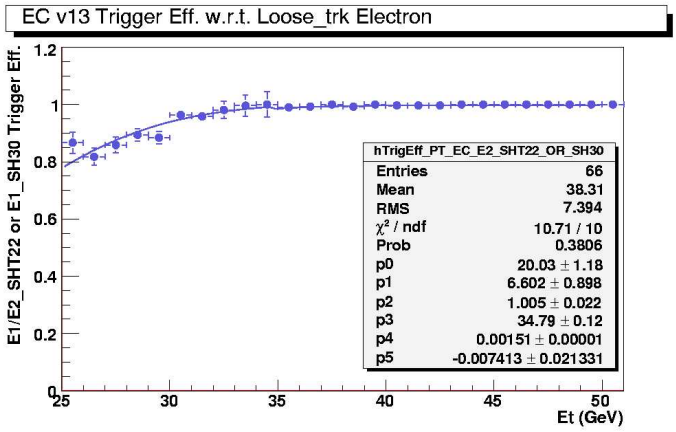

Figure B.20 Forward electron trigger efficiency for Group 2 triggers from the v13 trigger suite.

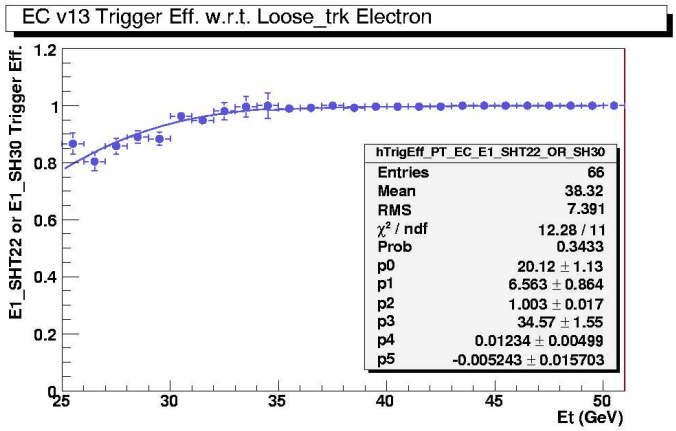

Figure B.21 Forward electron trigger efficiency for Group 3 triggers from the v13 trigger suite.

B.3 Identification Efficiencies

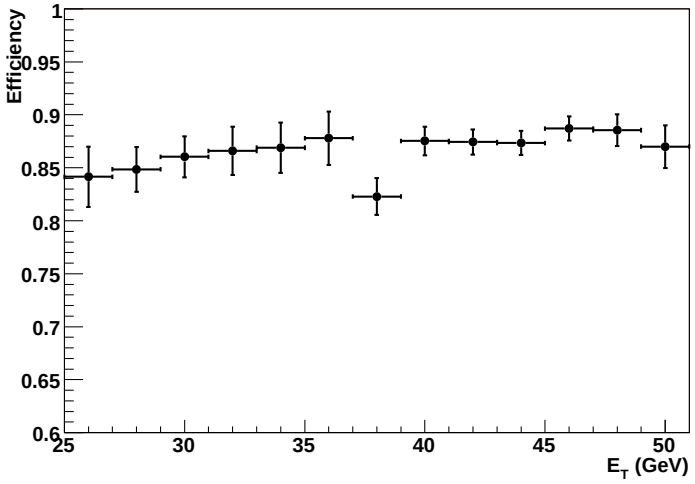

Figure B.22 Electron ID efficiency for $|\eta_{CAL^D}| < 0.1$.

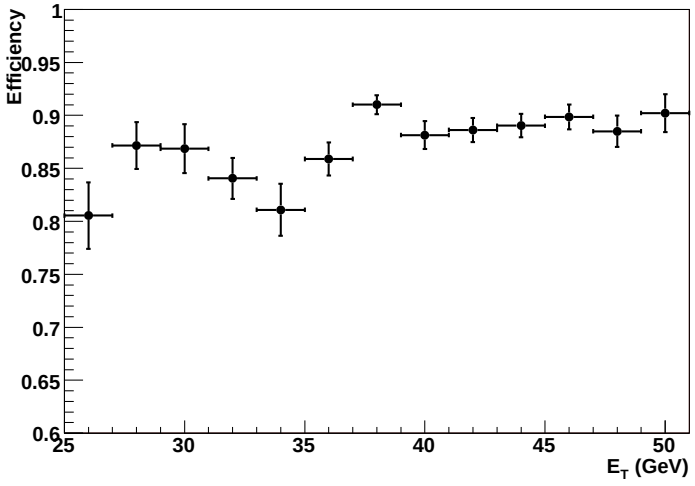

Figure B.23 Electron ID efficiency for $0.1 \leq |\eta_{CAL^D}| < 0.2$.

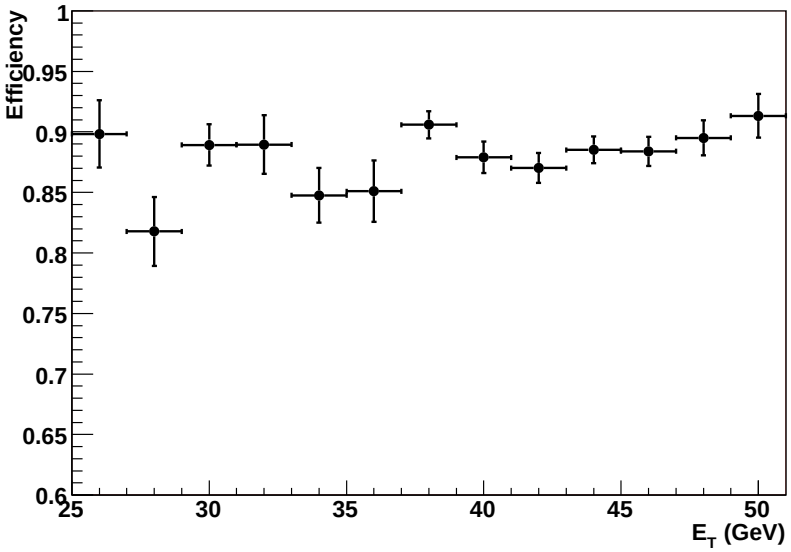

Figure B.24 Electron ID efficiency for $0.2 \leq |\eta_{CALD}| < 0.3$.

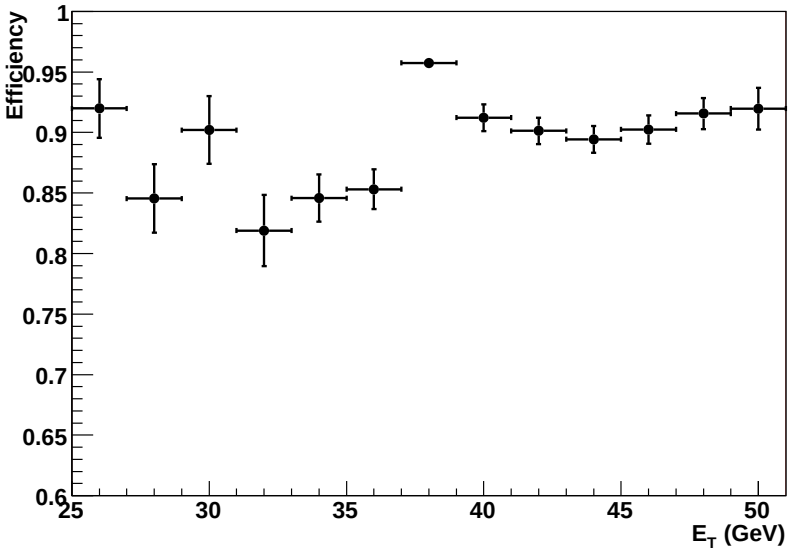

Figure B.25 Electron ID efficiency for $0.3 \leq |\eta_{CALD}| < 0.4$.

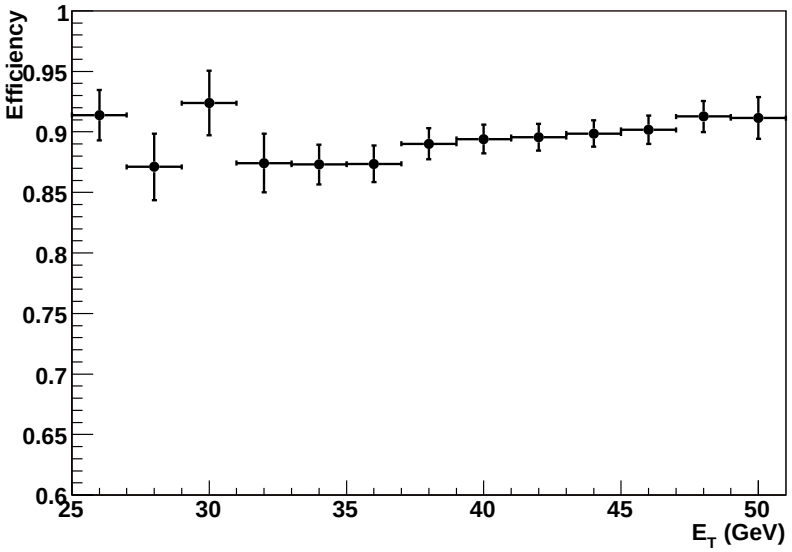

Figure B.26 Electron ID efficiency for $0.4 \leq |\eta_{CAL^D}| < 0.5$.

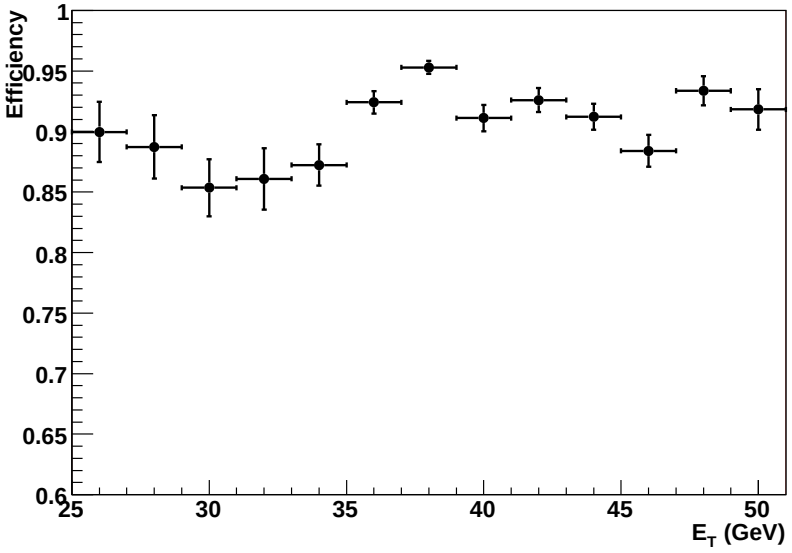

Figure B.27 Electron ID efficiency for $0.5 \leq |\eta_{CAL^D}| < 0.6$.

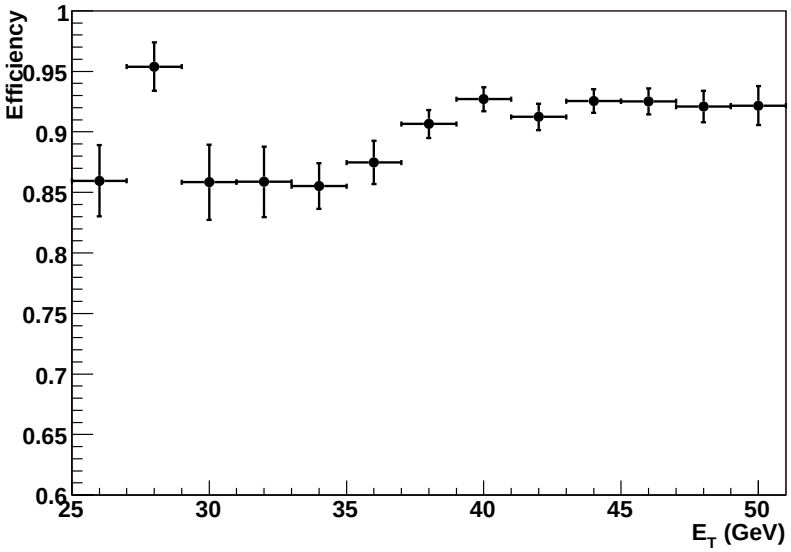

Figure B.28 Electron ID efficiency for $0.6 \leq |\eta_{CALD}| < 0.7$.

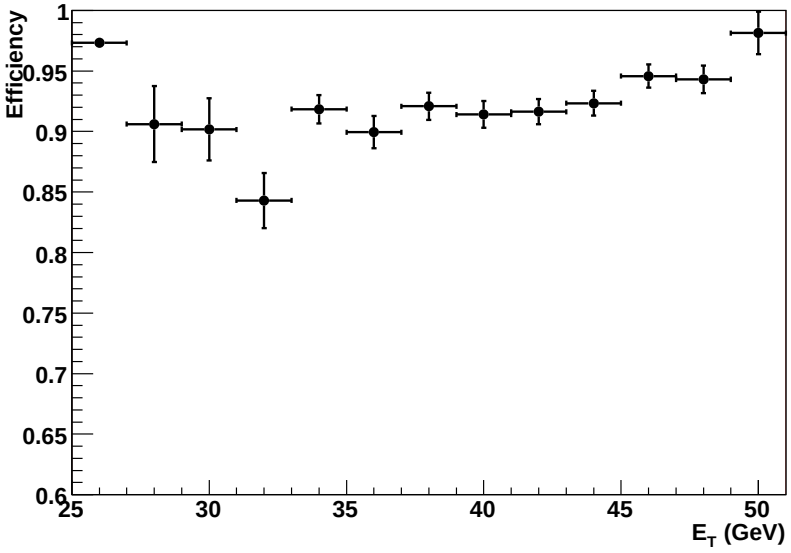

Figure B.29 Electron ID efficiency for $0.7 \leq |\eta_{CALD}| < 0.8$.

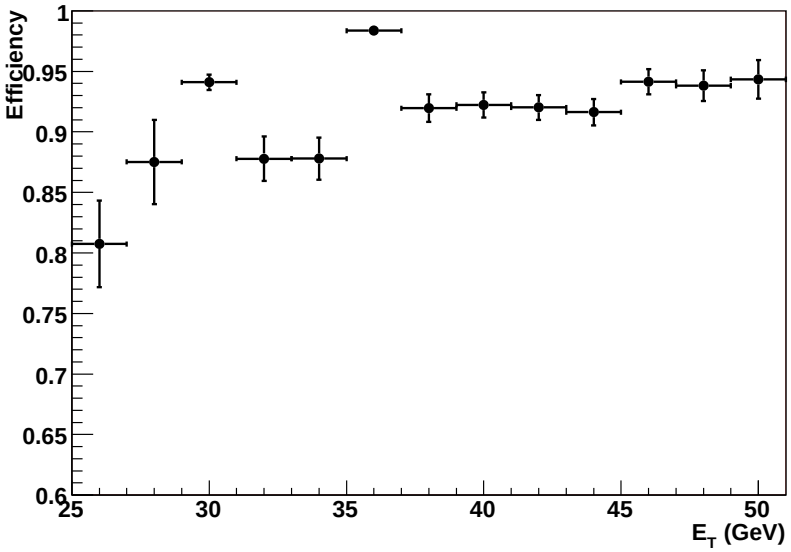

Figure B.30 Electron ID efficiency for $0.8 \leq |\eta_{CALD}| < 0.9$.

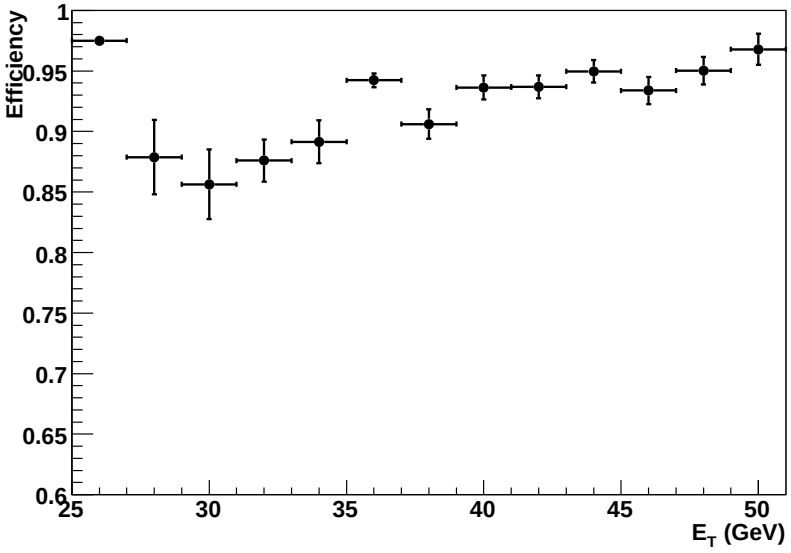

Figure B.31 Electron ID efficiency for $0.9 \leq |\eta_{CALD}| < 1.0$.

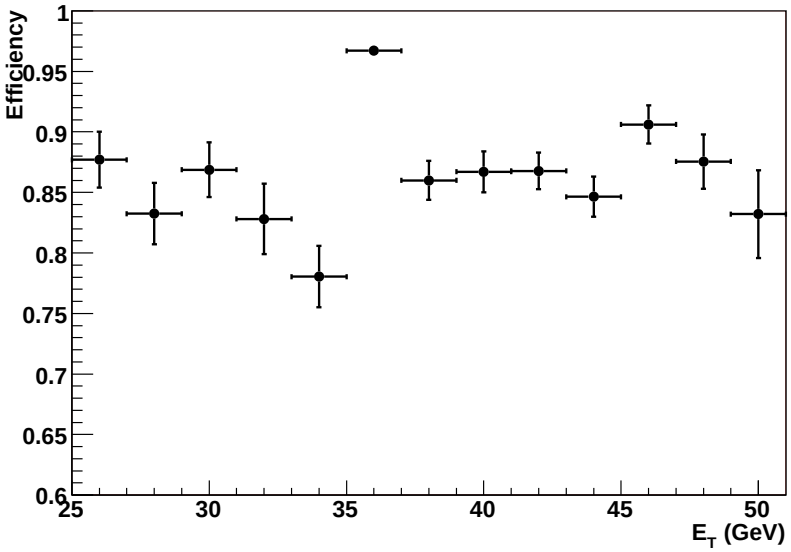

Figure B.32 Electron ID efficiency for $1.5 \leq |\eta_{CALD}| < 1.6$.

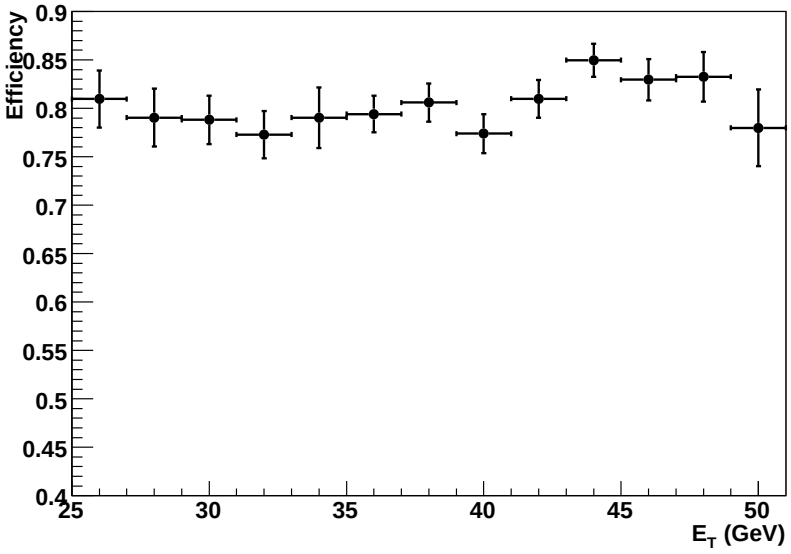

Figure B.33 Electron ID efficiency for $1.6 \leq |\eta_{CALD}| < 1.7$.

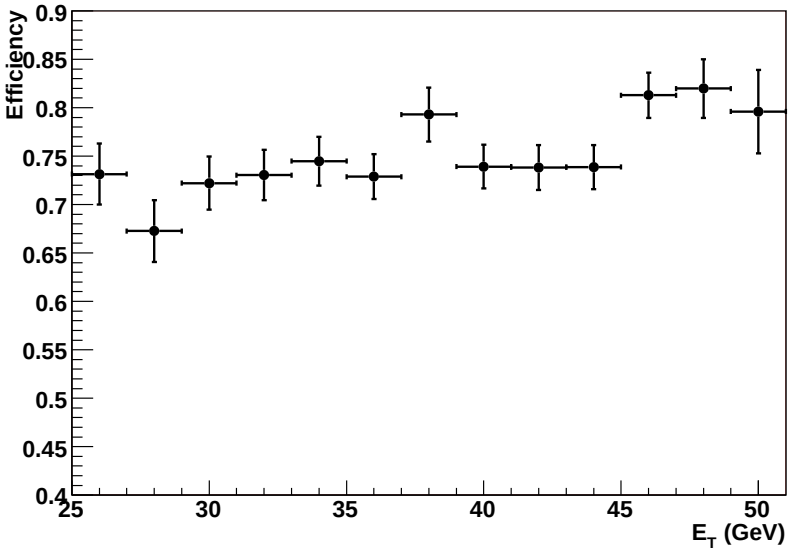

Figure B.34 Electron ID efficiency for $1.7 \leq |\eta_{CAL^D}| < 1.8$.

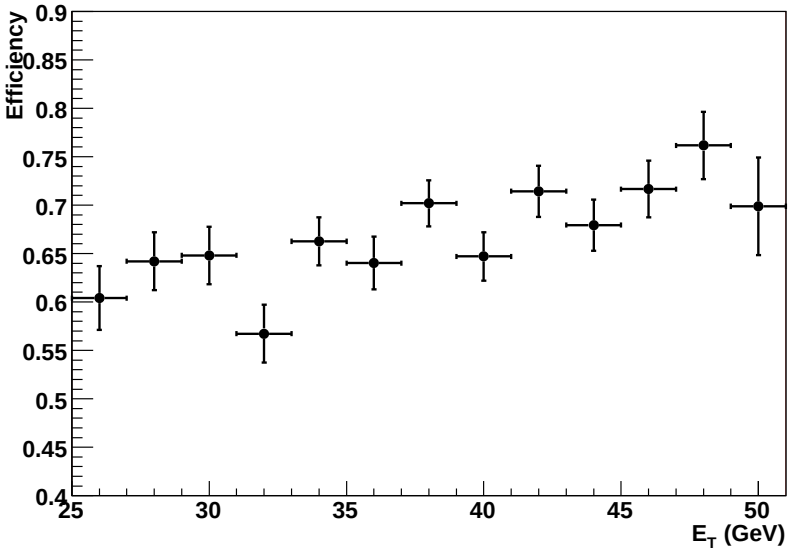

Figure B.35 Electron ID efficiency for $1.8 \leq |\eta_{CAL^D}| < 1.9$.

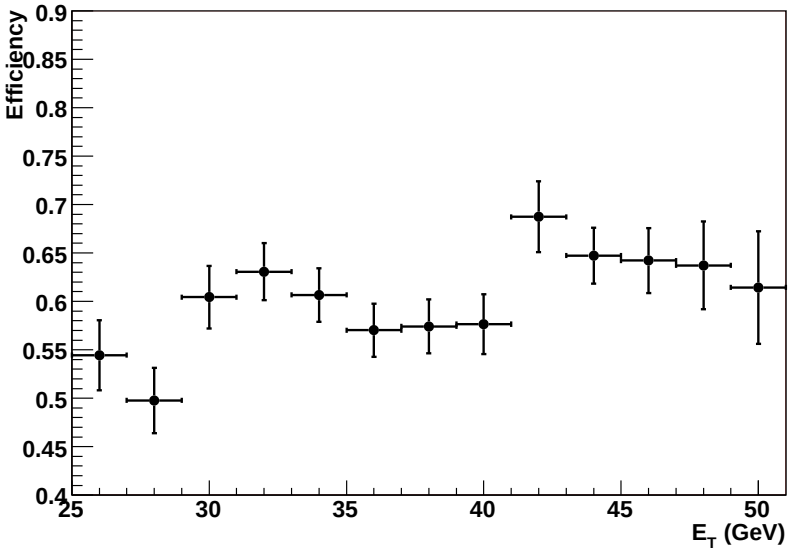

Figure B.36 Electron ID efficiency for $1.9 \leq |\eta_{CAL^D}| < 2.0$.

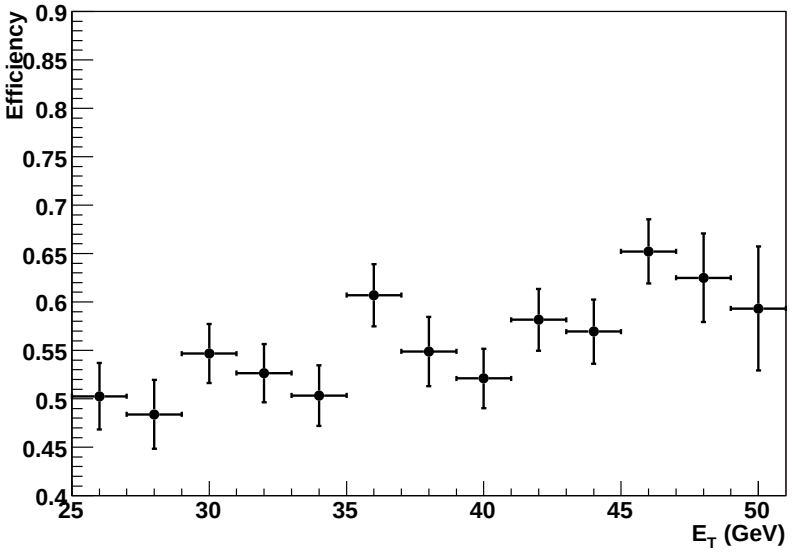

Figure B.37 Electron ID efficiency for $2.0 \leq |\eta_{CAL^D}| < 2.1$.

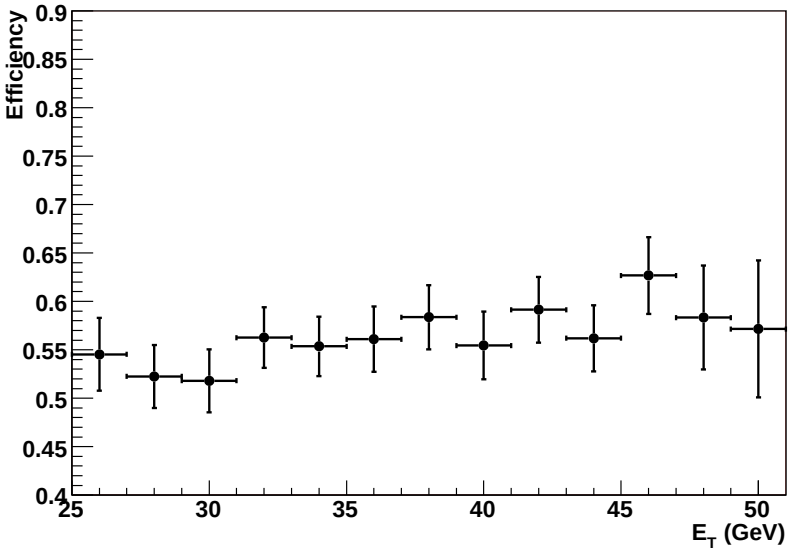

Figure B.38 Electron ID efficiency for $2.1 \leq |\eta_{CAL^D}| < 2.2$.

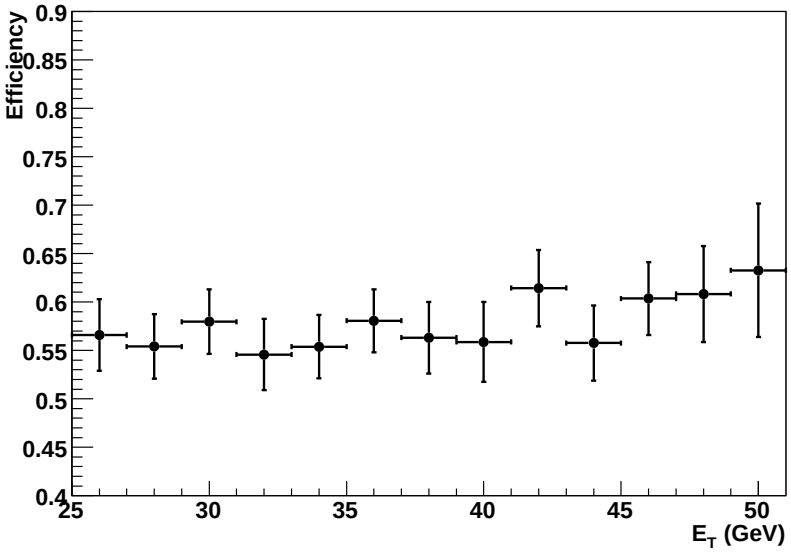

Figure B.39 Electron ID efficiency for $2.2 \leq |\eta_{CAL^D}| < 2.3$.

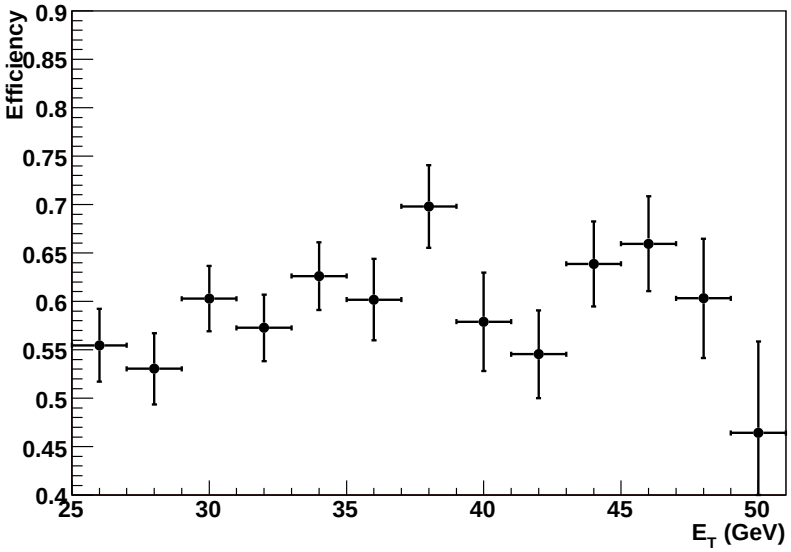

Figure B.40 Electron ID efficiency for $2.3 \leq |\eta_{CAL^D}| < 2.4$.

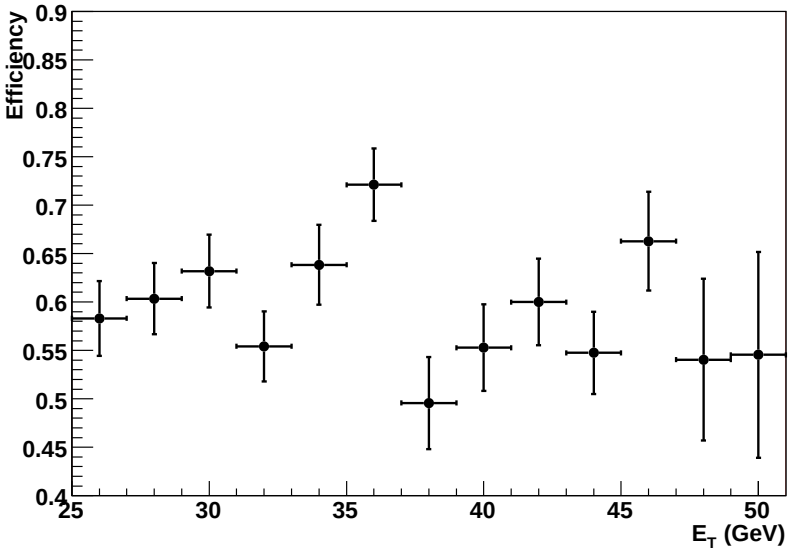

Figure B.41 Electron ID efficiency for $2.4 \leq |\eta_{CAL^D}| < 2.5$.

Appendix C
Additional Analysis Information

C.1 Monte Carlo Smearing Parameters

C.1.1 Calorimeter Energy

For an EM particle with energy, E_{true}, the observed calorimeter energy, $E_{smeared}$, is modeled with the following parameterization:

$$E_{smeared} = E' + (x\sigma_{res}), \tag{C.1}$$

$$E' = (\alpha E_{true}) + \beta. \tag{C.2}$$

Here E' takes into account the calorimeter energy scale (α) and offset (β), x is a random number from a standard normal distribution, and σ_{res} is the energy resolution. The determination of E' and σ_{res} is dependent on the energy and position of the EM particle. The calorimeter is composed of three distinct detectors with one CC detector and two EC detectors, and hence there are three different parameterizations for the three regions.

For the CC, the energy resolution is described by the following equation:

$$\frac{\sigma_{res}}{E'} = \sqrt{C^2 + \frac{N^2}{E'^2} + (\frac{p_0 e^{p_1/sin(\theta)}}{e^{p_1}})^2}, \tag{C.3}$$

where C is a constant term that results from inhomogeneities in the detector response, N is the effect of noise, and the third term is related to sampling fluctuations and is

dependent on the energy and the angle the particle make with respect to the beam line (θ). The parameters p_0 and p_1 are defined below:

$$p_0 = \frac{0.164 \cdot \sqrt{GeV}}{\sqrt{E'}} + \frac{0.122 \cdot GeV}{E'} \tag{C.4}$$

$$p_1 = 1.35193 - \frac{2.09564 \cdot GeV}{E'} - \frac{6.98578 \cdot GeV^2}{E'^2}. \tag{C.5}$$

For the EC detectors, the energy resolution is described by the following equation:

$$\frac{\sigma_{res}}{E'} = \sqrt{C^2 + \frac{N^2}{E'^2} + [p \times (\frac{s_0 \cdot \sqrt{GeV}}{\sqrt{E'}} + \frac{s_1 \cdot GeV}{E'})/(\frac{s_0}{\sqrt{45.0}} + \frac{s_1}{45.0})]^2}, \tag{C.6}$$

where C and N have the same physical interpretation as before, and the third term is related to sampling fluctuations. The values of p, s_0, and s_1 are different for the two endcaps. For the calorimeter located at positive values of the z-coordinate the terms are defined as:

$$s_0 = 0.217 + 0.003|\eta| - 0.007|\eta^2|, \tag{C.7}$$

$$s_1 = 57.247 - 104.577|\eta| + 71.148|\eta^2| - 21.127|\eta^3| + 2.306|\eta^4|, \tag{C.8}$$

$$\begin{aligned} p &= 14.808 - 53.358|\eta| + 80.874|\eta^2| - 66.687|\eta^3| + 32.331|\eta^4| \\ &- 9.222|\eta^5| + 1.434|\eta^6| - 0.094|\eta^7|. \end{aligned} \tag{C.9}$$

For the calorimeter located at negative values of the z-coordinate the terms are defined as:

$$s_0 = 0.221 - 0.025|\eta| + 0.002|\eta^2|, \tag{C.10}$$

$$s_1 = 9.479 - 21.201|\eta| + 17.503|\eta^2| - 6.027|\eta^3| + 0.734|\eta^4|, \quad \text{(C.11)}$$

$$p = -9.507 + 27.044|\eta| - 31.337|\eta^2| + 19.008|\eta^3| - 6.364|\eta^4|$$
$$+ 1.115|\eta^5| - 0.080|\eta^6|. \quad \text{(C.12)}$$

The values of α, β, C, and N are given in Table C.1.

$\boldsymbol{\alpha}$		
	CC	1.0002 ± 0.0003
	−EC	1.0004 ± 0.0010
	+EC	0.9987 ± 0.0008
$\boldsymbol{\beta}$		
	CC	(0.324 ± 0.017) GeV
	−EC	(-0.207 ± 0.123) GeV
	+EC	(-0.233 ± 0.233) GeV
$\boldsymbol{C}$		
	CC	0.028 ± 0.001
	−EC	0.033 ± 0.002
	+EC	0.038 ± 0.002
$\boldsymbol{N}$		(0.4 ± 0.4) GeV*

Table C.1 Calorimeter energy smear parameters.

C.1.2 Missing Transverse Energy

The missing transverse energy is calculated from the smeared p_T of the charged-lepton, the photon, the recoil jet from the Pythia boost, the **underlying event**, and **multiple interactions**. The transverse momentum from the underlying event and

*For this analysis a conservative error a conservative error value is accessed on this term with minimal impact.

multiple interactions is modeled with the following parameterization:

$$p_x(u.e.) = p_{under}x, \tag{C.13}$$

$$p_y(u.e.) = p_{under}y, \tag{C.14}$$

where $p_x(u.e.)$ is the x-component of the transverse momentum, $p_y(u.e.)$ is the y-component of the transverse momentum, x and y are random numbers from a standard normal distribution and $p_{under} = 3.183 \pm 0.04\ GeV$.

The smeared transverse momentum, $p_{T_{smeared}}(recoil)$, of the true recoil jet transverse momentum, $p_{T_{true}}(recoil)$, is modeled with the following parameterization:

$$p_{T_{smeared}}(recoil) = p'_T(recoil) + \sigma_{recoil}z, \tag{C.15}$$

$$p'_T(recoil) = p_{T_{true}}(recoil)\alpha_{recoil}, \tag{C.16}$$

$$\frac{\sigma_{recoil}}{p'_T(recoil)} = \sqrt{C^2_{recoil} + \frac{S^2_{recoil}}{p'_T(recoil)}}, \tag{C.17}$$

$$p_{x_{smeared}}(recoil) = p_{T_{smeared}}(recoil)\cos(\phi_{recoiljet}), \tag{C.18}$$

$$p_{y_{smeared}}(recoil) = p_{T_{smeared}}(recoil)\sin(\phi_{recoiljet}), \tag{C.19}$$

where z is a random number from a standard normal distribution. The value of the constant term (C_{recoil}), the sampling term (S_{recoil}), and the energy scale (α_{recoil}) are given in Table C.2.

$\boldsymbol{\alpha_{recoil}}$	0.67 ± 0.02
$\boldsymbol{C_{recoil}}$	0.05 ± 0.01
$\boldsymbol{S_{recoil}}$	$(0.80 \pm 0.20)\ \sqrt{GeV}$

Table C.2 $\not\!\!E_T$ smear parameters.

The smearing for the muon transverse momentum comes from the tracking resolution which is discussed in the next section. The smearing on the photon and electron transverse energy follows from the EM particle smearing that is provided in the previous section. It is also necessary to include a 3 GeV correction for the electrons in the sample:

$$p_x(bias) = 3\cos(\phi_{electron})GeV, \tag{C.20}$$

$$p_y(bias) = 3\sin(\phi_{electron})GeV, \tag{C.21}$$

The smeared $\not\!\!E_T$ measurement is calculated with the following equations:

$$\not\!\!E_x = -(p_{x_{smeared}}(recoil) + p_x(u.e.) + p_{x_{smeared}}(lepton) + p_{x_{smeared}}(photon) + p_x(bias)), \tag{C.22}$$

$$\not\!\!E_y = -(p_{y_{smeared}}(recoil) + p_y(u.e.) + p_{y_{smeared}}(lepton) + p_{y_{smeared}}(photon) + p_y(bias)), \tag{C.23}$$

C.1.3 Track Momentum

For a charged particle with transverse momentum, $p_{T_{true}}$, the observed track transverse momentum, $p_{T_{smeared}}$, is modeled with the following parameterization:

$$p^{-1}_{T_{smeared}} = \alpha_{track} \times (p^{-1}_{T_{true}} + \sigma_{res} x), \tag{C.24}$$

$$\sigma_{res} = \sqrt{C^2_{track} + \frac{S^2_{track}\cosh(\eta)}{p^2_{T_{true}}}}, \tag{C.25}$$

where x is random number from a standard normal distribution and α_{track} is a scale factor. The first term in the resolution is a result of the detector spatial resolution for the hits, while the second term arises from particle scattering in the tracking medium. The values of α_{track}, C_{track}, and S_{track} are provided in Table C.3.

$\boldsymbol{\alpha_{track}}$	0.9921 ± 0.0099
$\boldsymbol{C_{track}}$	$(0.00267 \pm 0.00020)\ GeV^{-1}$
$\boldsymbol{S_{track}}$	0.0258 ± 0.0008

Table C.3 Tracking smear parameters.

C.1.4 Muon Momentum

The momentum resolution of the muon spectrometer is less precise than the measurement from the central tracker. For a muon with transverse momentum, $p_{T_{true}}$, the observed transverse momentum, $p_{T_{smeared}}$, as measured by the muon spectrometer is modeled with the following parameterization:

$$p^{-1}_{smeared} = p^{-1}_{true} + \sigma_{res} x, \tag{C.26}$$

$$\sigma_{res} = \sqrt{C^2_{muon} + \frac{[\alpha_{muon} \times (p_{true} - \beta_{muon})]^2}{p^4_{true}}}, \tag{C.27}$$

The first term in the resolution is a result of the detector spatial resolution. The second term arises from the muon scattering in the muon detector. The offset, β_{muon}, is introduced to model energy loss that occurs before the muon eneters the muon spectrometer. The muon smear parameters are provided in Table C.4.

$\boldsymbol{\alpha_{muon}}$		
	Central	.3621 ± 0.0376
	Forward	.2108 ± 0.0101
$\boldsymbol{\beta_{muon}}$		
	Central	(3.089 ± 0.2048) GeV
	Forward	(1.785 ± 0.1557) GeV
$\boldsymbol{C_{muon}}$		
	Central	(0.0314 ± 0.00297) GeV^{-1}
	Forward	(0.00575 ± 0.00048) GeV^{-1}

Table C.4 Muon smear parameters.

C.1.5 Vertex Position

The hadronic collisions occur near the center of the DØ detector with an RMS that varies from 20−30 cm in the z-coordinate. The spread in the collision vertex varies with the instantaneous luminosity of the collider with the least spread occurring at the highest instantaneous luminosities. The vertex distribution has been studied in [51], and the distributions corresponding to the maximum observed spread and the minimum observed spread are shown in Figures C.1 and C.2. The z-position of the

collision vertex will affect the event acceptance. To estimate the overall effect, the Monte Carlo events are produced with the vertex distribution that has the minimal observed spread and the vertex distribution that has the maximal observed spread. The average values for the resulting acceptance and event distributions are used in the model predictions, and the variation with choice of vertex distribution is included in the systematic errors.

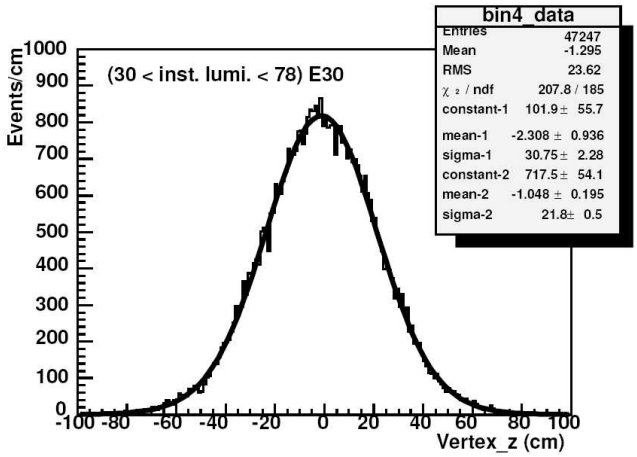

Figure C.1 Minimal spread in the z-vertex position of DØ collisions. [51]

C.1.6 Position

The measured η and ϕ position of the photon depends on the calorimeter spatial resolution while the position measurement of the lepton takes advantage of the more precise central tracker. For the charge-signed rapidity difference, the effect of the calorimeter resolution will dominate the tracking position resolution. For the EM

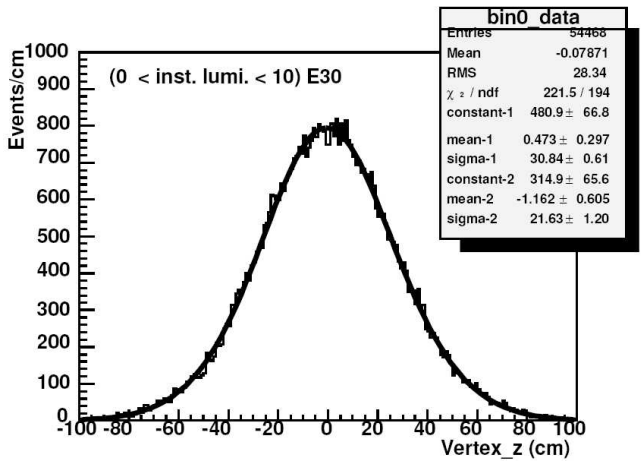

Figure C.2 Maximal spread in the z-vertex position of DØ collisions. [51]

objects, the calorimeter η resolution is 0.0073 $\pm$ 0.0035 in the CC and 0.0029 $\pm$ 0.0035* in the EC. For the EM objects, the calorimeter ϕ resolution is 0.0070 $\pm$ 0.0034 in the CC and 0.0041 $\pm$ 0.0034† in the EC.

C.1.7 Charge Misidentification

The observed charge-signed rapidity difference will be altered if the track that is associated with the charged-lepton is reconstructed with the opposite sign. To estimate this effect, it is necessary to measure the chare misidentification rate for a muon and an electron. Earlier analyses, [52] and [53], have study the charge misidentification rate for muons and electrons. For the muon study, the charge misidentification rate was found for muons that passed the same selection requirements as the $W\gamma$

*For this analysis a conservative error value is accessed on this term with minimal impact.

†For this analysis a conservative error value is accessed on this term with minimal impact.

analysis and was shown to be (1.62 ± 0.04)%. However, the electron analysis measured the misidentification rate for a different set of selection criteria, hence for this analysis it is necessary to remeasure the electron charge misidentification rate for the appropriate set of selection criteria.

To measure the electron charge misidentification rate, a sample of $Z \rightarrow ee$ events is collected from the collider data. The events are selected by requiring that there be two electromagnetic objects with $E_T > 15\ GeV$ in the fiducial region of the calorimeter. One of the electrons (the probe) must pass the $W\gamma$ selection criteria, while the other (the tag) must pass the following set of tight track quality cuts:

- There must be 16 hits in the CFT.
- There must be at least 4 hits in the SMT.
- The χ^2 must be smaller than 3.
- $0.8 > \frac{E_{CAL}}{P_{trk}} > 1.2$.

Charge conservation demands that the electrons have opposite charges. If the tracks have the same sign then it is assumed that charge from the lower quality track must have been mismeasured. The fraction of misidentified tracks is found as a function of η and is shown in Figure C.3. The observed misidentification rate is consistent with the measurements from [52] and [53].

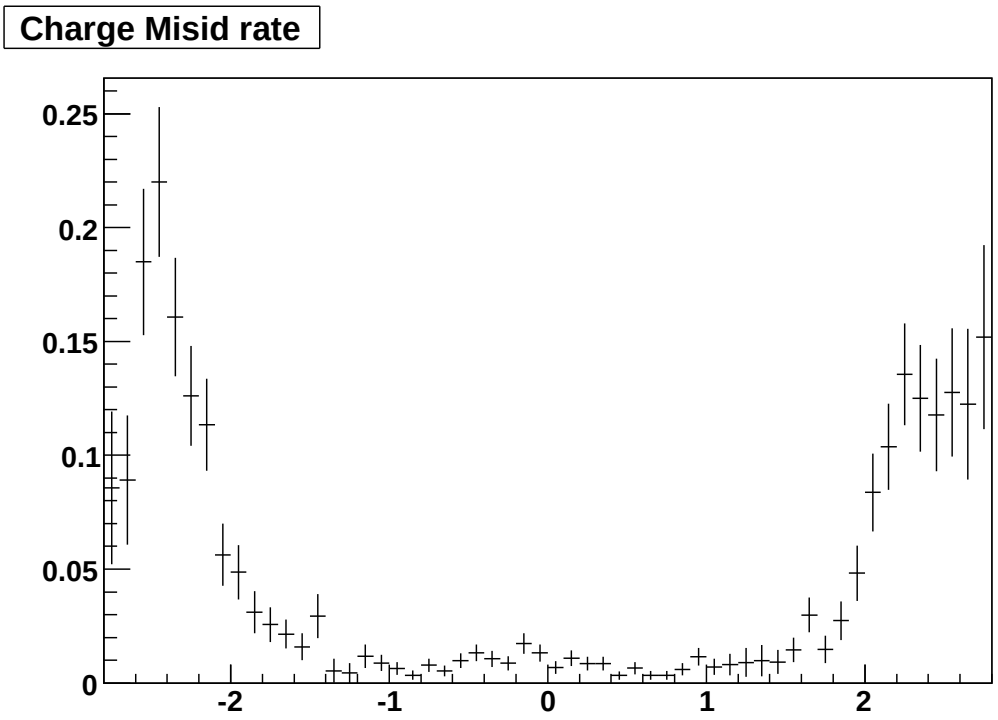

Figure C.3 Electron charge misidentification rate.

C.2 Jet Ratio Plots

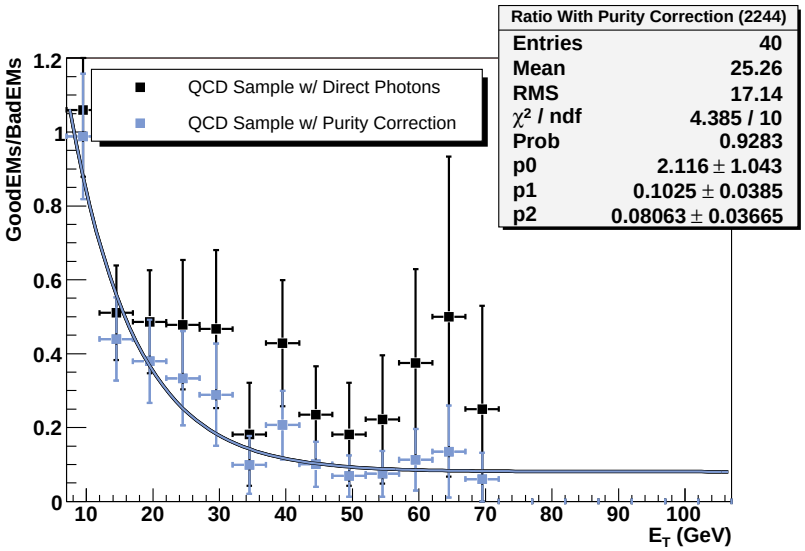

Figure C.4 Jet ratio with MC purity correction for $0.22 <| \eta_{CAL^D} |< 0.44$

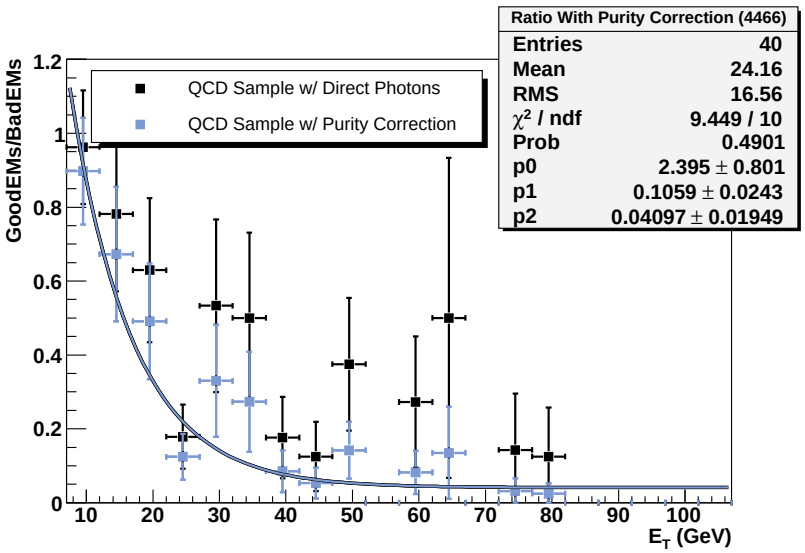

Figure C.5 Jet ratio with MC purity correction for $0.44 <| \eta_{CAL^D} |< 0.66$

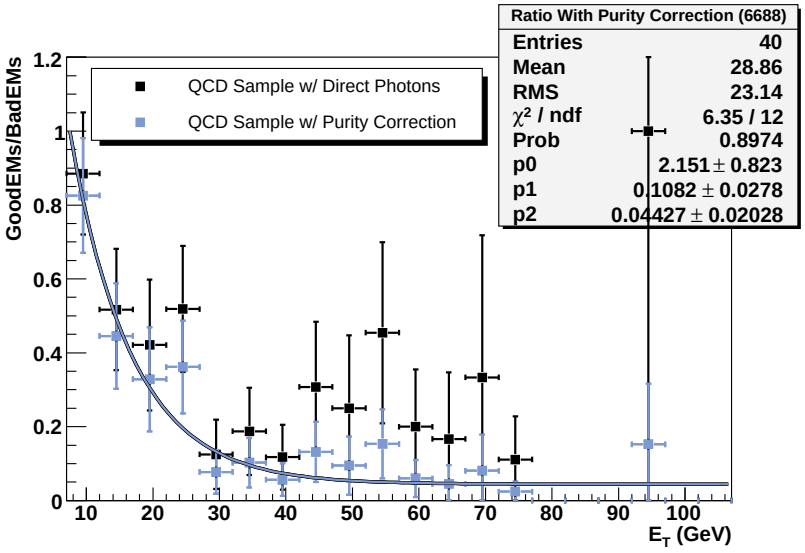

Figure C.6 Jet ratio with MC purity correction for $0.66 < |\eta_{CAL^D}| < 0.88$

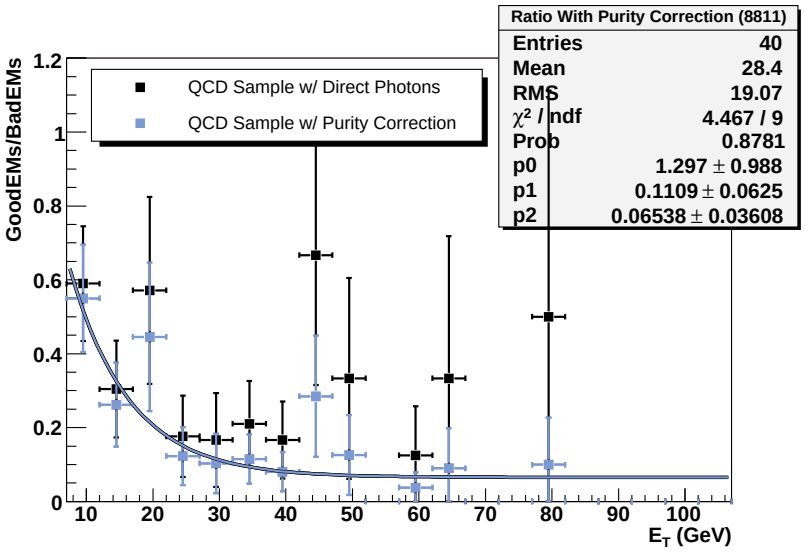

Figure C.7 Jet ratio with MC purity correction for $0.88 < |\eta_{CAL^D}| < 1.1$

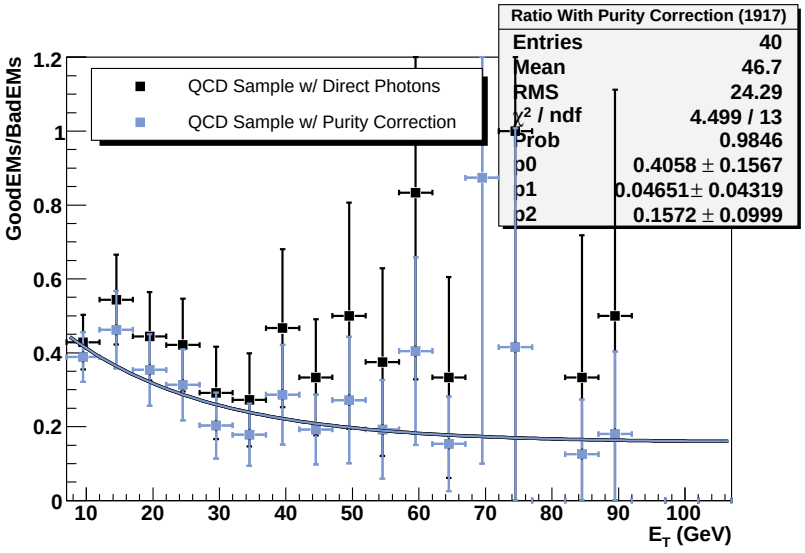

Figure C.8 Jet ratio with MC purity correction for $1.7 < |\eta_{CALD}| < 1.9$

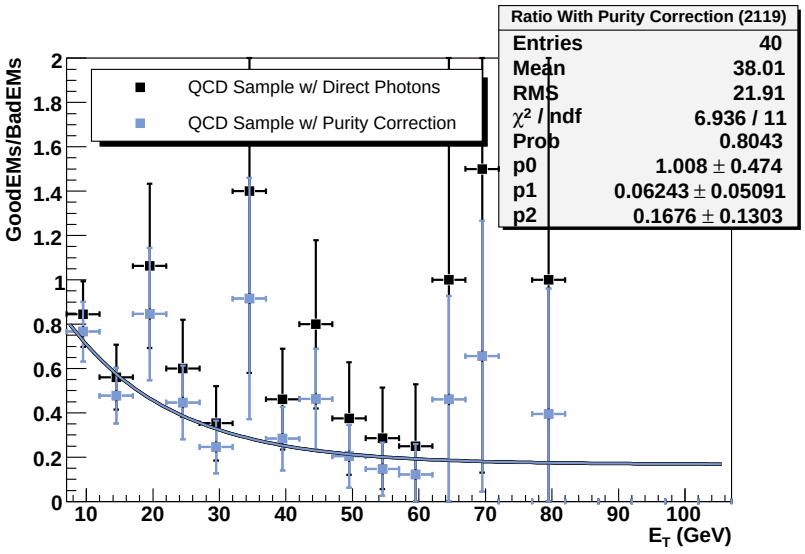

Figure C.9 Jet ratio with MC purity correction for $1.9 < |\eta_{CALD}| < 2.1$

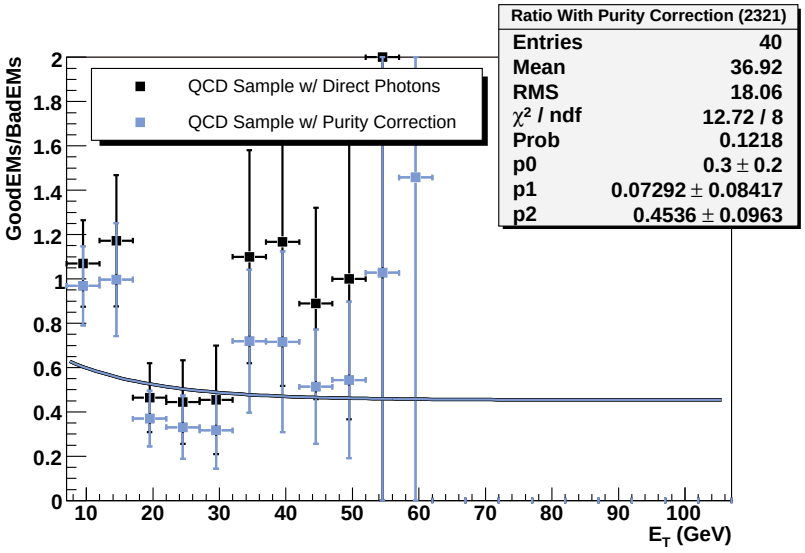

Figure C.10 Jet ratio with MC purity correction for $2.1 < |\eta_{CALD}| < 2.3$

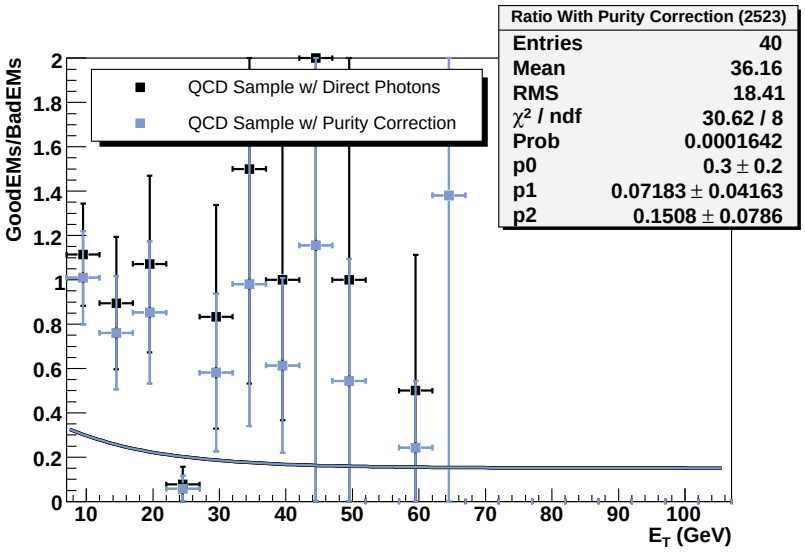

Figure C.11 Jet ratio with MC purity correction for $2.3 < |\eta_{CALD}| < 2.5$

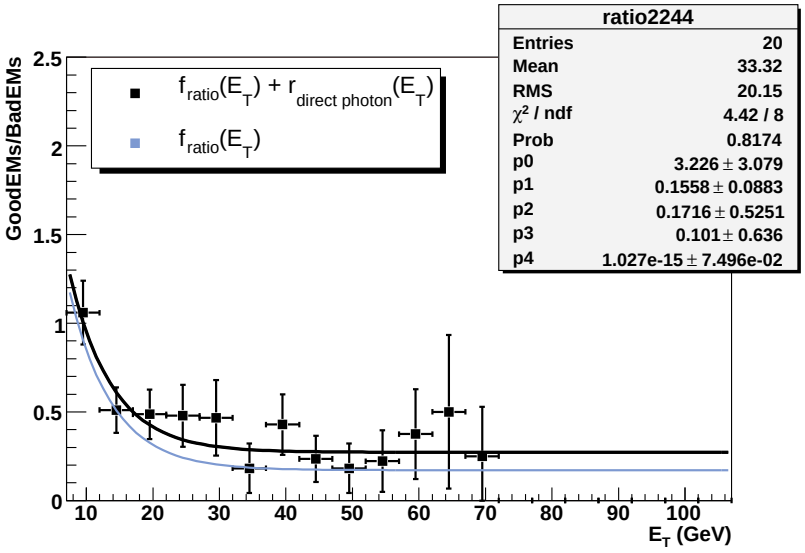

Figure C.12 Jet ratio with fit method for $0.22 < |\eta_{CALD}| < 0.44$

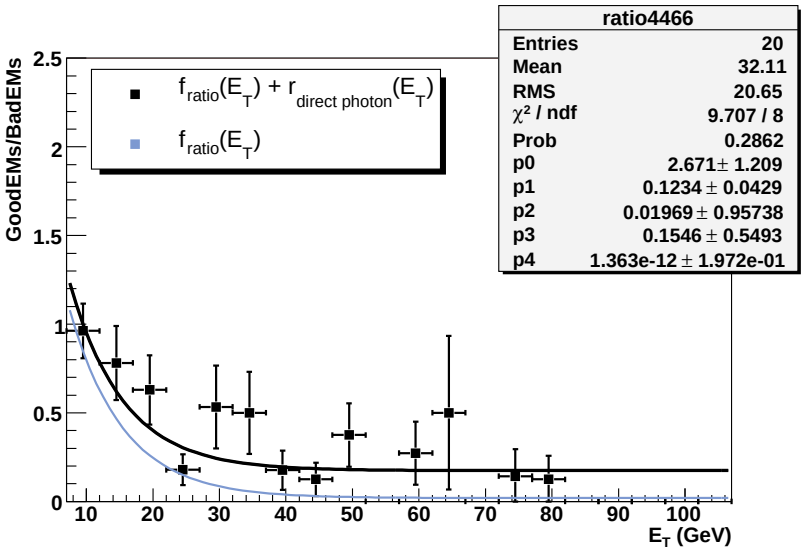

Figure C.13 Jet ratio with fit method for $0.44 < |\eta_{CALD}| < 0.66$

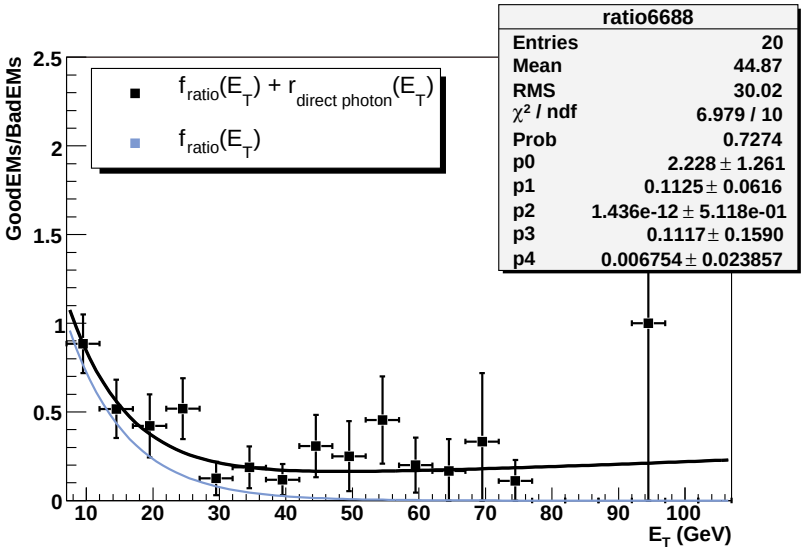

Figure C.14 Jet ratio with fit method for $0.66 < |\eta_{CALD}| < 0.88$

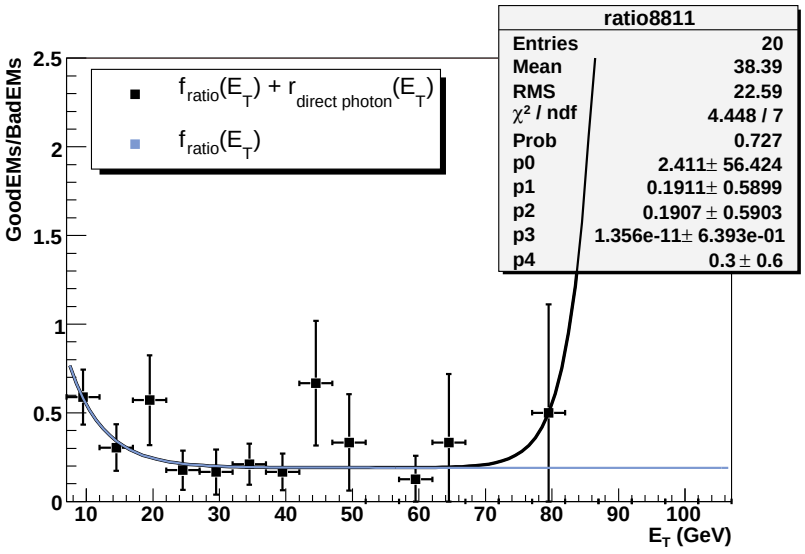

Figure C.15 Jet ratio with fit method for $0.88 < |\eta_{CALD}| < 1.1$

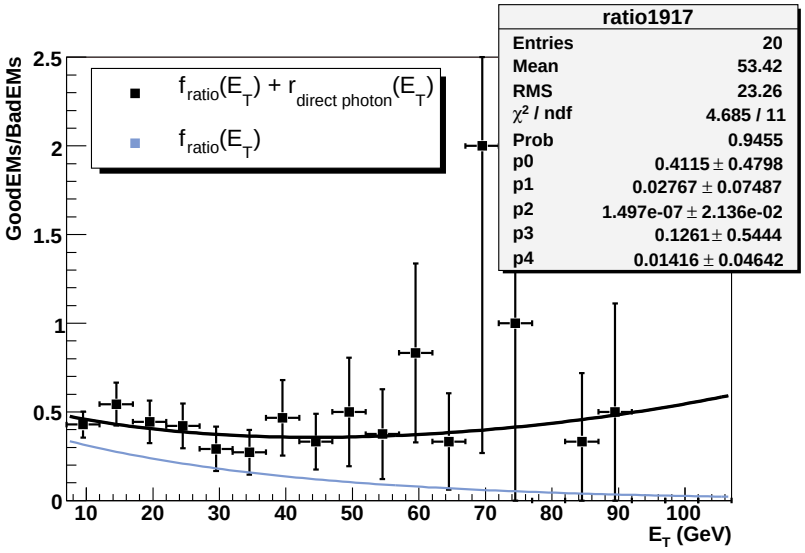

Figure C.16 Jet ratio with fit method for $1.7 <| \eta_{CALD} |< 1.9$

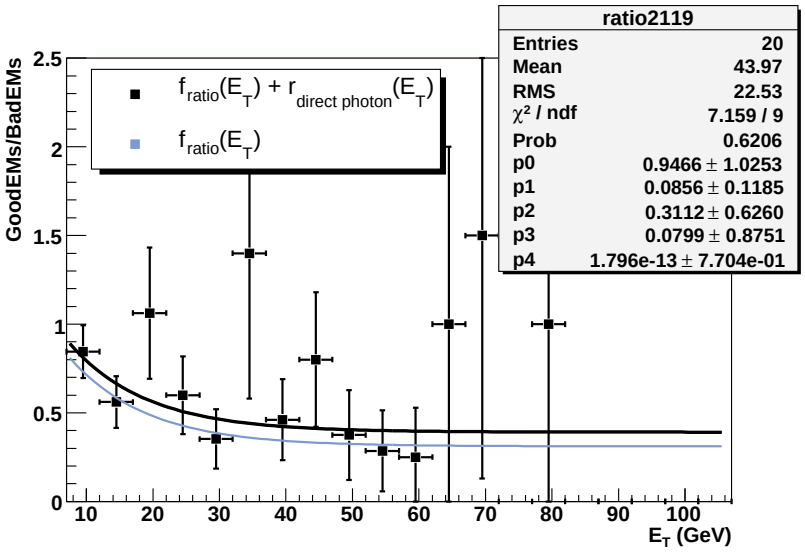

Figure C.17 Jet ratio with fit method for $1.9 <| \eta_{CALD} |< 2.1$

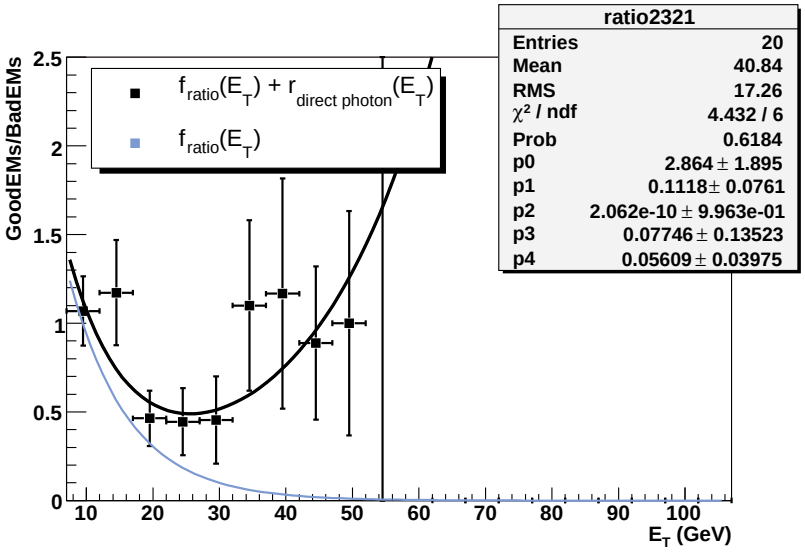

Figure C.18 Jet ratio with fit method for 2.1 $<|\ \eta_{CALD}\ |<$ 2.3

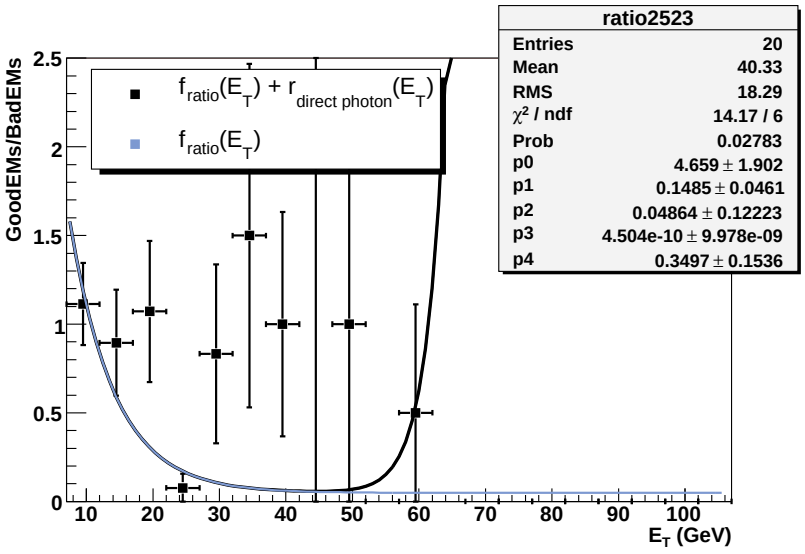

Figure C.19 Jet ratio with fit method for 2.3 $<|\ \eta_{CALD}\ |<$ 2.5

C.3 Extrapolation Fits to the MC Photon E_T Spectra

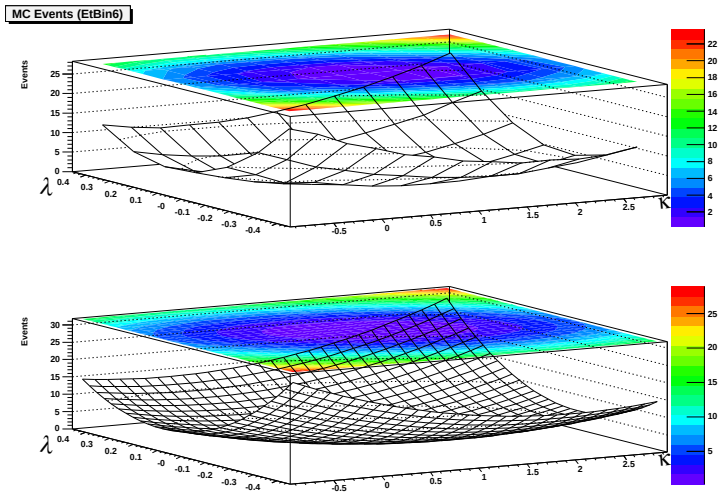

Figure C.20 Expected number of $W\gamma$ Monte Carlo events for photons with 176 GeV < E_T < 241 GeV. The top plot is the expectation from 91 Monte Carlo samples. The bottom plot is a fit to the top plot.

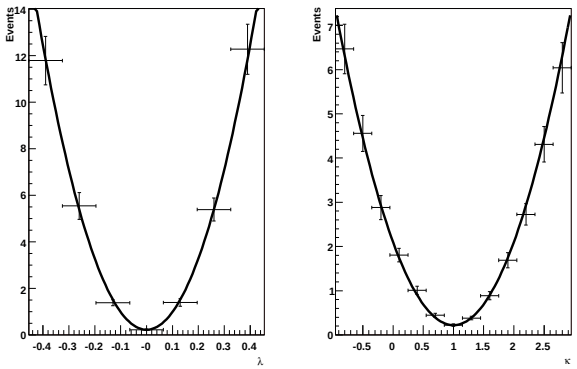

Figure C.21 Expected number of $W\gamma$ Monte Carlo events for photons with 176 GeV < E_T < 241 GeV. The plot on the left is for $\kappa = 1$. The plot on the right is for $\lambda = 0$. The points with errors are from the Monte Carlo samples. The black curve is the fit to the expected number of events.

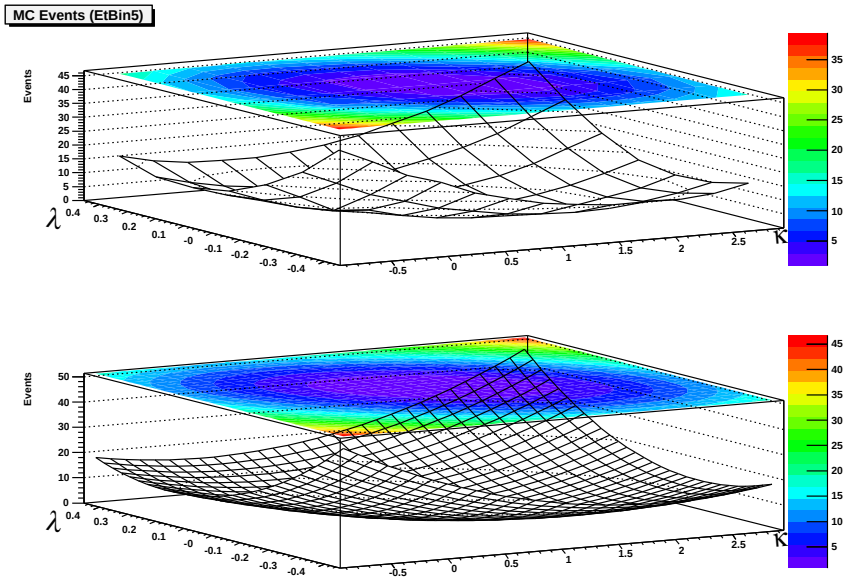

Figure C.22 Expected number of $W\gamma$ Monte Carlo events for photons with 128 GeV < E_T < 176 GeV. The top plot is the expectation from 91 Monte Carlo samples. The bottom plot is a fit to the top plot.

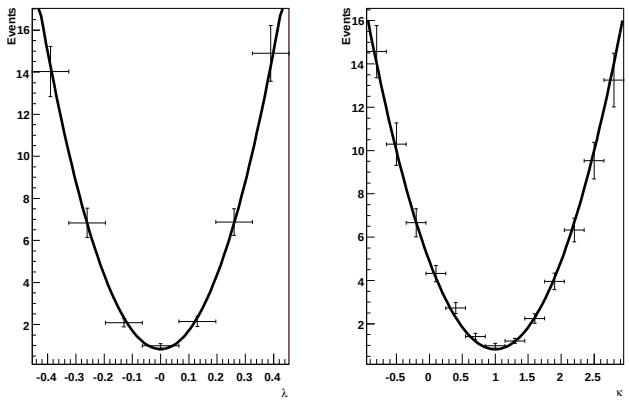

Figure C.23 Expected number of $W\gamma$ Monte Carlo events for photons with 128 GeV < E_T < 176 GeV. The plot on the left is for $\kappa = 1$. The plot on the right is for $\lambda = 0$. The points with errors are from the Monte Carlo samples. The black curve is the fit to the expected number of events.

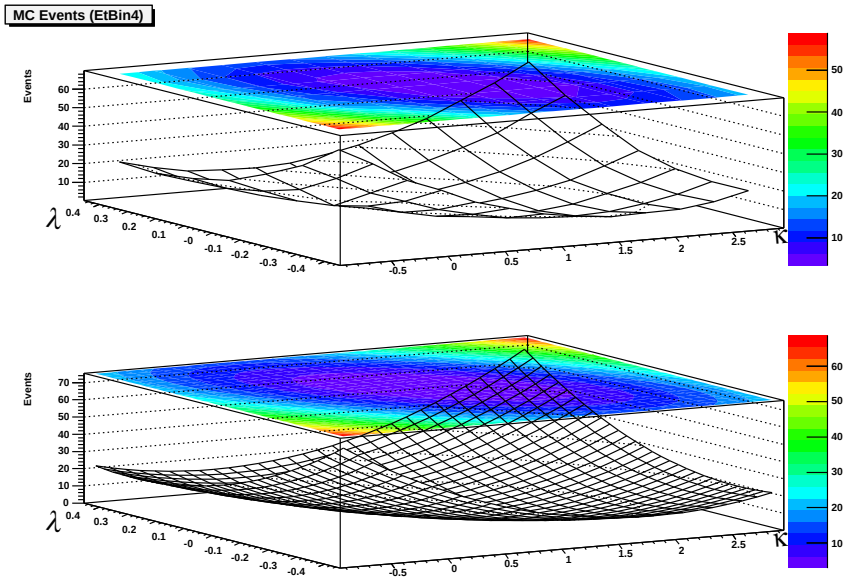

Figure C.24 Expected number of $W\gamma$ Monte Carlo events for photons with 91 $GeV < E_T < 176$ GeV. The top plot is the expectation from 91 Monte Carlo samples. The bottom plot is a fit to the top plot.

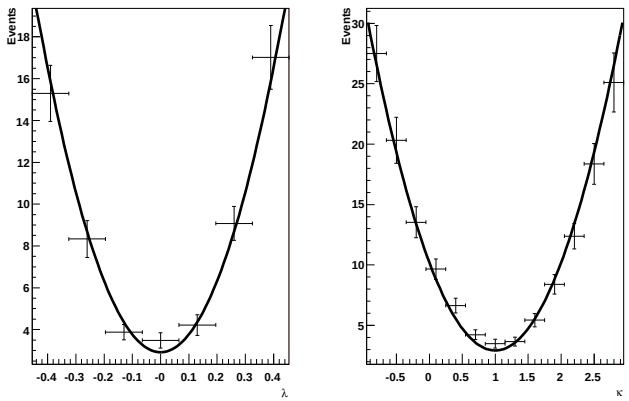

Figure C.25 Expected number of $W\gamma$ Monte Carlo events for photons with 91 $GeV < E_T < 176$ GeV. The plot on the left is for $\kappa = 1$. The plot on the right is for $\lambda = 0$. The points with errors are from the Monte Carlo samples. The black curve is the fit to the expected number of events.

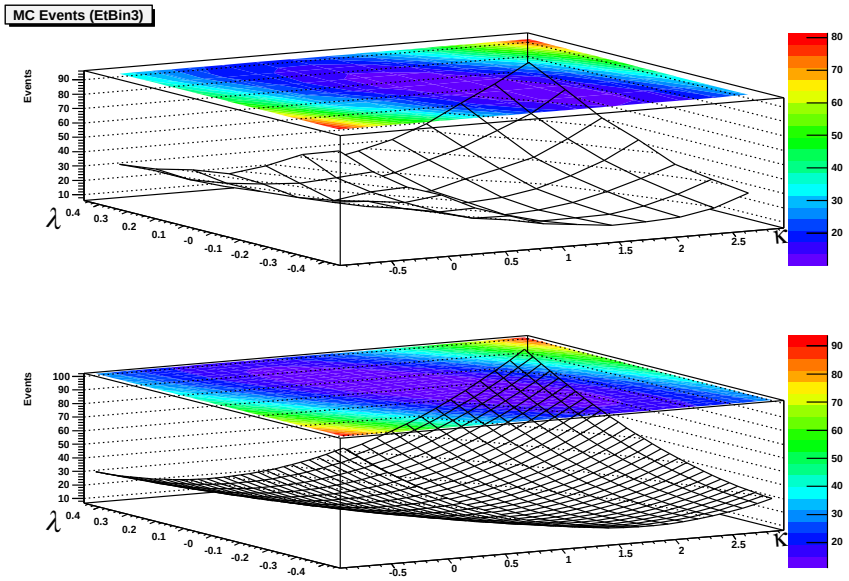

Figure C.26 Expected number of $W\gamma$ Monte Carlo events for photons with $62\ GeV < E_T < 91\ GeV$. The top plot is the expectation from 91 Monte Carlo samples. The bottom plot is a fit to the top plot.

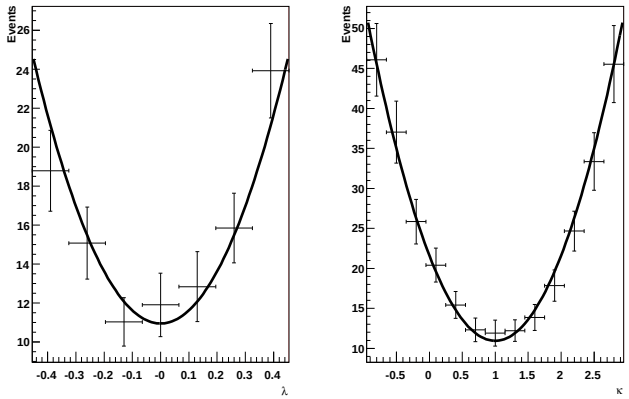

Figure C.27 Expected number of $W\gamma$ Monte Carlo events for photons with $62\ GeV < E_T < 91\ GeV$. The plot on the left is for $\kappa = 1$. The plot on the right is for $\lambda = 0$. The points with errors are from the Monte Carlo samples. The black curve is the fit to the expected number of events.

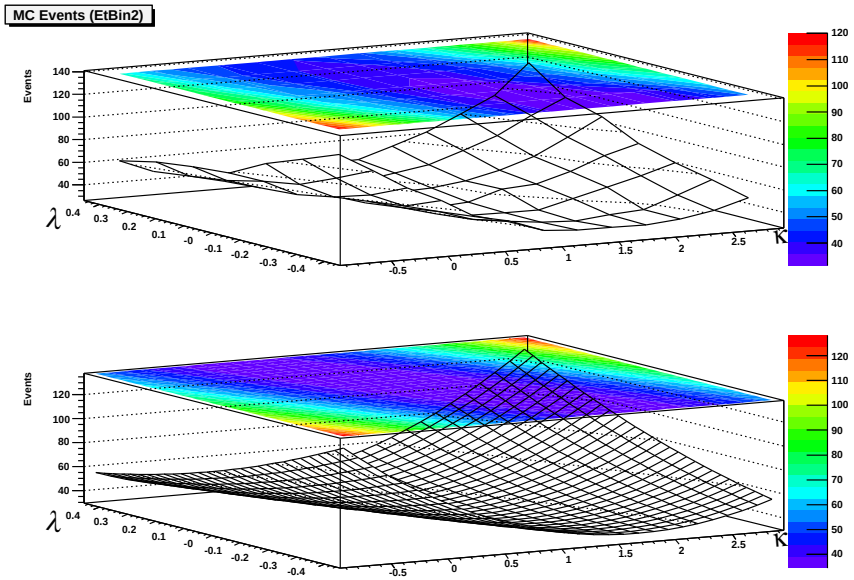

Figure C.28 Expected number of $W\gamma$ Monte Carlo events for photons with $40\ GeV < E_T < 62\ GeV$. The top plot is the expectation from 91 Monte Carlo samples. The bottom plot is a fit to the top plot.

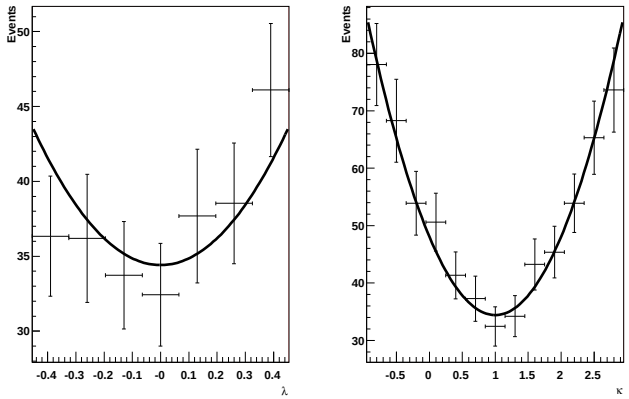

Figure C.29 Expected number of $W\gamma$ Monte Carlo events for photons with $40\ GeV < E_T < 62\ GeV$. The plot on the left is for $\kappa = 1$. The plot on the right is for $\lambda = 0$. The points with errors are from the Monte Carlo samples. The black curve is the fit to the expected number of events.

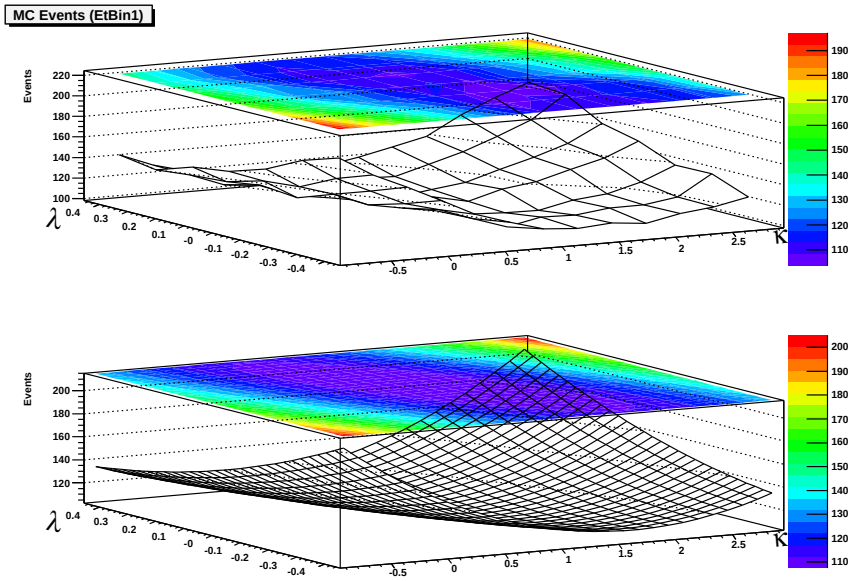

Figure C.30 Expected number of $W\gamma$ Monte Carlo events for photons with 23 $GeV <$ $E_T < 40$ GeV. The top plot is the expectation from 91 Monte Carlo samples. The bottom plot is a fit to the top plot.

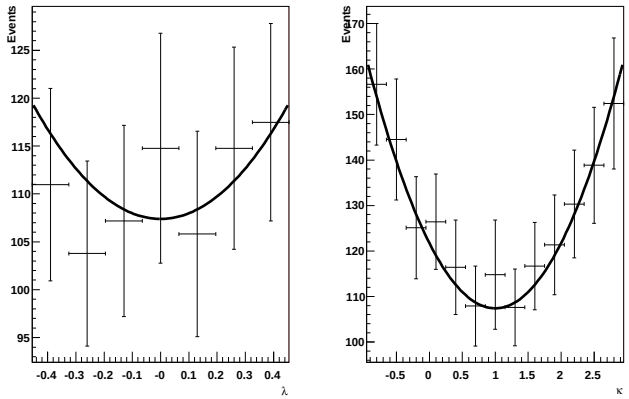

Figure C.31 Expected number of $W\gamma$ Monte Carlo events for photons with 23 $GeV <$ $E_T < 40$ GeV. The plot on the left is for $\kappa = 1$. The plot on the right is for $\lambda = 0$. The points with errors are from the Monte Carlo samples. The black curve is the fit to the expected number of events.

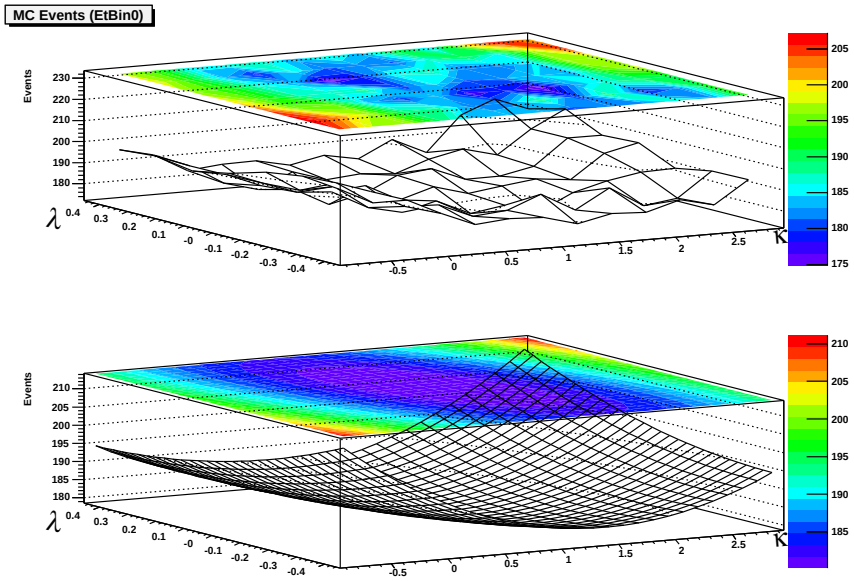

Figure C.32 Expected number of $W\gamma$ Monte Carlo events for photons with 11 $GeV < E_T < 23$ GeV. The top plot is the expectation from 91 Monte Carlo samples. The bottom plot is a fit to the top plot.

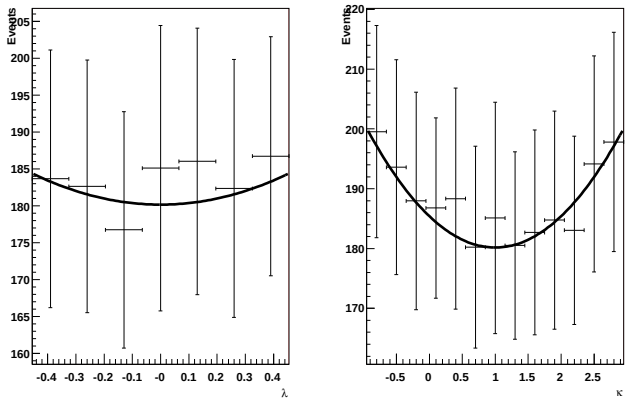

Figure C.33 Expected number of $W\gamma$ Monte Carlo events for photons with 11 $GeV < E_T < 23$ GeV. The plot on the left is for $\kappa = 1$. The plot on the right is for $\lambda = 0$. The points with errors are from the Monte Carlo samples. The black curve is the fit to the expected number of events.

Appendix D
Glossary of Terms

attenuation length: The attenuation length is a measure of the light intensity that is lost. It is related to the light intensity by the following relation: $I(d) = I_0 \mathrm{e}^{-\mathrm{d}/\tau}$, where I_0 is the initial intensity, d is the distance traveled, and τ is the attenuation length.

boson: Bosons are objects with an integer value of spin.

center-of-mass: The center-of-mass frame is the Lorentz frame in which the total vector momentum is zero.

compensating sampling calorimeter: Sampling calorimeters alternate between layers of inactive absorbers that induce particle showers and layers of active material that measure the shower propagation. Energy that is deposited in the inactive regions is not measured. Compensation is related to the hadronic showers which can have an EM shower component and a non-EM shower component. Calorimeters can have different responses for the EM and non-EM components. In a compensating calorimeter, the responses are designed to be equal. At DØ invisible channels of energy loss (nuclei recoil, binding energy of nucleon release from nuclei, *etc.*) are compensated for by the nuclear fission in the uranium absorbers.

coupling: A coupling is associated with an interaction vertex and represents

the probability amplitude for the vertex interaction. If applicable, the value of the coupling is related to the relevant classical force law. For example, consider the $ee\gamma$ vertex. The coupling value is equal to the electric-charge of the electron, $e = \sqrt{4\pi\alpha_e}$, just like in classical electrodynamics.

cross section: A cross section represents the probability that an interaction will occur for a given integrated luminosity (the integrated particle flux per unit area).

ΔR: ΔR is the radius in $\eta \times \phi$ space: $\Delta R^2 = \Delta\eta^2 + \Delta\phi^2$.

electroweak forces: The electroweak forces are comprised of the electromagnetic and weak forces. The electromagnetic force is a long-range interaction that is mediated by the massless photon. It is the dominant force of atomic interactions. The weak force is a short-range interaction that is mediated by the massive W and Z bosons. It is probably most commonly recognized as the forced involved in nuclear beta decay.

fermion: Fermions are objects that have a value of spin equal to $n/2$, where n is any odd integer.

field theory: Loosely defined, a field theory is the theory of dynamics for a continuous system. For a detailed introduction to classical field theory see [54]. For a detailed introduction to quantum field theory see [2].

four-momentum: The four-momentum is a Lorentz vector that consists of the energy and the 3-dimensional momentum components.

gauge transformations: A gauge transformation varies the complex phase of a field. For example, under a gauge transformation, one would replace the field, Ψ, with $e^{i\delta}\Psi$, where e is the Euler constant, $i = \sqrt{-1}$, and δ is the phase. The phase can be a scalar or a combination of operators. In the case of $U(1)$ transformations, the phase contains the generator of the $U(1)$ group and is a scalar. In the case of general $SU(N)$ transformations the phase is a linear combination of the generators of the $SU(N)$ group. If the phase is constant with respect to space-time, the transformation is called a global transformation. If the phase is a function of space-time, the transformation is called a local transformation.

hadron: A hadron is a composite particle that consists of quarks that are bound together by the strong color-charged force.

handedness Handedness refers to states that are projected out by the chirality operator, γ^5. A left-handed state (u_L) of a fermion field (u) is formed with the following relation: $u_L = \frac{1}{2}(1 - \gamma^5)u$. A right-handed state ($u_R$) of a fermion field ($u$) is formed with the following relation: $u_R = \frac{1}{2}(1 + \gamma^5)u$. In the limit that the ratio of particle mass to energy goes to zero ($E/m \to 0$), the right-handed state is identical to the positive helicity state, and the left-handed state is identical to the negative helicity state. More information on the chirality operator can be found in [1].

helicity: Particle helicity is defined as the spin component in the direction of the particle motion.

impact parameter: The impact parameter is the distance of closest approach to the beam line.

Lagrangian density: The Lagrangian is a functional formalism from which the equations of motion for a system can be obtained. A Lagrangian is a function of time, generalized coordinates, and the first derivate of the generalized coordinates with respect to time. It is typically taken as the difference between the kinetic energy and potential energy of a system; although it is possible for there to be additional Lagrangian functions that accurately describe the system. If the generalized coordinates are also functions of continuous space, then the Lagrangian becomes a Lagrangian density. It is conventional to simply use the term Lagrangian instead of Lagrangian density. More information about the Lagrangian formalism can be found in [54].

left-handed: See the definition of handedness.

luminosity: Luminosity is the particle flux per unit area. Depending on the context, the term can either refer to the instantaneous luminosity or the integrated luminosity. The instantaneous luminosity is a rate and is given in units of particles per unit area per unit time. The integrated luminosity is the integral of the instantaneous luminosity over time and is given in units of particles per unit area.

multiple interactions Collision events in which there are more than one inelastic collision.

nuclear absorption length: The nuclear absorption length is also known as the

nuclear interaction length. The probability that a hadron will undergo an inelastic nuclear collision while propagating through a medium is given by: $1 - \mathrm{e}^{-\mathrm{d}/\lambda}$, where d is the distance traveled and λ is the absorption length.

parton: A parton is the constituent matter that makes up a nucleon.

prescale: To control the rate of accepted events, it is sometimes necessary to apply a prescale. A prescale randomly inhibits a specified trigger term from firing. At the lowest DØ prescale level, a trigger is randomly considered for only half of the events. At the highest level, it is never considered.

pseudorapidity: The pseudorapidity of a particle is conventionally represented by the variable, η, and is equal to $-\ln[\tan(\theta/2)]$, where θ is the scattering angle of the particle. Pseudorapidity is equivalent to rapidity in the limit that the ratio of the particle mass to energy goes to zero ($m/E \to 0$).

quantum chromodynamics (QCD): QCD is the quantum field theory of the strong color-charge interaction. The term, QCD backgrounds, refers to collision events that are the result of the strong interaction.

quantum number: A quantum number is a conserved quantity of the particle. Examples of quantum numbers are electric-charge, color-charge, and spin.

radiation length: The radiation length is a measure of how much energy an electron will lose when propagating through a medium. It is related to the electron energy by the following relation: $E(d) = E_0 \mathrm{e}^{-\mathrm{d}/\mathrm{X}_0}$, where E_0 is the initial energy, d

is the distance traveled, and X_0 is the radiation length.

rapidity: The rapidity of a particle is equal to $\frac{1}{2}\ln(\frac{\mathrm{E}+\mathrm{p_z}}{\mathrm{E}-\mathrm{p_z}})$, where E is the particle energy and p_z is the projection of the momentum along the beam line. Differences in rapidity are Lorentz invariant. The variable, y, is conventionally used to represent rapidity.

right-handed: See the definition of handedness.

spin: Spin is the intrinsic angular momentum of a particle and is given in units of $\hbar$

strong color-charged force: The strong color-charged force is effectively a short-range force that is mediated by massless gluons. It is the force that binds nucleons inside the atomic nucleus and that binds the quarks inside of the nucleons.

transverse energy: Transverse energy (E_T) is given by the following relation: $E_T = E \times \sin(\theta)$, where E is energy and θ is the scattering angle with respect to the beam line.

underlying event In hadronic collisions, the underlying event refers to the debris of spectator partons which were not directly involved in the inelastic collision.

vector gauge boson: The vector gauge bosons are the mediators of the known forces. Their fields are described by four-vectors and are the theoretically produced in Quantum Field Theory by requiring invariance under local gauge transformations.

Appendix E
List of Acronyms

AA: Alternate Algorithm

AC: Anomalous Coupling

CC: Central Calorimeter

CDF: Collider Detector at Fermilab

CFT: Central Fiber Tracker

CHF: Coarse Hadronic Fraction

CL: Confidence Level

CPS: Central Preshower

DCA: Distance of Closest Approach

DSP: Digital Signal Processors

EC: Endcap Calorimeter

EM: Electromagnetic

EMF: Electromagnetic Fraction

FIFO: first-in/first-out

FPS: Forward Preshower

FSR: Final State Radiation

HTF: Histogram Track Finder

ICD: Intercryostat Detector

L1: Level-1

L1CAL: Level-1 Calorimeter Trigger

L1CTT: Level-1 Central Track Trigger

L1MUON: Level-1 Muon Trigger

L2: Level-2

L2CAL: Level-2 Calorimeter Trigger

L2CTT: Level-2 Central Track Trigger

L2GLOBAL: Level-2 Global Processors

L2MUON: Level-2 Muon Trigger

L2PS: Level-2 Preshower Trigger

L2STT: Level-2 Silicon Track Trigger

L3: Level-3

LM: Luminosity Monitor

LO: Leading-Order

NLLH: Negative Log LikeliHood

MDT: Mini Drift Tubes

MIP: Minimum Ionizing Particle

NLO: Next-to-Leading-Order

PDF: Parton Distribution Functions

PDT: Proportional Drift Tubes

PMCS: Parameterized Monte Carlo Simulation

PMT: Photomultiplier Tubes

PS: Preshower

QCD: Quantum Chromodynamics

RAZ: Radiation Amplitude Zero

RMS: Root Mean Square

SM: Standard Model

SMT: Silicon Microstrip Tracker

VLPC: Visible Light Photon Counter

References

1. F. Halzen, A. Martin, *Quarks and Leptons: An Introductory Course in Modern Particle Physics*. John Wiley and Sons. (1984).

2. M. Peskin, D. Schroeder, *An Introduction to Quantum Field Theory*. Westview Press. (1995).

3. A. Balantekin, Editor-in-Chief, *Journal of Physics G Nuclear and Particle Physics*. Institute of Physics Publishing. (2006).

4. R. Brown, U. Baur, *Zero Zeros After All These (20) Years*. HEP-PH/9909522. (1999).

5. J. Ohnemus, *QCD Corrections to Diboson Production*. Vector Boson Symp. 1995:60-71. (1995).

6. R. Brown, K. Mikaelian, D. Sahdev, *$W^{\pm}Z^0$ and $W^{\pm}\gamma$ Pair Production in νe, pp, and $\bar{p}p$ Collisions*. Phys. Rev. D 20, 1164-1174. (1979).

7. T. Appelquist, G.H. Wu, *The Electroweak Chiral Lagrangian and New Precision Measurements*. Phys. Rev. D 48:3235 (1993).

8. T. Appelquist, G.H. Wu, *The Electroweak Chiral Lagrangian and CP Violating Effects in Technicolor Theories*. Phys. Rev. D 51:240 (1995).

9. E.N. Argyres, *et al.*, *Trilinear Gauge Boson Couplings in the MSSM*. Phys. Lett. B 383:63 (1996).

10. G. Couture, *Anomalous Magnetic And Quadrupole Moments Of The W Boson In The Two Higgs Doublet Model*. Phys. Rev. D 36:859 (1987).

11. J. Ellison, J. Wudka, *Study of Trilinear Gauge Boson Couplings at the Tevatron Collider*. Annu. Rev. Nucl. Part. Sci. **48**, 33. (1998).

12. U. Baur, S. Errede, G. Landsberg, *Rapidity Correlations in $W\gamma$ Production at Hadron Colliders*. Phys. Rev. D **50**, 1917 (1994).

13. *Accelerator Concepts Rookie Books*. (2003). http://www-bdnew.fnal.gov/operations/rookie_books/rbooks.html

14. J. Thompson, *Introduction to Colliding Beams at Fermilab*. FERMILAB-TM-1909. (1994).

15. F. Abe, *et al.*, *The CDF II Detector Technical Design Report*. FERMILAB-PUB-96/390-E. (1996).

16. V. Abazov, *et al.*, *The Upgraded DØ Detector*. FERMILAB-PUB-05/341-E. (2005).

17. R. Yarema, *et al.*, *A Beginners Guide to the SVXII*. FERMILAB-TM-1892. (1994, revised 1996).

18. J. Kowalkowski, *et al.*, *The L2-Muon Trigger Methods and Algorithms*. DØ Note 4756. (2005).

19. A. Khanov, *HTF: Histogramming Method for Finding Tracks*. DØ Note 3778 (2000).

20. G. Borissov, *Ordering a Chaos or ... Technical Details of AA Tracking*. All DØ Meeting. (2003).
http://www-d0.fnal.gov/global_tracking/talks/20030228/talk-adm-030228.ps

21. H. Greenlee, *The DØ Kalman Track Fit*. DØ Note 4304. (2004).

22. Private communication with Andrew Askew. (2007).

23. D. Shpakov, *Forward Preshower Detector Offline Software*. DØ Note 3664. (1999).

24. F. Fleuret, *The DØ Electron/Photon Analysis Package EMAnalyze*. DØ Note 3888. (2001).

25. J. Hays, *et al.*, *Single Electron Efficiencies in p17 Data and Monte Carlo*. DØ Note 5025. (2006).

26. J. Hays, *et al.*, *Electron Likelihood Efficiencies in p17*. DØ Note 5114. (2006).

27. G. Blazey, *et al.*, *Run II Jet Physics*. HEP-EX/0005012v2. (2000).

28. B. Andrieu, E. Busato, *Jet Algorithms in the DØ Run II Software: Description and User's Guide*. DØ Note 4457. (2004).

29. A. Amnon, *Jet ID Optimization*. DØ Note 4919. (2005).

30. P. Calfayan, *et al.*, *Muon Identification Certification for p17 Data*. DØ Note 5157. (2007).

31. O. Peters, *Muon Segment Algorithm*. (2001).
http://www-d0.fnal.gov/nikhef/muon_reco/segmentreco

32. F. Deliot, *The Fit Algorithm in muo_trackreco*. (2000).
http://www-d0.fnal.gov/∼deliot/fitalg.ps

33. Private communication with Boris Tuchming. (2007).

34. A. Askew, A. Lyon, and G. Pawloski, *$W\gamma$ Production: Measurement of the Charge-Signed Photon-Lepton Rapidity Difference and Anomalous $WW\gamma$ Couplings Limits*. DØ Note 5256. (2007).

35. U. Baur, E.L. Berger, *Probing the $WW\gamma$ Vertex at the Tevatron Collider*. Phys. Rev. D **41**, 1476. (1990).

36. T. Sjöstrand *et al.*, *High-Energy-Physics Event Generation with PYTHIA 6.1*. Comp. Phys. Commun. **135**, 238 (2001).

37. *PMCS Home Page*.
http://www-d0.fnal.gov/computing/MonteCarlo/pmcs/pmcs_doc/pmcs.html

38. A. Askew, *Measurement of the $W\gamma \to \mu\nu\gamma$ Cross-Section, Limits on Anomalous Trilinear Vector Boson Couplings, and the Radiation Amplitude Zero in p anti-p Collisions at $\sqrt{s}$ = 1.96 TeV*. UMI-31-68055-MC. (2004).

39. J. Stark, *Understanding and Modelling the CAL Energy Resolution*. W Mass Meeting. (2006).
http://www-d0.hef.kun.nl//fullAgenda.php?ida=a0651

40. S. Eno, M. Verzocchi, J. Zhu, *Direct Measurement of the W Boson Width*. DØ Note 4563. (2004).

41. V.M. Abazov, *et al.*, *Measurement of the $p\overline{p} \to W\gamma + X$ Cross section and Limits on Anomalous $WW\gamma$ Couplings at $\sqrt{s}$=1.96 TeV*. Phys. Rev. D Rapid. Comm. 71, 091108 (2005).

42. V. Buescher *et al.*, *Conclusions of Mini-Workshop on PDF uncertainties and related topics*. DØ Note 4618. (2004).

43. muo_cert documents:
https://plone4.fnal.gov/P1/D0Wiki/object-id/mu_id/muo_cert/
http://www-d0.fnal.gov/d0dist/dist/releases/development/wzreco/doc/
http://www-d0.fnal.gov/d0dist/dist/releases/development/muo_cert/doc/
DØ Note in preparation

44. J. Hays, J. Mitrevski, C. Schwanenberger, *The Program Package em_cert: Version p18-br-20*. DØ Note 5070. (2006).

45. J. Hays, V. Kaushik, J. Mitrevski, O. Mundal, C. Schwanenberger, *Electron Trigger Efficiencies Using Calorimeter Information in p17 Data*. DØ Note 5138. (2006).

46. R. Brun, F. Rademakers, *ROOT - An Object Oriented Data Analysis Framework*. Proceedings AIHENP'96 Workshop, Lausanne, Sep. 1996, Nucl. Inst. & Meth. in Phys. Rev. A 389 (1997) 81-86.

47. Y. Fisyak, J. Womersley, *DØgstar DØ GEANT Simulation of the Total Apparatus Response*. DØ Note 3191. (1997).

48. G. Pawloski *et al.*, *Photon Identification in p17 Data*, DØ Note 4976

49. *Global Trigger Lists Description*.
http://www-d0.fnal.gov/trigger_meister/private/www/tl_desc/global.html

50. Private communication with Volker Buescher. (2007).

51. A. Baden *et al.*, *Measurement of* $d\sigma(Z/\gamma^* \rightarrow ee)/dy$ *at the Tevatron*. DØ Note 5247. (2006).

52. J. Hays, J. Torburg, *Measurement of the W Boson Production Charge Asymmetry in the Electron Channel*. (2005).
http://www-d0.fnal.gov/Run2Physics/d0_private/eb/Run2EB_021/Run2EB_021_03.html.

53. S. Sengupta, *The W Boson Production Charge Asymmetry in the Muon Channel at* $\sqrt{(s)}$*=1.96 TeV*. DØ Note 4855. (2006).

54. H. Goldstein, C. Poole, J. Safko, *Classical Mechanics (*3^{rd} *Edition)*. Addison Wesley. (2002).